

UC Santa Barbara

UC Santa Barbara Electronic Theses and Dissertations

Title

Models of boron nitride fiber coating recession and its impact on ceramic matrix composite strength

Permalink

<https://escholarship.org/uc/item/3gg1d5kz>

Author

Collier, Virginia Elaine

Publication Date

2022

Peer reviewed|Thesis/dissertation

University of California
Santa Barbara

Models of boron nitride fiber coating recession and its impact on ceramic matrix composite strength

A dissertation submitted in partial satisfaction
of the requirements for the degree

Doctor of Philosophy
in
Materials

by

Virginia Elaine Collier

Committee in charge:

Professor Matthew R. Begley, Chair
Professor Michael J. Gordon
Professor Carlos G. Levi
Professor Frank W. Zok

September 2022

The Dissertation of Virginia Elaine Collier is approved.

Professor Michael J. Gordon

Professor Carlos G. Levi

Professor Frank W. Zok

Professor Matthew R. Begley, Committee Chair

August 2022

Models of boron nitride fiber coating recession and its impact on ceramic matrix
composite strength

Copyright © 2022

by

Virginia Elaine Collier

Acknowledgements

I would be remiss to not acknowledge those who not only helped me through the trials and tribulations of graduate studies but also shaped me into a better scientist.

First, I would like to thank my advisor, Professor Matthew Begley, for his support and guidance. I am grateful for the opportunity he afforded me to bridge my interests in chemistry and mechanics (and his patience as he taught me the latter).

I am also deeply indebted to Professor Frank Zok for his technical expertise in ceramic composites and his mentorship in the art of communication. He played a critical role in teaching me how to effectively communicate my ideas and what it means to conduct research. I would also like to thank my other committee members Professors Carlos Levi and Michael Gordon for their guidance on my research.

Financial support from a variety of sources—the Office of Naval Research, the National Defense Science and Engineering Graduate (NDSEG) Fellowship, and the IHI Turbine Materials Research Center at the University of California, Santa Barbara—is gratefully acknowledged.

I would also like to thank my friends and colleagues at UC Santa Barbara for their feedback and their availability for commiseration and celebration. In addition to the Begley and Zok groups, past and present, I give a heartfelt thanks to Sara Messina, Bhavana Swaminathan, Stephen Sehr, Collin Holgate, and Victoria Christensen for being stalwarts in often turbulent times.

I am grateful for the friends I've made in Santa Barbara as they provided a much needed respite from the stressors of graduate studies. In particular, I am deeply grateful for the friendship and support of Morningstar Bloom and Grayson Baggiolini.

Finally, I thank my family, in particular my parents Susan and Warren and my sister Theo, for their enduring love and for believing in me even when I did not believe in

myself. I am grateful they made the trek to Santa Barbara when obligations made it difficult to travel to see them. I could not have accomplished all that I have without you.

Curriculum Vitæ

Virginia Elaine Collier

Education

- 2017 - 2022 Ph.D. in Materials, University of California, Santa Barbara
2011 - 2015 B.S. Chemical and Biomolecular Engineering, Georgia Institute of
Technology

Publications

6. **V.E. Collier**, F.W. Zok, and M.R. Begley, “Reductions in retained strength in SiC/SiC composites in water vapor due to BN coating recession.” (2022 *in preparation*)
5. S. Sehr, **V.E. Collier**, F.W. Zok, and M.R. Begley, “Oxide growth and stress evolution underneath cracked environmental barrier coatings.” (2022 *in preparation*)
4. S. Sehr, **V.E. Collier**, F.W. Zok, and M.R. Begley, “An integrated analysis of coupled transport, oxidation and creep during oxidation of interior pores in SiC.” *submitted to J. Am. Ceram. Soc.* (2022)
3. F.W. Zok, **V.E. Collier**, and M.R. Begley, “Coating recession effects in ceramic composite strength.” *J. Mech. Phys. Solids* (2021)
2. **V.E. Collier**, W. Xu, R.M. McMeeking, F.W. Zok, and M.R. Begley, “Recession of BN coatings in SiC/SiC composites through reaction with water vapor.” *J. Am. Ceram. Soc.* (2021)
1. **V.E. Collier**, N.C. Ellebracht, G.I. Lindy, E.G. Moschetta, and C.W. Jones, “Kinetic and Mechanistic Examination of Acid-Base Bifunctional Aminosilica Catalysts in Aldol and Nitroaldol Condensations.” *ACS Catal.* (2016)

Conference Presentations

4. V.E. Collier, F.W. Zok, M.R. Begley, “Impact of environmental conditions on coating recession effects in ceramic composite strength” *46th International Conference on Advanced Ceramics and Composites*, Daytona Beach, FL (2022)
3. V.E. Collier, F.W. Zok, M.R. Begley, “Coupling Chemistry and Mechanics to Model Oxidation Embrittlement of SiC/BN/SiC Ceramic Matrix Composites” *44th International Conference on Advanced Ceramics and Composites*, Daytona Beach, FL (2020)
2. V.E. Collier, F.W. Zok, M.R. Begley, “Modeling the Oxidation Embrittlement of SiC/BN/SiC Composites in Water Vapor Environments” *10th International Conference on High Temperature Ceramic Matrix Composites*, Bordeaux, France (2019)

1. V.E. Collier, F.W. Zok, M.R. Begley, “Modeling Oxidation Embrittlement of SiC/SiC Ceramic Matrix Composites” *43rd International Conference on Advanced Ceramics and Composites*, Daytona Beach, FL (2019)

Poster Presentations

2. V.E. Collier, W. Xu, F.W. Zok, R.M. McMeeking, M.R. Begley, “Modeling Interphase Recession in SiC/BN/SiC CMCs” *UCSB Winter Study Group*, Santa Barbara, CA (2020)
1. V.E. Collier, G. I. Lindy, E.G. Moschetta, C.W. Jones, “Mechanistic Examination of Acid-Base Bifunctional Aminosilica Catalysts Through Hammett Analysis” *Spring 2014 AIChE Annual Meeting*, Atlanta, GA (2014)

Research Experience

- 2017 - 2018 **University of California, Santa Barbara**
Research Area: chemo-mechanical response of ceramic composites
- 2013 - 2015 **Georgia Institute of Technology**
Research Area: carbon-carbon bond formation through bifunctional acid-base silica catalysts

Professional Experience

- 2015 - 2017 **BASF Corporation**
Professional Development Program Engineer
- 2013 - 2014 **ExxonMobil Corporation**
Co-op Engineer

Professional Service

- 2019 - 2021 **Beyond Academia**
Multiple leadership positions for annual student-run conference exploring career opportunities beyond the academic track
- 2021 **PIPELINES**
Problem-based Initiatives for Powerful Engagement and Learning In Naval Engineering and Science (PIPELINES)
Designed a project for and mentored a team of 3 undergraduate, community college students in collaboration with Naval Researchers and UC Santa Barbara

Abstract

Models of boron nitride fiber coating recession and its impact on ceramic matrix
composite strength

by

Virginia Elaine Collier

The mechanical response of ceramic matrix composites depends critically on slip along the matrix-fiber interface, which is usually achieved with thin coatings on the fibers. Environmental attack of such coatings (enabled by ingress of reactants through matrix cracks) often leads to significant degradation, through removal of the coating via volatilization and oxidation of exposed SiC surfaces. The extent of the volatilization region extending from the matrix crack plane (*i.e.* recession length) is strongly coupled to the formation of oxide, which ultimately fills open gaps and arrests further reactions. This dissertation presents models to quantify these effects over a broad range of environmental conditions, coating thickness and matrix crack opening. Analytical solutions are presented for the time to close recession gaps via oxidation, and the associated terminal recession lengths obtained near free surfaces. A broad parameter study illustrates that recession behaviors are controlled by a competition between volatilization and oxidation rates. As such, the extent of recession is highly sensitive to water vapor and temperature, providing an explanation for disparate observations of recession under seemingly similar conditions. The extent of recession in the interior of composites is also illustrated, using a straightforward reaction-transport model. Recession lengths decay rapidly away from the free surface, with the extent of recession penetration scaling with maximum recession at the free surface.

Models are also presented to quantify the impact of *BN* coating recession on *SiC/SiC* ceramic matrix composite strength as a function of environmental conditions and crack spacing. Under the assumption of uniform coating recession, an analytical expression for *BN* recession length is combined with composite fragmentation models to calculate retained strength. The results are characterized by two terminal conditions: (i) *SiC* oxidation seals gaps left by coating recession before the coating is entirely volatilized and the retained strength remains high (oxidation dominant); (ii) *BN* recession completely removes the fiber coating before fiber oxidation can seal the gaps and the retained strength hits a minimum (recession dominant). The composite strength of the oxidation dominant condition is described by the single fiber composite (SFC) while the composite strength of the recession dominant condition is described by the dry fiber bundle. The crack spacing sets the coating recession required to reach the minimum composite strength (*i.e.* that of a dry fiber bundle). Composites with large crack spacings exhibit a high residual strength (governed by the SFC model), while composites with small crack spacings always reach the dry fiber bundle limit prior to gap closure. Trends of retained strength with temperature and water vapor are complex, yet are generally inversely related to the coating recession length. Hot, wet environments (1000°C, 1 atm water vapor) lead to the oxidation dominant regime with minimal coating recession and high residual strength while cold, dry environments (700°C, 0.01 atm water vapor) lead to the recession dominant regime and low residual strengths.

Contents

Curriculum Vitae	vi
Abstract	viii
List of Figures	xii
List of Tables	xvii
1 Introduction	1
1.1 Background	1
1.2 Objective and Scope	8
2 Thermochemistry and Transport of Boron Nitride Recession	13
2.1 Introduction	13
2.2 <i>BN</i> oxidation and volatilization	16
2.3 <i>SiC</i> oxidation	20
2.4 <i>SiC</i> oxidation with interacting oxidants	29
2.5 Estimates for gas phase diffusivity	31
2.6 Key takeaways and future considerations	35
3 Numerical Models for Coupled Recession Along Fibers and Transport Along Matrix Crack	38
3.1 Introduction	38
3.2 Evolution of the recession length	41
3.3 Description of one-dimensional diffusion with a distributed source term	44
3.4 Governing equations for recession profile: normalization and simplification	46
3.5 Details of the numerical scheme and illustrative results	51
3.6 Model validation with experimental results	57
4 Recession of <i>BN</i> Coatings in <i>SiC/SiC</i> Composites through Reaction with Water Vapor	63
4.1 Introduction	63

4.2	Volatilization and oxidation chemistry	68
4.3	Recession at free surfaces: single fiber model	74
4.4	Interior recession: coupling with transport along matrix cracks	80
4.5	Results and discussion	82
4.6	Outlook	92
4.7	Conclusions	94
5	Factors influencing the spatial distribution of coating recession	96
5.1	Introduction	96
5.2	Impact of specimen size, crack opening and coating thickness on interior recession	99
5.3	Critical void volumes associated with rapid filling and rapid evacuation .	105
5.4	Discussion	110
6	Reductions in retained strength in <i>SiC/SiC</i> composites in water vapor due to <i>BN</i> coating recession	111
6.1	Introduction	111
6.2	Strength, recession and oxidation models	116
6.3	Results	122
6.4	Discussion	131
6.5	Conclusions	134
7	Conclusion and recommendations	136
7.1	General conclusions and impact	136
7.2	Future work	138
A	Finite element framework for transport-reaction equations	142
B	Recession Model Code	151
C	Single fiber composite strength	178
D	Strength reduction due to coating recession code	180

List of Figures

1.1	Schematic of (A) transverse view of unidirectional minicomposite architecture and (B) idealized stress-strain response of unidirectional composites	2
1.2	Schematic of the length scales and key mechanisms of fiber coating recession. (A) An applied load introduces matrix cracks that bridge fibers while enabling transport of oxygen and water vapor to the composite interior. (B) Reaction of the oxidants with <i>SiC</i> and <i>BN</i> leads to coating recession; the depth into the composite that experiences coating recession is the recession penetration depth. (C) The concurrent oxidation of <i>SiC</i> and volatilization of <i>BN</i> is illustrated at the fiber level.	6
2.1	Schematic for <i>BN</i> oxidation/volatilization and <i>SiC</i> oxidation	14
2.2	Comparison of manual calculations from Equation 2.8 at $p_{total} = 1$ atm with FactSage results for (A) 1% water vapor and (B) 10% water vapor. Boria activity was fixed at 0.25 for both conditions.	18
2.3	Change in free energy for commonly reported volatile borohydroxide species	19
2.4	Linear to parabolic transition for Hi-Nicalon-S fibers [1] at 1000°C. The transition from linear to parabolic occurs after approximately 12 minutes of exposure.	22
2.5	Parabolic rate constants for bulk <i>SiC</i> (Reference [2, 3]), various generations of <i>SiC</i> fibers (References [1, 4, 5]), and silicon (Reference [6]). All rate constants were determined in 1 atm O_2 with the exception of Hi-Nicalon-S and Tyranno SA fibers (dry air, 0.2 atm O_2)	25
2.6	Linear rate constants for CVD <i>SiC</i> (Reference [2]), Hi-Nicalon-S fibers (Reference [1]), and silicon in oxygen (Reference [6]). Rate constants for CVD <i>SiC</i> and silicon are from exposure to 1 atm O_2 while the rate constant for Hi-Nicalon-S is from dry air exposure (0.2 atm O_2).	27
2.7	Comparison of parabolic rate constants from oxidation experiments of CVD <i>SiC</i> at 1100°C (blue circles, from Reference[7]), results of curve fitting the oxidation data (black line), and rate constants calculated using oxidation data from Hi-Nicalon-S fibers in dry air and steam (green line, rate constants from References [1, 8]).	31

2.8	Diffusion coefficient behavior as a function of (A) normalized time and (B) initial channel width	35
3.1	Schematic of flux in composite	42
3.2	Impact of temperature and water vapor on (A) α_M and (B) α_A/\tilde{L}_R for crack length $a = 1\text{ mm}$, crack height $h = 1\ \mu\text{m}$, and initial <i>BN</i> coating thickness $\Delta_o = 0.35\ \mu\text{m}$	49
3.3	Impact of crack height h , initial <i>BN</i> coating thickness Δ_o , and crack length a on (A) α_M and (B) α_A/\tilde{L}_R at 1000°C and 1 atm water vapor.	50
3.4	Impact of number of elements, N_{el} , on (A) $H_xB_yO_z$ concentration and (B) recession length profile. The number of time steps, N_t , was held constant at 300. Simulations were run for 750°C , 0.1 atm water vapor, $0.3\ \mu\text{m}$ initial <i>BN</i> coating thickness, 1 mm crack length, and $1\ \mu\text{m}$ crack height.	54
3.5	Impact of number of time steps, N_t , on (A) $H_xB_yO_z$ concentration and (B) recession length profile. The number of elements, N_{el} , was held constant at 200. Simulations were run for 750°C , 0.1 atm water vapor, $0.3\ \mu\text{m}$ initial <i>BN</i> coating thickness, 1 mm crack length, and $1\ \mu\text{m}$ crack height.	55
3.6	A comparison of terminal ($t = t_c$) (A) $H_xB_yO_z$ concentration profile and (B) recession length profile for various environmental conditions. All results were run for the case of $0.3\ \mu\text{m}$ initial <i>BN</i> coating thickness, 1 mm crack length, and $1\ \mu\text{m}$ crack height.	57
3.7	Recession model comparison to experimental observations from Jacobson et al. [9] for (A) $\Delta_o \approx 0.5\ \mu\text{m}$, 700°C , 10% H_2O/O_2 ; (B) $\Delta_o \approx 1.0\ \mu\text{m}$, 700°C , 1% H_2O/O_2 ; (C) $\Delta_o \approx 1.0\ \mu\text{m}$, 800°C , 1% H_2O/O_2 . The <i>BN</i> coating recession model developed by Jacobson et al. is included as the dashed lines.	61
4.1	(A) Schematic illustration of a ceramic matrix composite with a matrix crack that allows ingress of reactants that lead to <i>BN</i> removal. (B) Schematic of recession gaps that allow for transport of reaction products from coating reaction fronts to the matrix crack plane that allows egress to the environment. (C) Schematic of behavior at the single fiber level, showing the volatilization front (in black) and the formation of oxides on the <i>SiC</i> surfaces that eventually close off the recession gap. The black region of the recession front consists of a liquid borosilicate whose exact composition is currently unknown.	64
4.2	Concentration of reaction products at the <i>BN</i> recession front (black regions in Figure 4.1(C)) as a function of temperature for two different boria activities, (A) $a_{B_2O_3} = 1$ and (B) $a_{B_2O_3} = 0.25$. Subsequent figures assume $a_{B_2O_3} = 0.25$	71

4.3	Critical time to close recession gaps (via oxidation of adjacent surfaces): (A) closure times as a function of temperature for various water concentrations, (B) closure times as a function of water concentration for various temperatures. The circles in (B) correspond to conditions with maximum recession lengths, shown in Figure 4.4.	83
4.4	Maximum recession length (at the free surface) as a function of (A) temperature and (B) water content. The result for $p_{H_2O} = 0$ shows increasing recession with increasing temperature because evaporation of boron is the only active mechanism. The maximum recession length for a given temperature is shown by red circles; these correspond to the corresponding circled closure times in Figure 4.3(B).	85
4.5	Maximum recession length (at the free surface) as a function of <i>BN</i> coating thickness, for lower temperatures (blue) and higher temperatures (red); the limits of both regions correspond to water partial pressure, $p_{H_2O} = 10^{-5} atm$ (dry, short recession lengths) and $p_{H_2O} = 1 atm$ (wet, long recession lengths).	87
4.6	(A) Concentration of reaction products at the matrix crack plane as a function of position, at various times during recession. (B) Recession lengths as a function of position along the matrix crack plane. The top curve represents the final recession profile when the recession gaps are filled with oxide.	89
4.7	(A) Recession profiles along the matrix crack plane shown on a log-linear scale, illustrating that the rapid decay towards the interior of the composite is exponential near the free surface. The location at which $L_R(x^*) = 0.37L_R^{max}$ is defined as the penetration distance, x^* , and indicated by the black circle. (B) Penetration distance versus maximum recession length for thousands of cases spanning the operational envelope. The specimen half-width is set to $10 mm$ such that the results are representative a semi-infinite half-space.	90
5.1	Illustration of the effects of void volume on $H_xB_yO_z$ concentration when the void acts as (A) a free surface and (B) a closed volume.	99
5.2	Terminal recession length profiles as a function of position and crack length a . All curves were run for the baseline conditions of $1000^\circ C$, $0.01 atm$ water vapor, and a crack opening of $1 \mu m$	100
5.3	Impact of temperature, water vapor, and initial coating thickness on the ratio of the terminal recession length at the composite interior and exterior as a function of crack length a . Upper bounds for each variable are indicated by solid lines while lower bounds are indicated by dashed lines. The baseline conditions are $1000^\circ C$, $0.01 atm$ water vapor, $0.3 \mu m$ initial <i>BN</i> thickness, and a crack opening of $1 \mu m$ (shown in black).	101

5.4	Terminal recession length profiles as a function of position and crack opening h . All curves were run for the baseline conditions of 1000°C, 0.01 atm water vapor, and a crack length of 1 mm	102
5.5	Contour plots for the ratio of the terminal recession length at the composite interior and exterior as a function of environment, crack opening h , and initial BN coating thickness. All curves were run for the baseline crack length of 0.5 mm	103
5.6	Critical volume required for a void to act as a free surface defined as $C_{void}(\tau = 1) = 0.1C^*$. Void volumes larger than these thresholds may act as perfect sinks, impacting recession at the composite interior.	106
5.7	Illustration of voids in unidirectional composites. If the void volume is large enough, voids can act as free surfaces, significantly decreasing the effective crack length for transport.	108
5.8	Critical volume required for a void to act as a closed volume defined as $C_{void}(\tau = 0.1) = 0.9C^*$. Void volumes smaller than these thresholds will rapidly fill and not impact interior recession.	109
6.1	(A) Schematic of macroscopic specimen with multiple matrix cracks and recession regions near the cracks. (B) Fiber stress distributions near matrix cracks for unit cells with recession. (C) Schematic of recession and oxidation behaviors near a single fiber.	114
6.2	Retained strength as a function of recession length relative to crack spacing for several gauge lengths. The transition from SFC to DFB is indicated by circle markers.	123
6.3	Retained strength as a function of time for several different crack spacings, coating thicknesses. The transition to dry fiber bundle is indicated by circles while closure of the recession gap is indicated by squares. Results were generated using 700°C, 0.15 atm water vapor, initial coating thickness of 0.35 μm , and gauge length of 100 mm	124
6.4	(A) Impact of water vapor on time to gap closure and time to reach bundle strength for various crack spacings and two different gauge lengths. (B) Impact of temperature on time to gap closure and time to reach bundle strength for various crack spacings and two different gauge lengths. . . .	125
6.5	(A) Domain map illustrating mechanism controlling terminal strength as a function of water vapor and temperature; various crack spacings are shown, illustrating that gap closure dominates as crack spacings get larger. (B) Domain map of terminal strength, σ_c^{ult} as a function of water vapor and temperature for a crack spacing of 2 mm	126

6.6	(A) Domain map of terminal strength, σ_c^{ult} ; when the composite reaches the dry fiber bundle limit, the strength is independent of the environment; conversely, the retained strength is high at elevated temperatures and water concentration, because oxidation halts recession prior to significant strength debits. (B) Domain map of terminal time, t_{term}	127
6.7	(A) Retained strength as a function of water vapor for several different temperatures, for a given gauge length and crack spacing. (B) Retained strength as a function of temperature for several different water concentrations, for a given gauge length and crack spacing. (C) Terminal time as a function of water vapor for different temperatures, for a given gauge length and crack spacing. (D) Terminal time as a function of temperature for several different water concentrations, for a given gauge length and crack spacing.	129
6.8	(A) Retained strength as a function of crack spacing as a function for several temperatures and fixed water concentration. (B) Retained strength as a function of crack spacing for several different water concentrations and fixed temperature.	130
6.9	(A) Retained strength as a function of crack spacing as a function for several temperatures and fixed water concentration. (B) Retained strength as a function of crack spacing for several different water concentrations and fixed temperature.	132

List of Tables

2.1	Composition and structure for selected <i>SiC</i> fibers from Reference [10] . . .	24
2.2	Material constants and calculated parameters for calculation of Chapman-Enskog correlation	34
6.1	Baseline properties used in parametric studies	118

Chapter 1

Introduction

1.1 Background

Ceramic matrix composites (CMCs) offer high temperature performance that rivals or exceeds that of metallic superalloys, making them an attractive pathway to improve the performance of gas turbines, nuclear components, and hypersonic vehicles[11–13]. As illustrated in Figure 1.1(A), state-of-the-art CMCs consist of coated fibers embedded in a ceramic matrix. The fine-grained fibers provide high strength at elevated temperatures, while the matrix holds the fibers in position, and enables load sharing between fibers. The fiber coating forms an interphase between the fibers and is included to control the evolution of damage in the composite and yield macroscopic ductility that far exceeds that of the constituents (which are essentially ideally brittle).

The critical role of the fiber coating can be understood by considering the sequence of material damage in a well-made SiC/SiC composite. An idealized stress-strain curve for this process is shown in Figure 1.1(B). Although the following is an idealized description of composite response, it provides a basic understanding of the core concepts guiding

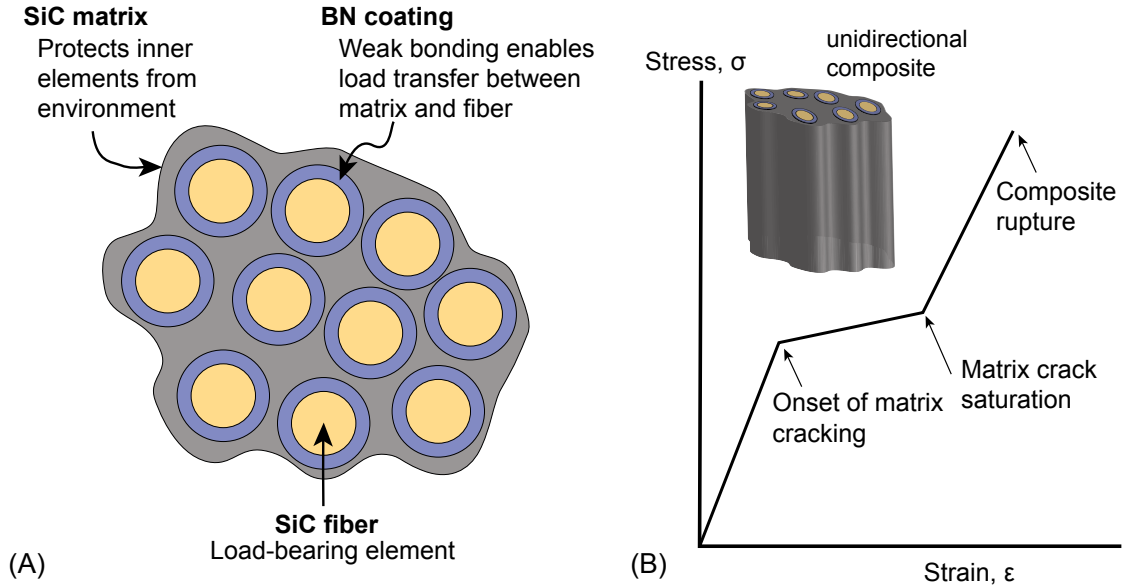


Figure 1.1: Schematic of (A) transverse view of unidirectional minicomposite architecture and (B) idealized stress-strain response of unidirectional composites

composite design and development.

Due to physical limitations of fabrication processes, the matrix has relatively large grains (compared to the fibers) and contains a significant number of either voids, microcracks, or both. As such, the matrix is considerably weaker than the fibers and matrix cracking precedes widespread fiber failures. As a matrix crack forms, it encounters the coating fibers spanning the crack plane; for sufficiently weak interphases, the crack initially deflects from the matrix into the coating (or between the coating and matrix) and reduces the driving force for the matrix crack to penetrate the fibers[14]. The matrix crack eventually works its way around the fibers to span a large (if not complete) fraction of the cross-section of the composite.

The composite can retain significant strength after the formation of a matrix crack

due to the presence of intact fibers that bridge the cracks. While the matrix carries zero stress at the matrix crack plane, frictional sliding between the fibers and matrix leads to increasing stress in the matrix as one moves away from the crack plane (and decreasing fiber stress)[15, 16]. At a sufficient distance from the crack plane, the stresses in the fiber and matrix reach that of the intact composite. That is, the impact of the crack on the fiber and matrix stresses are localized to the sliding region. The physical extent of this sliding region is controlled by the nature of the surfaces created by the fiber/matrix debond (originally triggered by the matrix crack)[17, 18].

Since matrix cracking is controlled by a statistical distribution of matrix flaws, matrix cracking occurs sequentially as the stress on the composite increases[19]. Eventually, the distance between matrix cracks decreases to the point that the sliding regions of two adjacent matrix cracks overlap. When this occurs, the stress on the matrix cannot be increased even upon further increases in applied load, such that the matrix crack spacing remains fixed; this is referred to as ‘crack saturation’. At this point, the matrix carries a small fraction of the overall load and the composite response is roughly equivalent to that of a dry fiber bundle. Subsequent damage to the composite is largely associated with fiber fragmentation, and is commonly described by models invoking Weibull weakest link statistics[16, 20–22].

With few and somewhat nuanced exceptions, disruptions to the above sequence of damage events lead to poor composite performance[23, 24]. If the fibers fail prior to complete matrix cracking (an indicator of low-quality fibers or structural evolution within the fibers [25–27]), strength will be limited and the material will likely fail catastrophically upon the formation of the first matrix crack. If the coating is too strong such that fiber/matrix debonding does not occur (or if frictional sliding is very limited), the stress

concentration of the matrix crack on the leading fibers leads to immediate fiber failures as the crack progresses, again leading to catastrophic failure upon matrix cracking[23]. If frictional sliding is absent between the fibers and matrix—*e.g.* upon chemical removal of the coating—the matrix essentially carries no load and the composite may be weaker, due to the increased fiber stresses[24]. (These qualitative descriptions can be translated into quantitative predictions of response using statistical fragmentation models, as described in Chapter 6 of this work.)

Material selection of the fibers, interphase, and matrix is paramount to the thermochemical stability and mechanical response of CMCs. Two classes of CMCs have been identified as attractive material systems: (*i*) oxide (typically alumina fibers in an aluminosilicate matrix) and (*ii*) non-oxide (typically *SiC* or carbon fibers in a *SiC* matrix). Compared to oxide CMC systems, *SiC*-based composites have nearly double the strength-to-weight ratio and survive at much higher temperatures [13]. To facilitate crack deflection, the interphase is commonly made of layered materials such as pyrolytic carbon (*PyC*) or boron nitride (*BN*)[28]. Although *PyC* has favorable interfacial properties, it undergoes oxidation at low temperatures, leaving *BN* as the most broadly used interphase [29]. As such, the most prevalent example of a high performance CMC for temperatures approaching 1500°C comprises silicon carbide (*SiC*) fiber coated with boron nitride (*BN*) and embedded in a *SiC* matrix; this architecture is referred to as a *SiC/BN/SiC* CMC.

In high temperature environments containing volatile reactive species (notably oxygen and water vapor), the loss of load transfer via frictional sliding is triggered by removal of the *BN* coating [9, 30–35]. The thermochemical processes that lead to this degradation, sometimes referred to as oxidative embrittlement, are illustrated in Figure 1.2. Upon exposure to oxygen and water vapor through a matrix crack (Figure 1.2(A)), the *BN* fiber

coating oxidizes to form boria (B_2O_3) that subsequently volatilizes into various borohydroxide species (generally referenced as $H_xB_yO_z$). This volatilization process creates a gap between the fiber and matrix and a recession length along the fiber axis (Figure 1.2(B, C)). With the fiber coating removed, frictional sliding is lost and the probability of fiber failure increases.

Concurrently, the annular gap created by coating recession exposes the *SiC* fiber and matrix to the oxidative environment, resulting in the formation of silica (SiO_2). Activation of small flaws in the silica scale can lead to the oxide scale acting as a critical flaw, leading to premature fiber failure and a decrease in composite mechanical response[36]. Additionally, growth of silica introduces local stresses that at temperatures below 1200°C can negatively impact fiber mechanical performance [37]. Over time, the silica fills in the gap created by fiber coating recession (Figure 1.2(C)). Upon cooling, the oxide solidifies and can lead to elevated stress concentrations on the fiber[38] and catastrophic failure upon subsequent loading.

While the above is generally appreciated based on observations that span a portion of the relevant environmental space[25–27, 35, 36, 39, 40], critical questions remain regarding the underlying mechanisms. First, the extent of these oxidation embrittlement behaviors is not well-characterized due to the challenge of longitudinal sectioning and imaging the thin fiber coatings (often less than 1 micron thick in the pristine state). Much of the limited experimental evidence for fiber degradation was conducted on bare fibers or fiber tows[25–27, 36]. Of the studies that examined coating recession in composites, most report qualitative observations[41]. Of the experimental observations that report coating recession lengths, average values are reported without spatial context [9, 42, 43]. As such, the recession length distribution along a matrix crack, and the impact of this distribution

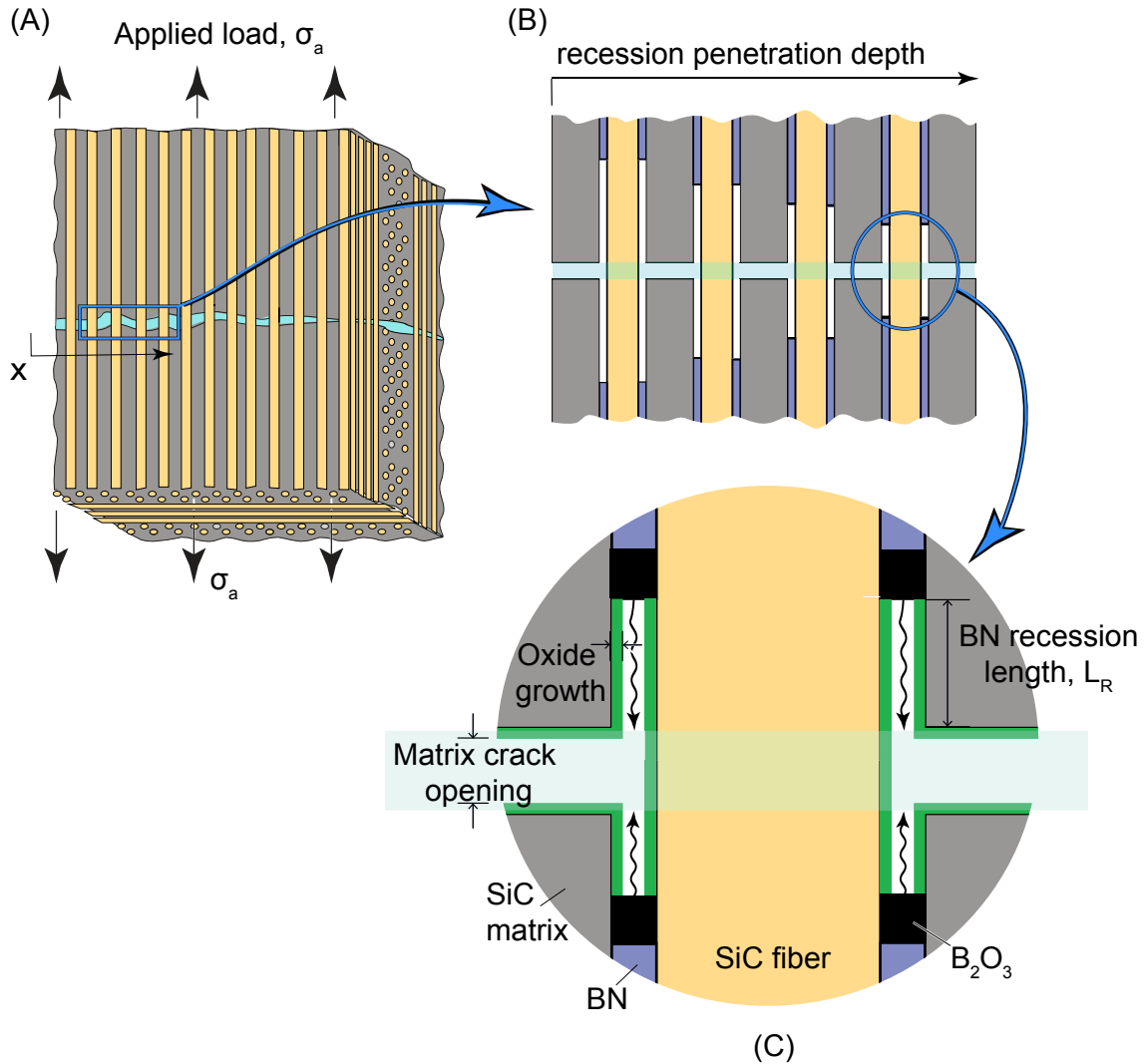


Figure 1.2: Schematic of the length scales and key mechanisms of fiber coating recession. (A) An applied load introduces matrix cracks that bridge fibers while enabling transport of oxygen and water vapor to the composite interior. (B) Reaction of the oxidants with *SiC* and *BN* leads to coating recession; the depth into the composite that experiences coating recession is the recession penetration depth. (C) The concurrent oxidation of *SiC* and volatilization of *BN* is illustrated at the fiber level.

on the extent of recession and composite strength is not well-characterized.

Second, the environmental space that has received experimental attention does not

encompass a significant fraction of the range of relevant operational conditions. Depending on the application, typical service environments for CMCs range from 1 - 30% water vapor and 500- 1500°C. Experiments have been primarily conducted in inert or oxygen-based environments [25–27, 36, 38]; while some attention has been devoted to the impact of water vapor on fiber coating recession, experiments were conducted at a single water vapor concentration [42]. The same limited scope is seen in the investigations of temperature effects on coating recession. Most experimental evidence of oxidative embrittlement has been collected at high temperatures (above 1200°C)[26, 27] or over a narrow temperature range for lower temperatures [9, 25, 36, 42].

Attempts have been made to fill in the above knowledge gaps with modeling[9, 38, 44–46]; while insightful, previous models miss important effects or details. Many theoretical models developed to investigate the impact of environment on the observed strength degradation in composites neglect the fiber coating completely; instead they considered oxidation of bare fibers in a matrix [38]or oxidation of bare tows[44]. Other models address relevant transport considerations such as oxidant transport parallel to and perpendicular to the fibers but do not account for closure of the recession gap due to fiber/matrix oxidation[45]. More recent modeling efforts incorporate *SiC* oxidation and *BN* coating volatilization to predict recession lengths at or near the composite surface [9, 46]. However, these models do not address the distribution of coating recession along the interior of the composite and only the model developed by Parthasarathy et al.[46] considers the impact of fiber coating recession on fiber tow strength.

1.2 Objective and Scope

In light of the background of the previous section, there is a critical need for more advanced models. The principal objective of this work is to develop such models to predict recession behaviors across a broad range of environments and quantify their impact on composite strength. These models are specifically designed to fill in knowledge gaps relating to interactions between coating volatilization, surface oxidation, diffusive transport, and load transfer in the composite, thereby supplementing limited experiments and providing greater insight regarding the breadth and depths of the behaviors described above.

The models presented in this work focus on the following effects: *(i)* volatilization of the fiber coating into volatile species, *(ii)* transport of these reaction products from the reaction site to the matrix crack plane, *(iii)* oxidation of *SiC* surfaces closing the recession channel, and *(iv)* transport along the matrix crack (from the interior of the composite to the free surface). Attention is focused on the intermediate temperature regime (500-1000°C) and mixed oxygen/water vapor environments. Idealization of geometry, chemistry, and mechanics are used to enable a comprehensive view across this broad environmental space without increasing computational cost. The code for these models is documented in the Appendices to allow for straight-forward adaptations to relax these idealizations and account for different thermochemical values and processes.

The models are used to address the following important questions:

- **What are the reactions that lead to coating removal and how do the reaction products change with environment?**
 - The equilibrium concentration of reaction products changes considerably across relevant temperatures and water content[9, 31, 35, 41, 47, 48]; this strongly

impacts recession near free surfaces (which is not transport limited) and interior recession (which can be transport limited). How do these changes impact the extent of recession?

- The composition of reaction products can vary significantly with environment. Does this have any impact on effective diffusivity, such that transport rates depend on composition?

To address these questions, an approach for calculating the volatilization of *BN* coating as a function of environment, namely temperature and water vapor, is presented in Chapter 2, leading to new insight into the environmental conditions that lead to a dominant reaction product. In the same chapter, the impact of reaction product composition on effective diffusivity is discussed.

- **How is transport of the reaction products impacted by coating thickness, matrix crack opening, and interior voids?**

- The extent of recession on the free surface (which is not limited by the build up of reaction products at the matrix crack plane) is strongly impacted by coating thickness, since removing thicker coatings provides faster egress of the reaction products. How strong is this effect over the relevant range of coating thickness?
- Extensive recession in the composite interior requires that reaction products be transported down the recession gap and along the matrix crack plane; under what conditions does the crack opening dominate (leading to more spatially uniform recession lengths)?
- The ideal CMC is fully dense but even in the pristine state, composites have some amount of porosity due to voids and microcracks. It is reasonable to ex-

pect large interior voids to act as effective sinks that store reaction products arriving from intersecting matrix cracks. If the concentration of the reaction products in the pore increase slowly, the edge of the void acts as a free surface. In this case, extensive recession should be observed near pores. On the other hand, if the voids are too small, they will quickly fill to the equilibrium concentration of reaction products and have very little impact on interior recession. What are the critical void sizes that bracket these two behaviors?

These questions are addressed by coupling mass transport and reaction along the fiber axis to mass transport along the matrix crack, resulting in a set of governing equations; these equations are derived in Chapter 3. The transport-reaction equation connects the concentration of the gaseous reaction products to recession length evolution, creating several computational challenges which are detailed and also addressed in Chapter 3. Implications of environmental conditions and key scaling relations on fiber coating recession are presented in Chapter 4 and provide new insights regarding the recession length profile and the maximum recession length at the composite free surface.

Chapter 3 addresses the relative transport rates down the annular gap created by fiber coating recession and the matrix crack that lead to a quasi-equilibrium state. This model is utilized to consider the impacts of matrix crack opening and interior voids on coating recession length distributions as a function of environment in Chapter 5.

- **How does concomitant oxidation of SiC surfaces impact recession?**
 - Like volatilization rates, SiC oxidation rates also vary across relevant tem-

perature and water vapor concentration ranges. If oxidation is sufficiently fast, the transport pathway from the recession site will close and recession will arrest. If oxidation is sufficiently slow, recession lengths may span the entire specimen. How does the controlling reaction (*i.e.* *SiC* oxidation or *BN* volatilization) change across a broad range of temperatures and water vapor concentrations?

- What are the relevant time scales for experiments where extensive recession will and will not be observed?

An overview of *SiC* oxidation constants from the literature is presented in Chapter 2. A framework for *SiC* oxidation in the presence of two independent oxidants (oxygen and water vapor) is developed in Chapter 2 and used in the reaction-diffusion equations to develop new insight into the time scales of *SiC* oxidation and fiber coating recession.

- **What is the impact of recession on composite strength?**

- Recession lengths will expose longer sections of fiber to high stresses associated with matrix cracks. Is this stress elevation large enough to reduce the overall retained strength of the composite?
- What controls the terminal strength– arrested recession lengths due to oxidation or the dry fiber bundle limit (reached when the entire fiber coating is removed?)
- How does crack spacing and coating thickness impact terminal strengths that are impacted by recession?
- What are the time scales needed to reach terminal strength? On the one hand, significant reductions in retained strength may occur after extensive recession.

On the other hand, these reductions may not be reached over relevant time scales. Since coating thickness has a significant impact on recession rates, the time scale to reach terminal strength will depend strongly on the pristine composite architecture.

The impact of fiber coating recession on composite mechanical response remains a critical yet unanswered question. Composite mechanical response is dictated by the load transfer between the matrix and fiber over a length scale that evolves as the fiber coating volatilizes[49]. The recession-driven transition from the single fiber composite to dry fiber bundle response is examined in Chapter 6. The time to achieve this transition and terminal residual strength are connected to environmental conditions and composite geometry through the fiber coating recession model presented in Chapter 4.

While each question reasonably correlates with a chapter in this work, some intra-chapter redundancy is introduced such that each chapter can be read independently.

Chapter 2

Thermochemistry and Transport of Boron Nitride Recession

2.1 Introduction

A durable ceramic matrix composite relies on the fiber coating to efficiently transfer load between fiber and matrix and protect the fibers from unstable matrix crack growth. Interference with this desirable response is initiated by oxidation of the base constituents, namely removal of the boron nitride (*BN*) fiber coating and oxidation of the silicon carbide (*SiC*) fibers and matrix. Previous investigations have established that this complex thermochemical evolution depends on the chemical composition and structure of the constituents in addition to the environmental conditions[9, 29, 41, 43, 50–53]. While the literature broadly agrees on the mechanisms and kinetics that control *SiC* oxidation, there is a lack of consensus on the mechanisms and kinetics of *BN* oxidation and volatilization.

The two concurrent reactions impacting fiber coating recession–*BN* volatilization and

SiC oxidation—are illustrated schematically in Figure 2.1. In the pristine state, the *SiC* and *BN* surfaces are intact. Upon exposure to elevated temperatures and water vapor, *BN* oxidizes to form boria (B_2O_3). In the presence of water vapor, boria can subsequently volatilize as various borohydroxide ($H_xB_yO_z$) species[9, 41, 43, 50–52]. This volatilization leads to recession of the fiber coating, creating a gap between the matrix and fiber.

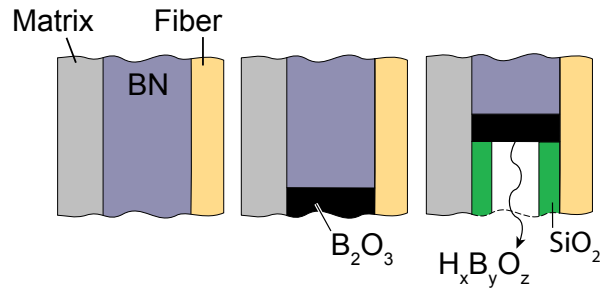


Figure 2.1: Schematic for *BN* oxidation/volatilization and *SiC* oxidation

Simultaneous to *BN* volatilization, oxidation of the fiber and matrix surface occurs. *BN* volatilization terminates once the recession gap is sealed due to *SiC* oxidation. Upon exposure to oxygen and water vapor, *SiC* oxidizes to form silica (SiO_2). This process follows the linear-parabolic behavior proposed by Deal and Grove where a linear rate constant describes early scale growth and a parabolic rate constant applies at later times[6]. The rate constants describing SiO_2 growth on *SiC* have been extensively studied with most attention devoted to the parabolic rate constant. Extensive experimental work has been conducted on bulk *SiC* specimens, such as chemical vapor deposited (CVD) *SiC* and single crystal *SiC*, in dry oxygen and water vapor environments[2, 3, 7, 54–56] but mixed O_2/H_2O environments have received significantly less attention.

SiC fibers, however, have different chemical compositions and crystal structures than the CVD *SiC* commonly used as matrix material[10, 57]. Newer generations of *SiC* fibers

are trending towards the stoichiometric carbon to silicon (C/Si) ratio of bulk SiC but still contain small amounts of oxygen and other elements that may impact oxidation behavior[10]. Once again, oxygen environments have received the most experimental attention.

Most studies have analyzed the previously described SiC oxidation and BN volatilization reactions independently; however, recent studies of the kinetics of SiC oxidation in the presence of BN indicate they may be linked. Silica thickness measurements taken from SiC oxidized in the presence of BN are greater than the thickness expected for oxidation of isolated SiC . This accelerated SiC oxidation has been attributed to various mechanisms such as (i) modification of the silica's network structure by the boron, resulting in a non-protective borosilicate that facilitates further oxidation [58–60] and (ii) etching of the SiC surface that accelerates the reaction of SiC with oxygen at the composite surface[61].

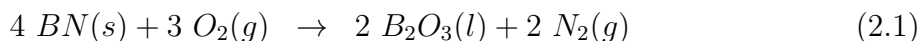
Rate constants have been proposed for the BN -accelerated oxidation of SiC in oxygen [60] but further investigations are needed to rigorously model the impact of boron concentration and water vapor on these values. Recent observations indicate this accelerated oxidation occurs at high boron concentrations (> 90 mol% boron), with minimal effect at lower concentrations[61]. The amount of boron produced by the thin BN coatings (typically < 1 micron) in CMCs and the subsequent volatilization of boron-containing species is assumed to keep the boron concentration below levels that would accelerate SiC oxidation. Given the current ambiguity regarding regimes where boron impacts SiC oxidation, boron-accelerated oxidation of SiC is not considered in this work.

The objective of this chapter is to model the thermochemistry and kinetics of SiC

oxidation and *BN* oxidation-volatilization and do so across a broad range of environments to allow for broad insights regarding coating recession. Volatilization of *BN* fiber coatings is discussed and a method to calculate the concentration of volatile reaction products as a function of environment is presented in Section 2.2. Next, a discussion of *SiC* oxidation is presented in Section 2.3 along with a summary of the existing oxidation constants from the literature. A model for *SiC* oxidation in the presence of both oxygen and water vapor is developed in Section 2.4. Transport considerations related to *SiC* oxidation and *BN* fiber coating recession are presented in Section 2.5. These results are utilized in the coating recession models in Chapter 4 and are applied to questions concerning the role of transport in coating recession in Chapter 5.

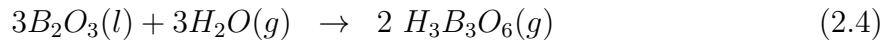
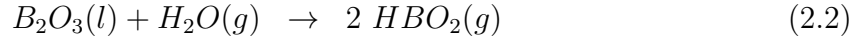
2.2 *BN* oxidation and volatilization

Despite numerous investigations on the oxidation of *BN*, there is little consensus on the rates, rate laws, and oxidation mechanisms. However, there is broad agreement that the process is complex and structure-dependent[29, 43, 50, 53]. Processing parameters such as deposition temperature and selection of pre-cursors also impact *BN* oxidation rates[29, 43, 53], further complicating kinetic analysis across different composites. The prevalent assumption is that *BN* reacts with oxygen to form boria (B_2O_3) in the following manner [41, 50, 51]:

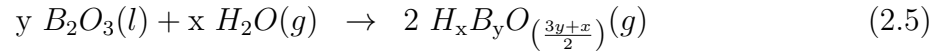


BN oxidation upon exposure to water vapor is not thermodynamically favored and is not considered here[51]. Boria exhibits a low melting temperature of approximately 410°C

and is liquid for the temperatures of interest (500-1000°C). Upon exposure to water vapor, the boria can form borohydroxides of the form $H_xB_yO_z$. The chemical equations for the three most commonly reported reactions are[9, 52]:



These equations can be expressed through a general reaction equation:



At very low water vapor concentrations, evaporation of the liquid boria becomes a plausible removal mechanism as well[50].

While the kinetics of these reactions are not well characterized, the equilibrium concentrations can be established using thermodynamics. The Gibbs free energy equation relates the equilibrium coefficient, K_{eq} to the Gibbs free energy of formation, ΔG :

$$K_{eq} = \exp\left(\frac{-\Delta G}{RT}\right) \quad (2.6)$$

where R is the universal gas constant and T is temperature. The general reaction equation given as Equation 2.5 is used to calculate K_{eq} :

$$K_{eq} = \frac{(C_{H_xB_yO_z})^2}{(a_{B_2O_3})^y (C_{H_2O})^x} \quad (2.7)$$

where $a_{B_2O_3}$ is the activity of boria in the borosilicate, and C is the concentration in

mol/m^3 . Combining Equations 2.6 and 2.7 and rearranging slightly, the general expression for the concentration of gaseous borohydroxide is:

$$C_{H_xB_yO_z} = \left[(a_{B_2O_3})^y (C_{H_2O})^x \exp\left(\frac{-\Delta G}{RT}\right) \right]^{1/2} \quad (2.8)$$

This result is used in Chapter 4 with several assumed values of $a_{B_2O_3}$. In order to account for gas species interactions, an additional set of calculations were computed using FactSage (a chemical thermodynamics database computing system). A comparison of these calculations with the results obtained via Equation 2.8 is shown in Figure 2.2.

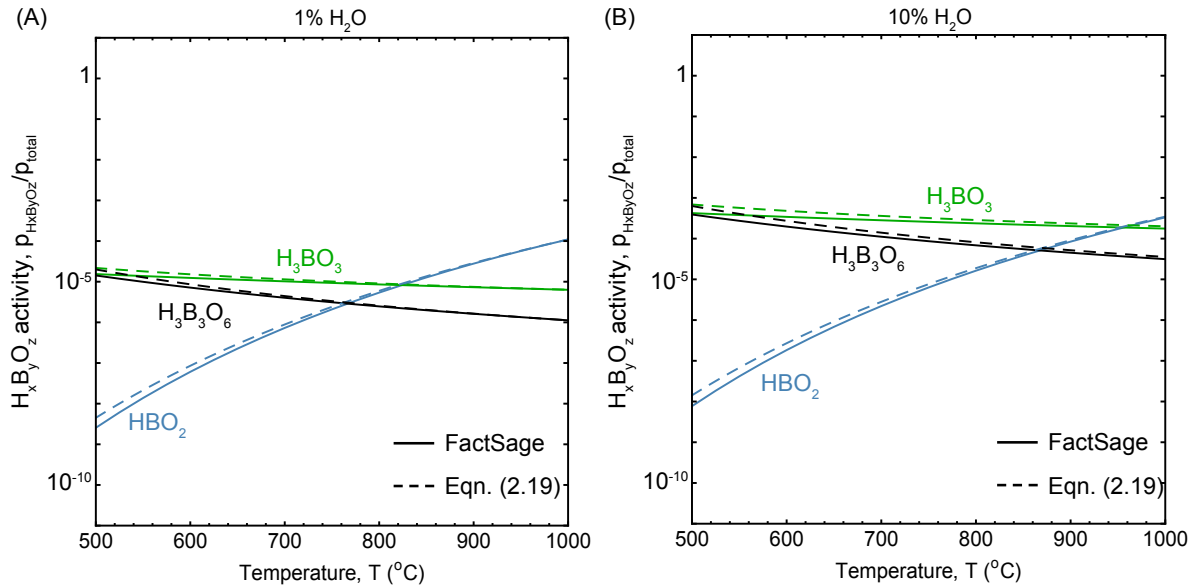


Figure 2.2: Comparison of manual calculations from Equation 2.8 at $p_{total} = 1$ atm with FactSage results for (A) 1% water vapor and (B) 10% water vapor. Boria activity was fixed at 0.25 for both conditions.

The change in free energy yields insight into thermodynamically favorable reactions. As illustrated in Figure 2.3, the two heaviest borohydroxides (H_3BO_3 and $H_3B_3O_6$) are the most thermodynamically favored for the conditions of interest. (Beyond 1100°C,

HBO_2 becomes the more favored volatile species.) Evaporation of liquid boria to gaseous boria is highly unfavorable and has negligible impact on fiber coating volatilization.

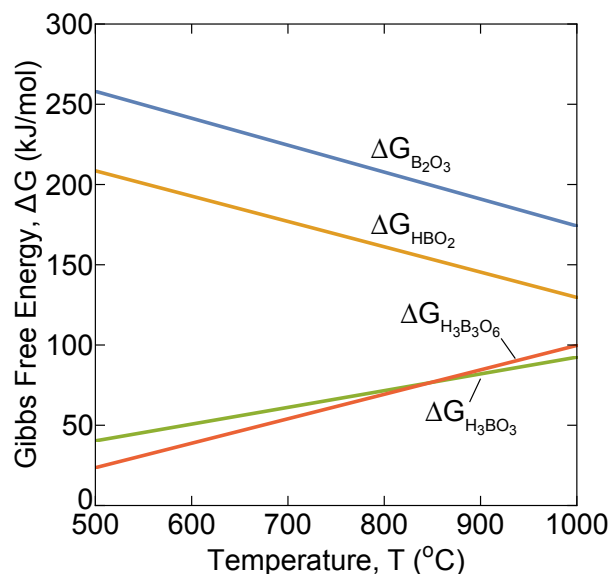
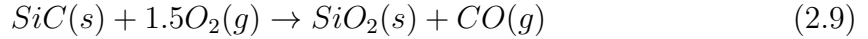


Figure 2.3: Change in free energy for commonly reported volatile borohydroxide species

Drawing comparisons between theory and experimental observations of reaction product partial pressures is restricted by the limited experimental evidence. Mass spectrometry experiments conducted at low oxygen partial pressures for 700°C[52] and 900 to 1100°C[50] indicate the presence of the lightest species, HBO_2 , and to a lesser extent, H_3BO_3 . As shown in Figure 2.2(A), it is evident these species do dominate above approximately 850°C for 1% water vapor. However, at lower temperatures and higher water vapor partial pressures, the partial pressure of $H_3B_3O_6$ is comparable with the lighter species and should be considered in volatilization calculations.

2.3 *SiC* oxidation

When exposed to oxygen or water vapor, *SiC* oxidizes to form a silica (SiO_2) scale, as described by the following reactions:



At short times oxidation is reaction-controlled, resulting in linear oxide growth. At longer times, oxidation is transport-controlled as transport through the existing scale is the rate-limiting step, resulting in parabolic oxide growth. A three-step process was postulated by Deal and Grove to model the growth of SiO_2 scales[6]: (i) transport to the outer surface and absorption at the surface, (ii) diffusion through the oxide, and (iii) reaction at the oxide-substrate interface [6]. Assuming steady-state—that is, the flux is spatially uniform and independent of time—a differential equation relating the oxide thickness as a function of time can be obtained.

$$\frac{d\delta}{dt} = \frac{kC^o/N_1}{1 + k/h + k\delta/D_{eff}} \quad (2.11)$$

where δ is the oxide thickness at time t , k is the first-order reaction rate, C^o is the equilibrium concentration of the oxidant in the oxide, N_1 is the number of oxidant molecules incorporated into a unit volume of the oxide layer, h is a gas-phase transport coefficient, and D_{eff} is the effective diffusion coefficient of the oxide. The solution to this equation is[6]:

$$\delta^2 + A\delta = B(t + \tau) \quad (2.12)$$

where $B = 2D_{eff}C^o/N_1$ is the parabolic rate constant, $B/A = khC^o/(N_1(k + h))$ is the linear rate constant, and τ is a time-shift accounting for any initial oxide. For typical processing pathways for CMCs, native oxides prior to exposure are negligible, hence the following assumes $\tau = 0$. Solving for the oxide thickness as a function of time yields the expression:

$$\frac{\delta}{A/2} = \left[1 + \frac{t}{A^2/4B} \right]^{1/2} - 1 \quad (2.13)$$

The linear and parabolic oxide growth regimes are recovered at short and long times, respectively. For short times (*i.e.*, $t \ll A^2/4B$) oxide growth is linear:

$$\delta \cong \frac{B}{A}t \quad (2.14)$$

The linear rate constant, B/A , is related to the reaction at the oxide-substrate interface and the transport of the oxidant to the substrate through the gas phase. At long times ($t \gg A^2/4B$), Equation 2.13 reduces to:

$$\delta^2 \cong Bt \quad (2.15)$$

The parabolic rate constant, B , is governed by the diffusion of the oxidant through the existing scale.

The transition between the linear and parabolic regimes is illustrated in Figure 2.4. The dashed green lines indicate the asymptotic behavior of the linear and parabolic regimes, while the solid line indicates the normalized scale thickness as a function of normalized time for the full linear-parabolic expression. Where the linear and parabolic projection lines intersect is defined as the time at which the linear regimes transitions to the parabolic expression and is indicated by the solid blue circle; at 1000°C, this transi-

tion occurs after approximately 12 minutes. For times greater than the transition time, oxidation can be accurately described solely by parabolic growth and the linear component can be neglected.

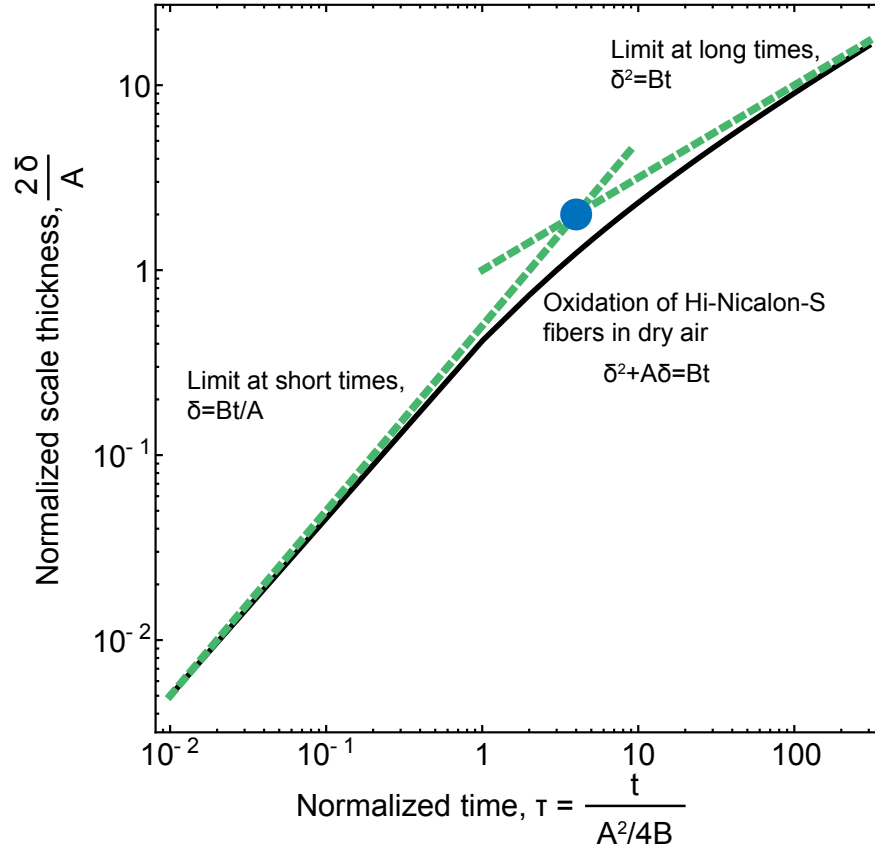


Figure 2.4: Linear to parabolic transition for Hi-Nicalon-S fibers [1] at 1000°C . The transition from linear to parabolic occurs after approximately 12 minutes of exposure.

Although the Deal-Grove model was originally formulated for oxidation of silicon, the framework has since been applied to *SiC* oxidation [7, 62, 63]. Experimental determination of *SiC* oxidation rate constants are established through two methods: (i) direct measurements of oxide thickness using scanning electron microscopy (SEM)[7] or transmission electron microscopy (TEM) [8] and (ii) conversion of mass change measurements to oxide thickness [7, 56, 64]. Direct measurement using TEM is the most

accurate, but requires multiple experiments to capture the time evolution of the oxide scale. Mass change experiments provide uninterrupted data collection but the results must be converted to scale thicknesses using an assumed chemical reaction. The presence of impurities such as aluminum in the reaction environment can impact the weight change, thus complicating interpretation of the kinetic data [63, 65].

Experimental measurements of *SiC* oxidation are most prevalent for high temperatures and dry air or oxygen environments[3, 7, 64, 66–68]. Experimentally derived oxidation constants in water vapor environments and temperatures below 1200°C are not as common but limited studies do exist[2, 7]. The vast majority of the studies from the literature consider bulk *SiC* such as single crystal *SiC* or CVD *SiC* (which is a common matrix material); oxidation data for *SiC* fibers is limited in comparison.

SiC fibers differ from CVD *SiC* in composition and structure but the implications of these differences for oxidation behavior is not well-established. Several generations of *SiC* fibers have been developed for high temperature applications, each with varying structure and chemical composition[10, 57, 69]; some examples are given in Table 2.1. First generation fibers such as Nicalon comprise of crystalline β -*SiC* grains surrounded by an amorphous *Si-C-O* phase and exhibit a high *C/Si* ratio. Process improvements led to second generation fibers (Hi-Nicalon, Tyranno Lox-E) that have a higher amount of crystalline *SiC* and lower oxygen contents. The third generation of fiber development yielded the current state-of-the-art fibers (Hi-Nicalon-S, Tyranno SA) that are nearly stoichiometric and have very low oxygen contents.

Table 2.1: Composition and structure for selected SiC fibers from Reference [10]

	Fiber type	C/Si ratio	Oxygen content (wt%)	Other elements (wt%)	Structure
First Gen	Nicalon 200	1.34	12.0	–	amorphous + crystalline
Second Gen	Hi-Nicalon	1.38	0.5	–	More crystalline
	Tyranno Lox-E	1.59	5.5	2.0 (Ti)	
Third Gen	Hi-Nicalon-S	1.05	<1.0	–	More crystalline
	Tyranno SA	1.10	<0.5	0.6 (Al)	

Of the studies that examine fiber oxidation kinetics, oxygen environments above 1000°C have received the most experimental attention. The following discussion of oxidation rate constants focuses on oxidation in dry oxygen environments, as the data for SiC fiber oxidation in water vapor environments is sparse. Figure 2.5 contains a selection of parabolic rate constants in dry oxygen as a function of temperature for bulk SiC and various generations of SiC fibers, each plotted over the reported experimental temperature ranges [1–5]. The parabolic rate constant for silicon in dry oxygen from Deal and Grove is included for reference [6].

Effects of structure and composition are clearly illustrated by the variation of parabolic rate constants shown in Figure 2.5. Bulk SiC is known to oxidize at different rates depending on the crystallographic orientation of the exposed face [2]. Studies do not consistently report the orientation of the exposed face (such as the case for the data labeled ‘CVD SiC ’ between 1200 and 1400°C in Figure 2.5), adding an additional degree of complexity in interpreting the effects of structure in SiC oxidation data.

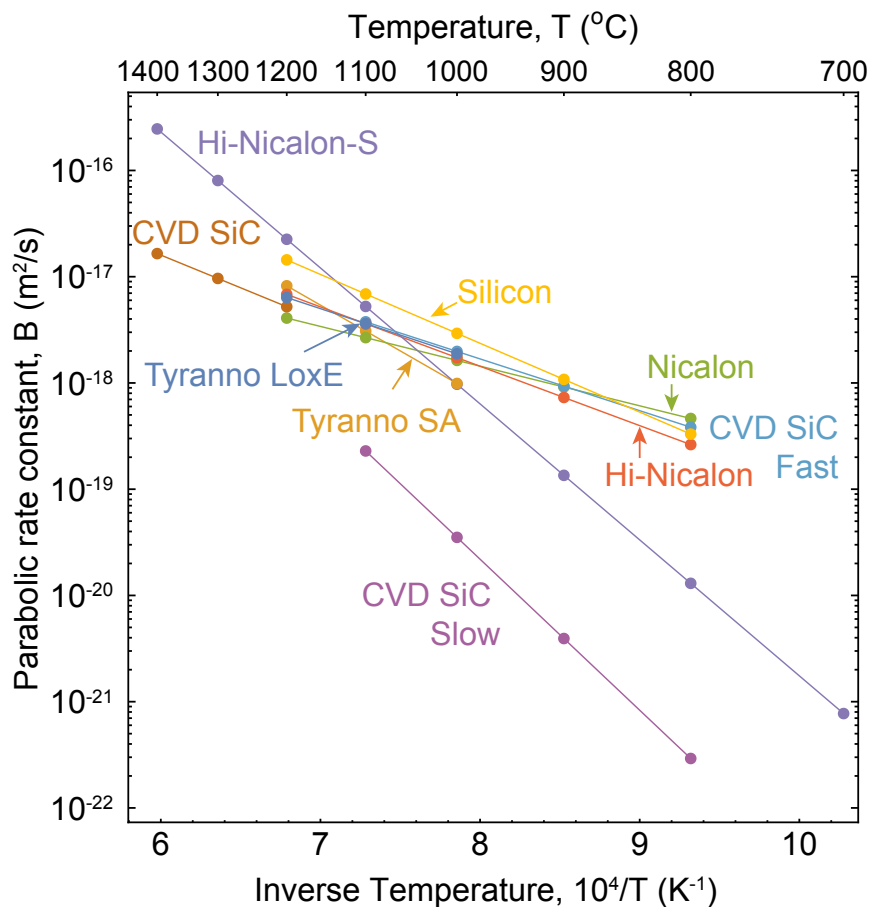


Figure 2.5: Parabolic rate constants for bulk *SiC* (Reference [2, 3]), various generations of *SiC* fibers (References [1, 4, 5]), and silicon (Reference [6]). All rate constants were determined in 1 atm O_2 with the exception of Hi-Nicalon-S and Tyranno SA fibers (dry air, 0.2 atm O_2)

Although isolating the impacts of composition and structure on parabolic oxidation is difficult, the oxidation data presented in Figure 2.5 suggests fiber composition plays an important role. Although the parabolic rate constant determined for Nicalon fibers shows good agreement with that of CVD *SiC*, the two types of *SiC* differ significantly in composition and structure. Conversely, the parabolic rate constant for the nearly stoichiometric and highly crystalline Hi-Nicalon-S fibers differs from the bulk *SiC* rate constants, sometimes by orders of magnitude.

These seemingly counterintuitive trends are potentially related to trade-offs made between oxidation performance and mechanical performance. The presence of free carbon near grain boundaries is suggested to prohibit explosive grain growth, thereby improving a fiber's mechanical properties at high temperatures at the expense of decreased oxidation resistance. This excess carbon, which oxidizes more readily than silicon, is found along grain boundaries and impacts crystalline fibers, such as Hi-Nicalon-S fibers, more than amorphous fibers. The presence of other species such as oxygen and aluminum can increase oxidation rates as well. While it is beyond the scope of this dissertation to investigate these differences, fiber composition is a critical factor when considering oxidation behavior.

The literature contains significantly less experimental data for the linear rate constant, B/A . Some articles instead report A , a pseudo-linear rate constant, in conjunction with the parabolic rate constant. Figure 2.6 plots the linear rate constant versus temperature for various *SiC* subtypes and silicon from Deal and Grove in dry oxygen. Note that the data for Hi-Nicalon-S was converted from reported B and A values while the CVD *SiC* data was reported as B/A . Values for the linear rate constant B/A (and the pseudo-linear rate constant A) exist for other types of *SiC* but exhibit significant scatter and are not reported here[2].

The scatter in linear rate constant is likely a result of the lack of data collection at sufficiently short times. Plotting the linear and parabolic rate constants for Hi-Nicalon-S fibers in dry oxygen [1] at 1000°C indicates the transition from linear to parabolic regimes occurs at roughly 12 minutes (Figure 2.4). Much of the literature does not report data at times less than 1 hour, suggesting the linear rate constants are not well represented by the bulk of the experimental evidence. Furthermore, the linear rate constant will not

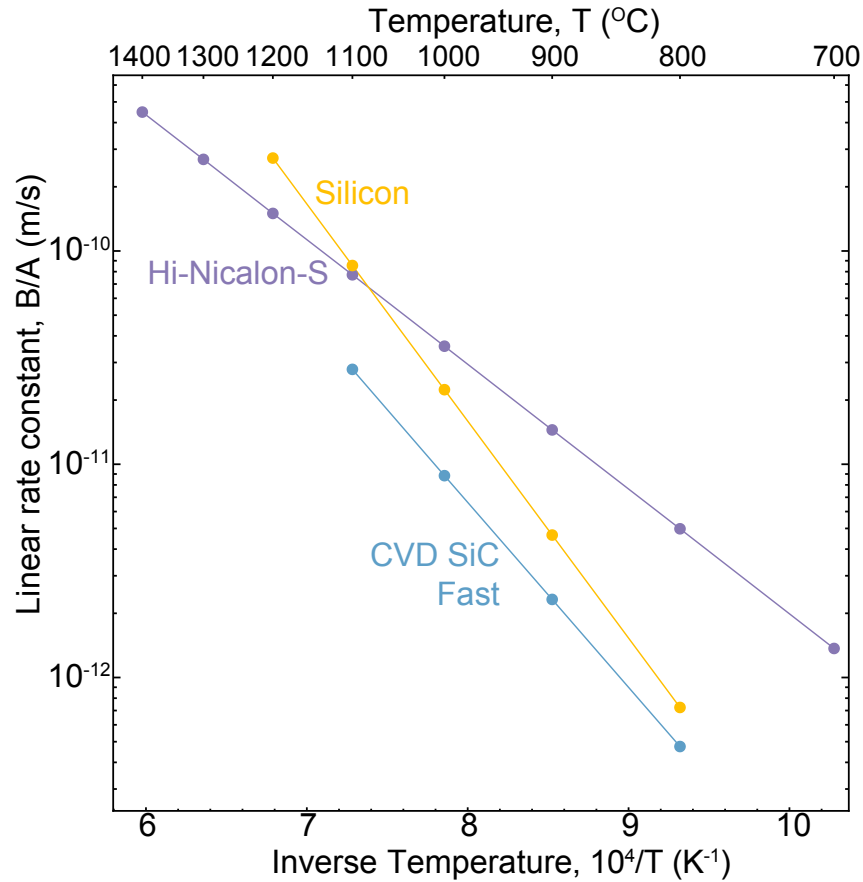


Figure 2.6: Linear rate constants for CVD SiC (Reference [2]), Hi-Nicalon-S fibers (Reference [1]), and silicon in oxygen (Reference [6]). Rate constants for CVD SiC and silicon are from exposure to 1 atm O_2 while the rate constant for Hi-Nicalon-S is from dry air exposure (0.2 atm O_2).

impact the oxide growth beyond the transition to parabolic growth. Therefore, given the long lifetimes required of CMCs and the larger amount of scatter in the literature data, the linear rate constant B/A is neglected in what follows.

Although the presence of water vapor is known to accelerate the oxidation of SiC to SiO_2 at low concentrations [7, 8], kinetic data on the oxidation of SiC fibers in water vapor is sparse [1, 8]. Of the data that does exist, attention has been primarily directed at environmental extremes—either less than 0.05 atm water vapor in air or 1 atm water

vapor (steam)–and third generation Hi-Nicalon-S fibers. Comparison of the rate constants for Hi-Nicalon-S fibers in dry (0.21 atm O_2) and wet air (0.21 atm O_2 , 0.03 atm H_2O) indicate low water vapor partial pressures do not have a significant impact on oxidation[1]. This finding is supported by theoretical calculations that indicate water vapor concentrations must be greater than approximately 8% in oxygen and 2% in air to accelerate SiC oxidation[56]. Limited steam exposure experiments indicate high water vapor partial pressures enhance the parabolic rate constant for Hi-Nicalon-S fibers as compared to the dry and wet air experiments. However the effects of intermediate compositions (*e.g.* 40% O_2 /60% H_2O , 25% O_2 /75% H_2O) are not well-characterized[8].

The parabolic rate constants found in the literature assume a dominant oxidant and report data in terms of the dominant species. Parabolic rate constants are commonly described using a power law dependence:

$$B \propto k_p \propto P_{oxidant}^n \quad (2.16)$$

where B is the parabolic rate constant in m^2/s , k_p is the parabolic rate constant in $mg^2/(cm^4h)$, $P_{oxidant}$ is the oxidant partial pressure, and n is the power-law exponent. Studies of SiC oxidation in oxygen environments found reaction orders ranging from $n = 0.15 - 1.0$ [53, 63]. The reaction orders in water vapor fell in a narrower range, $n = 0.67 - 1.0$ [7, 53, 55, 56]. Note that these studies focused on temperatures above 1100°C, leaving lower temperatures unaddressed.

The variability in these values can be attributed to a host of possible causes, including: (*i*) the presence of impurities[3, 56], (*ii*) changes in the oxidation mechanism (*i.e.* from molecular permeation to ionic transport)[53], and (*iii*) changes in the oxide

crystallinity[8, 70]. While it is beyond the scope of this dissertation to investigate these possible causes, future care should be taken in selection of *SiC* oxidation rate constants for mixed environments.

While assuming a dominant oxidant may hold in the extremes of vanishingly small oxygen partial pressure in water vapor and vice versa, this approach underpredicts the impact of the ‘lesser’ oxidant in conditions where the oxidant partial pressures are closer to parity. In order to investigate oxidation behavior in these mixed environments, a framework for *SiC* oxidation with two independent oxidants is presented in the next section.

2.4 *SiC* oxidation with interacting oxidants

When two oxidants (O_2 and H_2O) are present together and each behaves independently of the other, their net effect on oxide scale growth is characterized by the sum of the parabolic rate constants for the two oxidants alone, as in:

$$B = \bar{B}_{O_2} p_{O_2} + \bar{B}_{H_2O} p_{H_2O} \quad (2.17)$$

where p_{O_2} and p_{H_2O} are partial pressures of each species and

$$\bar{B}_{O_2} = B_{O_2}^o \exp\left(\frac{-Q_{O_2}}{RT}\right); \quad \bar{B}_{H_2O} = B_{H_2O}^o \exp\left(\frac{-Q_{H_2O}}{RT}\right), \quad (2.18)$$

where \bar{B}_{O_2} and \bar{B}_{H_2O} represent properties when only a single (pure) oxidant is present, and Q is the activation energy for the indicated species. Values for \bar{B}_{O_2} and \bar{B}_{H_2O} are taken from oxidation data for Hi-Nicalon-S fibers in dry air and steam and are given

as[1, 8]

$$\bar{B}_{H_2O} = (4.8 \times 10^{-14} \text{ m}^2/\text{s}) \cdot \exp\left(\frac{-75 \text{ kJ/mol}}{RT}\right) \quad (2.19)$$

$$\bar{B}_{O_2} = (1.1 \times 10^{-8} \text{ m}^2/\text{s}) \cdot \exp\left(\frac{-245 \text{ kJ/mol}}{RT}\right) \quad (2.20)$$

To account for interaction effects for the two oxidants, we expand \bar{B}_{O_2} about p_{H_2O} , and expand \bar{B}_{H_2O} about p_{O_2} , using Taylor series expansions:

$$\bar{B}_{O_2}^i = \bar{B}_{O_2} + \frac{\partial \bar{B}_{O_2}}{\partial p_{H_2O}} p_{H_2O}; \quad \bar{B}_{H_2O}^i = \bar{B}_{H_2O} + \frac{\partial \bar{B}_{H_2O}}{\partial p_{O_2}} p_{O_2} \quad (2.21)$$

We define non-dimensional interaction parameters as:

$$\gamma_{O_2}^{H_2O} = \frac{1}{\bar{B}_{O_2}} \frac{\partial \bar{B}_{O_2}}{\partial p_{H_2O}}; \quad \gamma_{H_2O}^{O_2} = \frac{1}{\bar{B}_{H_2O}} \frac{\partial \bar{B}_{H_2O}}{\partial p_{O_2}}; \quad (2.22)$$

The scripts on γ are read, for example, for the case of $\gamma_{O_2}^{H_2O}$ as the effect of H_2O on the rate constant of O_2 , and vice versa. Combining Equations (2.17), (2.18) and (2.21), and assuming $\gamma_{O_2}^{H_2O} = \gamma_{H_2O}^{O_2} = \gamma$, we have:

$$B = \bar{B}_{O_2} p_{O_2} + \bar{B}_{H_2O} p_{H_2O} + \gamma (\bar{B}_{O_2} + \bar{B}_{H_2O}) p_{O_2} p_{H_2O} \quad (2.23)$$

With $\gamma = -1$, this representation of the combined effects of O_2 and H_2O is consistent with the parabolic rate constants for CVD *SiC*[7] in mixed O_2/H_2O environments, as illustrated in Figure 2.7. Fitting Equation 2.23 to the oxidation rate constants experimentally determined for CVD *SiC* at 1100°C in mixed O_2/H_2O environments yields $\bar{B}_{O_2} = 1.1 \times 10^{-17} \text{ m}^2/\text{s}$ and $\bar{B}_{H_2O} = 8.5 \times 10^{-17} \text{ m}^2/\text{s}$. When parabolic rate constants determined for Hi-Nicalon-S fibers in dry air and steam are compared, the values are slightly lower for all conditions than the CVD *SiC*[1, 7, 8].

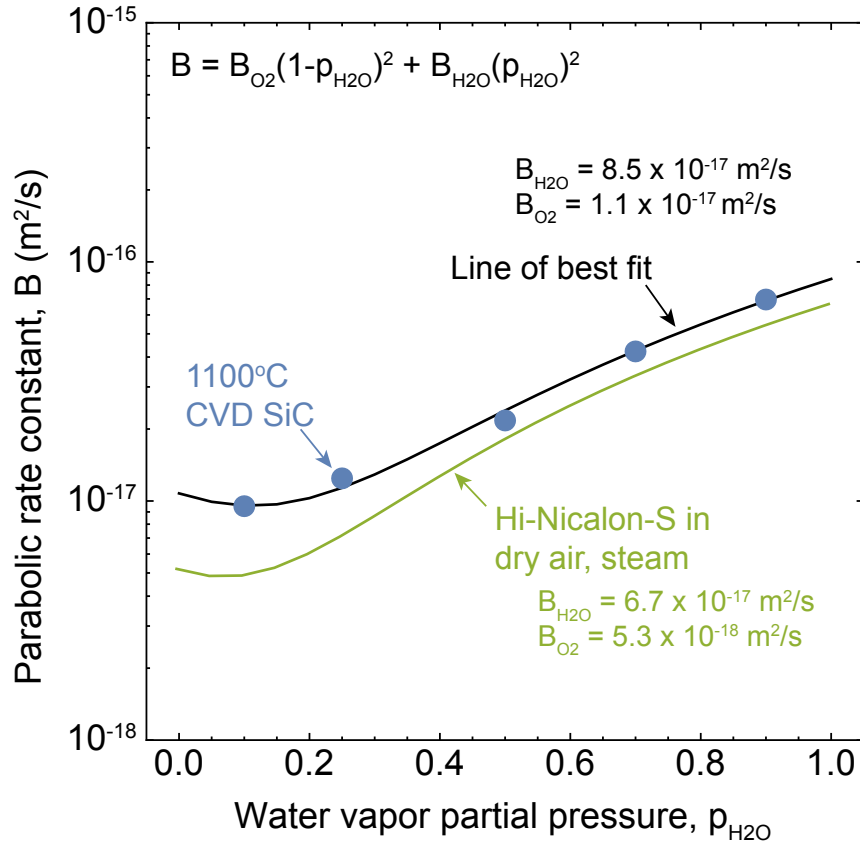


Figure 2.7: Comparison of parabolic rate constants from oxidation experiments of CVD *SiC* at 1100°C (blue circles, from Reference[7]), results of curve fitting the oxidation data (black line), and rate constants calculated using oxidation data from Hi-Nicalon-S fibers in dry air and steam (green line, rate constants from References [1, 8]).

2.5 Estimates for gas phase diffusivity

The previous sections yield descriptions of the gaseous reaction products formed by coating volatilization and a description for the evolution of the recession gap width as a function of time. In order to account for transport of these gaseous products down an evolving pathway, an expression for gas phase diffusivity is needed. Here the relevant

equations to calculate gas phase diffusivities as a function of environment (temperature, gas composition, and transport pathway) are introduced and key scalings are discussed. The results are utilized in the coating recession models in Chapters 4 and 5.

Coating recession relies on two transport pathways: (i) the gap created between fiber and matrix and (ii) the matrix crack connected to the outer surface of the composite. The first pathway is initially set by the fiber coating thickness, which is typically less than 1 micron. Therefore transport may be strongly influenced by Knudsen diffusion, as given by[71]:

$$D_K = \frac{2\Delta}{3} \sqrt{\frac{8RT}{\pi M}} \quad (2.24)$$

where Δ is the channel width, and M is the molecular mass of the diffusing species (in kg/mol).

The second pathway is characterized by the matrix crack opening. This opening is a function of applied load but is typically greater than 1 micron. Here, molecular diffusion plays a key role and is estimated using the Chapman-Enskog correlation[71]:

$$D_M = \frac{YT^{3/2}}{p\sigma_{AB}^2\Omega} \sqrt{\frac{1}{M_A} + \frac{1}{M_B}} \quad (2.25)$$

where Y is an empirical coefficient ($0.001859 \text{ atm } \text{\AA}^2 \text{ cm}^2 \sqrt{g/mol}/K^{3/2}$), p is total pressure, σ_{AB} is the average molecular diameter of the two gas species A and B involved in the diffusion process, M_A and M_B are their molecular masses, and Ω is the reduced (non-dimensional) collision integral.

While the molecular diameters are known for many gas species, for cases where they

are not they can be estimated using established correlations. One broadly used correlation to estimate molecular diameter is given by[72–74]:

$$\sigma = 0.841 (20.1 + 0.88M + 13.4n_t)^{1/3} \quad (2.26)$$

Here σ is in units of Å, n_t is the number of atoms per molecule, and M is molecular mass in g/mol . Values of σ for the gas species of interest calculated via Equation 2.26 are summarized in Table 2.2. These values are used to calculate diffusivities of the $H_xB_yO_z$ reaction products and analyze the impact of transport on fiber coating recession in Chapters 4 and 5.

The variation in the collision integral with temperature is given by[75]:

$$\Omega = \frac{1.06036}{(T_{AB}^*)^{0.15610}} + \frac{0.193}{\exp 0.47635 T_{AB}^*} + \frac{1.03587}{\exp 1.52996 T_{AB}^*} + \frac{1.76474}{\exp 3.89411 T_{AB}^*} \quad (2.27)$$

where the dimensionless temperature for two interacting gases, T_{AB}^* , is given by:

$$T_{AB}^* = T \left[\left(\frac{\epsilon}{\kappa} \right)_A \left(\frac{\epsilon}{\kappa} \right)_B \right]^{-1/2} \quad (2.28)$$

where ϵ/κ is the intermolecular force parameter. In cases where ϵ/κ has not been determined independently for a gaseous species, it can be estimated using correlations with boiling temperature T_b and melting temperature T_m of the diffusing species, in accordance with $\epsilon = 1.15kT_b$ and $\epsilon = 1.92kT_m$. [72] Values of ϵ obtained either from previous reports or computed using these correlations are summarized in Table 2.2 (see table for sources).

Table 2.2: Material constants and calculated parameters for calculation of Chapman-Enskog correlation

	O_2	H_2O	HBO_2	H_3BO_3	$H_3B_3O_6$
Boiling temperature, T_b (K)	–	–	764 [76]	573 ^[76]	–
Melting temperature, T_m (K)	–	–	–	–	449 [76]
Molecular weight, M (g/mol)	32.0	18.0	43.8	61.8	131.4
Collision diameter, σ (Å)	3.5 ^[71]	2.6 ^[71]	# 4.1	# 4.6	# 5.6
Intermolecular force, ϵ/κ (K)	106.7 [71]	809.1 [71]	* 879	* 659	& 862

Eqn. (2.26) * $1.15 T_b$ & $1.92 T_m$

Knudsen diffusion and molecular diffusion exhibit different temperature sensitivities: Knudsen diffusion $\propto \sqrt{T}$ while molecular diffusion $\propto T^2$. (The exponent on the latter term comes from a combination of the $T^{3/2}$ dependence in the numerator of Equation 2.25 and the approximately inverse root scaling with temperature of the collision integral in the denominator of the same equation.) Relative to the temperature sensitivities of the oxidation and volatilization processes, the temperature dependency of these diffusivities are very small.

The width of the recession gap decreases as oxide forms along the fiber and matrix surfaces, such that Knudsen diffusivity eventually dominates transport in the recession gaps. To account for the transition between Knudsen and molecular diffusion, the effective diffusivity, D_c , is computed using a series approximation that combines the effective molecular and Knudsen diffusivities, *i.e.*:

$$\frac{1}{D_c(t)} = \frac{1}{D_M} + \frac{1}{D_K(t)} \quad (2.29)$$

Using water and oxygen as the primary oxidants, Figure 2.8 illustrates the impact of channel width on the diffusion coefficient. The effective diffusivity decreases with time; once the transport pathway is approximately 70% sealed, a rapid decrease in diffusivity occurs for all environments of interest. Once the channel is wider than $1\ \mu\text{m}$, the effective diffusivity is dominated by molecular diffusion. For channels less than $0.5\ \mu\text{m}$ wide, Knudsen diffusion plays a significant role in transport.

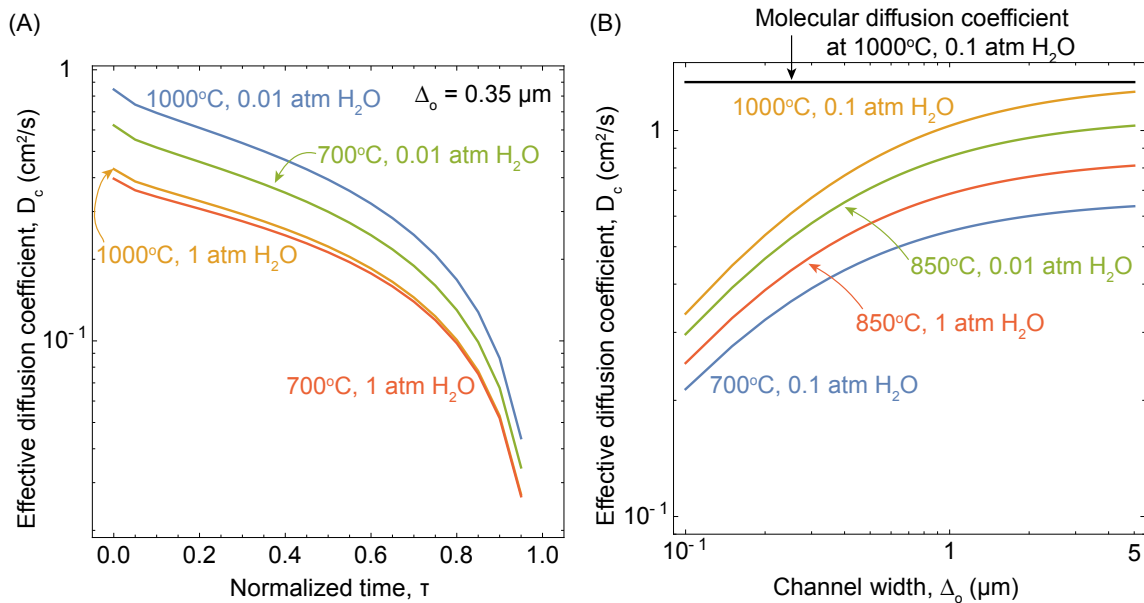


Figure 2.8: Diffusion coefficient behavior as a function of (A) normalized time and (B) initial channel width

2.6 Key takeaways and future considerations

In summary, temperature and water vapor play significant roles in the rates of *SiC* oxidation and *BN* volatilization. The models developed in Chapter 3 and discussed in Chapter 4 make the following thermochemical assumptions:

- With the exception of a brief exploration of the impact of boron activity on $H_xB_yO_z$

concentration in Chapter 4, the activity of boria is otherwise set to 0.25 and volatilization of $H_xB_yO_z$ products is assumed to occur at equilibrium.

- As is elucidated in Chapter 3, the concentration of the volatile reaction products is represented by a concentration-weighted average.
- Following the precedent of other studies[9, 46] and in the absence of more concrete oxidation data, the fibers and matrix are assumed to oxidize with the same parabolic rate constant. Oxidation of the fibers and matrix is assumed to be well-described solely by parabolic oxidation (*i.e.* the linear rate constant for SiC oxidation is neglected). The parabolic rate constant is taken to be a function of the dry air and steam rate constants for Hi-Nicalon-S fibers[1, 8] as derived in Equation 2.23.
- Gas phase diffusivity down an evolving recession gap is described by an effective diffusion coefficient that combines Knudsen and molecular diffusion behavior.

One should be cognizant that the previous descriptions oversimplify BN volatilization and SiC oxidation. Additional considerations include boria acceleration of SiC oxidation and fiber composition. Improved understanding of SiC oxidation rate constants in the presence of BN and boria is critical to accurately predicting coating recession lengths. While some work has begun on this task in oxygen environments[61], water vapor environments must also be addressed. The models compared in this section assume volatilization is the rate-limiting step in BN coating recession but the rate of boria formation plays a critical role in the evolution of boria activity with time.

The kinetics of BN oxidation and volatilization must also be further explored. Generation of boria from additional BN oxidation replenishes the boria lost due to $H_xB_yO_z$ volatilization in the borosilicate. In this case, the time rate of change of boria concentra-

tion changes and so does the activity of boria; ultimately the recession lengths predicted by the present model may overpredict coating recession.

Chapter 3

Numerical Models for Coupled Recession Along Fibers and Transport Along Matrix Crack

3.1 Introduction

As suggested by the wide range of *BN* volatilization and *SiC* oxidation behaviors illustrated in Chapter 2, observations of recession and its impact on composite response reveal significant variations that are strongly dependent on the operating environment[9, 31, 32, 42, 43, 50, 77–79]. To date, a systematic understanding of connections between environment and recession behavior has been elusive, indubitably due to the time and expense demanded by experiments. Aside from challenges associated with material variability and availability, comprehensive characterization of recession requires exposure experiments conducted across a broad parameter space, followed by high resolution microscopy at repeated intervals.

These challenges strongly motivate the development of recession models for unidirectional composites, which can predict the impact of composite architecture and environment. As outlined in Chapters 1 and 2, insightful models of recession require the integration of multiple behaviors: (i) the rate of *BN* recession, (ii) transport of volatile *BN* recession reaction products away from the recession front (impacted by the time-dependent size of the transport channel (recession gap), and (iii) transport of the volatile *BN* recession products from the composite interior to the surface.

Prior models of coating recession have addressed some of these behaviors. Oxidant diffusion transverse to the fibers[80] and parallel to the fibers[45] has been considered, but these studies did not address removal of fiber coatings. Later theoretical models considered *SiC*-based systems in an attempt to address the coupling of internal *SiC* oxidation and composite or fiber rupture [34, 38, 44]. The most relevant computational models developed by Jacobson et al. [9] and Parthasarthy et al.[46] address gaseous transport transverse to and parallel to the fibers as well as the key reactions discussed in Chapter 2 (namely, *SiC* oxidation and *BN* volatilization).

While insightful, the above modeling efforts have differences or limitations that are addressed in the models developed in this work. Early models developed for carbon composites did not address closure of the recession gap (Oxidation of the carbon fiber and matrix results in weight loss whereas weight gain is observed during oxidation of *SiC* surfaces)[45, 80]. Later work attempting to address the coupling of internal *SiC* oxidation and composite rupture did not consider both oxidation of the *SiC* matrix[34] or the presence of a fiber coating[38, 44]. While the most recent published frameworks address the *SiC/BN/SiC* architecture considered in this work, previous models do not address recession length profiles along the composite interior[9, 46].

The framework described here advances the state-of-the-art by being an efficient numerical framework that enables study of coating recession across the entire range of environments described in previous chapters and the consideration of interior recession. The key features of the framework are: (i) an integrated description of *BN* recession accounting for multiple species, (ii) an ability to span a wide range of environments and specimen geometries, and (iii) recognition (through dimensional analysis) that quasi-steady state assumptions are justified. The models that make up this framework are easily modified; the thermochemical values can be adjusted to account for different fiber types and alternative methods to calculate the concentration of volatile *BN* recession products can be incorporated.

The objective of this chapter is to present a computational approach to fiber coating recession in *SiC/BN/SiC* CMCs; the development of a finite element framework for simulating coupled transport-reaction behaviors is summarized. The final framework consists of two integrated models: (i) evolution of *BN* recession length, discussed in Section 3.2 and (ii) reaction-diffusion along the matrix crack plane with a source term, discussed in Section 3.3. The experimental models of *SiC* oxidation and *BN* volatilization discussed in Chapter 2 serve as the inputs. Section 3.4 derives the governing equations for the system and justifies assumption of a quasi-equilibrium state. Convergence studies indicating the model produces stable, convergent results are discussed in Section 3.5 while illustrative results for concentration and coating recession length profiles are illustrated in Section 3.6. The framework is subsequently used in Chapter 4 to fully quantify the impact of temperature and water vapor on fiber coating recession.

3.2 Evolution of the recession length

Fiber coating recession in a unidirectional composite is illustrated schematically in Figure 3.1. Boria (B_2O_3) formed from the oxidation of BN reacts with silica (SiO_2) to form a borosilicate glass. In the presence of water vapor, B_2O_3 in the glass volatilizes as described by Reactions 2.2, 2.3, and 2.4 in Chapter 2, leading to recession of the BN . The gaseous $H_xB_yO_z$ species diffuse along the annular gap to the matrix crack and then along the matrix crack to the free surfaces. Meanwhile, the SiO_2 scale thickens and eventually fills the resulting gap, effectively terminating the recession process.

The rate-limiting step in BN recession is assumed to be the transport along the recession channel to the matrix crack. Assuming a uniform concentration gradient along the gap, the flux of gaseous $H_xB_yO_z$ (in moles per unit area per unit time) can be expressed as:

$$J_{H_xB_yO_z} = D_{H_xB_yO_z} \frac{C_{H_xB_yO_z}^* - C_{H_xB_yO_z}}{L_R} \quad (3.1)$$

where L_R is the length of the channel created by BN removal (i.e. the recession length), $D_{H_xB_yO_z}$ is the effective diffusivity within the channel, and $C_{H_xB_yO_z}^*$ and $C_{H_xB_yO_z}$ are the concentrations of $H_xB_yO_z$ species at the channel tip and in the matrix crack where the fiber intersects it, respectively (See Figure 3.1). The recession rate is proportional to the sum of the fluxes for the three reaction products and can be inferred from Equation 3.1 to be

$$\begin{aligned} \frac{\partial L_R}{\partial t} = \frac{V_{BN}}{L_R} & \left[D_{HBO_2} (C_{HBO_2}^* - C_{HBO_2}) + \right. \\ & D_{H_3BO_3} (C_{H_3BO_3}^* - C_{H_3BO_3}) + \\ & \left. 3D_{H_3B_3O_6} (C_{H_3B_3O_6}^* - C_{H_3B_3O_6}) \right] \quad (3.2) \end{aligned}$$

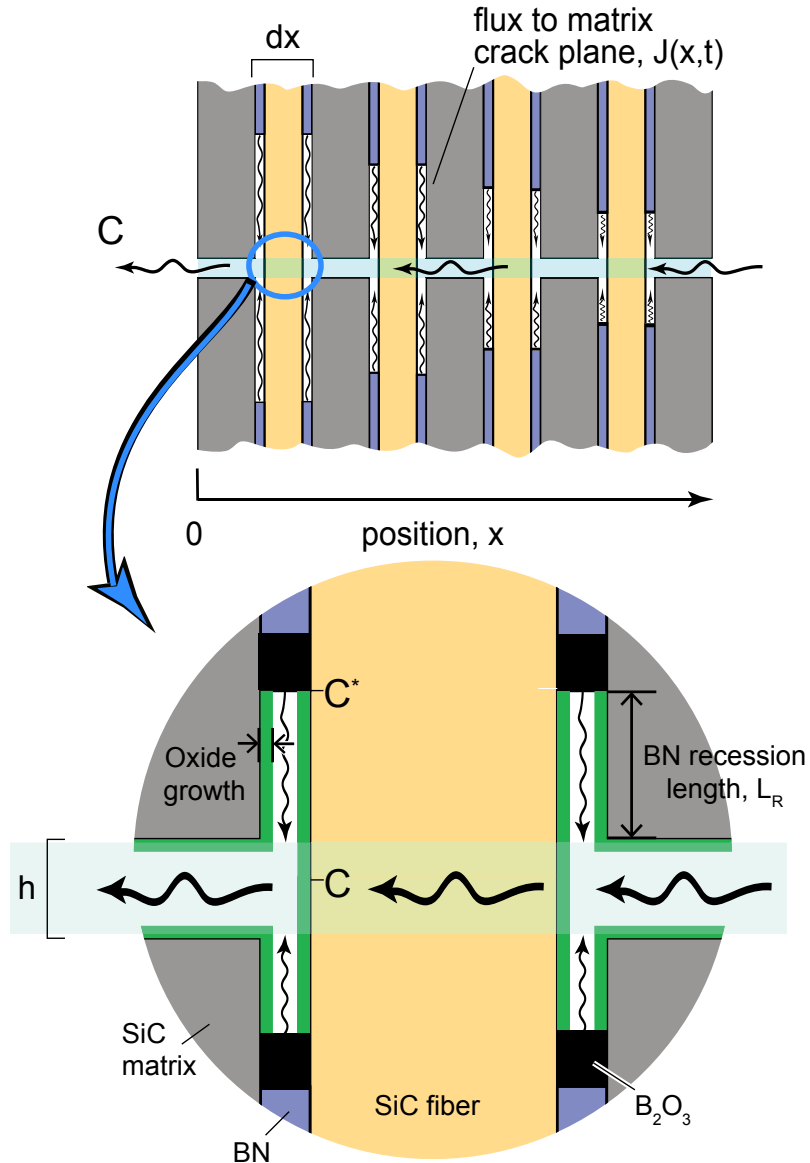


Figure 3.1: Schematic of flux in composite

where V_{BN} is the molar volume of BN . The factor of 3 in the last term comes from the fact that $H_3B_3O_6$ molecule contains three boron atoms. Instead of tracking the individual species concentrations, the concentrations are combined such that the recession rate can

be expressed as

$$\frac{\partial L_R(x, t)}{\partial t} = V_{BN} \bar{m} D_c(t) \frac{(C^* - C(x, t))}{L_R(x, t)} \quad (3.3)$$

where D_c is the effective diffusivity of the combined borohydroxide species, \bar{m} accounts for the number of boron atoms per mole of reaction product, C^* is the combined borohydroxide concentration at the reaction site and C is the combined borohydroxide concentration at the matrix crack. The effective diffusivity is calculated using a weighted-average as detailed below:

$$C_{total}^* = C_{HBO_2} + C_{H_3BO_3} + C_{H_3B_3O_6} \quad (3.4)$$

$$w_{HBO_2} = \frac{C_{HBO_2}}{C_{total}^*}; \quad w_{H_3BO_3} = \frac{C_{H_3BO_3}}{C_{total}^*}; \quad w_{H_3B_3O_6} = \frac{C_{H_3B_3O_6}}{C_{total}^*} \quad (3.5)$$

$$\bar{m} = (1)w_{HBO_2} + (1)w_{H_3BO_3} + (3)w_{H_3B_3O_6} \quad (3.6)$$

$$D_c = w_{HBO_2} D_{HBO_2} + w_{H_3BO_3} D_{H_3BO_3} + w_{H_3B_3O_6} D_{H_3B_3O_6} \quad (3.7)$$

In what follows, diffusivities and concentrations of the $H_x B_y O_z$ species will be discussed in terms of this combined concentration and species subscripts are dropped.

In order to solve for the recession length as a function of position along the crack, a reaction-diffusion partial differential equation for $H_x B_y O_z$ concentration must be solved (this is presented in the following section). However, for the location of the composite free surface, the concentration in the matrix crack is assumed to be zero since free space (immediately adjacent to the surface) acts as an infinite sink. Combining this boundary condition with an expression for time-dependent diffusivity due to closure of the recession gap, Equation 3.3 can be solved analytically to obtain a closed-form expression for recession at the composite free surface (The full derivation of this equation is presented in Chapter 4).

3.3 Description of one-dimensional diffusion with a distributed source term

Transport within the matrix crack is a process that (i) replenishes the gaseous oxidants consumed in the reactions and (ii) removes the gaseous $H_x B_y O_z$ products generated at the reaction site. Therefore, a source term is needed to account for the in-flux arriving from the recession sites along the matrix crack. The net change of molecules due to flux in the matrix crack opening direction in an infinitesimal time is:

$$\Delta N = [J(x) - J(x + dx)] z h dt \quad (3.8)$$

where the flux $J(x)$ is entering the control volume of length dx and $J(x + dx)$ is leaving the control volume (Recall x indicates the position along the crack, see Figure 3.1). Here, h is the height of the matrix crack channel and z is the out-of-plane depth of the channel. This corresponds to a concentration decrease in the small segment of the matrix crack given by:

$$\Delta C = \frac{\Delta N}{z h dx} \quad (3.9)$$

The net increase of molecules in the matrix crack due to the flux of molecules arriving at the crack plane after transport down the recession channel is given by:

$$\Delta N_R = R z h dx dt \quad (3.10)$$

where R is the production rate of the species in the control volume due to an internal reaction. (R has units of molecules per unit volume per unit time.) This corresponds to an increase in concentration within the small segment of channel given by:

$$\Delta C_R = \frac{\Delta N_R}{zh dx} \quad (3.11)$$

Over an increment of time, this implies:

$$C(t + dt) - C(t) = \Delta C + \Delta C_R = \left(\frac{J(x + dx) - J(x)}{dx} + R \right) dt \quad (3.12)$$

In the limit of a small time step, the total change in concentration is given by:

$$\frac{\partial C}{\partial t} = -\frac{\partial J}{\partial x} + R \quad (3.13)$$

$$\frac{\partial C}{\partial t} = D \frac{\partial^2 C}{\partial x^2} + R \quad (3.14)$$

where the flux J is given by Equation 3.1. This is the partial differential equation (PDE) governing diffusion in one direction where there is a reaction occurring in the system that generates additional molecules of the diffusing species.

The flux of reaction product exiting the recession gap and entering the channel comprising the matrix crack acts as a point-source in a continuum description of transport along the matrix crack. Consider a small volume ΔV formed by the matrix crack channel with height h over a small patch of crack area defined by $\Delta x \Delta z$. The corresponding volume of that portion of the matrix crack channel is $\Delta V = \Delta x \Delta z \cdot h$. The time rate of

change of concentration in that volume is:

$$R(x, t) = \frac{\text{molecules per unit time}}{\text{volume of crack channel}} = \frac{2N_f J(x, t) A_g}{\Delta x \Delta z \cdot h} \quad (3.15)$$

where N_f is the number of fibers that fall within the crack area $\Delta x \Delta z$, $J(x, t)$ is the flux coming from the recession gap for each fiber (assumed to be approximately constant across the matrix crack area), and A_g is the area of the recession gap. The factor of two arises from the fact that product enters the matrix crack from recession gaps above and below the matrix crack. The number of fibers in the given area is $N_f = f \Delta x \Delta z / (\pi r^2)$, where f is fiber volume (or area) fraction of the fibers and πr^2 is the fiber area. The area of the recession gap is $A_g = \pi((r + \Delta_o)^2 - r^2) \approx 2\pi r \Delta_o$. Using these relationships, the rate of change of concentration in the matrix crack in the vicinity of x is then given by:

$$R(x, t) = \frac{4f}{rh} J(x, t) = \frac{4f \Delta_o D_c(t) \bar{m}}{rh} \left(\frac{C^* - C(x, t)}{L_R(x, t)} \right) \quad (3.16)$$

As indicated by Equation 3.14, this distributed source term is added to the rate of change of concentration in that volume that arises from diffusion along the channel in the x -direction, leading to the final governing equation:

$$\frac{\partial C}{\partial t} = D_m \frac{\partial^2 C}{\partial x^2} + \frac{4f \Delta_o D_c(t) \bar{m}}{rh} \left(\frac{C^* - C(x, t)}{L_R(x, t)} \right) \quad (3.17)$$

3.4 Governing equations for recession profile: normalization and simplification

The solution to the system described by Equation 3.17 is greatly simplified by assuming the system is in quasi-equilibrium. Under this assumption, changes to the concentra-

tion along the matrix crack occur so quickly that $\partial C/\partial t \approx 0$. To facilitate analysis of this quasi-equilibrium assumption, Equation 3.17 is expressed in terms of the following normalizations (These normalizations are discussed in further detail in Chapter 4):

$$\begin{aligned}\tilde{C} &= \frac{C}{C^*} \\ \bar{x} &= \frac{x}{a} \\ \tilde{L}_R &= \frac{L_R}{\Delta_o} \\ \tau &= \frac{t}{t_c} = \frac{4(\gamma - 1)^2 B}{\gamma^2 \Delta_o^2} t\end{aligned}$$

to yield the following dimensionless equation:

$$\frac{\partial \tilde{C}}{\partial \tau} = \frac{\Delta_o^2 \gamma^2 D_h}{4(\gamma - 1)^2 B a^2} \frac{\partial^2 \tilde{C}}{\partial \bar{x}^2} + \frac{f \bar{m} \Delta_o^2 \gamma^2 D_c(\tau)}{(\gamma - 1)^2 B r h} \left(\frac{C^* - \tilde{C}(\bar{x}, \tau)}{\tilde{L}_R(\bar{x}, \tau)} \right) \quad (3.18)$$

Grouping the prefactors of each term gives a dimensionless transport coefficient, α_M :

$$\alpha_M = \frac{\Delta_o^2 \gamma^2 D_h(\tau)}{4(\gamma - 1)^2 B a^2} \quad (3.19)$$

and a dimensionless reaction coefficient, α_A :

$$\alpha_A = \frac{f \bar{m} \Delta_o^2 \gamma^2 D_c(\tau)}{(\gamma - 1)^2 B r h} \quad (3.20)$$

Using these coefficients, the dimensionless governing equation can be written as:

$$\frac{\partial \tilde{C}}{\partial \tau} = \alpha_M(\tau) \frac{\partial^2 \tilde{C}}{\partial \bar{x}^2} + \frac{\alpha_A(\tau)}{\tilde{L}_R(\tau)} (1 - \tilde{C}) \quad (3.21)$$

The dimensionless parameters α_M and α_A represent the role of oxide growth in reducing the transport pathways governing diffusivity of the matrix crack and recession

gap, respectively. As oxide growth narrows the transport pathways, α_M and α_A decrease until they reach a minimum at $\tau = 1$. At this point the recession gap is sealed and α_A equals zero while α_M is reduced but non-zero as the matrix crack is constrained but not sealed (provided $h > \Delta_o$).

The normalized variables \tilde{C} , \bar{x} , and τ all vary from zero to unity; as such, to first order, the terms in Equation 3.21 without the coefficients are all scaled to have the same order of magnitude. The assumption of quasi-equilibrium corresponds to neglect of the left-hand side of Equation 3.21, which is valid when α_A/\tilde{L}_R and α_M are much greater than unity.

Analysis of α_A/\tilde{L}_R as a function of environmental conditions depends on the recession length used, which evolves spatially and temporally. The maximum recession length is found at the composite surface while the recession length profile decreases along the composite interior due to transport restrictions. In the interest of identifying the conditions that violate the quasi-equilibrium assumption, this maximum recession length serves as an upper bound for the recession length along the composite interior and is used to calculate α_A/\tilde{L}_R (An analytical model for coating recession can be found in Chapter 4).

The evolution of α_M and α_A/\tilde{L}_R as a function of environment is illustrated in Figure 3.2. The initial values for α_M and α_A/\tilde{L}_R , depending on the environment, range from 10^5 to over 10^{12} . Values of α_M across all environmental conditions are nearly constant with time, indicating transport along the matrix crack plane is not significantly restricted by oxide growth. Although α_A/\tilde{L}_R decreases with time due to decreasing diffusivity (as the recession gap closes) and increasing recession length, the values remain above 10^5 until the last few moments before the gap closes. Like the results for α_M , transport down the

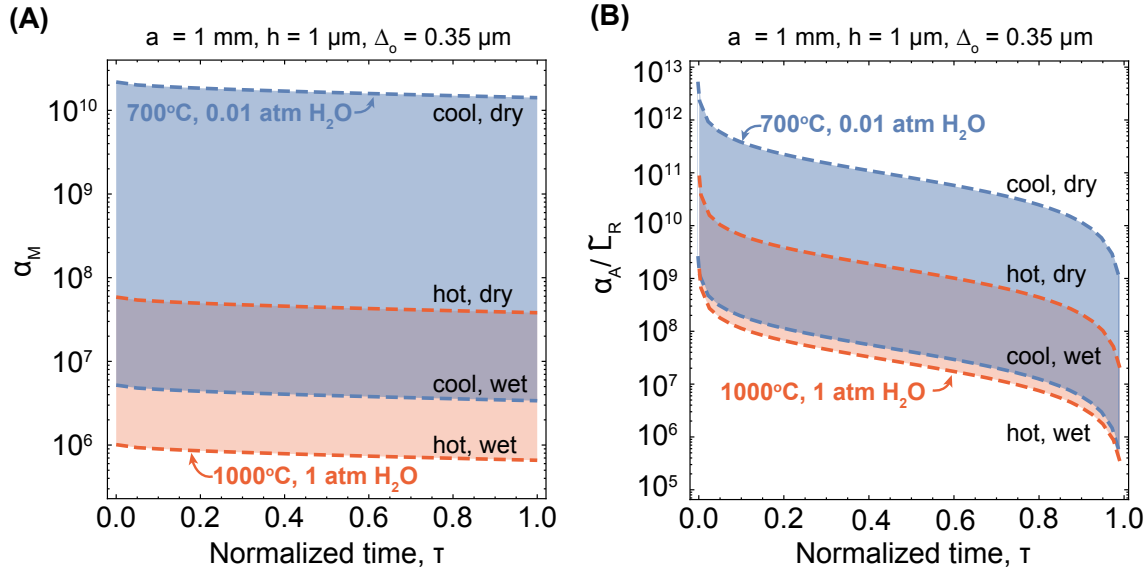


Figure 3.2: Impact of temperature and water vapor on (A) α_M and (B) α_A/\tilde{L}_R for crack length $a = 1 \text{ mm}$, crack height $h = 1 \text{ }\mu\text{m}$, and initial *BN* coating thickness $\Delta_o = 0.35 \text{ }\mu\text{m}$.

recession gap, represented by α_A/\tilde{L}_R , is more sensitive to changes in water vapor than changes in temperature.

In the interest of finding the combination of parameters that violate the quasi-equilibrium assumption, the environmental conditions that led to the lowest values of α_M and α_A/\tilde{L}_R (1000°C and 1 atm water vapor) were selected as a baseline to investigate the impact of composite geometry. As illustrated in Figure 3.3, when crack length is held constant at 1 *mm*, wide cracks and thick coatings led to the highest values of α_M while narrow cracks and thin coatings led to lower values. Values of α_M are again roughly constant with time except for the case where the crack height and initial coating thickness are the same. Here, α_M exhibits a noticeable decrease with time and channel oxidation impacts transport along the matrix crack. Note that α_M depends on crack height h through the effective diffusivity D_h . The most impactful parameter on α_M is

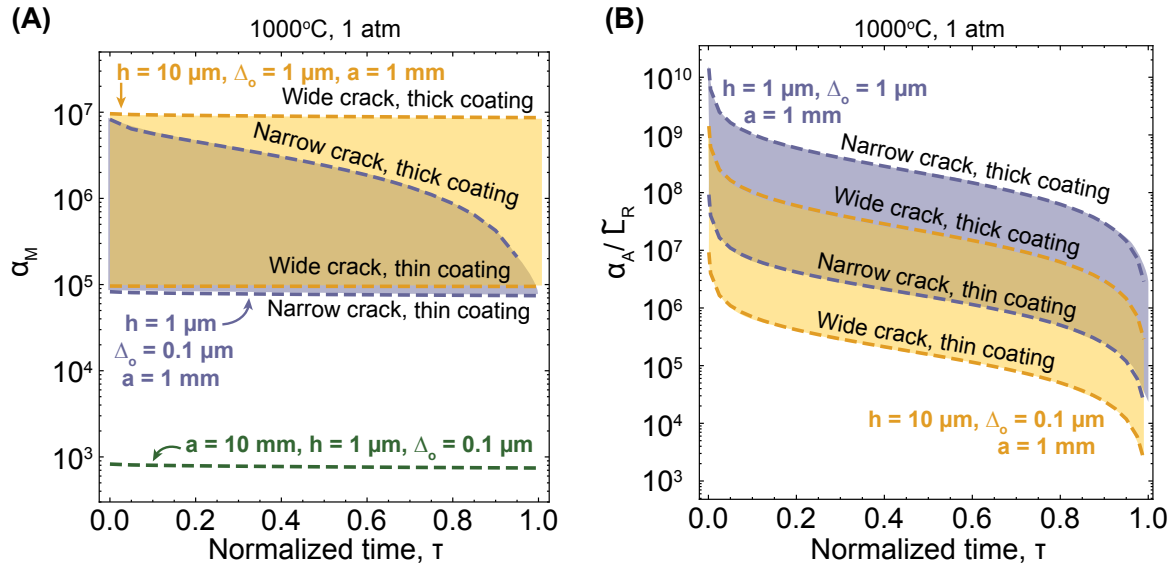


Figure 3.3: Impact of crack height h , initial BN coating thickness Δ_o , and crack length a on (A) α_M and (B) $\alpha_A/\tilde{\Lambda}_R$ at 1000°C and 1 atm water vapor.

the crack length. The dashed green line at the bottom of Figure 3.3 was calculated for the same conditions as the bottom purple line ($h = 1 \mu\text{m}, \Delta_o = 0.1 \mu\text{m}$) but for $a = 10 \text{mm}$. Under these conditions α_M is less than 10^3 and the quasi-equilibrium assumption is of increasing concern.

For $\alpha_R/\tilde{\Lambda}_R$ (also for $h = 1 \text{mm}$) the combination of a narrow crack and thick coating results in the highest values, while a wide crack and thin coatings are the lowest. (Note that α_A is independent of crack length.) This result indicates the in-flux of $H_xB_yO_z$ from the reaction sites significantly impacts the transport-reaction equation when the composite has thin initial coatings and a wide crack. This can be understood in physical terms as a scenario wherein the source term no longer dominates transport rates along the crack such that transients are increasingly important.

While all dimensionless coefficients decrease as time progresses (due to diffusivities

that depend on gap width), they remain much larger than unity until the final stages of gap closure, *i.e.* when $\tau \approx 1$. As such, over the vast majority of times where recession occurs, the system is in quasi-equilibrium. At the very last stages of gap closure, this assumption is not valid; however, since recession rates will go to zero in this limit, neglect of transient behaviors near the instant of gap closure does not impact the prediction of final recession length.

3.5 Details of the numerical scheme and illustrative results

The simplified partial differential equation (PDE) identified (Equation 3.17) must now be solved to find the concentration distributions. The PDE represents the “strong” form, which governs the concentration at every point in space and time. Finite element analysis (FEA) seeks an approximate solution, which corresponds to solving a “weak” form. In this case, the solution does not satisfy the above at every point in space and time, but rather, the governing PDE is satisfied in an average sense. That is, the weak FEA approximate solution minimizes the average error of the approximation within the specified domain.

Combining the quasi-equilibrium assumption from Section 3.4 with the weighted residual approach (also known as the Galerkin-Bubnov approach) yields a matrix equation cast in terms of the concentrations at discrete points in space. This approach discretizes the matrix crack plane into elements joined at nodes (gridpoints) and uses the recession length concentration at these nodes as variables. The value at each node

is connected by linear interpolation. The result is a system of equations that can be summarized as:

$$\begin{aligned} \alpha_M(\tau) [D]_{n \times n} [\tilde{C}(\tau)]_{n \times 1} - \alpha_A(\tau) [R(L_i)]_{n \times n} [\tilde{C}(\tau)] + \\ \alpha_A(\tau) [R(L_i)]_{n \times n} [1]_{n \times 1} = [0]_{n \times 1} \end{aligned} \quad (3.22)$$

where n is the number of nodes in the discretized domain, $[1]_{n \times 1}$ is a vector with unity as all entries (reflecting the fact the concentration at the reaction site C^* is assumed to be spatially uniform and constant), $[D]$ is the diffusivity matrix, and $[R]$ is the reaction matrix reflecting the source term, which depends on the nodal values of the recession length. Given an initial set of nodal recession lengths, the equation can be solved for the nodal concentrations. The nodal recession lengths are then updated according to Equation 3.3, *i.e.* $L_i(t + dt) = L_i(t) + \dot{L}_i dt$ where \tilde{L}_i is the recession length at node i , using the concentration value for that node. The coefficients $\alpha_A(t + dt)$ and $\alpha_M(t + dt)$ are updated by computing the channel diffusivities at $t + dt$ using the oxide thickness at $t + dt$. The process then repeats and the nodal values of concentration and recession length are tabulated as functions of time.

The concentration distribution can exhibit sharp gradients near the free surface ($\tilde{x} \sim 0$), which requires a non-uniform grid with more nodes near the free surface. Likewise, the time rate of change of recession length at early times is quite high, such that non-uniform time steps are required, with small initial steps required to accurately predict the early evolution of recession length. At later times, the gradients in the concentration distribution and the time rate of change of recession length are smaller and larger steps can be taken without a loss of accuracy.

To address these considerations, the calculations presented in Chapter 4 were performed with a non-uniform spatial grid and non-uniform time-steps defined by:

$$\bar{x}_i = 1 - \cos \frac{\pi(i-1)}{N_{el}} \quad i = 1, N_{el} + 1 \quad (3.23)$$

$$\tau_i = \left(1 - \cos \frac{\pi(i-1)}{N_t}\right)^2 \quad i = 1, N_t \quad (3.24)$$

where N_{el} is the number of elements and N_t is the number of time steps. This scheme places a node at $\bar{x} = 0$ and $\bar{x} = 1$, and computes a final distribution at $\tau_{N_t} \approx 1$. (At $\tau \equiv 1$, the recession stops completely due to gap closure; system evolution near this limit is negligible, such that one need not stop precisely at $\tau = 1$.) This discretization approach captures the initial behaviors with small steps and transitions to larger steps to maintain efficiency without sacrificing accuracy.

Selection of the number of time steps and elements was based on convergence studies. The objective of these studies is to establish that the numerical description produces results independent of numerical parameters when sufficient discretization is used. The results are said to be convergent when subsequent refinement does not change the results. To establish convergence, the FEA model was run for the base conditions of 750°C, 0.1 atm water vapor, and an initial coating thickness of 0.3 μm using different numbers of elements and time steps. The concentration and recession length profiles for each combination of numerical inputs were compared to identify when changes to the number of steps did not produce a significant difference in the calculated profiles.

The results of the number of element studies are presented in Figure 3.4 for the final time step of $\tau = 0.99$. Results are plotted on a *log-log* scale to highlight the change in mesh size. The number of elements was varied from 50 to 200; note that the calculated

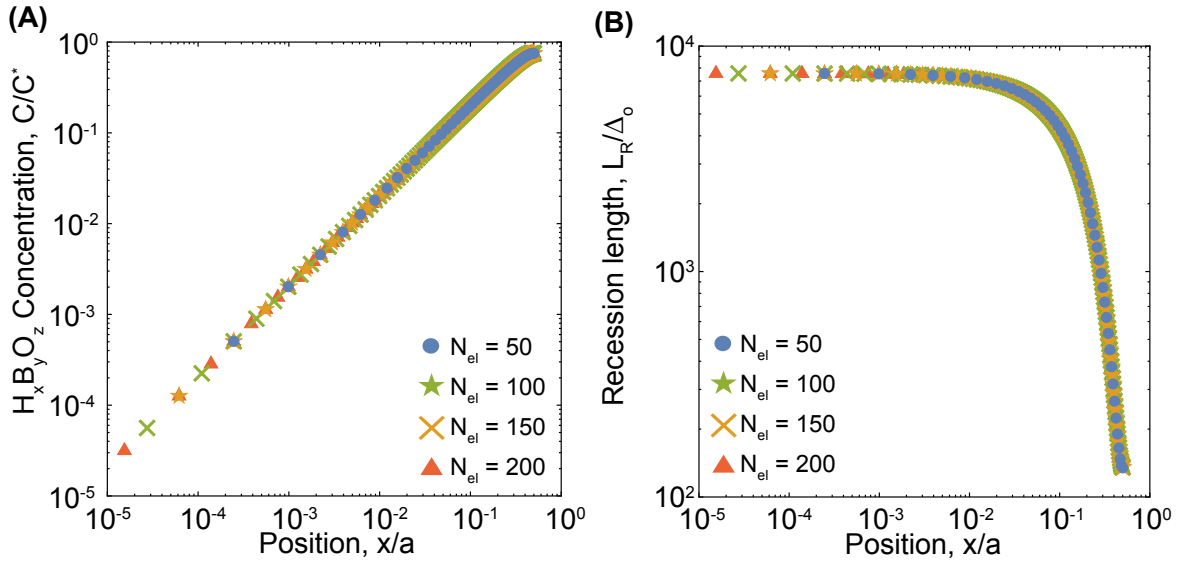


Figure 3.4: Impact of number of elements, N_{el} , on (A) $H_x B_y O_z$ concentration and (B) recession length profile. The number of time steps, N_t , was held constant at 300. Simulations were run for 750°C , 0.1 atm water vapor, $0.3 \mu\text{m}$ initial BN coating thickness, 1 mm crack length, and $1 \mu\text{m}$ crack height.

concentration and recession length profiles do not change significantly with decreasing number of elements. Using as few as 50 elements resulted in profiles that matched the results calculated with 200 elements.

The time step convergence study varied the number of time steps from 100 to 300; the resulting concentration and recession length profiles are shown in Figure 3.5. For times less than $\tau = 0.8$, no noticeable change was observed in the concentration profiles. For the final time step ($\tau = 0.99$), the concentration profile appeared to have slight time dependence. However, this apparent inconsistency is due to the non-linear time stepping scheme. Consider the cases $N_t = 250$ and $N_t = 300$. When searching for the time step closest to $\tau = 0.99$, the non-linear time stepping scheme (Equation 3.24) yields 0.9896 and 0.9875, respectively. Using the temperature, water vapor, and initial BN thickness

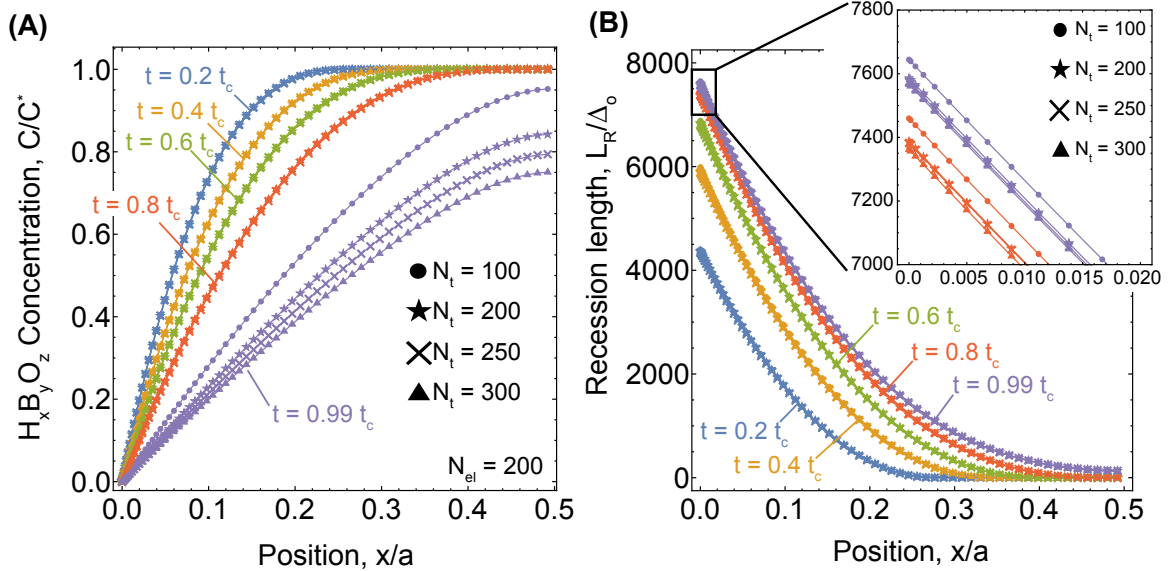


Figure 3.5: Impact of number of time steps, N_t , on (A) $H_x B_y O_z$ concentration and (B) recession length profile. The number of elements, N_{el} , was held constant at 200. Simulations were run for 750°C , 0.1 atm water vapor, $0.3 \mu\text{m}$ initial BN coating thickness, 1 mm crack length, and $1 \mu\text{m}$ crack height.

to calculate the time to closure yields a value of 428.7 hours. Using the values from the time stepping scheme, the real times for the terminal concentration profiles for $N_t = 250$ and $N_t = 300$ are 423 hours and 424 hours, respectively.

These different terminal times, however, do not result in significantly different recession profiles. The terminal recession profiles (shown in purple on Figure 3.5(B)) overlay nicely for all values of N_t . Closer examination of the recession profile at the composite surface (inset on Figure 3.5) indicates the terminal recession profile does not change significantly above $N_t = 200$. This result justifies the earlier assertion that the time rate of change of recession length is vanishingly small just before the recession gap is sealed with oxide.

As this non-linear scheme produced stable, convergent results that did not depend on chosen parameters when $N_{el} = 200$ and $N_t = 300$, the results in Chapter 4 are calculated with these values. Care was taken to ensure the algorithm converges for the cases considered in this work; however, one should note other environmental conditions may require more refined discretization to achieve convergence.

Figure 3.6 provides illustrative results for various temperatures and water vapor partial pressures. For all conditions, the concentration profile increases from zero at the composite outlet and reaches a maximum at the composite interior. Where C/C^* equals 1, no recession can occur because there is no driving force for diffusion needed to carry reaction products away from the reaction site, allowing reaction to continue (see Equation 3.3). Note the complicated coupling of temperature and water vapor on the concentration profiles; while increasing water vapor at low temperatures increases the concentration profile, the impact is nearly negligible at high temperatures.

For high temperatures, the concentrations at the composite interior when the gap closes are equal to 1.0. Accordingly, coating recession is not seen at the composite interior (red and green curves, Figure 3.6(B)). (Note the initial value is $\tilde{L}_R(\bar{x} = 0, \tau = 0) = 1$, *i.e.* $L_R(x = 0, t = 0) = \Delta_o$). Low temperature conditions, however, exhibit recession along the entire crack plane, regardless of water vapor. The recession profiles for 1000°C at 0.01 and 1.0 atm water vapor are nearly identical but exhibit slight differences. The 0.01 atm water vapor environment has a slightly shorter terminal recession length at the composite surface but the recession length profile extends slightly deeper into the composite interior. The relationship between maximum recession length and recession penetration is further explored in Chapter 4.

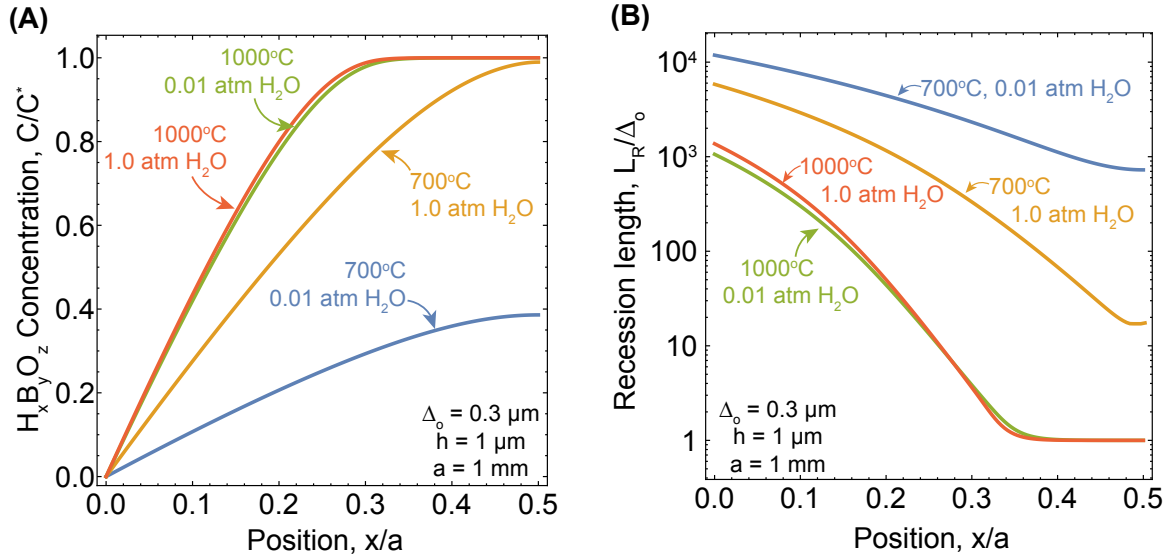


Figure 3.6: A comparison of terminal ($t = t_c$) (A) $H_x B_y O_z$ concentration profile and (B) recession length profile for various environmental conditions. All results were run for the case of $0.3 \mu m$ initial BN coating thickness, $1 mm$ crack length, and $1 \mu m$ crack height.

The cases in Figure 3.6 are a subset from a much larger examination of the environmental parameter range and are broadly illustrative of the key features and relationships between $H_x B_y O_z$ concentration and coating recession length profiles across temperature and water vapor conditions. The numerical frameworks discussed in this chapter are utilized in Chapter 4 to comprehensively analyze the impacts of temperature, water vapor, and coating thickness on fiber coating recession. The impacts of crack height and crack length on recession length profiles are discussed in more depth in Chapter 5.

3.6 Model validation with experimental results

Experimental measurements of BN recession in composites are difficult to make given the complexity of multi-layered systems; accordingly, the literature is sporadic. Some

studies avoided the microstructural complexity of minicomposites and instead investigated *BN* recession using layered structures[9, 43]. The study conducted by Carminati et al. heated *SiC/BN/SiC* multilayer stacks to 800°C in wet air (10% H_2O)[43]. Recession length measurements were taken by TGA and SEM but only the SEM results were reported. The authors[43] noted the TGA results did not agree with the SEM observations and attributed the difference to exposed sections of *BN* due to *SiC* spallation. An average recession length of 25 μm was achieved after 60 hours for a 0.5 μm thick layer while the same average recession length was achieved in 1 hour for a 4 μm thick *BN* layer.

In addition to qualitative observations of *BN* recession in layered systems, Jacobson et al. quantified recession lengths in single-tow unidirectional *SiC/BN/SiC* minicomposites [9]. One face of the minicomposite was ground in order to expose the fibers and fiber coatings to the oxidation environment. Minicomposites were heated in a mixture of oxygen and water vapor (either 1% or 10% H_2O/O_2) at 700°C and 800°C. The coating recession length was determined by energy dispersive spectroscopy (EDS) measurements, which identified the transition from as-deposited *BN* to oxidized *BN*. As noted by the authors, this method of identifying recession lengths introduces significant scatter as the transition from *BN* to glass is gradual and introduces subjectivity when identifying the transition point. As a complement to their experimental results, Jacobson et al. proposed a model for *BN* recession at an exposed surface. A comparison between their model and the model developed in this work is discussed later in this section.

Although these experiments cannot be used to fully validate the results of the FEA model (as there is no reported recession distribution), the analytical model introduced in Section 3.2 and fully derived in Chapter 4 can be applied with reasonable fidelity. The analytical model assumes an infinite sink at the composite free surface, which is a

similar to the case of coating recession from an exposed surface as done in both studies. The reported environmental conditions and *BN* coating thickness serve as inputs to the analytical model to generate predictions of *BN* coating recession as a function of time.

First, compare the analytical model predictions of recession length (as a function of time) to the values determined in layered composites by Carminati et al.[43]. The analytical model significantly overpredicts the recession lengths; recession lengths of 1320 μm are predicted at 60 hours for a 0.5 μm thick *BN* layer and 210 μm at 1 hour for a 4 μm thick *BN* layer. These are over 50 times greater than the 25 μm observed for the respective conditions.

One potential source of discrepancies between the model and the observation pertains to the oxidation of *SiC*. If the oxidation of *SiC* surfaces occurred faster due to boron-enhanced oxidation, the recession gaps would close earlier in the experiment, leading to the shorter recession lengths. The layers of *BN* used in the study would have significantly larger surface area in contact with the *SiC* surfaces, likely leading to the high boron concentrations that are known to accelerate *SiC* oxidation.

Second, compare the analytical model derived in this work to the model developed by Jacobson et al.[9]. The two models are similar in construction—both consider equilibrium conditions for *BN* volatilization, transport from the reaction site to the free surface, and closure of the recession gap. However, the models differ in their treatment of boron activity and *SiC* oxidation. The model developed by Jacobson et al. assumes a boron activity of 0.5, uses the linear and parabolic rate constants to describe *SiC* oxidation, and treated the parabolic rate constant B as a variable parameter. By fitting the model to the experimental data and solving for B , Jacobson et al. attempted to account for

the uncertainty surrounding the impact of water vapor and boron on *SiC* oxidation[9]. In contrast, the model developed in this work assumes a boron activity of 0.25 and calculates *SiC* oxidation using only the parabolic rate constant. To facilitate a more equitable comparison between the two models, the parabolic rate constant used in this work's model was determined by fitting the experimental data reported in Jacobson et al.[9].

Figure 3.7 illustrates the comparison of experimental *BN* recession lengths from Jacobson et al.[9] (filled plot markers), the results from the model developed by Jacobson et al.(dashed black lines), and the analytical model prediction from this work (black solid lines). The plateaus observed for both model predictions indicate the time at which the recession gap is calculated to be sealed and no further recession is expected. Note that predictions from this work's model assume a single *BN* thickness for each set of environmental conditions. Although individual *BN* thicknesses are recorded, the values for a given set of experimental conditions were similar. It is unclear whether Jacobson et al. used the individual coating thickness values or the approximate value.

Given the limited experimental conditions, firm conclusions about the model's accuracy as a function of temperature, water vapor, and initial coating thickness are difficult. However, the analytical model generally agrees with the experimental data at early times while significantly overpredicting recession lengths at long times. The model results presented by Jacobson et al. (plotted as a dashed line in Figure 3.7) do not predict recession lengths at early times particularly well but show good agreement at long times, once the recession gap has closed.

These promising but frustratingly inconclusive comparisons indicate additional validation efforts are needed to validate and improve the existing models. Although TGA

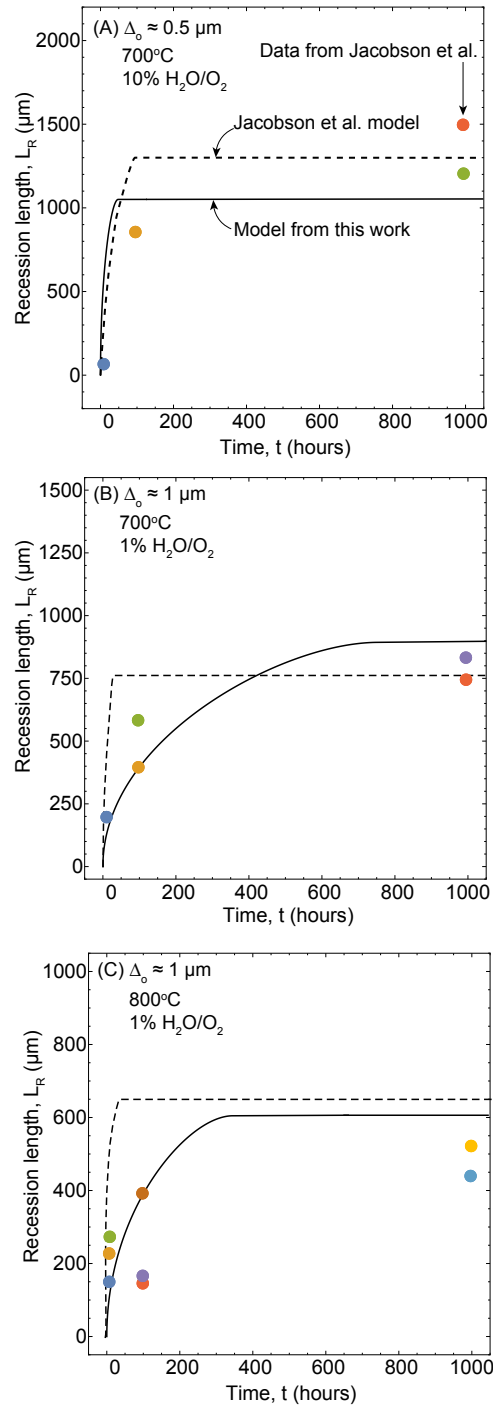


Figure 3.7: Recession model comparison to experimental observations from Jacobson et al. [9] for (A) $\Delta_o \approx 0.5 \mu\text{m}$, 700°C , $10\% \text{H}_2\text{O}/\text{O}_2$; (B) $\Delta_o \approx 1.0 \mu\text{m}$, 700°C , $1\% \text{H}_2\text{O}/\text{O}_2$; (C) $\Delta_o \approx 1.0 \mu\text{m}$, 800°C , $1\% \text{H}_2\text{O}/\text{O}_2$. The BN coating recession model developed by Jacobson et al. is included as the dashed lines.

can provide insight into volatilization behavior of exposed *BN*, the multiple oxidation and volatilization processes occurring in CMCs can complicate analysis of TGA results. SEM measurements of longitudinally sectioned composites, although more time-consuming, offer clear evidence of *BN* recession and quantification of those recession lengths in context with the local microstructure.

Chapter 4

Recession of BN Coatings in SiC/SiC Composites through Reaction with Water Vapor

4.1 Introduction

Due to their low density and attractive high temperature properties—including high strength, toughness, and thermal shock resistance—*SiC/SiC* composites are strong candidates for turbine components in next-generation aircraft propulsion and power generation systems. In ideal systems, the composite achieves high toughness by deflecting matrix cracks around the fibers. Frictional sliding along the debonded interfaces provides load transfer between the matrix and the fibers, such that regions with highly-stressed fibers are confined to a small region near the matrix crack. In the cases of current interest, these behaviors are affected by coating the fibers with *BN* prior to fabrication.

Environmentally-driven changes to the *BN* coating therefore play a critical role in

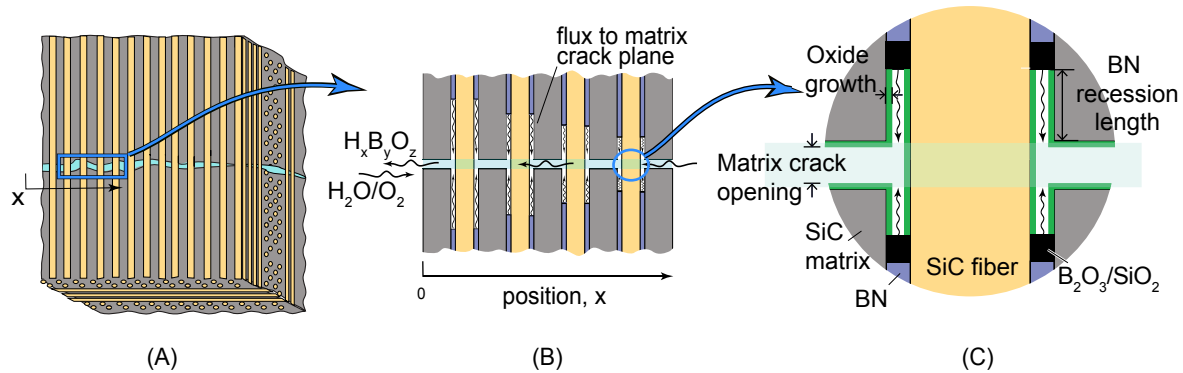


Figure 4.1: (A) Schematic illustration of a ceramic matrix composite with a matrix crack that allows ingress of reactants that lead to *BN* removal. (B) Schematic of recession gaps that allow for transport of reaction products from coating reaction fronts to the matrix crack plane that allows egress to the environment. (C) Schematic of behavior at the single fiber level, showing the volatilization front (in black) and the formation of oxides on the *SiC* surfaces that eventually close off the recession gap. The black region of the recession front consists of a liquid borosilicate whose exact composition is currently unknown.

the composite response, since coating degradation exposes fibers to chemical attack, reduces or eliminates shear transfer between fibers and matrix, and increases the volume of highly-stressed fibers near the matrix crack plane. Figure 4.1 provides an overview of key features of this process; matrix cracks allow for ingress and egress of reactants and reaction products, which lead to *BN* volatilization. As the coating is volatilized, the reaction front recedes from the crack plane; herein, the recession length is defined as the distance from the matrix crack plane to the edge of the intact coating. Oxidation of exposed *SiC* surfaces occurs simultaneously, ultimately terminating reactions when the recession gap is closed by merging oxide layers from adjacent *SiC* surfaces.

Both water vapor and gaseous oxygen are known to react with both *BN* and *SiC*. Prior work has shown that the deleterious effects of these reactions are most pronounced in the temperature range of 500°C to 1000°C [31, 35, 77]. The rates of *BN* removal and

SiC oxidation are a strong function of environmental conditions (temperature and concentration of the contaminant species), leading to significant variations in observations of microscale (fiber scale) phenomena[9, 31, 33, 35, 41, 43, 47, 77, 81].

In some cases, complete removal of the *BN* coating is observed, as manifested by the presence of narrow, unfilled annular gaps around the fibers[33, 41, 43, 82]. Observations of recession are typically limited to surface views of gaps surrounding fibers[79, 82] with little direct evidence regarding the extent of recession along the fiber. However, when the gap between fiber and matrix is free of oxide, as observed by Morscher[82] after 100h exposure in humid air at 500°C, the recession length is extensive. More recently Carminati et al. reported an average recession length of 25 μm after 60h exposure in wet air (10% H₂O) at 800°C in a *SiC/BN/SiC* multilayer stack (*BN* layer thickness = 0.5 μm)[43]. In other cases, in seemingly similar environments, few or no recession gaps are observed [9, 35, 47]; instead, glass reaction products are often found around the fibers and on fiber fracture surfaces. Micrographs illustrating both recession of the *BN* coating and formation of glass reaction products are presented in Figure 1 of Jacobson et al.[9]

Specimen size and uniformity further complicate the interpretation of these observations. As described by Morscher[82], both significant *BN* recession and formation of glassy reaction products can be present in the same specimen. A mini-composite heated for 98h at 950°C in humid air exhibited a planar fracture surface with significant oxide formation for a region within the hot zone; however, evidence of extensive recession was present at a location roughly 22 *mm* away (local temperature of approximately 500°C), complete recession was observed. The thickness of the *BN* interphase is also known to impact the observed recession. For a *SiC/BN/SiC* multilayer stack heated to 800°C in 10% H₂O, an average recession length of 25 μm was achieved after 60h for a *BN* layer

thickness of $0.5 \mu\text{m}$ [43]. The same average recession length was achieved in 1h for a *BN* layer thickness of $4 \mu\text{m}$. Given that the *BN* coating thickness is rarely uniform across a composite cross-section, oxidation and recession behaviors are expected to vary with position.

These two disparate observations—*i.e.* significant *BN* recession (with long interface gaps) versus the formation of reaction products at the matrix crack plane (with limited to no recession gaps)—stem from a competition between the rate of volatilization of the *BN* and the rate of oxidation of the matrix and fibers. In environments that produce rapid *SiO₂* growth, the recession gap that provides access to the volatilization front quickly fills with oxide and recession quickly arrests. In environments that lead to slower oxide growth, the recession channel remains open for longer time periods, allowing recession to proceed further prior to arrest.

The principal aim of this chapter is to fully characterize this competition across a broad range of environmental conditions, coating thickness, and matrix crack opening. This is achieved by coupling models of volatilization, oxidation and transport [9, 44–46]. The model for *BN* volatilization assumes *BN* is converted to boria, which is then volatilized by water vapor; the model for *SiC* oxidation is based on oxidation to pure *SiO₂*. While presence of both *BN* and *SiC* at the reaction site likely impacts oxide composition (and hence oxidation and volatilization kinetics), salient details of the process at the recession front have yet to be established.[60, 61, 83] As such, we present models based on the direct volatilization of boria in a borosilicate glass and the formation of pure silica. The models are sufficiently general to allow for straightforward modifications to describe alternative reactions as details emerge regarding oxidation in the presence of both *BN* and *SiC*.

The work here builds on previous modeling efforts of related phenomena[9, 44–46] to provide several key advances: (*i*) a detailed thermochemical analysis of volatilization products and the impact of multiple reaction products on recession, (*ii*) a closed-form solution for recession lengths near free surfaces that enables rapid analysis of a broad operational envelope, and (*iii*) the development of quasi-equilibrium descriptions for transport along matrix cracks that enable rapid predictions for the spatial distribution of recession lengths. Together, these advances provide a highly efficient framework to identify environments and composites most prone to mechanical degradation arising from recession and to quantify changes to matrix/fiber interactions that are needed to predict mechanical response.

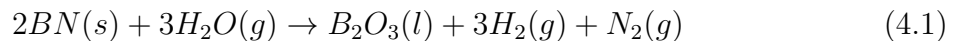
The remainder of the chapter is organized as follows. Section 4.2 describes the chemical processes involved in volatilization of *BN* and oxidation of *SiC*, which are used in Section 4.3 to describe recession along a single fiber. The single fiber recession model leads directly to a closed form expression for the recession length near the free surfaces of a composite. Section 4.4 then utilizes the single fiber recession model to construct a coupled analysis of recession and transport along a matrix crack, which enables calculations of recession length in the composite interior. Section 4.5 presents results generated by the models and illustrates the role of environment on gap closure times, recession lengths at the free surface, and recession in the composite interior. A summary and conclusions are presented in Section 4.7.

4.2 Volatilization and oxidation chemistry

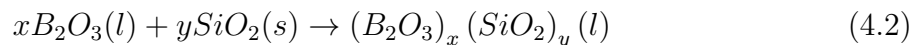
BN reacts with both oxygen and water vapor to form boria, which then reacts further with water vapor to form gaseous borohydroxides. Likewise, *SiC* reacts with both water vapor and oxygen to form silica. The present study focuses on the role of water vapor, as it controls the volatilization of boria and dominates the oxidation of *SiC* for the temperature range of interest (500°C to 1200°C), even for low concentrations of water. The formulation can be easily adapted to include other reactants as required by other environmental conditions. Given the small size of water molecules, water diffuses far more rapidly than any reaction products. As such, it is reasonable to assume that water vapor is present everywhere in the system at sufficient concentrations to sustain the volatilization and oxidation reactions. The thermodynamics of these reactions are summarized in the sub-sections that follow. Again, it should be noted that in systems involving both *BN* and *SiC*, there may be additional reactions between boria and silica that may play important roles. Adaptation of present models to alternative chemical evolution pathways is straightforward.

4.2.1 Volatilization

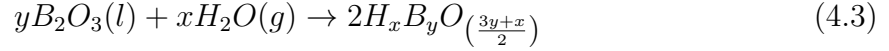
At the recession front (*i.e.* edge of the intact coating shown Figure 1), *BN* reacts with water to form boria (B_2O_3), hydrogen gas and nitrogen gas:



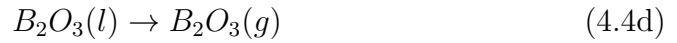
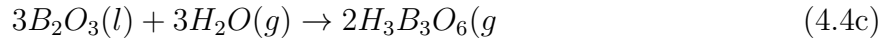
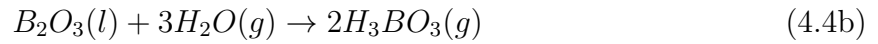
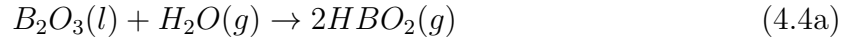
The boria may then interact with silica to form a borosilicate glass, according to:



The glass composition dictates the boria activity during subsequent volatilization reactions. The boria present in the glass reacts with water to form gaseous borohydroxides, via reactions of the general form:



Four specific species are known to form[50, 84]:



Lacking data on the kinetics of product formation, volatilization is assumed to occur at equilibrium (as done by Jacobson et al. [9]). That is, it is assumed that there is always enough boria present to support the volatilization reactions.

The concentration of each of the four $H_xB_yO_z$ species at the reaction site is obtained from the standard free energy change, $\Delta G_{H_xB_yO_z}^o$, and reaction quotient, $K_{H_xB_yO_z}$, for each species, related to one another by:

$$\Delta G_{H_xB_yO_z}^o = -RT \ln K_{H_xB_yO_z} \quad (4.5)$$

where R is the universal gas constant and T is absolute temperature. The free energies

were computed using data in the NIST-JANAF tables [85] and are given by:

$$\Delta G_{HBO_2}^o (kJ/mol) = 330.6 - 0.158 (T/K) \quad (4.6a)$$

$$\Delta G_{H_3BO_3}^o (kJ/mol) = -40.4 + 0.1044 (T/K) \quad (4.6b)$$

$$\Delta G_{H_3B_3O_6}^o (kJ/mol) = -94.3 + 0.1523 (T/K) \quad (4.6c)$$

$$\Delta G_{B_2O_3}^o (kJ/mol) = 393.5 - 0.174 (T/K) \quad (4.6d)$$

The concentrations of the volatilization products, expressed in terms of number of moles per unit volume, are (from Equation (4.5) and the ideal gas law):

$$C_{HBO_2}^* = \frac{p_{HBO_2}}{RT} = \frac{(K_{HBO_2} p_{H_2O} a_{B_2O_3})^{1/2}}{RT} \quad (4.7a)$$

$$C_{H_3BO_3}^* = \frac{p_{H_3BO_3}}{RT} = \frac{(K_{H_3BO_3} p_{H_2O}^3 a_{B_2O_3})^{1/2}}{RT} \quad (4.7b)$$

$$C_{H_3B_3O_6}^* = \frac{p_{H_3B_3O_6}}{RT} = \frac{(K_{H_3B_3O_6} p_{H_2O}^3 a_{B_2O_3}^3)^{1/2}}{RT} \quad (4.7c)$$

$$C_{B_2O_3}^* = \frac{p_{B_2O_3}}{RT} = \frac{K_{B_2O_3} a_{B_2O_3}}{RT} \quad (4.7d)$$

where p is partial pressure (in atm) and $a_{B_2O_3}$ is chemical activity of boria.

The concentrations of the reaction products in Eqns 4.7a-4.7d are shown in Figure 4.2 as functions of temperature for varying water vapor pressures, assuming two values for boria activity: $a_{B_2O_3} = 0.25$ or 1. The selections are based on the understanding that the compositions of borosilicate glasses in equilibrium with solid silica vary over a wide range, from 15 mole% boria/85% silica at 1200°C to 90 mole% boria/10 mole% silica at 500°C[86]. Furthermore, the actual compositions of glasses formed during concurrent oxidation of *BN* and *SiC* in close proximity will depend on the rates at which the two oxidation processes proceed, the rate at which diffusion occurs in the glass, and the rate

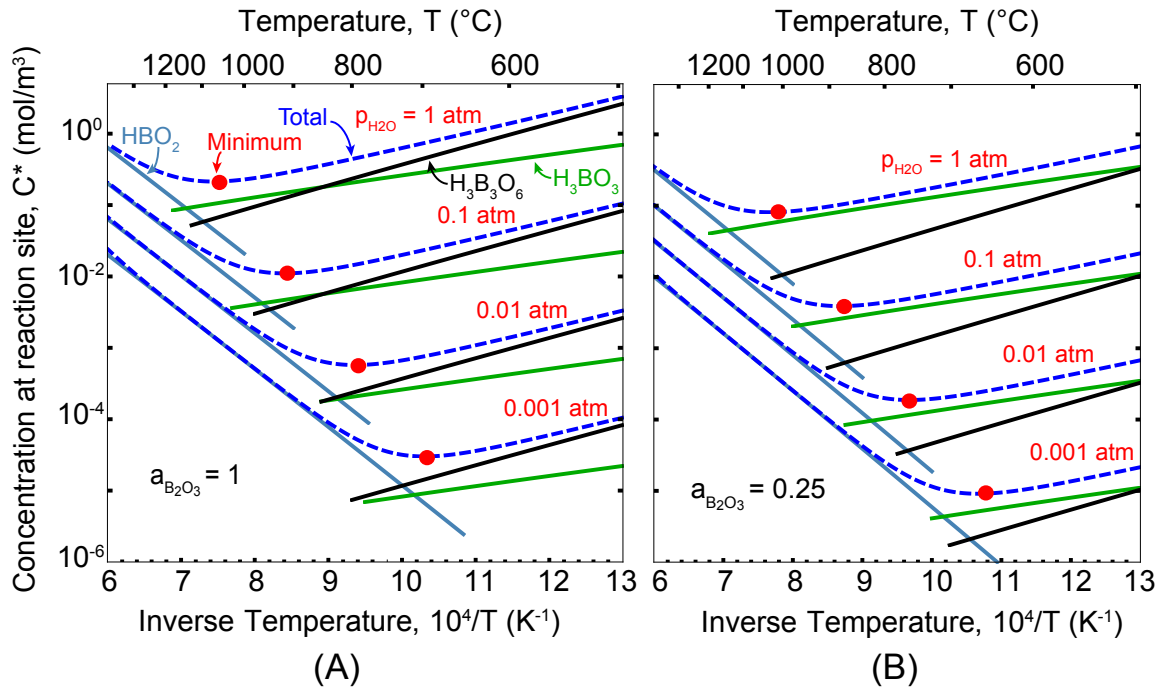


Figure 4.2: Concentration of reaction products at the *BN* recession front (black regions in Figure 4.1(C)) as a function of temperature for two different boria activities, (A) $a_{B_2O_3} = 1$ and (B) $a_{B_2O_3} = 0.25$. Subsequent figures assume $a_{B_2O_3} = 0.25$.

of boria volatilization. Thus the glass composition may vary spatially and temporally, from 100% boria to 15% boria (over the temperature range 500-1200°C). In the absence of information about the kinetic processes involved, the results in Figure 4.2 assume that the boria concentration is constant, at a value of either 0.25 (the equilibrium value at 1000°C) or unity. A separate set of calculations using FactSage to account for gas species interactions yielded results that are essentially the same as those in Figure 4.2.

The results exhibit three important features. First, the dominant volatilization product is a strong, non-monotonic function of temperature, regardless of boria activity. Second, the assumption of a single dominant species of volatilization product (as is commonly done in the literature) may significantly underestimate the total concentration driving

recession, particularly if the temperature of interest is between 500°C and 1200°C. Third, there exists a critical temperature at which the concentration of volatilization products is at a minimum, and this critical temperature depends on the partial pressure of water vapor.

The root cause of these features stems from the fact the temperature sensitivity is positive for HBO_2 but negative for H_3BO_3 and $H_3B_3O_6$. This difference is a result of the entropy changes associated with each of the reactions. That is, the formation of HBO_2 involves consumption of one mole of H_2O and production of two moles of HBO_2 and thus the entropy change is positive. Conversely, the formation of H_3BO_3 and $H_3B_3O_6$ each involve consumption of three moles of H_2O and production of only two moles of borohydroxide gas species and thus the entropy change of each is negative.

These features figure prominently in recession calculations that follow, since the recession rate scales linearly with the concentration at the reaction site. Hence, we can expect recession rates that exhibit a complicated dependence on temperature. It should be emphasized that these calculations were conducted assuming an equilibrium state; additional experimental studies on the kinetics of the volatilization reactions are needed to validate this assumption. Experimental attention should also be given to the composition of the borosilicate glass.

4.2.2 Oxidation

When exposed to water or oxygen, the *SiC* fibers and the *SiC* matrix oxidize to form silica and product gases. Over the time scales and oxide thickness relevant to this

work, the oxidation rate of *SiC* is dictated by the rate of inward diffusion of oxidant molecules through the *SiO₂* scale [7]. The scale thickness, δ , is therefore calculated using the parabolic oxidation model of Deal and Grove [6]:

$$\delta(t) = \sqrt{Bt} \quad (4.8)$$

where B is the parabolic rate constant. The rate constant depends on the partial pressures of water vapor and oxygen; in this work, we prescribe the partial pressure of water vapor, assume that oxygen is the remaining balance, and that the total pressure is 1 *atm*. Effects of impurities on scale growth are neglected, and the silica thickness is assumed to be spatially uniform on all *SiC* surfaces.

The rate constant as a function of temperature and environment is computed as follows. The parabolic growth constants for water and oxygen are given as [1, 8]

$$B_{H_2O} = \bar{B}_{H_2O} \cdot p_{H_2O} \quad ; \quad \bar{B}_{H_2O} = (4.8 \times 10^{-14} \text{ m}^2/\text{s}) \cdot \exp\left(\frac{-75 \text{ kJ/mol}}{RT}\right) \quad (4.9)$$

$$B_{O_2} = \bar{B}_{O_2} \cdot p_{O_2} \quad ; \quad \bar{B}_{O_2} = (1.1 \times 10^{-8} \text{ m}^2/\text{s}) \cdot \exp\left(\frac{-245 \text{ kJ/mol}}{RT}\right) \quad (4.10)$$

The present model accounts for interaction effects of oxygen and water vapor on *SiO₂* growth through the expression:

$$B = (\bar{B}_{O_2} p_{O_2} + \bar{B}_{H_2O} p_{H_2O}) - (\bar{B}_{O_2} + \bar{B}_{H_2O}) p_{H_2O} p_{O_2}, \quad (4.11)$$

which is fully derived in Chapter 2. The parabolic rate constants obtained via Equations 4.9-4.11 agree well with those reported elsewhere [7]. It should be kept in mind, however, that there is significant variability in the available data, particularly at low water con-

centrations.

Using Equations 4.8-4.11, one can compute the width of the interface gap Δ as a function of time:

$$\Delta(t) = \Delta_o - 2 \left(1 - \frac{1}{\gamma}\right) \delta(t) = \Delta_o - 2 \left(\frac{\gamma - 1}{\gamma}\right) \sqrt{Bt} \quad (4.12)$$

where γ is the ratio of molar volumes of amorphous *SiO*₂ and *SiC* ($\gamma \approx 1.8$) and Δ_o is the initial *BN* coating thickness. The variation in matrix crack opening and the time needed for matrix crack closure can be calculated in an analogous manner.

BN volatilization ceases once oxide has filled the recession gap. The critical time t_c is defined by $\Delta(t_c) = 0$, which yields:

$$t_c = \frac{\gamma^2 \Delta_o^2}{4(\gamma - 1)^2 B} \quad (4.13)$$

Section 4.5.1 presents a discussion of the effects of temperature and water vapor content on gap closure times.

4.3 Recession at free surfaces: single fiber model

4.3.1 Recession rates

The single fiber geometry in Figure 4.1 depicts recession gaps surrounding a fiber that bridges a matrix crack. The recession length, L_R , is defined by the distance between the volatilization reaction site and the matrix crack plane. As the *BN* coating is consumed via oxidation and volatilization, the reaction site recedes away from the matrix crack

plane, and the products are transported from the reaction site along the annular recession gap to the matrix crack plane. It is the flux of the reaction products, as dictated by diffusion along the gap, that controls the recession rate. This flux can be expressed in general as:

$$J(x, t) = \frac{\bar{m}D_c(t) [C^* - C(x, t)]}{L_R(x, t)} \quad (4.14)$$

where x denotes the position of the fiber along the matrix crack plane, t is time, \bar{m} is a unitless factor resulting from a mass balance on boron ($H_3B_3O_6$ molecules contain three boron atoms while HBO_2 and H_3BO_3 only have one boron atom each), C^* is the total concentration of reaction products at the reaction site (determined via Equations 4.7a-4.7d), and $C(x, t)$ is the total concentration at the matrix crack plane. $D_c(t)$ is the effective diffusivity of the reaction products in the recession gap; since this quantity evolves as oxide fills the recession gap, its calculation deserves special attention, and is covered in detail in Section 4.3.2.

The recession rate is defined by the velocity of the reaction front and found by a mass balance via the following:[46]

$$\frac{\partial L_R(x, t)}{\partial t} = V_{BN}J(x, t) = \frac{V_{BN}\bar{m}D_c(t) [C^* - C(x, t)]}{L_R(x, t)} \quad (4.15)$$

where V_{BN} is the molar volume of *BN*. Recession arrests when either (i) the recession gap filled by oxide, or (ii) the concentration of reaction products at the matrix crack plane is equal to the concentration at the reaction site. Further, the recession rate decreases with time, as larger recession lengths lead to larger diffusion distances.

This description of recession along a single fiber is combined with a time-dependent

channel diffusivity (described in Section 4.3.2) to develop a closed-form expression of the recession length at free surfaces (described in Section 4.3.3). It is also used to predict recession lengths in the composite interior, through coupling with diffusion along the matrix crack (described in Section 4.4).

4.3.2 Time-dependent diffusivity in the recession gap due to oxide growth

The diffusivity down the recession gap, $D_c(t)$, changes with time due to oxidation of the fibers and the matrix, which decreases the gap width and limits diffusion. The effective diffusivity in the recession gap includes contributions from (i) the molecular diffusion coefficient, D_m , for transport in channels larger than the molecular mean free path, and (ii) the Knudsen diffusion coefficient, $D_K(t)$, for transport in channels smaller than the molecular mean free path.[71] The latter depends on the gap width, which decreases with time as oxidation of the *SiC* proceeds.

The relevant terms are calculated as follows; more complete details are given in Chapter 2. First, the concentrations of the $H_xB_yO_z$ species at the reaction site are calculated for the condition of interest. Second, the molecular diffusion coefficient, D_m , is calculated from the Chapman-Enskog equation, using concentration-weighted average properties based on the results of the first step. [71] Third, Knudsen diffusion coefficients, D_K , are calculated using:

$$D_K(t) = \frac{2}{3} \sqrt{\frac{8RT}{\pi M_A}} \Delta(t) \quad (4.16)$$

where M_A is the concentration-weighted average of molar mass, and again $\Delta(t)$ is the

instantaneous gap width, given as Equation 4.12. Finally, the effective diffusivity down the recession channel, D_c , is computed using a series approximation that combines the effective molecular and Knudsen diffusivities, *i.e.*:

$$\frac{1}{D_c(t)} = \frac{1}{D_m} + \frac{1}{D_K(t)} \quad (4.17)$$

Using Equations 4.16-4.17 with the expression for the time-dependent gap width, the time-dependent effective diffusivity in the recession channel can be written concisely as:

$$D_c(\tau) = D_m \left(\frac{D_K^o(1 - \sqrt{\tau})}{D_m + D_K^o(1 - \sqrt{\tau})} \right) \quad (4.18)$$

where $\tau = t/t_{cr}$ is normalized time (with t_{cr} given as Equation 4.14), and D_K^o is the initial value of the Knudsen diffusion coefficient (defined by Equation 4.16) and $\Delta(\tau = 0) = \Delta_o$. Note that $D_c(\tau = 1) = 0$, since this is the time at which oxide fills the recession gap.

The time-average of the effective diffusivity provides insight regarding the importance of constrained diffusion in the recession gap (*i.e.* the Knudsen contribution) and factors directly into subsequent calculations of recession length. The time-average of Equation 4.18 is given by:

$$\langle D_c \rangle = \int_0^1 D_c(\tau) d\tau = D_m \left(1 + 2 \frac{D_m}{D_K^o} + 2 \frac{D_m (D_m + D_K^o)}{(D_K^o)^2} \ln \left[\frac{D_m}{D_m + D_K^o} \right] \right) \quad (4.19)$$

Note that the time-averaged diffusivity involves only *time-independent* properties defined by the environment and the initial state of the composite.

The value of the term in parentheses in Equation 4.19 provides an indication as to the impact of a closing recession gap on transport. For the conditions of interest here

($500^\circ\text{C} < T < 1200^\circ\text{C}$, $0.01 \text{ atm} < p_{\text{H}_2\text{O}} \leq 1 \text{ atm}$ and $100 \text{ nm} \leq \Delta_o \leq 500 \text{ nm}$), one computes $4 \geq D_m/D_K^o \geq 0.2$. Using Equation 4.19, this implies that the time-averaged diffusivity of the thicker coatings is about 50% of the value computed from molecular diffusion alone, while that for the thinner coatings is only about 7%. Simply put, the constraint of the channel walls as the gap closes due to oxidation significantly retards transport down the recession gap, and, in turn, the extent of recession.

4.3.3 Analytical solution for recession at the composite free surface

Near a free surface ($x = 0$), it is reasonable to assume that the concentration of reaction products is negligible, since reaction products diffusing out of the matrix crack into the surrounding atmosphere are rapidly diluted. Assuming $C(0, t) \approx 0$ enables a closed form expression for the recession length at the free surface, since all other parameters in the model are independent of position. Since other positions along the matrix crack plane crack (*i.e.* $x \neq 0$) involve non-zero concentrations, their recession rates will be smaller; hence, recession rate and length will be maximum at the free surface.

In light of the numerous model parameters, significant benefit is gained by re-stating the descriptions of recession in compact, dimensionless forms. Here we define dimensionless parameters as follows: $\tilde{C} = C/C^*$, $\tilde{x} = x/a$, $\tilde{L} = L/\Delta_o$, and $\tilde{\Delta} = \Delta/\Delta_o$. Again, we utilize the dimensionless time $\tau = t/t_{cr}$. With these definitions, Equations 4.12 and 4.15 are re-expressed as:

$$\tilde{\Delta}(\tau) = 1 - \sqrt{\tau} \quad (4.20)$$

$$\frac{\partial \tilde{L}(\tilde{x}, \tau)}{\partial \tau} = \alpha_R(\tau) \cdot \left(\frac{1 - \tilde{C}(\tilde{x}, \tau)}{\tilde{L}_R(\tilde{x}, \tau)} \right) \quad (4.21)$$

where $\alpha_R(\tau)$ is a dimensionless parameter that evolves with time due to narrowing of the recession gap:

$$\alpha_R(\tau) = \frac{\bar{m}\gamma^2 D_c(\tau)}{4(\gamma - 1)^2 B} V_{BN} C^* \quad (4.22)$$

The recession length at the free surface, $\tilde{L}_R(\tilde{x} = 0, \tau)$, can be found via direct integration of Equation 4.21 with respect to time (after noting $\tilde{C}(0, \tau) \approx 0$). One obtains:

$$\tilde{L}_R^{max} = \sqrt{\frac{\gamma^2 V_{BN} C^* \bar{m}}{2(\gamma - 1)^2 B} \langle D_c \rangle} \quad (4.23)$$

$$= \sqrt{\frac{\gamma^2 V_{BN} C^* \bar{m} D_m}{2(\gamma - 1)^2 B} \cdot \left(1 + 2 \frac{D_m}{D_K^o} + \frac{2D_m(D_m + D_K^o)}{(D_K^o)^2} \ln \left[\frac{D_m}{D_m + D_K^o} \right] \right)^{1/2}} \quad (4.24)$$

This result involves the integration of the time-dependent diffusivity, such that the time-averaged diffusivity controls the maximum recession length.

This analytical solution for the recession length at the outlet provides an efficient means to calculate the maximum recession length across a broad range of operating conditions. The concentration of reaction products C^* are computed using Equations 4.7a-4.7d, the parabolic growth constant B is computed using Equations 4.9-4.11, and the relevant diffusivities are computed via Equations 4.16-4.18 (with additional well-established expressions provided in Chapter 2).

4.4 Interior recession: coupling with transport along matrix cracks

In this section, we outline a simple approach to computing the spatial distribution of reaction product concentration, $C^*(\bar{x}, \tau)$, and the recession length, $\tilde{L}_R(\bar{x}, \tau)$. We assume that ingress of water vapor along the matrix crack plane is rapid, such that interior reactions are not affected by reagent availability.* To determine the spatial extent of recession into the composite, one must couple the diffusion of reaction products down the recession gap (in the y -direction) to transport along the matrix crack (in the x -direction).

This coupling is achieved by using the single fiber analysis to describe the flux of reaction products arriving at the matrix crack plane. Following the procedure outlined in Chapter 3, the average flux from a collection of fibers in the vicinity of x is converted to a ‘source’ term that appears in the continuum description of transport along the matrix crack. The result is a standard diffusion-reaction description:

$$\frac{\partial C}{\partial t} = D_h(t) \frac{\partial^2 C}{\partial x^2} + \frac{4f\Delta_o \bar{m} D_c(t)}{rhL_R(x, t)} [C^* - C] \quad (4.25)$$

where $D_h(t)$ is the effective diffusivity for the matrix crack, computed in the same manner as that for the recession gap. (See Section 4.3.2). The second term on the right side reflects the arrival of reaction products at the matrix crack, after being transported down the recession gaps. This equation can be solved together with results presented earlier for the oxide thickness (Equation 4.12) and recession rate (Equation 4.15).

*This can be justified by computing the relative diffusion rates of water vapor and the $H_xB_yO_z$ reaction products; one finds that water diffuses orders of magnitude faster than the much larger reaction products.

The numerical solution can be greatly simplified by recognizing that diffusion along the matrix crack is much faster than the evolution of terms arising from recession. This implies that the concentration profile at any point in time is dictated by quasi-equilibrium between the source term and diffusion along the matrix crack; *i.e.* $\partial C/\partial t \approx 0$ in Equation 4.25. A quantitative justification of this is provided in Chapter 3.

Using this assumption and the same normalizations presented in Section 4.3, the corresponding equations for recession length and concentration distribution are given by:

$$\frac{\partial}{\partial \tau} \tilde{L}_R(\tilde{x}, \tau) = \alpha_R(\tau) \left(\frac{1 - \tilde{C}(\tilde{x}, \tau)}{\tilde{L}_R(\tilde{x}, \tau)} \right) \quad (4.26)$$

$$\alpha_M(\tau) \frac{\partial^2 \tilde{C}(\tilde{x}, \tau)}{\partial \tilde{x}^2} = -\alpha_A(\tau) \left(\frac{1 - \tilde{C}(\tilde{x}, \tau)}{\tilde{L}_R(\tilde{x}, \tau)} \right) \quad (4.27)$$

The dimensionless parameters α_M and α_A reflect the role of oxide growth in reducing the gap sizes governing diffusivity in the matrix crack and recession gap, respectively. These time-dependent, dimensionless parameters are given by:

$$\alpha_M(\tau) = \frac{\gamma^2 \Delta_o^2 D_h^o}{4(\gamma - 1)^2 B a^2} \tilde{D}_h(\tau); \quad \alpha_A = \frac{f \gamma^2 \Delta_o^2 \bar{m} D_c^o}{r h (\gamma - 1)^2 B} \tilde{D}_c(\tau) \quad (4.28)$$

where $\tilde{D}_h(\tau)$ and $\tilde{D}_c(\tau)$ are the diffusivity of the matrix crack and recession gap normalized by their initial values, defined as D_h^o and D_c^o , respectively.

Equations 4.26-4.28 are solved using a finite element scheme obtained via weighted residuals, with concentration and recession length as nodal variables. We impose $\tilde{C}(0, \tau) = 0$ (the free surface is a perfect sink), and $\tilde{C}'(1, \tau) = 0$ (symmetry at the specimen centerline). As with calculations of recession length at the free surface, calculations were performed for $0 \leq \tau \leq 1$ (*i.e.* up until gap closure), assuming the initial conditions

$\tilde{C}(\bar{x}, 0) = 1$ and $\tilde{L}_R(\bar{x}, 0) = 1$.[†] At any instant in time, the finite element matrix equation is solved using the current nodal values of recession length to obtain the nodal concentrations.

Once the concentration distribution is obtained, the recession lengths are updated with Equation 4.26. At each time step, the oxide thickness is used to update gap diffusivities and compute updated values of α_M and α_R . As oxidation is assumed to occur uniformly along the matrix crack, these parameters do not depend on position (*i.e.* all recession gaps close at the same instant in time, regardless of the local recession length). The numerical value of recession at the free surface from the finite element solution matched the analytical solution presented earlier to within numerical precision. Details of the numerical procedures are included in Chapter 3.

4.5 Results and discussion

This section presents results for the critical time to close recession gaps (Equation 4.13, Section 4.2.2), the maximum recession length at the composite surface (Equation 4.24, Section 4.3.3), and the extent of interior recession (Equation 4.26-4.28, Section 4.4). The environmental domain of interest is defined by the temperature range $500^\circ C \leq T \leq 1200^\circ C$ and the partial pressure of water vapor in the range $0 \leq p_{H_2O} \leq 1$. (Recall that the balance of vapor pressure corresponds to the partial pressure of oxygen.) The geometric domain of interest is defined by the coating thickness range $0.1 \leq \Delta_o \leq 0.5 \mu m$ and the crack opening range $0.1 \leq h \leq 5 \mu m$. The fiber radius is set to $5 \mu m$ for all results that follow.

[†]Simply put, we assume very short initial recession lengths that are the same as the coating thickness, in which case the concentration at the matrix crack plane reaches C^* virtually instantaneously.

4.5.1 Time to close the recession gap

The time to close the recession gap (t_c) is completely defined by the rate of SiC oxidation and plays a defining role in the extent of recession, as it sets the time scale over which recession can occur. Results for this critical time are shown in Figure 4.3(A) as a function of temperature and water vapor pressure, for two values of BN thickness that bound the domain of interest ($\Delta_o = 0.1 \mu\text{m}$ and $0.5 \mu\text{m}$). It is important to note that t_c varies enormously over the domain considered, ranging from several minutes to tens of thousands of hours; this is a consequence of vast range of oxidation rates observed over the relevant range of temperatures and water vapor pressure.

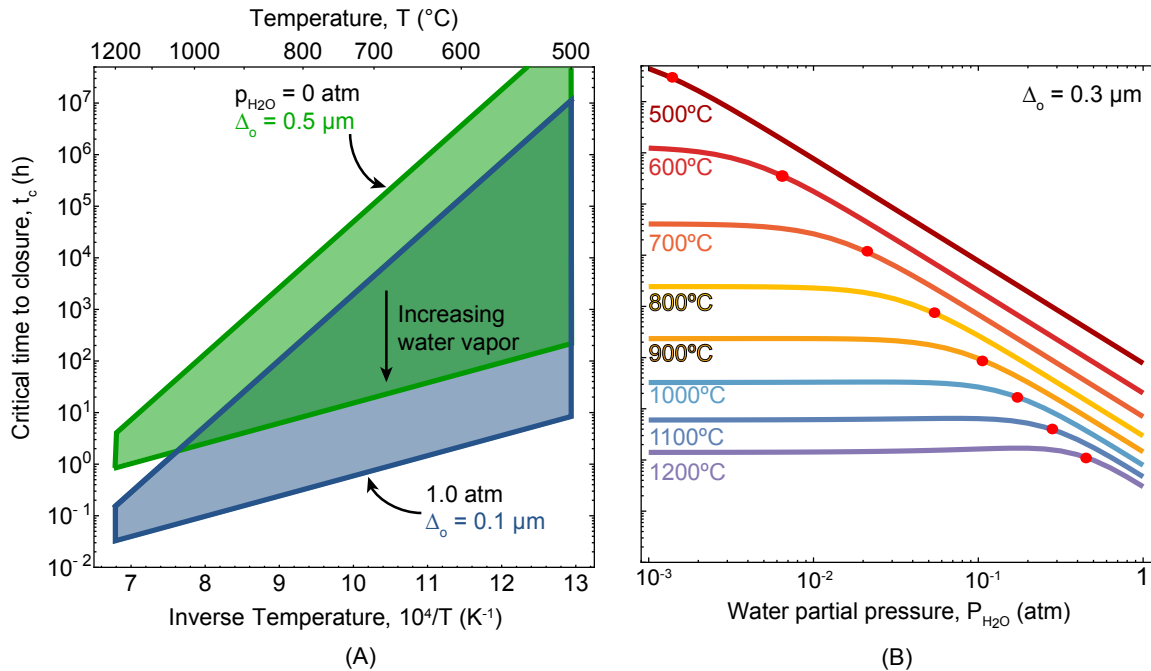


Figure 4.3: Critical time to close recession gaps (via oxidation of adjacent surfaces): (A) closure times as a function of temperature for various water concentrations, (B) closure times as a function of water concentration for various temperatures. The circles in (B) correspond to conditions with maximum recession lengths, shown in Figure 4.4.

The dominant species (water or oxygen) that controls the time to closure can be in-

ferred from the slopes of the results in Figure 4.3(A). As dictated by Equations 4.9-4.11, higher slopes reflect behavior dominated by oxygen, while lower slopes reflect behavior dominated by water vapor. It is clear that even low concentrations of water vapor will significantly reduce critical times to closure. While regimes dominated by water vapor are less sensitive to temperature than dry environments, oxidation rates are much faster at lower temperatures and closure times are orders of magnitude smaller.

The strong interplay between temperature and environment is shown in a different fashion in Figure 4.3(B), where the closure time is plotted as a function of water vapor concentration at fixed temperatures. At high temperatures ($\sim 1200^\circ C$), oxygen dominates oxidation even for up to 30% water vapor, as reflected in the zero slope in Figure 4.3(B). Conversely, at low temperatures ($\sim 500^\circ C$), even very low water content will lead to oxidation that is dominated by water vapor. At water vapor concentrations above a transition value that depends on temperature (see points in Figure 4.3(B)), the closure times scale with $1/p_{H_2O}$, as dictated by Equations 4.11 and 4.14.

Interestingly, these transition points also indicate the environmental conditions that lead to maximum recession lengths. While it is broadly true that shorter closure times will lead to smaller recession lengths, conditions that lead to short closure times may also lead to high volatilization rates. This competition is highlighted and discussed in the next section.

4.5.2 Maximum recession lengths (at the free surface)

The maximum recession length, which occurs at the composite free surface, is shown in Figure 4.4(A) (as a function of temperature) and Figure 4.4(B) (as a function of water

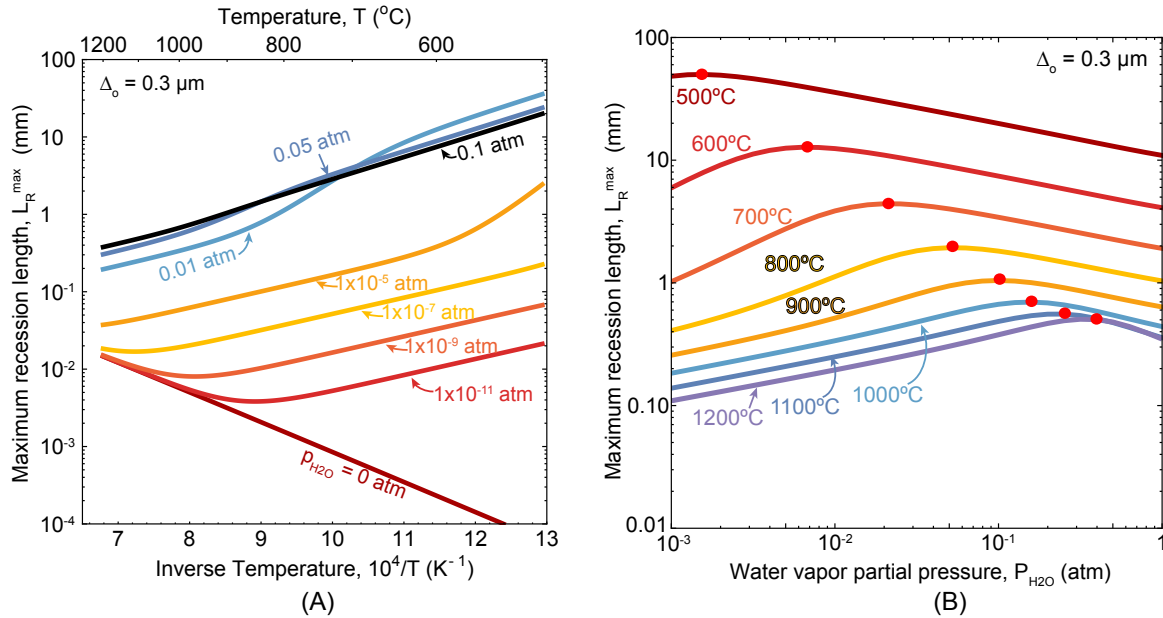


Figure 4.4: Maximum recession length (at the free surface) as a function of (A) temperature and (B) water content. The result for $p_{H_2O} = 0$ shows increasing recession with increasing temperature because evaporation of boron is the only active mechanism. The maximum recession length for a given temperature is shown by red circles; these correspond to the corresponding circled closure times in Figure 4.3(B).

vapor partial pressure). A comparison of Figure 4.3(B) and Figure 4.4(B) illustrates that maximum recession lengths are not perfectly correlated with maximum closure time. That is, for fixed temperature and starting at the water vapor pressure that leads to maximum recession length in Figure 4.4(B), decreasing the water content will decrease the recession length while the closure time in Figure 4.3(B) increases slightly.

In the absence of water vapor ($p_{H_2O} = 0$, Figure 4.4(A)), boron is only removed from the system via evaporation, such that recession rates increase with increasing temperature. However, even trace amounts of water vapor will reverse this trend; with water present, additional volatilization mechanisms are active, and these generally increase with decreasing temperature (see Figure 4.2). As a result, recession rates and lengths increase with decreasing temperature.

The non-monotonic behavior exhibited in Figure 4.4(B) (*i.e.* the effect of water vapor content) can be understood by examining the scaling of C^* and B with water vapor pressure at the extremes of temperature. First, consider the response at 1200°C and water vapor pressure less than 0.1%. In this regime, Figure 4.2 reveals that HBO_2 is the dominant reaction product; therefore, Equation 4.7 dictates that $C^* \propto p_{\text{H}_2\text{O}}^{1/2}$. In the limit of low water vapor, oxidation is dominated by oxygen, such that B is independent of water vapor. In this case, $L_R^{\text{max}} \propto \sqrt{C^*/B} \propto p_{\text{H}_2\text{O}}^{1/4}$. This power-law scaling is observed in Figure 4.4(B) on the bottom left of the plot. Second, consider the opposite extreme of low temperature, *i.e.* 500°C . In this limit, the dominant reaction product is $\text{H}_3\text{B}_3\text{O}_6$ as illustrated in Figure 4.2. Water dominates oxidation kinetics above $p_{\text{H}_2\text{O}} > 10^{-2}$. As such, $C^* \propto p_{\text{H}_2\text{O}}^{3/2}$ (Equation 4.7b, 4.7c) and $B \propto p_{\text{H}_2\text{O}}^2$ (Equation 4.9, 4.11), leading to the scaling $L_R^{\text{max}} \propto p_{\text{H}_2\text{O}}^{-1/4}$. This is the power law scaling observed in Figure 4.4(B) on the right side of the peaks.

In between these two extremes in temperature, the behavior is influenced by a number of interactions that lead to a maximum recession length that occurs at a critical water concentration. The maximum recession length occurs when there is sufficient water vapor to increase volatilization rates, while still maintaining moderate closure times. Above the critical water vapor concentration, the oxidation rates increase faster (with increasing water content) than the increase in volatilization rate, such that recession is limited. Below the critical water vapor concentration, volatilization rates decrease faster than the decrease in oxidation rate, such that recession lengths are shorter (even though closure times are higher).

The results in Figure 4.4 take a significant step towards explaining the variability

in experimental observations of recession; similar recession lengths can be observed for either extremely low or extremely high water partial pressure. This point is further illustrated in Figure 4.5, where the maximum recession lengths is plotted against the coating thickness for four environmental extremes. Here, similar recession behaviors are obtained for highly disparate environments, provided there are corresponding variations in coating thickness. Similarly, variations in coating thickness can lead to significant differences in recession lengths under identical conditions.

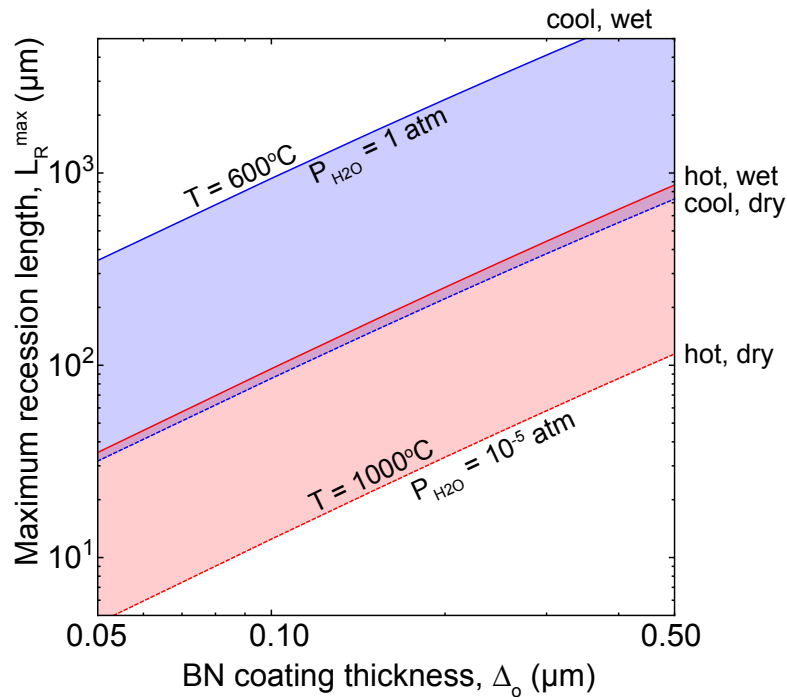


Figure 4.5: Maximum recession length (at the free surface) as a function of *BN* coating thickness, for lower temperatures (blue) and higher temperatures (red); the limits of both regions correspond to water partial pressure, $p_{\text{H}_2\text{O}} = 10^{-5} \text{ atm}$ (dry, short recession lengths) and $p_{\text{H}_2\text{O}} = 1 \text{ atm}$ (wet, long recession lengths).

4.5.3 Spatial distribution of recession lengths

Numerical solutions to Equations 4.26-4.28 yield the extent of recession in the composite interior along the matrix crack plane. As will be illustrated, the maximum recession at the composite free surface is a controlling feature, such that the scaling discussed in the previous section can be used to predict the extent of recession into the composite.

Figure 4.6(A) shows the spatial distribution of reaction products at the matrix crack plane obtained via Equation 4.28, for a set of parameters in the middle of the parameter domain described earlier and various times. The concentration distribution at closure neglects the final seconds of closure, when the last arriving reaction products are ejected rapidly out of the matrix crack. (This is a consequence of the quasi-equilibrium simplification, where such transients are ignored.) Over the entire parameter domain of interest, the concentration distributions are qualitatively similar to those shown in Figure 4.6(A). Over most of the time prior to gap closure, the concentration of reaction products is equal to that at the recession front over much of the matrix crack. This is because reaction products arriving from recession along interior fibers are hindered from transport out of matrix crack by products generated from fibers closer to the free surface.

As a result of the trapped reaction products in the interior regions, interior recession lengths are much smaller than those near the surface, as illustrated in Figure 4.6(B) for the same cases shown in Figure 4.6(A). Small recession lengths arise from the fact that the recession rate at a given location is proportional to $C^* - C(x, t)$, and for interior locations $C(x, t) \approx C^*$.

The recession lengths decay rapidly with distance from the free surface (Figure

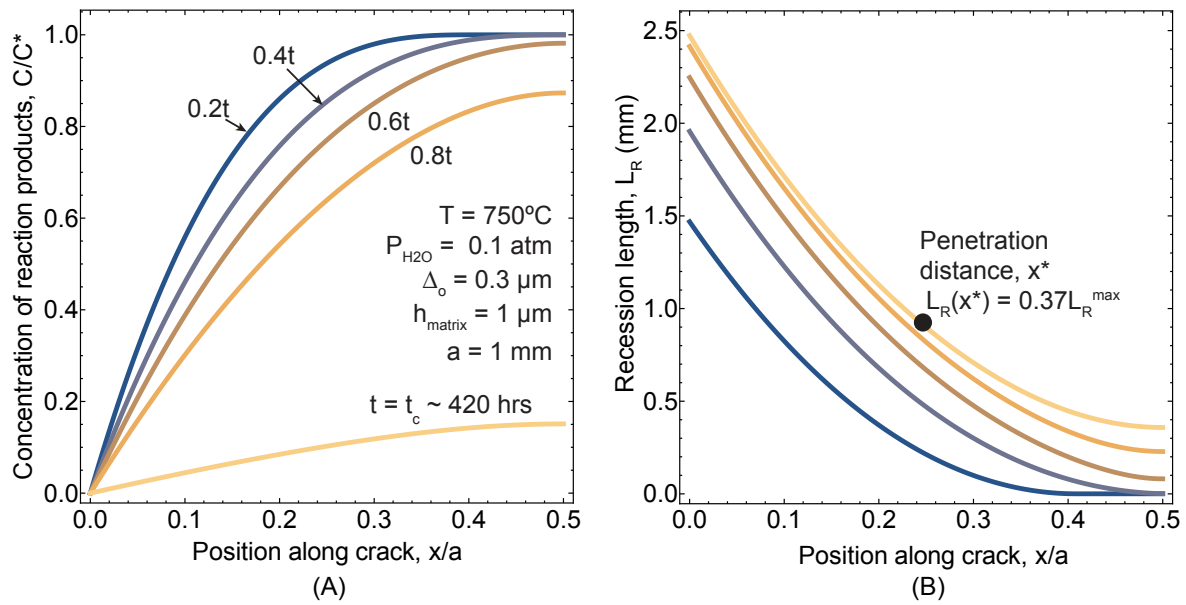


Figure 4.6: (A) Concentration of reaction products at the matrix crack plane as a function of position, at various times during recession. (B) Recession lengths as a function of position along the matrix crack plane. The top curve represents the final recession profile when the recession gaps are filled with oxide.

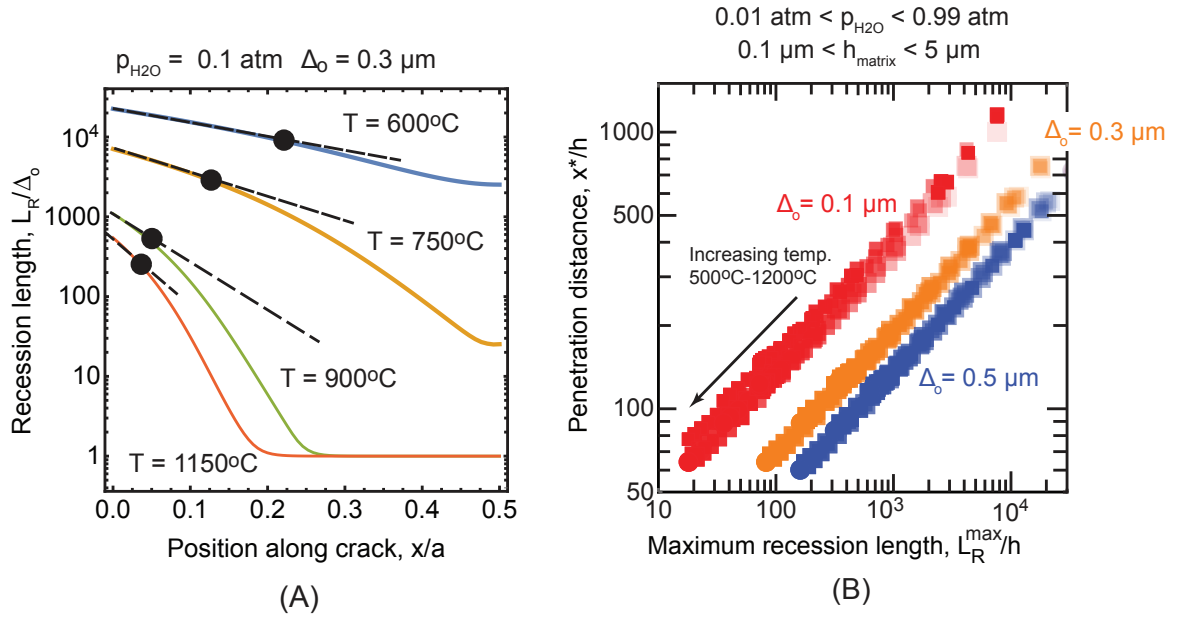


Figure 4.7: (A) Recession profiles along the matrix crack plane shown on a log-linear scale, illustrating that the rapid decay towards the interior of the composite is exponential near the free surface. The location at which $L_R(x^*) = 0.37L_R^{max}$ is defined as the penetration distance, x^* , and indicated by the black circle. (B) Penetration distance versus maximum recession length for thousands of cases spanning the operational envelope. The specimen half-width is set to 10 mm such that the results are representative a semi-infinite half-space.

4.6(B)). The rate of decay is nearly exponential, as illustrated in Figure 4.7(A) where the results in Figure 4.6(B) are re-plotted on a log-linear scale. The spatial extent of significant recession (as compared to that at the free edge) is therefore well characterized by a decay length-scale, x^* , defined here as $L_R(x^*) = 0.37L_R^{max}$. While recession lengths are finite for $x \geq x^*$, they are typically at least an order of magnitude smaller than that near the surface. Indeed, for coating thickness on the order of 250 nm , recession lengths beyond $x = x^*$ are smaller than a single fiber diameter over much of the parameter space considered here.

To establish the scaling of the decay distance x^* with relevant system parameters,

calculations were run for a large specimen ($a = 10 \text{ mm}$) such that complete saturation of the matrix crack plane is maintained at the specimen centerline. That is, for this crack length, $C(a, t) \approx C^*$ for all cases; in essence, the crack length is immaterial as the results are representative of a semi-infinite half-space. The decay length x^* was then tabulated for inputs ranging from $0.01 < p_{H_2O} < 1$, $500^\circ\text{C} < T < 1200^\circ\text{C}$, $0.1 \mu\text{m} < h < 5 \mu\text{m}$ and $0.1 \mu\text{m} < \Delta_o < 0.5 \mu\text{m}$. Based on these tabulated results, it is clear that decay distance of the recession lengths scales strongly with that of the free surface, L_R^{max} .

This scaling is illustrated in Figure 4.7(B). Here, the normalized penetration distance, x^*/h , is plotted against the normalized maximum recession length, L_R^{max}/h . For fixed coating thickness, *all* results obtained for *any* combination of temperatures, water vapor partial pressure, and crack opening displacement broadly collapse onto a single curve. The scatter shown in Figure 4.7(B) for a given coating thickness Δ_o corresponds to the scatter resulting from subtle dependence on other parameters. As there is no consistent and significant variation due to other inputs, no distinction is made between the data points. The clear and consistent scaling that emerges for the recession penetration distance is:

$$\frac{x^*}{h} = \beta(\Delta_o) \sqrt{\frac{L_R^{max}}{h}} \quad (4.29)$$

where $\beta(\Delta_o)$ is a dimensionless constant that depends only on coating thickness. As illustrated in Figure 4.7(B), this scaling holds over a very broad range of parameters, with $3 < \beta(\Delta_o) < 9$ for plausible *BN* coating thickness. The dependence on coating thickness is rather small, as compared to the inherent scaling with recession at the free edge, which can vary by many orders of magnitude.

As a consequence of this scaling, the previous discussion of factors controlling maximum recession length holds with regards to the extent of interior recession. One should note from Figure 4.6(B) that in instances where maximum recession lengths are small (say tens of microns), the number of fibers near the free edge that experience significant recession may be very small. This is an important consideration when interpreting experiments, as conclusions about recession based on the specimen interior could be very different from those based on the near-surface regions.

It should be noted that when the specimen width becomes comparable to the penetration distance, *i.e.* $x^* \sim a$, the preceding scaling no longer holds, due to the interaction of both free surfaces. In this regime, the recession profile is more uniform, with the minimum recession length (at the composite mid-plane) is comparable to that at the free surfaces. Calculations from the present framework illustrate that such effects are only important for specimen widths less than $\sim 1\text{ mm}$. Hence, one can expect more uniform recession lengths in single-tow composites or in composites with large interior voids that act effectively as free surfaces (*i.e.* sinks for reaction products). The effects of non-uniform composite properties is the focus of on-going work.

4.6 Outlook

Validation of the present model predictions will require experimental measurements of recession lengths under a variety of test conditions (temperatures, water vapor concentrations, etc.). Equally importantly it will require detailed examinations of *reaction fronts* to address questions of:

1. the nature of the reaction fronts, including the distributions and compositions of various oxidation products;

2. spatial uniformity, at the scales of composite coupons (several *mm*), individual tows (≤ 1 *mm*), and individual fibers (≤ 10 μm);
3. dependence of recession extent on proximity to free surfaces and on matrix crack openings,
4. correlations between recession non-uniformities and coating thickness variations, and
5. effects of B-containing species on oxidation of *SiC* (heretofore assumed to be independent of B).

While some such data are available [9], the requisite set of parameter values and observations needed for comparing experimental measurements with model predictions is presently lacking. Experimental assessment of the model is the focus of an ongoing activity.

With respect to design of ceramic composites, the model suggests that the coating thickness plays a prominent role in delaying fiber/matrix lock-up. This stems from the prediction that the time for gap closure scales with the *square* of the coating thickness. Thick coatings are therefore preferred, subject to constraints associated with fiber spacings.

The model presented here is predicated on a set of assumptions concerning oxidation and volatilization of *BN* that are unlikely to encompass the entire range of possible scenarios. Improved understanding of reaction pathways and kinetics may be required, as well as representations of heterogeneous composite properties (*e.g.* coating thickness and interior pores). Once established, such advances could be integrated into the current

modeling framework in a straight forward manner.

While the present model provides a mechanistic basis for designing critical experiments and interpreting experimental measurements and observations of *oxidation and volatilization*, it will eventually need to be coupled to mechanics models that address effects of recession on fiber stresses and fiber bundle strength. To this end, a comprehensive framework for predicting composite strength following recession but prior to gap closure has been developed[49]. One future goal is to explicitly link the thermochemical processes involved in recession with composite strength degradation.

4.7 Conclusions

We have presented a model for internal oxidation of *SiC/SiC* composites with *BN* fiber coatings that couples volatilization and recession of *BN* coatings, oxidation of exposed fiber and matrix surfaces, and diffusion of gaseous species through matrix cracks. The computational efficiency of the present framework allows for rapid analysis over a broad parameter domain. Several key insights emerge:

1. A detailed examination of the thermochemistry of *BN* volatilization indicates that the assumption of a single dominant reaction product is only valid in certain temperature domains, dependent mainly on water content in the environment and weakly on boria activity. Assumption of a single volatilization product may severely underestimate recession rates.
2. The time to close gaps created by coating recession via the formation of oxide on *SiC* surfaces varies strongly with temperature and gas composition. Most realistic experimental or service conditions correspond to the regime dominated by water

- vapor concentration.
3. The recession rate is determined by a competition between two competing factors: volatilization which advances the recession front and oxidation which closes transport gaps and arrests recession. The partial pressure of water vapor plays a dominant role; even at low partial pressures where oxygen dominates oxidation, small levels of water vapor can increase volatilization rates appreciably. At sufficiently high water vapor concentrations, the increase in oxidation rate lowers closure times and leads to smaller recession lengths. Hence, there is a critical, temperature-dependent water vapor concentration that maximizes recession length.
 4. Recession in the composite interior can be determined via coupling of diffusion along recession gaps to diffusion along the matrix crack plane. Over the vast parameter domain considered here, transport occurs via a quasi-equilibrium process, greatly facilitating the calculation of recession length distributions. Recession in the composite interior is very limited for specimens greater than 1 *mm* in width, due to saturation of reaction products at the matrix crack plane.
 5. The extent of recession along the matrix crack plane scales with the square root of maximum recession length and matrix crack opening. As such, the present closed-form expression for maximum recession at a free surface can be used to estimate recession penetration.

Chapter 5

Factors influencing the spatial distribution of coating recession

5.1 Introduction

Coating recession in CMCs is governed by four different rates: *(i)* the rate of *BN* volatilization, *(ii)* the rate of transport of reaction products from the reaction site to the matrix crack plane, *(iii)* the rate of oxidation closing the recession channel, and *(iv)* the rate of transport along the matrix crack (from the interior of the composite to the free surface).

The first three of these rates is embedded in the expression for the recession length of the free surface; the rate of oxidation is accounted for in the dimensionless time τ , which casts the problem in terms of the termination of recession due to recession gap closure. The rate of volatilization is controlled by the equilibrium concentration of reaction products, C^* , and the instantaneous value of the recession length itself reflects the fact transport down the recession gap slows down as its diffusion length increases).

The fourth rate, *i.e.* that of transport along the matrix crack plane, is controlled by the opening of the crack and the diffusion length along the crack (*i.e.* the specimen width). In previous chapters, the impact of transport along the matrix crack plane was characterized in a limited way; the crack opening was fixed throughout the parameter study, while the specimen width was chosen to be relative large (10 mm). Under these conditions, the results reflect those of a semi-infinite half-space. Recession along the interior of the specimen is repressed due to the fact that only the reaction products from the fibers near the surface have sufficiently short diffusion distances to find egress to the surrounding space.

The wide specimen sizes and reasonably narrow crack openings led to sharp gradients in recession length, with characteristic decay lengths defined by: $x^* = \beta(\Delta_o)\sqrt{hL_{max}}$, such that crack opening and coating thickness have the largest impact on the spatial variation of recession along the matrix crack plane[87]. Here, the scaling with coating thickness $\beta(\Delta_o)$ is a decreasing function due to the fact that thicker coatings generate more reaction products, which increases the volume of material that must be ejected along the crack plane, creating a bottleneck that localizes recession near the free surface. Note that specimen width (or crack length) does not factor into this scaling due to the fact that the width is assumed to be large – large enough to ensure that the volume of reaction products on the interior the composite is always larger than the volume that can be efficiently transported out of the crack.

As the specimen width (crack length) decreases, however, the decay length may become comparable to the specimen width. In such instances, the volume of reaction product produced on the interior of the composite may not be much larger than the

volume that can be effectively ejected out of the crack. This leads to increased interior recession, and more spatially uniform recession profiles across the specimen. Noting that many studies utilize mini-composites with sub-millimeter specimen widths, it is important to revisit recession profiles and identify instances where recession is nearly uniform. This exercise is important to align expectations for experimental observations, and also identifies conditions for which recession models can be combined with fragmentation models that assume uniform recession. Calculations to this effect are presented in Section 5.2.

Specimen widths that lead to relatively uniform recession also yield insight into the role of interior voids in the composite. For sufficiently large voids, it is reasonable to suppose that the interior void acts as free surface, *i.e.* the background concentration inside the void remains small and does little to alter the boundary condition from that of a free surface.* (Figure 5.1(A)) Alternatively, for sufficiently small voids, it is reasonable to expect that they fill up with reaction product and effectively act identically as the matrix crack volume located in the composite interior (Figure 5.1(B)). As a first step towards quantifying the role of voids, in this chapter we compute critical void sizes associated with large voids that effectively act as sinks, and small voids that effectively fill quickly to reach the equilibrium concentration of reaction products. Calculations to this effect are presented in Section 5.3.

*This naturally assumes that the convection coefficient for the matrix crack exit into the void is sufficiently high, which may be dubious. As the results will show, this effect is likely immaterial.

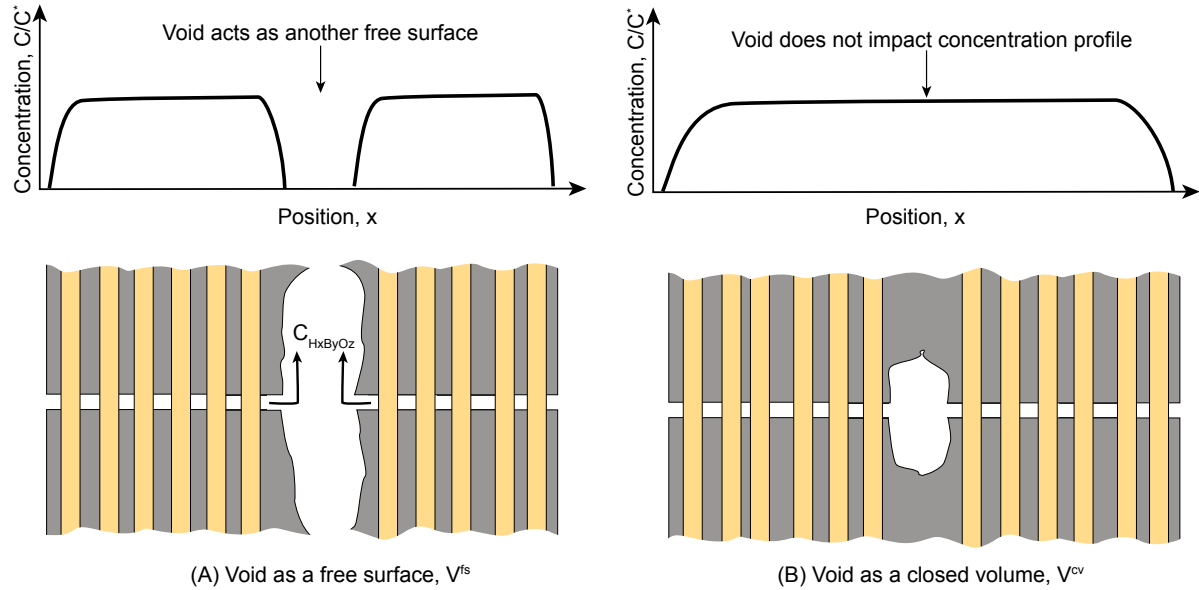


Figure 5.1: Illustration of the effects of void volume on $H_xB_yO_z$ concentration when the void acts as (A) a free surface and (B) a closed volume.

5.2 Impact of specimen size, crack opening and coating thickness on interior recession

Recall that specimen size, crack opening, and coating thickness are the three length-scales that impact transport along the matrix crack. The extent of interior recession is assessed in this section using the ratio of recession at the centerline of the specimen (representing the minimum in all cases) to that at the free surface (representing the maximum in all cases). This ratio provides a direct measure of coating uniformity. The calculations are performed using the frameworks described in Chapters 3 and 4 (*i.e.* the full recession profile is obtained for a given set of conditions by solving the transport-reaction equation described earlier). The terminal recession lengths along the crack, *i.e.* the recession profile, are defined as the lengths obtained when the gap fills with oxide.

Figure 5.2 illustrates the terminal recession profiles as for a single environmental condition and several different values of specimen width. Note the log-scale on recession length, which illustrates significant differences between the surface recession length ($x/a = 0$) and the interior recession length at the symmetry plane ($x/a = 0.5$). The results clearly indicate that recession uniformity increases with decreasing specimen size; however, for this low partial pressure of water, uniform recession is only obtained for specimens that have on the order of ten fibers across the width. At higher temperatures, however, recession becomes more uniform.

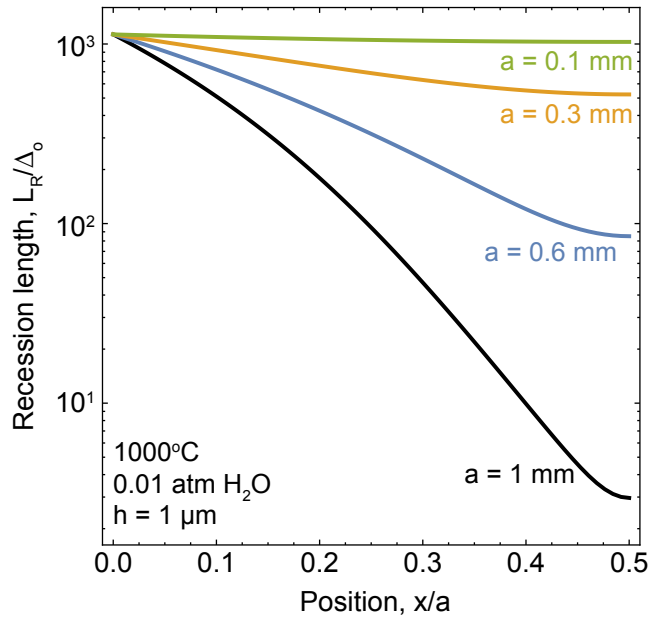


Figure 5.2: Terminal recession length profiles as a function of position and crack length a . All curves were run for the baseline conditions of 1000°C, 0.01 atm water vapor, and a crack opening of 1 μm .

This is illustrated in Figure 5.3, which depicts the interior to exterior recession ratios as a function of crack length, with upper and lower bounds illustrated for a range of temperatures, water vapor content, and BN coating thickness. For specimens on the order

of 0.5 mm in width, interior and exterior recession lengths are within a factor of two. Increasing the coating thickness, temperature, and water vapor concentration decreases the uniformity ratio because the interior is flooded with more reaction products.

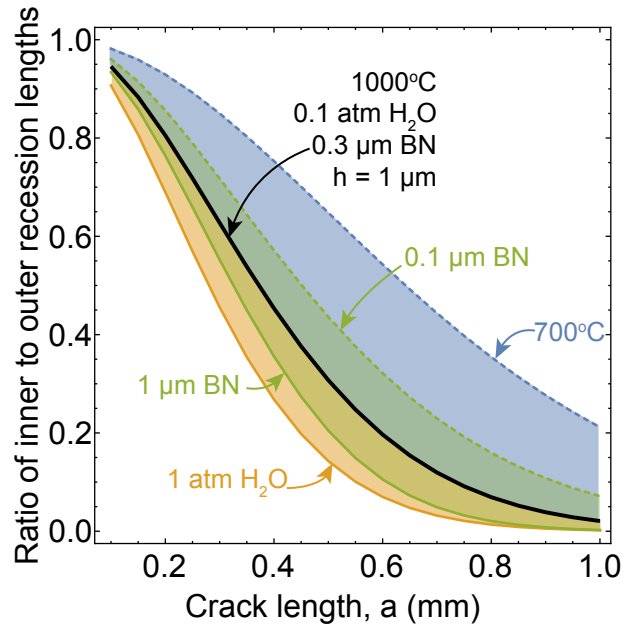


Figure 5.3: Impact of temperature, water vapor, and initial coating thickness on the ratio of the terminal recession length at the composite interior and exterior as a function of crack length a . Upper bounds for each variable are indicated by solid lines while lower bounds are indicated by dashed lines. The baseline conditions are 1000°C, 0.01 atm water vapor, 0.3 μm initial BN thickness, and a crack opening of 1 μm (shown in black).

Figure 5.4 illustrates that matrix crack opening has an effect that opposite role of specimen width; increases to the crack opening increase recession uniformity. The underlying reason for this trend is that larger crack openings have larger diffusion constants due to smaller contributions to Knudsen diffusion. In limit of still larger crack openings, the results are nonetheless similar to those shown for $h = 10 \mu\text{m}$; this is because the diffusion constant along the matrix crack is essentially the same as arising from molecular diffusion in free space. That said, again note the log-scale in Figure 5.4; even the most

uniform profile (for $h = 10 \mu m$) still has rather large differences between interior and exterior recession for this coating thickness.

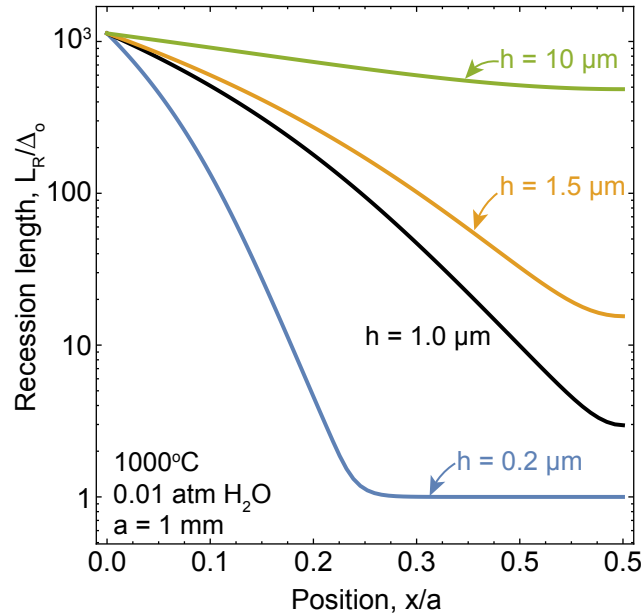


Figure 5.4: Terminal recession length profiles as a function of position and crack opening h . All curves were run for the baseline conditions of 1000°C , $0.01 \text{ atm H}_2\text{O}$ vapor, and a crack length of 1 mm .

Given the substantial differences in the equilibrium concentration of reaction products C^* as a function of environment, it is worth examining recession ratios across the entire space. Figure 5.5 presents contour maps of interior-to-exterior recession lengths across a broad temperature and water content range, for four limiting cases. Ostensibly, the most relevant crack openings fall between $1 - 10 \mu m$ [82, 88, 89], while the most relevant coating thickness values fall between $0.1 - 1 \mu m$. Figure 5.5 presents contour maps for the extremes of this range.

Consider the map smallest crack opening and largest coating thickness; over the bulk

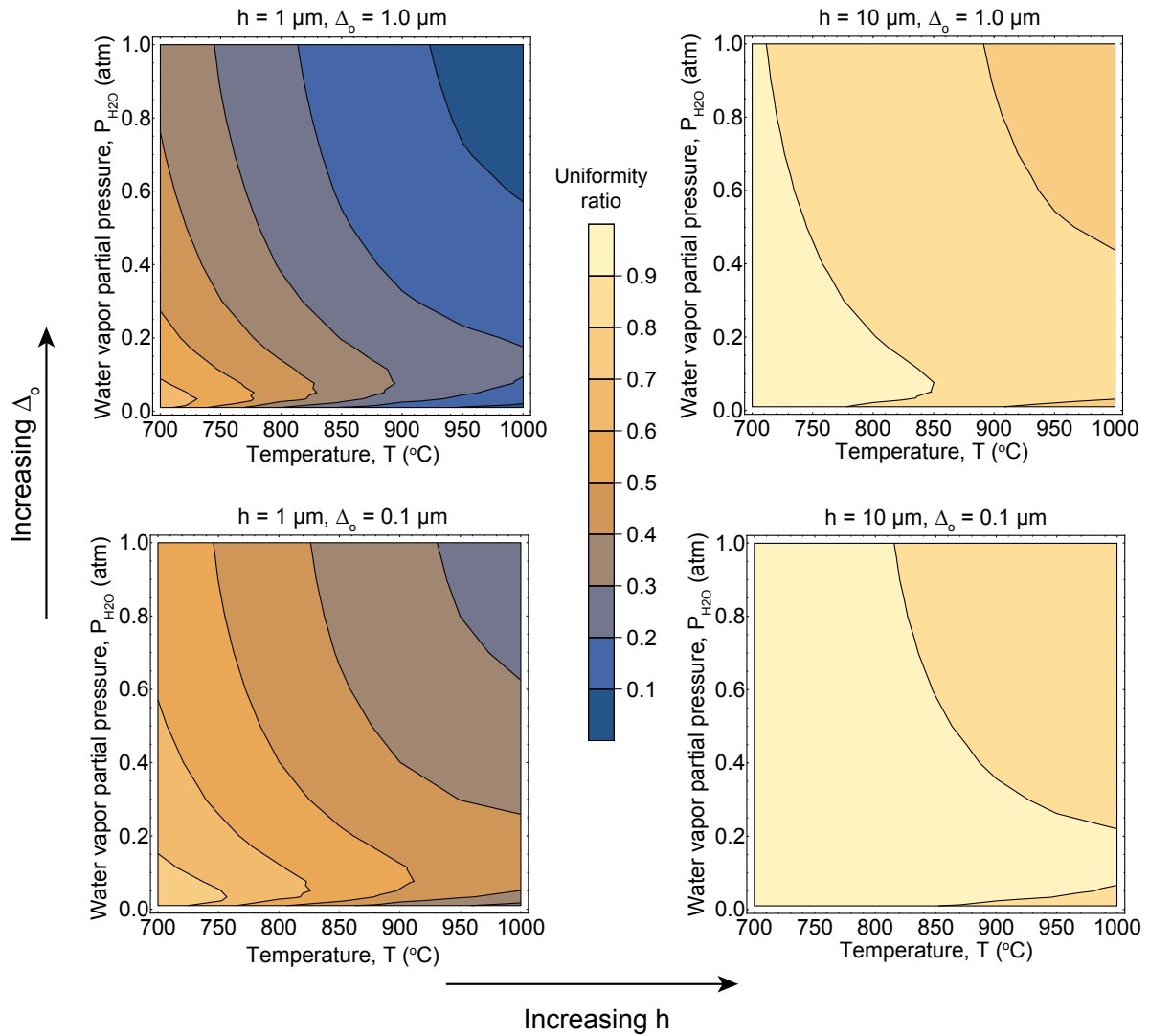


Figure 5.5: Contour plots for the ratio of the terminal recession length at the composite interior and exterior as a function of environment, crack opening h , and initial BN coating thickness. All curves were run for the baseline crack length of 0.5 mm .

of the environmental domain considered, interior coating recession is less than 30% of the recession predicted at the free surface. In this case, the narrow crack opening restricts diffusion of the reaction products to the exterior surface; the thicker coating implies that the interior is well supplied by reaction products (whose molar volume scales with coating thickness). Simply put, there is too much reaction product generated in the interior of

the specimen and too small an exit for recession to continue in the interior of the specimen.

The reverse is true for large openings and thin coatings, as shown in the bottom right corner map of Figure 5.5. In this instance, the diffusion pathways to the exterior of the composite allow for effective transport of limited reaction products generated on the interior. The ratio of interior to exterior recession length is above 80% over the entire domain. Considering that crack openings $10\ \mu\text{m}$ or larger are effectively open to free space (because molecular diffusion dominates), one expects the same behavior as a half-space exposed to a uniform environment, *i.e.* uniform recession across the free surface. The results for wide openings and thicker coatings confirm this; while more reaction products are generated for thicker coatings, there is still relatively little impact of environment on recession uniformity. (Naturally, there will be large variations in the baseline recession as a function of environment.)

Finally, one may note that small crack openings and thin coatings exhibit high variability in recession uniformity, with the interior-to-exterior ratio varying from less than 30% at high temperature and water content to greater than 80% for low temperatures and low water vapor concentrations. Clearly, these openings and coating thicknesses represent scenarios where the competing effects of reaction product generation and transport rate along the crack are in a delicate balance.

5.3 Critical void volumes associated with rapid filling and rapid evacuation

Strictly speaking, whether an interior void fills rapidly with reaction products or effectively serves as a sink analogous to a free surface requires that the transport-reaction product be solved with new boundary conditions. However, significant insight into critical void volumes can be generated by assuming that the concentration of recession reaction products in the void is spatially uniform within the void, and is governed by the volume of reaction product generated along the entire recession front. That is, we assume uniform recession and assume that the reaction products generated during recession are dumped into the void. This is justifiable for many composites, which exhibit voids that are spaced on the order of 100-500 μm apart [39, 82]; at this spacing, voids that act as perfect sinks would indeed produce uniform recession profiles for reasonable crack openings and coatings at thinner end of the range described in the previous section.

For a specimen of width a , depth b , the concentration of the void (if it is filled with the total volume reaction products generated during recession) is given by:

$$\tilde{C}_v(\tau) = \frac{C_v}{C^*} = \frac{2\bar{m}f\Delta_o}{\Omega_{BN}R} \cdot \frac{L_R(\tau)ab}{V_v C^*} \quad (5.1)$$

where \tilde{C}_v is the concentration in the void relative to the equilibrium concentration C^* , \bar{m} is a correction factor that accounts for the weighted-average number of boron atoms in a mole of product species, Ω_{BN} is the molar volume of BN , f is the fiber volume fraction, R is the fiber radius, Δ_o is the initial BN coating thickness, $L_R(\tau)$ is the recession length at time τ , and V_v is the void volume.

To address the question of whether or not a void is large enough to effectively act as a free surface, the critical volume is defined such that $\tilde{C}_v = 0.1$ at the end of recession, *i.e.* $\tau = 1$. This is an arbitrary cut-off; presumably if the concentration of the void rises to significant levels relative the equilibrium concentration of reaction products, the void no longer acts as an open volume since the reaction product in the void will begin to suppress diffusion out of the matrix crack. Results for this critical volume are shown in Figure 5.6 as a function of coating thickness, for several different environmental conditions. Note that the analytical model for recession at the free surface does not depend on crack opening; transport at the free surface is controlled by the infinite sink condition and not transport along the matrix crack.

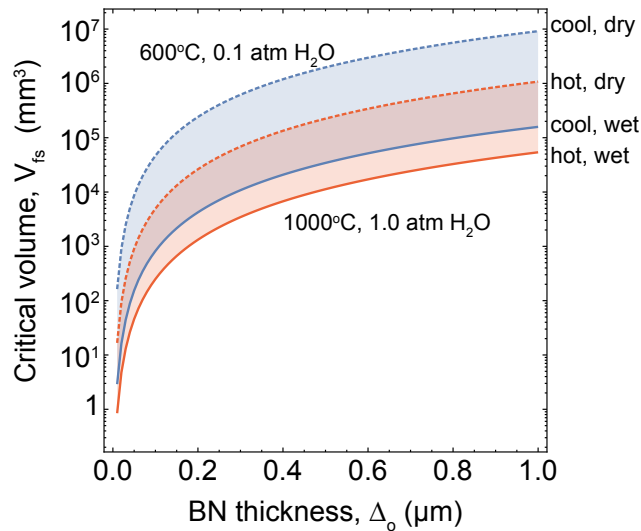


Figure 5.6: Critical volume required for a void to act as a free surface defined as $C_{void}(\tau = 1) = 0.1C^*$. Void volumes larger than these thresholds may act as perfect sinks, impacting recession at the composite interior.

The critical volume sizes shown in Figure 5.6 reflect the minimum void size to ensure that C_v is low relative to C^* . Voids smaller than the boundary will have concentrations larger than 10% of the equilibrium concentration, and therefore *will not* act as free space.

Voids larger than the boundaries in Figure 5.6 are able to maintain low concentration of reaction products and therefore it may be reasonable to expect them to behave as perfect sinks. It is unlikely that an interior void that is not connected to the exterior of the composite ever acts as a sink.

To understand this, consider the schematic of voids in a mini-composite shown in Figure 5.7, which is roughly to scale. A very large void may be $0.3 \times 0.3 \text{ mm}$ in the plane orthogonal to the fibers, and 10 mm in height in the fiber direction. Roughly, this corresponds to $\sim 1 \text{ mm}^3$. Even in conditions that lead to low recession (*e.g.* hot, dry environments), the size of a void that would not fill significantly with reaction product is at least two orders of magnitude. One may note that the critical volume is not dictated solely by recession length; the equilibrium concentration plays a significant role in determining trends of critical volume as a function of environmental conditions. Although hot, dry environments lead to low recession lengths, these conditions lead to higher equilibrium concentrations and overall smaller critical volumes. Though approximate, the results in 5.6 strongly suggest that any reasonable *interior* void (not connected to the free surface) will contain enough reaction product that it cannot be treated as free space, *i.e.* a perfect sink.

In fact, the results suggest that even large test chambers such as quartz tubes, will contain a significant concentration of reaction products to limit recession, *provided* the atmosphere surrounding the specimen is not replaced. However, most experiments are conducted with flowing atmospheres with sufficient velocities to replace the chamber atmosphere many, many times over the course of complete recession, such that the assumption the chamber is a perfect sink is virtually always valid.

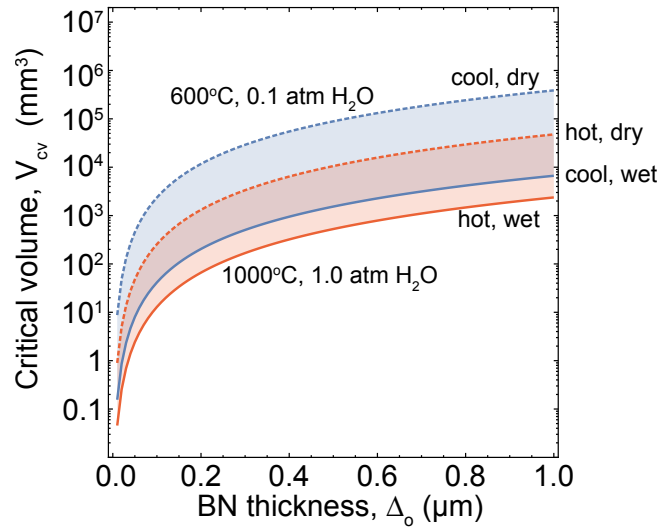


Figure 5.7: Illustration of voids in unidirectional composites. If the void volume is large enough, voids can act as free surfaces, significantly decreasing the effective crack length for transport.

Given that the largest *interior* voids imaginable will fill to concentrations likely to impact transport from the matrix crack, it is instructive to examine the other limit; when do voids quickly reach their maximum capacity, *i.e.* the equilibrium concentration of reaction products? To address this question, the critical void volume is redefined such that $\tilde{C}_v \geq 0.9$ for times less than $\tau = 0.1$. That is, does the concentration in the void reach greater than 90% of the equilibrium concentration in less than 10% of the time it takes to reach complete recession? Figure 5.8 illustrates this critical void volume as a function of coating thickness, again for a range of environments that bracket recession behaviors. For void sizes above the curves shown in the figure, the concentration in the void at short times will not be close to the equilibrium concentration, implying that the rate of void filling will impact recession next to the void. For void sizes below the line, the void fills in earliest stages of recession to the equilibrium concentration, effectively shutting off transport into the void. In such instances, the void has no impact on interior recession and one can assume recession profiles near the void that are comparable to

intact composite interiors.

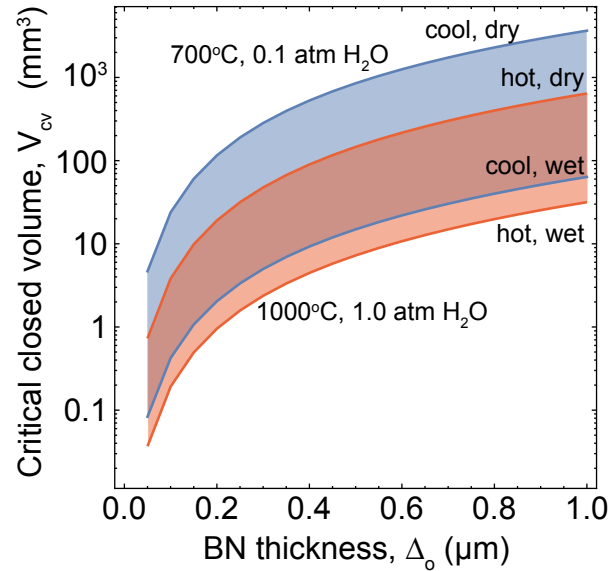


Figure 5.8: Critical volume required for a void to act as a closed volume defined as $C_{void}(\tau = 0.1) = 0.9C^*$. Void volumes smaller than these thresholds will rapidly fill and not impact interior recession.

Once again, the critical void volumes for this limit are substantially larger than typical void sizes in CMCs. This implies that in virtually all cases, even for what may appear visually as large voids, the concentration of reaction products in the voids will quickly reach high enough concentration to shut off transport into the void. As such, there will not be significantly greater recession adjacent to the void as there is in intact, interior regions of the composite. A brief discussion of the implications of this finding, and potential limitations of the underlying assumptions, is provided in the next section.

5.4 Discussion

The principal findings of the study of recession uniformity are that *(i)* relatively uniform recession profiles are expected for large crack openings and for smaller crack openings when coating thickness values are small at low temperature and water content, and *(ii)* interior voids likely have surprisingly small impact on recession uniformity. Of course, there are other reasons recession may vary significantly within the composite.

The principal source for non-uniformity in recession is likely variations in coating thickness, both throughout the composite and around individual fibers. Local variations in coating thickness will lead to local variations in gap closure times, which implies recession lengths will arrest at different exposure times in different locations. All of the above results assume coating thickness is uniform throughout the composite, and that an accurate accounting for the volume of reaction products filling voids or being ejected from the matrix crack can be obtained from a uniform recession length. Experimental observations strongly suggest this highly idealized scenario does not occur in actual specimens; variation in coating thickness from 0 to 500 μm are readily observable.

In light of this, future work should focus on applying the principles of the preceding section to distributions of fiber coating thickness to quantify the effect of such variations on the total volume of reaction products that must be ejected in the surrounding atmosphere or into internal voids. The development of such models would clearly benefit from more extensive experimental correlations between recession lengths, coating thickness, and fiber spacings.

Chapter 6

Reductions in retained strength in *SiC/SiC* composites in water vapor due to *BN* coating recession

6.1 Introduction

High performance ceramic matrix composites (CMCs) rely critically on controlled frictional sliding at the fiber/matrix interface, which provide damage tolerance by redistributing loads near matrix cracks and fiber breaks[15, 24]. Fiber coatings serve as an intermediate phase between the fibers and matrix and ensure matrix cracks will deflect around fibers (preventing simultaneous fiber failures) and into the matrix/coating interface, the coating/fiber interface, or within the coating itself. The deflected cracks running parallel to and around the fibers correspond to mating surfaces that allow for frictional sliding[18].

As shown schematically in Figure 6.1(A), a well-made composite with suitable crack

deflection and subsequent sliding, the composite can sustain multiple matrix cracks and fiber breaks prior to final failure and exhibit in turn remarkable strength and toughness. Composites with such properties are well-described by a model that consists of a unit cell of a fiber surrounded by matrix and allows for multiple matrix cracks and multiple internal fiber breaks (between matrix cracks); this model is referred to as the single fiber composite (SFC) model[47, 90, 91] and is shown schematically in Figure 6.1(B).

Mechanisms that disrupt the above behaviors invariably degrade the overall mechanical performance of the composite, as illustrated in Figure 6.1(C). Fiber/matrix interfaces that fail to debond or are highly resistant to sliding lead to simultaneous fiber and matrix cracking at very low loads, due to the defect sensitivity of ceramics. Likewise, systems with very low friction along the sliding interface severely limit the load transfer from the fiber to the matrix and extend the length of the fibers experiencing elevated stress, lowering the composite strength. In the limit of no sliding resistance, the strength of the composite is governed by the dry fiber bundle (DFB) strength, *i.e.* that describing a bundle of disconnected fibers.

For *SiC/SiC* composites, boron nitride (*BN*) has emerged as the dominant choice for coatings due to its efficacy in ensuring proper interface debonding and sliding behaviors. However, at high temperatures *BN* reacts with oxygen to form liquid boria, which then can then be volatilized by reactions with water vapor[9, 41, 50]. Hence, exposed *BN* surfaces are prone to chemical etching in the environments where high temperature CMCs are most desirable, such as gas turbines for power and propulsion systems.

In CMCs, this etching process starts along matrix crack planes that provide ingress to environmental reactants, as shown in Figure 6.1(C). The process then proceeds as the

reaction site moves away from the matrix crack plane, consuming the coating to create an annular gap between the fiber and the matrix. This damage mechanism is referred to as recession, since the edge of the intact coating recedes from the matrix crack plane. Recession eliminates frictional sliding along the interface, and lowers the strength of the composite by exposing increasingly large sections of the fibers to large stresses (*i.e.* the applied stress divided by the fiber volume fraction). In the limit that recession lengths reach one half the matrix crack spacing, matrix/fiber interactions are completely eliminated and the specimen consists of a dry fiber bundle.

Recession arising from environmental exposure therefore represents a timed march from the initial high strength of the pristine composite (described by the SFC model) towards the lower strength of the dry fiber bundle (described by the DFB model). Hence, the time-dependence of recession places a central role in the stress-rupture behavior of composite and environmental effects on this response. Recession may arrest prior to reaching the DFB limit, however, due to the formation of silica (SiO_2) on the matrix and fibers surfaces. Eventually, the oxide fills the annular gap that provides the transport channel to the reaction front and blocks reactants from reaching the recession front.

This work combines composite failure models that account for coating loss [49], a comprehensive recession model [87], and a standard *SiC* oxidation model [6] to quantify the time-dependent strength of *SiC/SiC* composites as a function of water vapor and temperature. A key contribution is the mapping of critical times to reach the dry fiber bundle limit and gap closure, as a function of composite properties, matrix crack spacing, and environment. These have important implications with regards to the design and interpretation of experiments that quantify environmental effects on performance, and for in-service performance.

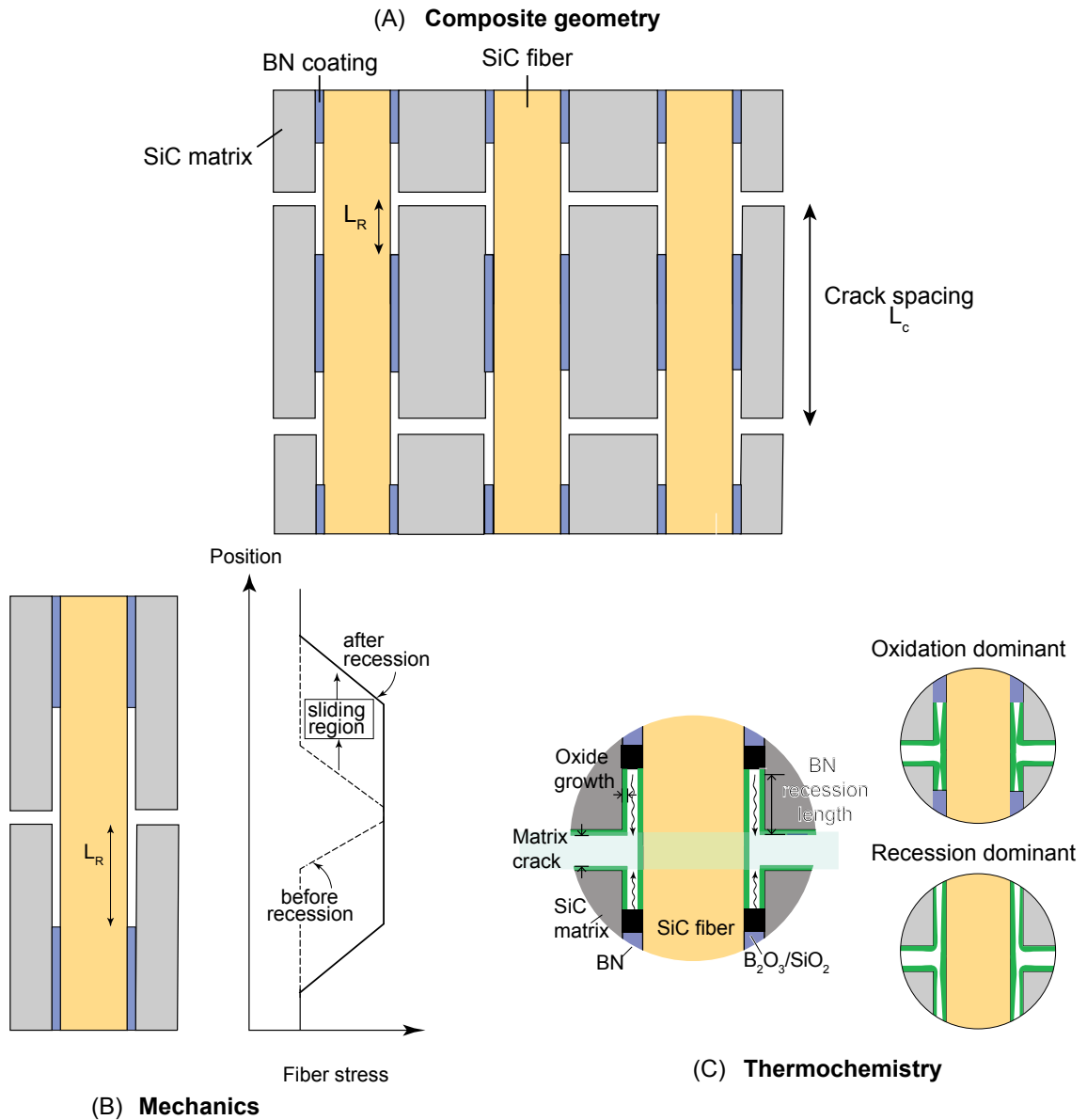


Figure 6.1: (A) Schematic of macroscopic specimen with multiple matrix cracks and recession regions near the cracks. (B) Fiber stress distributions near matrix cracks for unit cells with recession. (C) Schematic of recession and oxidation behaviors near a single fiber.

The present modeling effort focuses on retained strength, *i.e.* the peak allowable stress on a composite defined by a pre-defined crack spacing and recession length. The

relevant loading scenario consists of a composite that is (i) stressed above the matrix cracking stress, and below the ultimate composite strength that produces complete rupture, and (ii) exposed to the environment. The model predicts the maximum allowable stress after exposure, which is necessarily above the initial applied load. That is, the retained strength is the maximum allowable stress after the initial loading and exposure, as would occur during a sudden overload.

A closely related behavior is the time to rupture the composite at the initial fixed stress that sets the matrix crack spacing. In that scenario, one must solve for the crack spacing at the stress of interest while simultaneously ensuring the stress is above the dry fiber bundle limit and below the strength of the composite. One then must determine the time required to drop the retained strength of the composite to the applied stress (which may or may not happen). The present treatment of retained strength represents a critical step towards constructing such stress-rupture models, by quantifying relevant exposure times and stresses as a function of environment and crack spacing.

The remainder of this chapter is organized as follows. Section 6.2 summarizes the composite strength, recession and oxidation models used in this work; key assumptions embedded in the models are highlighted. Section 6.3 illustrates the relationships between retained strength, environmental conditions and exposure time. Particular focus is placed on the role of environment, matrix crack spacing and coating thickness on the ‘terminal strength’, *i.e.* that reached at gap closure or the dry bundle strength (whichever is reached first). A brief discussion of the implications of the predictions for experiments and in-service use is provided in Section 6.4, followed by summary conclusions in Section 6.5.

6.2 Strength, recession and oxidation models

6.2.1 Composite strength models

Models of composite strength have been developed for various regimes identified by the extent of both matrix and fiber fracture; a comprehensive review of these regimes and associated modeling is available in Reference [49]. In this work, we neglect the possibility of a single matrix crack exists in the specimen that leads to concomittant fiber failures during matrix cracking, or immediately after the appearance of the first (and only) matrix crack. (That is, we neglect domains labeled III and IV in the comprehensive map discussed in Reference [49].)

The present models assume that, in the pristine composite, both the matrix and fibers experience multiple cracks through the specimens. This is achieved when the characteristic shear transfer lengths defining stress build-up in the matrix and fibers are smaller than the gauge length of the specimen. (This is domain labeled I in Reference [49], and corresponds to the single fiber composite (SFC) model). The SFC model predicts the strength of the pristine composite as:

$$\sigma_c^I = f \sigma_f^o \left(\frac{\tau_s L_o}{\sigma_f^o R} \right)^{\frac{1}{m+1}} g(m) \quad (6.1)$$

where f is the fiber volume fraction, σ_f^o is a reference strength of the fibers corresponding to a reference gage length defined by L_o , τ_s is the shear sliding stress, R is the fiber radius, m is the Weibull modulus of the fibers. The dimensionless factor $g(m)$ varies between 0.68 and 0.87 for $m = 3$ to $m = 25$; the complete expression is given in Appendix C.

As recession progresses, the effective transfer length defining stress build-up in the

fibers increases (due to coating loss); the net effect of coating loss due to recession is to lower the average sliding stress in the composite. As elucidated in Reference [49], the corresponding adjustment to the SFC model above simplifies to:

$$\sigma_c^r = f\sigma_f^o \left(\frac{\tau_s L_o}{\sigma_f^o R} \right)^{\frac{1}{m+1}} \left[1 - 2 \frac{L_r}{L_c} \right]^{\frac{1}{m+1}} g(m) \quad (6.2)$$

where L_r is the recession length (defined as the distance from the matrix crack plane to the reaction front) and L_c is the matrix crack spacing. This expression is valid until the fiber transfer length exceeds twice the gauge length, L_g ; at this point, the strength is more accurately predicted by the dry fiber bundle model. The dry fiber bundle strength is given by:

$$\sigma_c^b = f\sigma_f^o \left(\frac{L_o}{m \epsilon L_g} \right)^{\frac{1}{m}} \quad (6.3)$$

As the dry fiber bundle strength does not depend on effective transfer lengths, it is independent of recession and hence constant in time. Note that the dry fiber bundle strength depends strongly on gauge length, whereas the single fiber composite model strength does not.

Thus, for a fixed crack spacing, the present models predict the strength will decrease as a function of recession (and time, using the recession models that follow) until σ_c^b is reached, at which point the strength remains constant. This assumes, of course, that the recession gap remains open through this process; if oxide closes this gap, the strength arrests at the value predicted by the recession length that is reached at closure. The mechanism controlling the terminal strength for a given condition is discussed in detail in the sections that follow.

It should be noted that the transition to the dry fiber bundle strength may occur prior to complete coating removal, *i.e.* prior to the point that the recession length reaches twice the crack spacing. One can obtain an estimate for the fraction of coating that remains when the dry fiber bundle limit is reached by equating $\sigma_c^r = \sigma_c^b$. The result is:

$$\frac{\ell_{intact}}{L_c} = \left(\frac{1}{g(m)} \right)^{m+1} \left(\frac{L_o}{m e L_g} \right)^{\frac{m+1}{m}} \left(\frac{\sigma_f^o R}{\tau_s L_o} \right) \quad (6.4)$$

where ℓ_{intact} is the length of intact coating left when the predicted strength reaches the DFB limit. Typical properties for well-made composites are listed in Table 6.1. For composites with these properties, ℓ_{intact}/L_c is less than 0.02, except for very low sliding stresses or exceedingly small gauge sections. Hence, for all practical purposes, the transition to the dry fiber bundle strength coincides with complete coating removal.

Table 6.1: Baseline properties used in parametric studies

<i>Interfaces</i>	$\tau_s = 20$ MPa
<i>Matrix</i>	$E_m = 400$ GPa
	$\sigma_m^o = 100$ MPa ($L_o = 1$ m)
	$m_m = 5$
<i>Fibers</i>	$f = 0.3$
	$R = 5$ μ m
	$E_f = 400$ GPa
	$\sigma_f^o = 1500$ MPa ($L_o = 1$ m)
	$m_f = 5$
<i>Composite</i>	$L_g = 100$ mm

6.2.2 Recession and oxidation model

Recession of the *BN* coating is assumed to occur as a two step chemical process; first, oxygen reacts with *BN* to produce boria, which will be a liquid at relevant temperatures. The boria then reacts with water vapor, forming gaseous $H_xB_yO_z$ species that diffuse away from the reaction site. Here, we assume the consumption of *BN* is limited by transport of the reaction products away from the reaction site, and not reaction kinetics. In other words, we assume chemical equilibrium. A detailed accounting of the thermochemistry of these reactions and transport along annular recession gaps has been previously published.[87] Here, we present key outcomes from that study and describe how they are used in conjunction with the strength models in the previous section.

The evolution of coating consumption (described by the recession length) is controlled by the balance of transport from the reaction site along the fiber to the matrix crack plane, and transport along the matrix crack from the fiber to the exterior of the composite. For fibers near the free surface, reaction products are quickly removed due to the short diffusion path along matrix crack plane. Hence, the recession rate and associated lengths are greatest near the free edge and decrease as one moves towards the composite interior. However, for small specimen widths typical of mini-composites, the difference between interior and exterior recession can be modest, such that recession lengths along the matrix crack plane are roughly uniform.

We therefore make the assumption of a uniform recession profile across the specimen, and estimate the recession length using the recession at the free surface. Since the recession length is largest at this location, the strength prediction will be conservative in the sense that it will predict the maximum possible impact of coating loss.

The recession at the free surface can be predicted using a single, closed-form expression that accounts for two important effects.[87] First, it accounts for the environmental dependence of the equilibrium concentration of reaction products, C^* . Second, it accounts for the decreasing diffusivity of the recession gap that stems from oxide growth on the fiber and matrix. Using suitable models for these two effects, one ultimately arrives at the following expression for the recession length:

$$L_r(\tau) = \sqrt{\frac{\bar{m}\gamma^2\Delta_o^2V_{BN}C^*D_m}{2B(\gamma-1)^2} \left(\tau + 2\frac{D_m}{D_k^o}\sqrt{\tau} + \frac{2D_m(D_m+D_k^o)}{(D_k^o)^2} \ln \left[\frac{D_m+D_k^o(1-\sqrt{\tau})}{D_m+D_k^o} \right] \right)} \quad (6.5)$$

where \bar{m} accounts for the number of boron atoms in the product gases, V_{BN} is the molar volume of BN, Δ_o is the initial coating thickness, C^* is the concentration of reaction products at the reaction site, D_m is the molecular diffusion coefficient, and D_k^o is the Knudsen diffusion constant for the annular channel, B is the parabolic growth constant for the oxide and γ is the molar volume ratio of *SiC* to *SiO₂*. The dimensionless time parameter is given by:

$$\tau = \frac{4B(\gamma-1)^2t}{\gamma^2\Delta_o^2} \quad (6.6)$$

where t is time expressed in the same temporal units as B . Here, the time is normalized by the time required to grow an oxide that completely closes the recession gap. That is, at $\tau = 1$ the oxide has completely blocked off the reaction site at the receding edge of the coating and recession arrests. The somewhat complicated time-dependence of Equation 6.5 is a result of an effective diffusivity model that accounts for slower diffusion in narrow gaps (*i.e.* Knudsen diffusion); oxide growth is incorporated into the effective diffusivity model by replacing the instantaneous gap size with the coating thickness minus the oxide

thickness.

6.2.3 Integration of the strength and recession models

At any given instant in time, the current recession length can be computed via Equation 6.5. This length can then be used in Equation 6.2 to predict retained strength up until gap closure; if the predicted strength is larger than the dry fiber bundle limit given as Equation 6.3, the latter is taken as more accurate model and hence defines the retained strength of the composite. The ‘terminal strength’ is defined as the strength at the first occurrence of either gap closure or reaching the dry fiber bundle limit; this is ‘terminal’ in the sense that continued environmental exposure does not lead to further decreases in strength.

Note that for conditions where the dry fiber bundle limit is reached (*e.g.* for environments corresponding to fast recession and slow oxide growth), the terminal strength is independent of environment and matrix crack spacing and depends strongly on gauge length. Conversely, for conditions where the terminal strength is controlled by gap closure (*e.g.* for environments corresponding to slow recession and fast oxide growth), the results are strongly dependent on environment and crack spacing, but independent of gauge length.

Prior to gap closure, the environment impacts strength principally through two variables; the equilibrium concentration of reaction products, $C^* = f(T, p_{H_2O})$, and the parabolic growth parameter $B = f(T, p_{H_2O})$, where T is temperature and p_{H_2O} is the partial pressure of water vapor. (We assume oxygen is the remaining balance). The functional dependence of C^* and B on environment is rich behavior in and of itself

[1, 8, 87], and can lead to recession lengths that vary non-monotonically with water concentration and temperature.

As a practical matter, the strength at any given time can be obtained by tabulating the predictions given by Equation 6.5, and compared to the dry fiber bundle limit; if the latter is reached prior to closure, this value is taken as the constant strength. The critical exposure time to reach the dry fiber bundle limit can also be solved for directly by (i) substituting Equations 6.5 and 6.6 into Equation 6.2, (ii) equating the result to Equation 6.3, and (iii) conducting a line search for the time.

6.3 Results

6.3.1 Illustrative results

Figure 6.2 illustrates the retained strength as a function of recession length divided by the crack spacing, for several different gauge lengths. Here the effects of environment are neglected such that the impact of gauge length on transition to the dry fiber bundle limit is clearly portrayed. Increasing the gauge length increases the recession length required to transition to the DFB; for the two longest gauge lengths this transition occurs when the coating is, for practical purposes, completely removed. However, in all cases, the terminal condition occurs when recession length is very close to the crack half-spacing.

Figure 6.3 plots the retained strength as a function of time, for several different crack spacings and two different recession conditions. For large matrix crack spacings (*e.g.* $L_c = 20\text{ mm}$), the terminal strength is set by oxide closing the recession gap, due to the fact that significant recession lengths are needed to drop the strength to the dry fiber

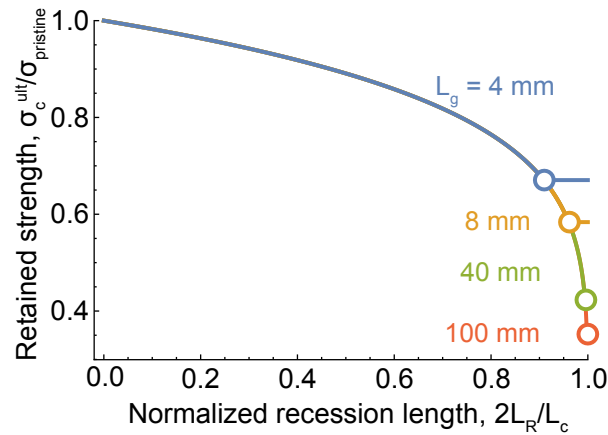


Figure 6.2: Retained strength as a function of recession length relative to crack spacing for several gauge lengths. The transition from SFC to DFB is indicated by circle markers.

bundle limit. Conversely, for smaller crack spacings, the terminal strength is set by the dry fiber bundle limit, due to the fact smaller recessions lengths are sufficient to reach this limit.

Note, however, that the results are a strong function of coating thickness, as shown for two $L_c = 8$ mm cases; thicker coatings imply faster recession, such that the strength drops to that of the dry fiber bundle limit even before gap closure. The impact of coating thickness can be quite dramatic over time scale relevant to testing; after ~ 250 hrs, the composite with the thicker coating ($0.6 \mu\text{m}$) has less than 50% of the retained strength of the composite with the thinner coating ($0.35 \mu\text{m}$).

The results in Figure 6.3 clearly indicate that crack spacing and coating thickness play an outsized role in the strength reduction observed in experiments; these are frequently conducted over time scales where gap closure and complete recession (*i.e.* reaching the dry fiber bundle limit) are active mechanisms controlling strength.

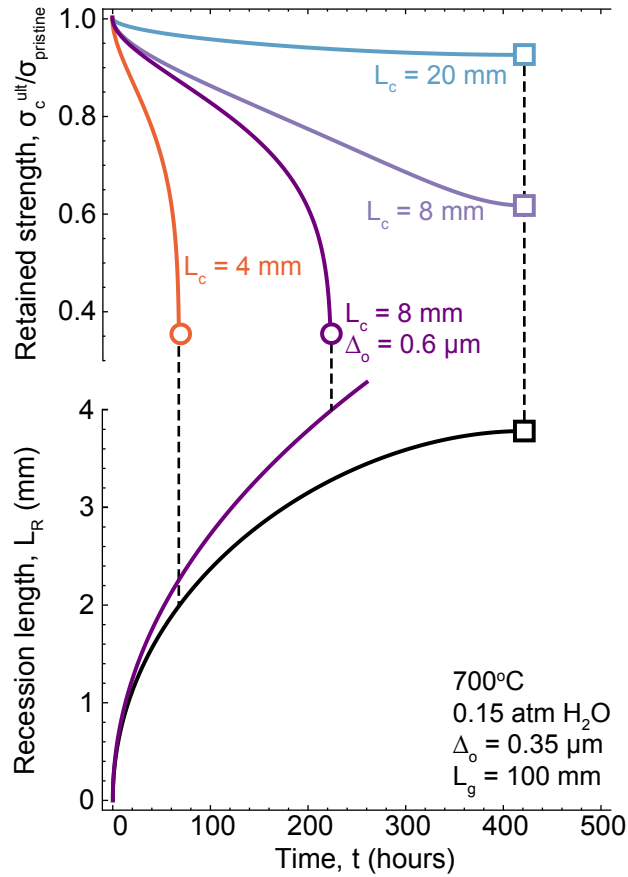


Figure 6.3: Retained strength as a function of time for several different crack spacings, coating thicknesses. The transition to dry fiber bundle is indicated by circles while closure of the recession gap is indicated by squares. Results were generated using 700°C , 0.15 atm water vapor, initial coating thickness of $0.35 \mu\text{m}$, and gauge length of 100 mm .

6.3.2 Impact of water vapor and temperature on critical times and retained strength

The critical time to reach either gap closure or the dry fiber bundle limit are shown in Figure 6.4 as a function temperature and water vapor. Several features of the plots provide general insight; first, gap closure controls retained strength only when the crack spacing is less than $\sim 5 \text{ mm}$. Second, for relatively wet environments (high water vapor concentrations), temperature is the controlling feature that sets the time to reach

the terminal condition (and in turn the strength). Third, while gauge length strongly impacts the retained strength when the fiber bundle limit is reached, it has a negligible impact on the time to reach minimum retained strength.

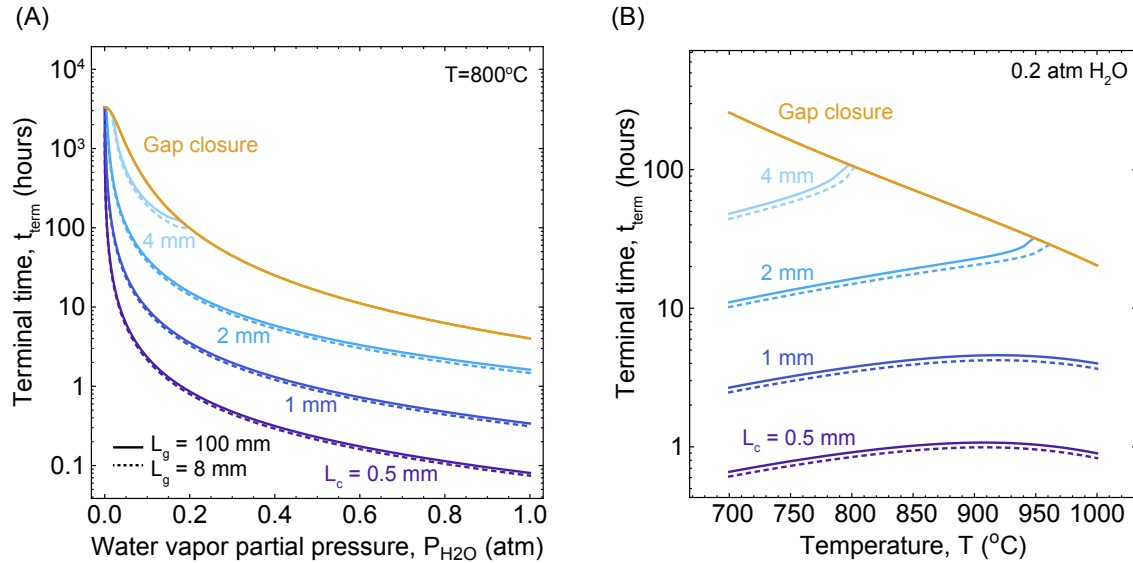


Figure 6.4: (A) Impact of water vapor on time to gap closure and time to reach bundle strength for various crack spacings and two different gauge lengths. (B) Impact of temperature on time to gap closure and time to reach bundle strength for various crack spacings and two different gauge lengths.

The complex behaviors that can result from dry environments, lower temperatures and small crack spacing are illustrated more clearly in Figure 6.5, which presents contour maps of the mechanism controlling terminal strength and the resulting retained strength. Combinations of water concentration and temperature that fall with the dark blue regions correspond to specimens reaching the dry fiber bundle limit. In this limit, the strength is relatively low and governed exclusively from the gauge length. Note from Figure 6.5A that the size of this domain is strongly dependent on crack spacing; for crack spacings larger than 10 mm, gap closure sets the retained strength, and the retained strength is

relatively high. One should also note the use of log-log scale for water concentration, indicating the retained strength may change dramatically in ‘dry’ environments with otherwise seemingly variations in composition. (See Figure 6.5B.)

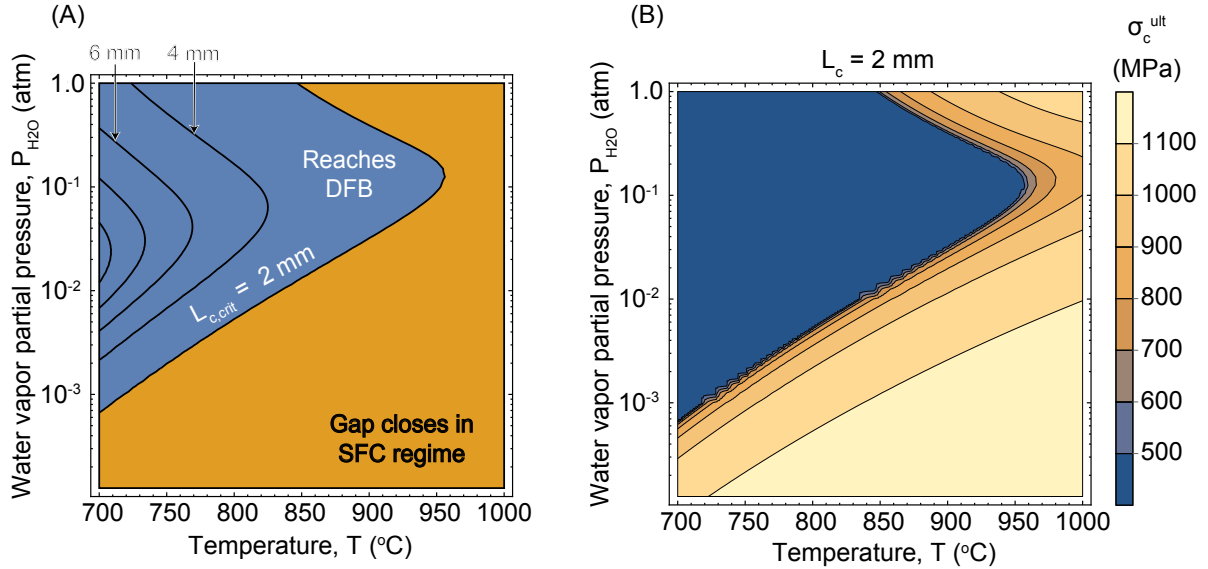


Figure 6.5: (A) Domain map illustrating mechanism controlling terminal strength as a function of water vapor and temperature; various crack spacings are shown, illustrating that gap closure dominates as crack spacings get larger. (B) Domain map of terminal strength, σ_c^{ult} as a function of water vapor and temperature for a crack spacing of 2 mm.

Figure 6.6 highlights that behaviors associated with environments with $p_{H_2O} \geq 0.1$ are somewhat simpler. In this regime, temperature is the dominant variable that dictates whether the dry fiber bundle limit is reached, while water content is arguably the dominant variable that sets the critical time associated with the terminal retained strength. That being said, one may note that at $p_{H_2O} = 0.2$, one anticipates reaching a terminal retained strength of 35% of the original strength after about 50 hours at $T = 750^\circ\text{C}$, or a terminal strength of 80% of the original strength for the same exposure time at $T = 900^\circ\text{C}$. Holding temperature constant at 800°C , one observes dramatic changes in

retained strength and the time to reach that value for water contents of $p_{H_2O} = 10\%$ (35% retained strength, ~ 150 hours) and of $p_{H_2O} = 50\%$ (85% retained strength, ~ 20 hours).

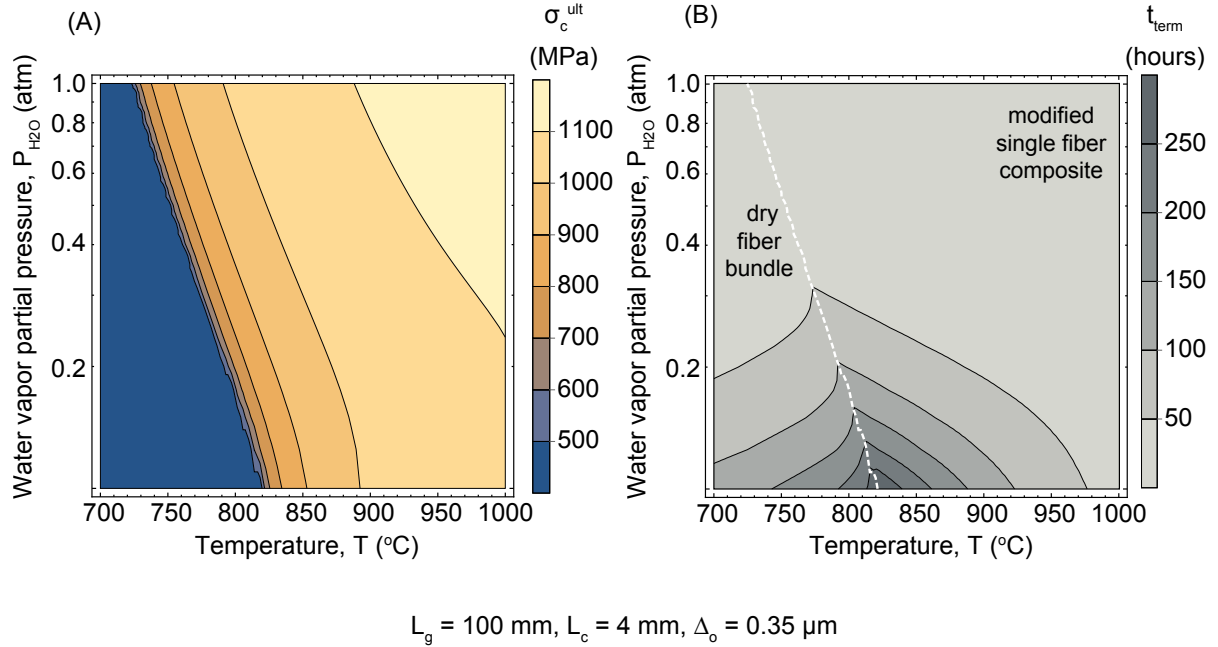


Figure 6.6: (A) Domain map of terminal strength, σ_c^{ult} ; when the composite reaches the dry fiber bundle limit, the strength is independent of the environment; conversely, the retained strength is high at elevated temperatures and water concentration, because oxidation halts recession prior to significant strength debits. (B) Domain map of terminal time, t_{term} .

Figure 6.7 more clearly highlights the dramatic transitions that can occur when crossing the boundaries shown in Figures 6.5 and 6.6. The non-monotonic strength behavior illustrated in Figure 6.7A with varying water vapor concentration reflects twice crossing the boundaries seen in the earlier figures. The correlation of strength and time (seen by comparing (A) with (C), and (B) with (D)) illustrates the importance of considering exposure time for any given environment. For example, the sharp drop in strength that

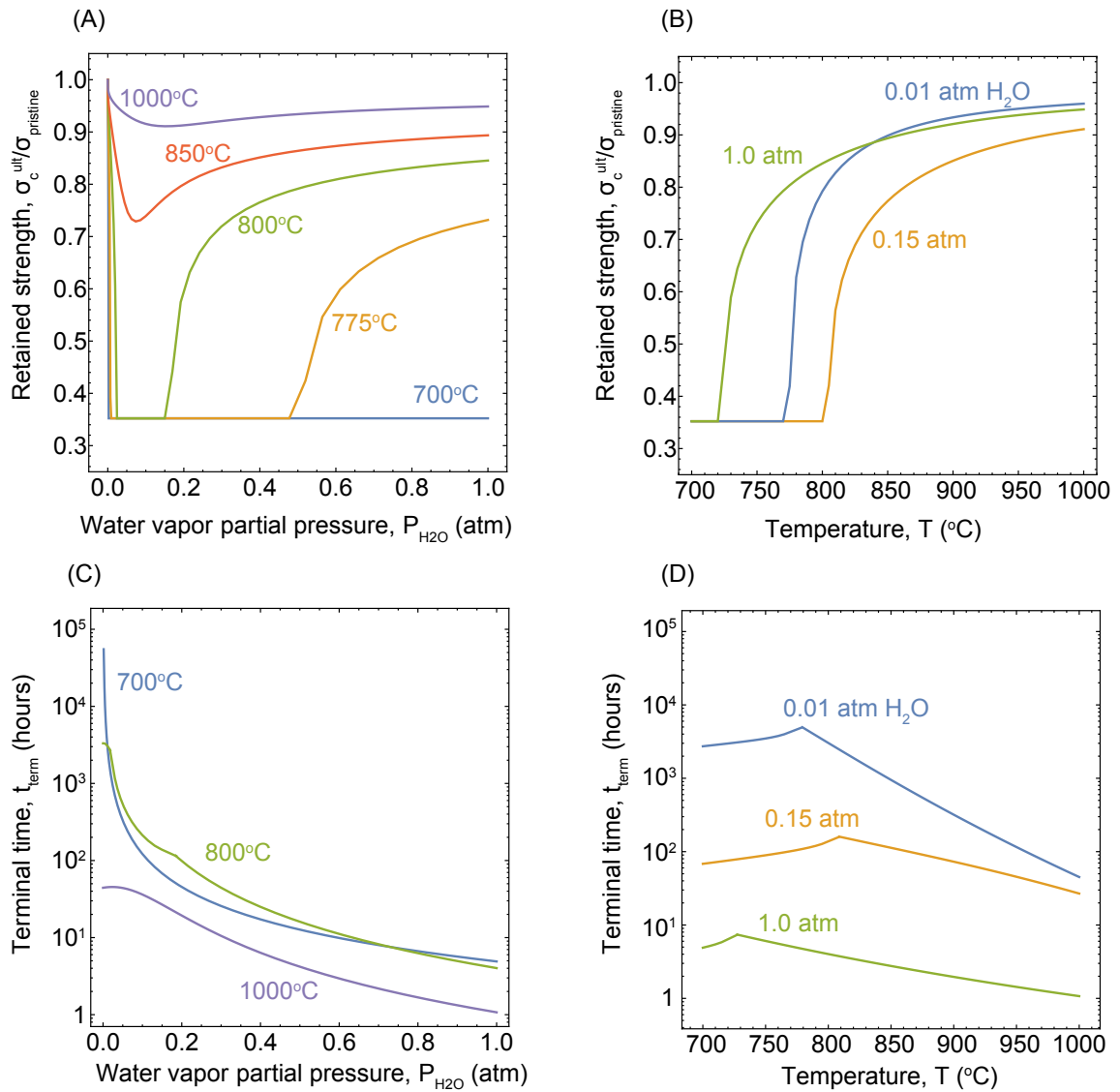
occurs with minute increases in water content in Figure 6.7A occurs over extremely long times, as shown by the results in Figure 6.7C. Conversely, the modest environmental debit observed at 1000 °C is associated with rapid oxidation and hence very short observation times. Generally speaking, high retained strengths are associated with relatively short times to reach the terminal condition, as shown in both sets of plots in Figure 6.7.

6.3.3 Impact of crack spacing and coating thickness on environmental degradation

Figures 6.3 and 6.4 illustrate that crack spacing and coating thickness play an important role in terminal retained strength. Figures 6.8 and 6.9 illustrate their role more clearly, by plotting retained strength directly in terms of these variables.

Generally, higher terminal retained strengths are obtained for large crack spacing, since it is less likely one will reach the dry fiber bundle limit prior to gap closure. However, as shown in Figure 6.8, given the rapid decline in strength as the dry fiber bundle limit is approached, small changes in crack spacing can lead to abrupt changes in terminal retained strength. It is interesting to note that factors of two in crack spacing are sufficiently to shift the terminal strength from 80% of the original strength to less than 30%; the critical spacing for this abrupt shift is strongly dependent on temperature but less so on water content, provided the water content is above 10%. Again, one should note the dramatic variations in time needed to reach this terminal strength, emphasizing that experimental observations will depend critically on whether or sufficient time has passed to reach gap closure or the dry fiber bundle limit.

Figure 6.9 illustrates that the role of *BN* coating thickness is paramount, if for no



$$L_g = 100 \text{ mm}, L_c = 4 \text{ mm}, \Delta_o = 35 \text{ }\mu\text{m}$$

Figure 6.7: (A) Retained strength as a function of water vapor for several different temperatures, for a given gauge length and crack spacing. (B) Retained strength as a function of temperature for several different water concentrations, for a given gauge length and crack spacing. (C) Terminal time as a function of water vapor for different temperatures, for a given gauge length and crack spacing. (D) Terminal time as a function of temperature for several different water concentrations, for a given gauge length and crack spacing.

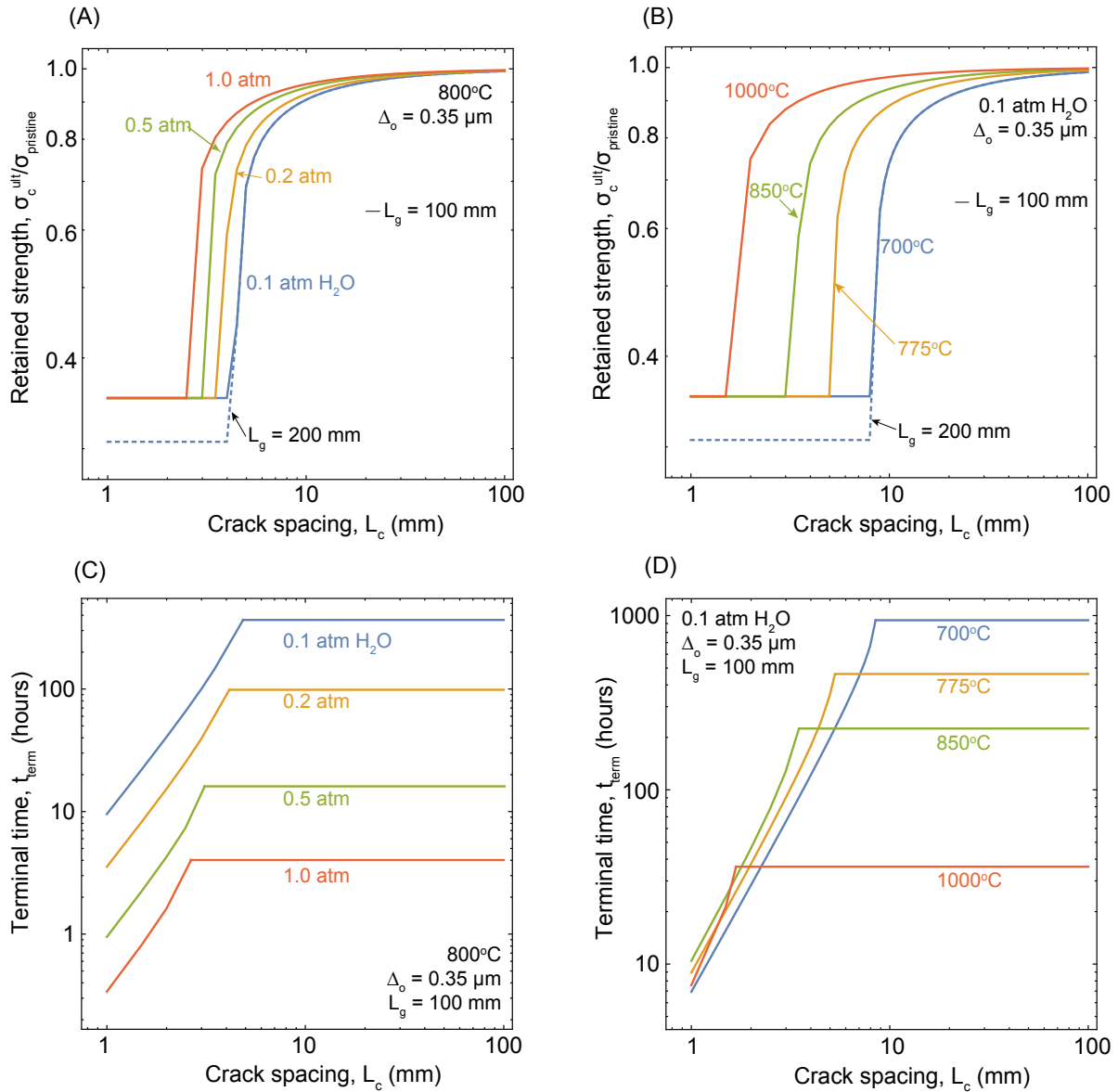


Figure 6.8: (A) Retained strength as a function of crack spacing as a function for several temperatures and fixed water concentration. (B) Retained strength as a function of crack spacing for several different water concentrations and fixed temperature.

other reason than it is a composite design variable. (Arguably, the composite must live within an environment imposed by a larger context.) Even modest variations in the sub-micron coating thickness can dramatically shift both the terminal strength and

the exposure time required to achieve it. Consider the results for a coating thickness of 300 *nm* in Figure 6.9; assuming terminal time is reached (a reasonable assumption noting the modest exposure times in Figures 6.9C,D), shifts in water content lead to rather modest changes in retained strength. Shifts in temperature from 800 °C to higher values also lead to modest shifts. However, shifts in coating thickness from 300 *nm* to 500 *nm* in most cases can lead to dramatic changes in retained strength, as one shifts from high values associated with rapid gap closure to low values associated with complete recession (or vice versa).

6.4 Discussion

The results presented earlier strongly emphasize the importance of understanding recession rates, oxidation rates and crack spacing in the characterization of composite strength. Clearly, modest changes in these variables, coupled with concomitant variations in exposure times, can lead to dramatic changes in observed retained strength. While such variability is clearly evident in the literature, identifying the root cause (and thus creating the opportunity to validate the present models) will require careful monitoring of the matrix crack spacing present during exposure, post-exposure strength measurements, and post-test characterization to quantify the extent of recession and oxidation in the interior of the specimen. This is clearly a daunting task, given the environmental resolution needed to confirm transition in mechanisms controlling strength.

There are several aspects of the current modeling framework that undoubtedly deserve future attention. First, it would be highly useful to establish a quantitative relationship between applied load and crack spacing; this would enable a quantitative relationship between service loads and terminal retained strength. Aside from directly informing al-

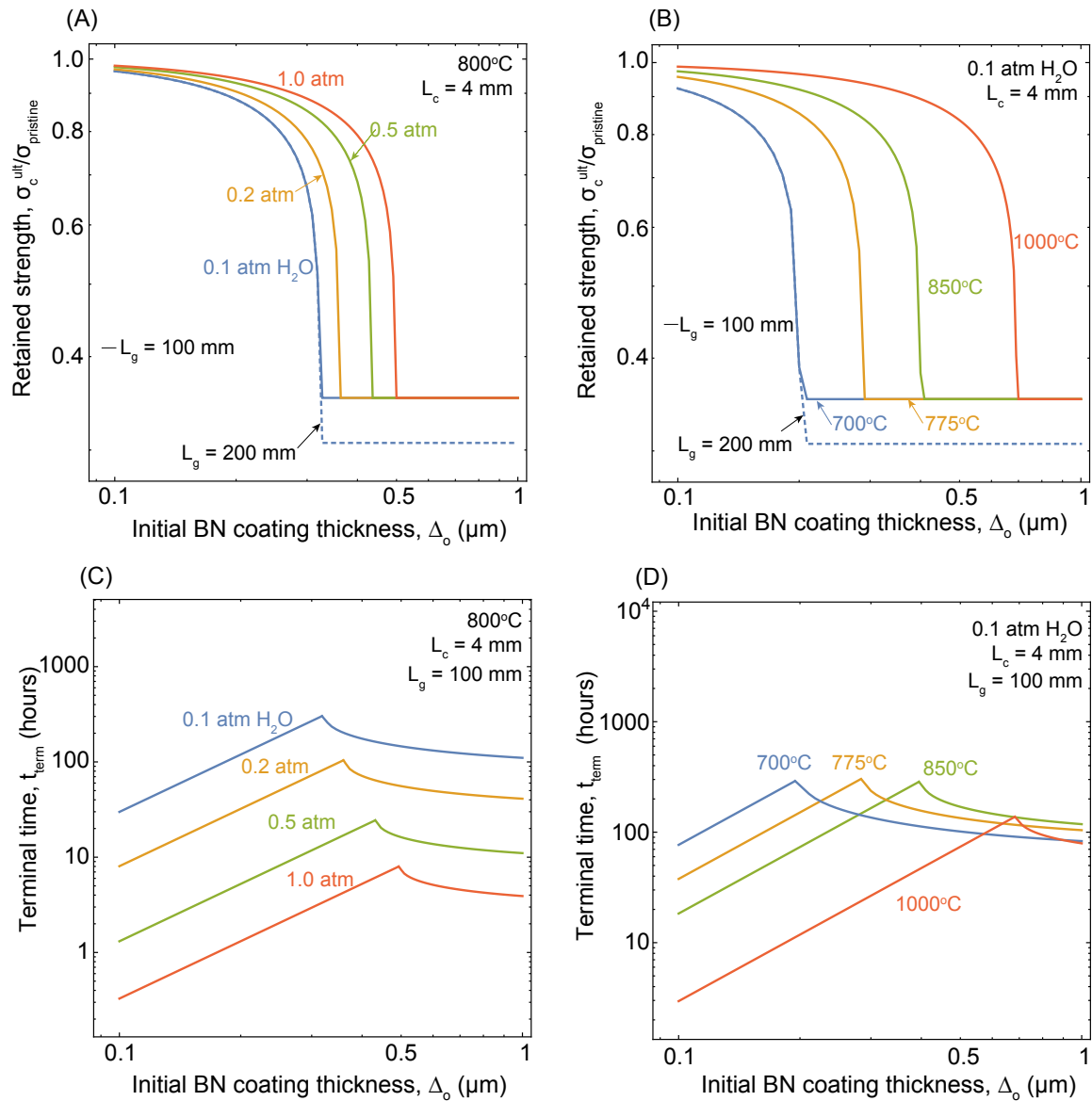


Figure 6.9: (A) Retained strength as a function of crack spacing as a function for several temperatures and fixed water concentration. (B) Retained strength as a function of crack spacing for several different water concentrations and fixed temperature.

lowable overloads in service, it would enable one to identify scenarios where the applied load falls between the initial strength of the composite and retained strengths. In such scenarios, true ‘strength-rupture’ plots can be created wherein the time-to-rupture is cal-

culated as the time required to drop the composite strength via recession to value of the retained strength.

Second, it is important to note again that the present modeling assumes a uniform recession profile along all matrix cracks. This is motivated in the present case by the prevalence of testing mini-composites, whose millimeter-scale widths are sufficiently small to allow for rapid transport from the center of the specimen. However, coupons or components with larger widths are likely to exhibit localized recession near the specimen surface, with little to recession along the interior. This naturally would mitigate the impact of recession. New models are needed to account for such effects, such as one that averages the results of the single fiber composite model using spatial distributions of recession (such as those shown in Reference [87]).

Third and finally, it is more than likely that retained strength predictions will need to be developed that account for cyclic loading. If the fiber bundle limit is reached in a single exposure, and, subsequent exposures do not achieve gap closure, cycling will have no effect. However, if cyclic loading involves full gap closure via oxidation, the response of the oxide to decreasing temperatures and load reversals will play a critical role. Temperature changes alone are likely to have a profound influence; as the specimen is cooled, CTE mismatch between the oxide, matrix and fibers, as well as potential phase changes in the oxide, will induce significant stresses that alter fiber and matrix fragmentation models.[37, 38] As yet, fragmentation models accounting for oxide stresses and cooling have not been developed.

6.5 Conclusions

The present framework provides an effective tool to evaluate the impact of coating recession on the retained strength of CMCs; direct quantitative connections between temperature, water content, coating recession and strength enable new opportunities to predict environmentally-controlled composite failures. The present study has generated the following important insights:

- Crack spacing is a dominant factor in strength reduction, as it sets the time required to effectively remove the coating and reach the dry fiber bundle limit. Small crack spacings require very little recession to reach this limit, leading to the most dramatic reductions in strength. Larger crack spacings require long recession lengths that are often not achieved prior to gap closure via oxidation; retained strengths are much higher in these scenarios.
- Coating thickness is also a dominant factor in strength reductions, as it strongly impacts the recession rate; thin coatings lead to short times for oxidation to close the recession gap, leading to higher retained strength from arrested recession. Thick coatings can lead to dramatic strength reductions due to the fact closure times are long and the dry fiber bundle limit is reached under a broad range of environments and crack spacings.
- The principal role of gauge length is to set the strength of the composite in the dry fiber bundle limit; however, gauge length has a relative small impact on the critical crack spacing that ensures the dry fiber bundle limit is reached, as the critical crack spacing varies by only 0.1 *mm* for gauge lengths spanning 8 to 100 *mm*.
- Strength degradation due to coating recession is most sensitive to temperatures between 800°C and 900°C. In this range, the volatilization and oxidation rates are

fairly equal, such that small changes in temperature shift the mechanism arresting degradation (*i.e.* gap closure, or reaching the dry fiber bundle limit). This temperature range is consistent with the environmental conditions associated with embrittlement in the literature.

- The strong sensitivity of the mechanisms controlling retained strength to temperature and water vapor highlights the importance of environmental conditions in experiments, since seemingly inconsequential changes can lead to strength variations of a factor of two (or more, depending on gauge length).

Chapter 7

Conclusion and recommendations

7.1 General conclusions and impact

The work presented in this dissertation contributed to the understanding of the role of fiber coating removal on *SiC/BN/SiC* ceramic composite strength. The major impacts are as follows:

1. Quantifying the composition and equilibrium concentration of reaction products at the leading edge of recession is critical to a variety of mechanisms that degrade composite performance. When considering multiple reaction products, the total concentration of reaction products exhibits a minimum that depends strongly on temperature and water content. Therefore, recession rates should also exhibit non-monotonic behavior.
2. The analytical expression for recession lengths near free edges provides an efficient means to quantify the extent of the most severe recession in a sample, and enables one to identify important scaling relationships between recession lengths and environment and coating thickness. Under cool, wet conditions, recession lengths

- can exceed 1 *mm*; on the other hand, under hot, dry conditions, recession lengths should arrest after approximately one fiber radius due to slow recession and fast *SiC* oxidation.
3. The reaction-diffusion model developed to predict transport down recession gaps and along matrix cracks clearly indicates that interior recession behaviors occur in a quasi-steady state, wherein the time scale to change the concentration along the matrix crack is much smaller than the time scales needed to transport reaction products from the recession site to the matrix crack plane. That is, the set of equations that describe the spatial distribution of concentrations (and recession lengths) can be written in matrix form with time-dependent pre-factors. This dramatically speeds the analysis of recession profiles.
 4. The spatial distribution of recession is most uniform for thin coatings and wide matrix cracks, which produce comparatively low concentrations of reaction products and provide efficient pathways for egress. Thicker coatings imply recession distributions will be highly non-uniform, with extensive recession lengths at the free surface and virtually no recession at the composite interior.
 5. Equilibrium concentrations of reaction products are relatively low; this implies that interior voids can reach these concentrations quickly even with thin coatings. That is, small amounts of recession are sufficient to fill interior voids to reach the concentration at the reaction site, such that they have little to no impact on interior recession lengths.
 6. Recession eliminates shear transfer between the fibers and matrix, effectively lowering the average sliding stress. This leads to a decrease in retained composite strength. The relevant limits for composite strength are defined by the single fiber

composite model (in the pristine state, prior to any recession) and the dry fiber bundle model (after composite coating removal). If SiC oxidation is sufficiently rapid, however, the lower limit will not be attained because coating recession will arrest prior to complete coating removal.

7. When recession is spatially uniform, coating thickness plays an important role in recession-driven changes in composite strength. Thicker coatings lead to rapid recession rates such that the dry fiber bundle limit can be reached quickly. Conversely, thinner coatings lead to slow recession and the terminal state is defined by the single fiber composite model, with slight to modest reductions in strength associated with interrupted coating recession.

7.2 Future work

Based on these contributions, the following suggestions for future work are presented.

- **Improved reaction front models that account for more complex spatial variations in composition and the impact of BN on the recession and SiC oxidation processes that are likely intertwined.**

There is much uncertainty surrounding the kinetics of BN oxidation and volatilization in SiC systems. Improving the understanding of these kinetics will improve modeling results and understanding of the critical time scales for oxidation. The model presented here could be updated with improved rate constants for the oxidation and volatilization of boria. This would include tracking the oxidant partial pressure along the matrix crack as a function of time. Improved understanding of SiC oxidation rate constants in the presence of BN and boria is critical to accurately predicting coating recession lengths. While some work has begun on this

task in oxygen environments[61], water vapor environments must also be addressed.

The rate-limiting step of BN oxidation and volatilization must also be further explored. The models developed in this dissertation assume volatilization is the rate-limiting step in BN coating recession but the rate of boria formation plays a critical role in the evolution of boria activity with time. Generation of boria from additional BN oxidation replenishes the boria lost due to $H_xB_yO_z$ volatilization in the borosilicate. If the time rate of change of boria concentration varies, then so does the activity of boria and the recession lengths predicted by the analytical model may overpredict fiber coating recession.

- **Improved oxidation models that are fiber and matrix specific and have spatial variations in coating thickness that also incorporate the oxidation rate constant changes arising in the improved reaction front models.**

The fibers and matrix are typically made of different types of SiC , each with different oxidation rate constants. Coupling an improved representation of fiber and matrix oxidation with improved BN kinetics would lead to a refined understanding of the dominant reaction and the time scales controlling the terminal composite strength. Furthermore, the fiber coating thickness is not uniform along the fiber axis. New models are needed to account for such effects and to develop insight into the controlling reactions and time scales for more complex composites.

- **Coupling of non-uniform recession distributions and composite fragmentation models to predict the impact of highly localized recession near edges. In other words, the study of retained strength could be broadened to include regimes where recession is non-uniform.**

It would be highly useful to establish a quantitative relationship between applied load and crack spacing; this would enable a quantitative relationship between service loads and terminal retained strength. Aside from directly informing allowable overloads in service, it would enable one to identify scenarios where the applied load falls between the initial strength of the composite and retained strengths. In such scenarios, true ‘strength-rupture’ plots can be created wherein the time-to-rupture is calculated as the time required to drop the composite strength via recession to value of the retained strength.

It is important to note again that the present modeling assumes a uniform recession profile along all matrix cracks. This is motivated in the present case by the prevalence of testing mini-composites, whose millimeter-scale widths are sufficiently small to allow for rapid transport from the center of the specimen. However, coupons or components with larger widths are likely to exhibit localized recession near the specimen surface, with little to no recession along the interior. This naturally would mitigate the impact of recession. New models are needed to account for such effects, such as one that averages the results of the single fiber composite model using spatial distributions of recession (such as those shown in Chapter 4).

- **Model the impact of filled recession channels upon cooling to understand the impact of coefficient of thermal expansion (CTE) mismatch and possible changes in oxide structure on damage to the fibers and matrix.**

It is more than likely that retained strength predictions will need to be developed that account for cyclic loading. If the fiber bundle limit is reached in a single exposure, and, subsequent exposures do not achieve gap closure, cycling will have

no effect. However, if cyclic loading involves full gap closure via oxidation, the response of the oxide to decreasing temperatures and load reversals will play a critical role. Temperature changes alone are likely to have a profound influence; as the specimen is cooled, CTE mismatch between the oxide, matrix and fibers, as well as potential phase changes in the oxide, will induce significant stresses that alter fiber and matrix fragmentation models.[37, 38] As of yet, fragmentation models accounting for oxide stresses and cooling have not been developed.

Appendix A

Finite element framework for transport-reaction equations

Let the domain of interest be from $x = 0$ to $x = \ell$, where ℓ is the length of the “element” (the domain over which a solution is sought). In the end, we will find that the absolute values of x are immaterial, and that the element we derive is valid for a domain running from one end located at x_1 to the other end, located at x_2 .

Assume the approximate solution can be written as:

$$C(x, t) \approx C_1(t) \left(1 - \frac{x}{\ell}\right) + \left(\frac{x}{\ell}\right) C_2(t) \quad (\text{A.1})$$

$$= C_1(t)N_1(\tilde{x}) + C_2(t)N_2(\tilde{x}) \quad (\text{A.2})$$

$$= [N_1(\tilde{x}) \ N_2(\tilde{x})]_{1 \times 2} \begin{bmatrix} C_1(t) \\ C_2(t) \end{bmatrix}_{2 \times 1} \quad (\text{A.3})$$

where $C_1(t)$ represents the concentration at $x = 0$ and $C_2(t)$ represents the concentration at $x = \ell$, *i.e.* the two nodes of the element. Here, we use $\tilde{x} = x/\ell$ as shorthand. The

functions (linear in this case) defined by $N_1(\tilde{x})$ and $N_2(\tilde{x})$ are called ‘shape functions’ (or interpolation functions) because they describe the shape of the concentration distribution between the nodes.

The weak form of the governing equation computes the sum of the error in the PDE multiplied by a ‘weight function’ that weighs the error ϵ at different locations, as in:

$$\epsilon_i = \int_0^\ell W_i(x) \left(D \frac{\partial^2 C(x,t)}{\partial x^2} + R(x,t) - \frac{\partial C(x,t)}{\partial t} \right) dx \quad (\text{A.4})$$

where ϵ_i is the residual error (hopefully driven to zero) associated with a given function, and $W_i(x)$ is the weight function. The weight function essentially allows one to adjust the relative contribution of various locations to the overall error – *i.e.* error in some locations is ‘counted’ less than others. In normalized space, this expression becomes:

$$\epsilon_i = \ell \int_0^1 W_i(\tilde{x}) \left(\frac{D}{\ell^2} \frac{\partial^2 C(\tilde{x},t)}{\partial \tilde{x}^2} + R(\tilde{x},t) - \frac{\partial C(\tilde{x},t)}{\partial t} \right) d\tilde{x} \quad (\text{A.5})$$

It is convenient to choose the weight functions to be the shape functions (one can also show this leads to be best performance for a given element size). Then, we have two error estimates associated with the two shape functions. This is called the Galerkin or Galerkin-Bubnov method[92]. Using matrix notation, we have:

$$[\epsilon]_{2 \times 1} = \ell \int_0^1 \left(\frac{D}{\ell^2} [N(\tilde{x})]_{2 \times 1}^T C''(\tilde{x},t) + [N(\tilde{x})]_{2 \times 1}^T R(\tilde{x},t) \right) d\tilde{x} - \ell \int_0^1 [N(\tilde{x})]_{2 \times 1}^T \dot{C}(\tilde{x},t) d\tilde{x} \quad (\text{A.6})$$

where the derivative notation has been replaced by $\partial^2/\partial \tilde{x}^2 = ()''$ and $\partial/\partial t = ()\dot{}$. We

can integrate the first term by parts, such that we have:

$$\begin{aligned}
 [\epsilon]_{2x1} = & \frac{D}{\ell} C'(\tilde{x}, t)|_0^1 - \frac{D}{\ell} \int_0^1 [N(\tilde{x})]_{2x1}^T C(\tilde{x}, t)' d\tilde{x} \\
 & + \ell \int_0^1 [N(\tilde{x})]_{2x1}^T R(\tilde{x}, t) d\tilde{x} \\
 & - \ell \int_0^1 [N(\tilde{x})]_{2x1}^T \dot{C}(\tilde{x}, t) d\tilde{x} \quad (\text{A.7})
 \end{aligned}$$

Here, we note that flux into an element is positive, and flux out of the element is negative (since the original PDE is based on molecule conservation in the control volume). Since the flux is given by $J = -DC'$, the above implies:

$$\begin{aligned}
 [\epsilon]_{2x1} = & \begin{bmatrix} J_0 \\ J_1 \end{bmatrix} - \frac{D}{\ell} \int_0^1 [N(\tilde{x})]_{2x1}^T C(\tilde{x}, t)' dx \\
 & + \ell \int_0^1 [N(\tilde{x})]_{2x1}^T R(\tilde{x}, t) d\tilde{x} \\
 & - \ell \int_0^1 [N(\tilde{x})]_{2x1}^T \dot{C}(\tilde{x}, t) d\tilde{x} \quad (\text{A.8})
 \end{aligned}$$

where J_0 is the flux into the element, and J_1 is the flux out of the element. We can substitute for the concentration gradient and time derivatives using the shape functions,

such that we have:

$$\begin{aligned}
[\epsilon]_{2 \times 1} = & \begin{bmatrix} J_0 \\ J_1 \end{bmatrix} + \ell \int_0^1 [N(\tilde{x})]_{2 \times 1}^T R(\tilde{x}, t) d\tilde{x} \\
& - \frac{D}{\ell} \left(\int_0^1 [N(\tilde{x})]_{2 \times 1}^T [N'(\tilde{x})]_{1 \times 2} dx \right) \begin{bmatrix} C_1(t) \\ C_2(t) \end{bmatrix} \\
& - \ell \left(\int_0^1 [N(\tilde{x})]_{2 \times 1}^T [N(\tilde{x})]_{1 \times 2} dx \right) \begin{bmatrix} \dot{C}_1(t) \\ \dot{C}_2(t) \end{bmatrix} \quad (\text{A.9})
\end{aligned}$$

where the nodal concentrations can be taken outside the integrals because they are not functions of space, and the spatial derivative is transferred to the shape functions for the same reason. The integrals in the 2x2 matrices in front of the temperatures can be integrated term by term to yield constant matrices that multiple the nodal concentrations and their time derivatives. Ignoring for the moment the generation term (represented by R in Eqn. A.9), this yields:

$$[\epsilon]_{2 \times 1} = \begin{bmatrix} J_0 \\ J_1 \end{bmatrix} - \frac{D}{\ell} \begin{bmatrix} 1 & -1 \\ -1 & 1 \end{bmatrix} \begin{bmatrix} C_1(t) \\ C_2(t) \end{bmatrix} - \ell \begin{bmatrix} \frac{1}{3} & \frac{1}{6} \\ \frac{1}{6} & \frac{1}{3} \end{bmatrix} \begin{bmatrix} \dot{C}_1(t) \\ \dot{C}_2(t) \end{bmatrix} \quad (\text{A.10})$$

Assuming we enforce the residuals to be zero, we have:

$$[D]_{2 \times 2} \begin{bmatrix} C_1(t) \\ C_2(t) \end{bmatrix} + [M]_{2 \times 2} \begin{bmatrix} \dot{C}_1(t) \\ \dot{C}_2(t) \end{bmatrix} = \begin{bmatrix} J_0 \\ J_1 \end{bmatrix} \quad (\text{A.11})$$

Note that we could have followed the same procedure, only with the first node and concentration located at position x_1 and the second node and concentration located at x_2 , with linear shape functions defined such that $N_1(x_1) = 1$ and $N_1(x_2) = 0$ and $N_2(x_1) = 0$ and $N_2(x_2) = 1$, and we would obtain the same same result, only with $\ell = x_2 - x_1$. Hence, this formulation is valid for any element lying on the x -axis between x_1 and x_2 , and we only need the element length connecting the two ends.

Let us now return to the generation term, which is time-dependent, but this temporal dependency is dropped for convenient notation in what follows:

$$R(\tilde{x}) = \frac{4f\Delta(\tilde{x})D_c(\tilde{x})}{h(\tilde{x})L(\tilde{x})} [C^*(\tilde{x}) - C(\tilde{x})] = \alpha(\tilde{x}) [C^*(\tilde{x}) - C(\tilde{x})] \quad (\text{A.12})$$

A linear distribution is a good approximation to any function over a short enough distance; hence we can interpolate values of the reaction terms computed at the nodes as:

$$R(\tilde{x}) = R_1(1 - \tilde{x}) + R_2\tilde{x} = \alpha_1 C_1^*(1 - \tilde{x}) + \alpha_2 C_2^*\tilde{x} - \alpha_1 C_1(1 - \tilde{x}) - \alpha_2 C_2\tilde{x} \quad (\text{A.13})$$

Multiplying by the shape functions, and then integrating, and then factoring out the

concentration terms, we can show that:

$$\ell \int_0^1 [N(\tilde{x})]_{2 \times 1}^T R(\tilde{x}) d\tilde{x} = \ell \begin{bmatrix} \frac{\alpha_1}{3} & \frac{\alpha_2}{6} \\ \frac{\alpha_1}{6} & \frac{\alpha_2}{3} \end{bmatrix} \begin{bmatrix} C_1^* \\ C_2^* \end{bmatrix} - \ell \begin{bmatrix} \frac{\alpha_1}{3} & \frac{\alpha_2}{6} \\ \frac{\alpha_1}{6} & \frac{\alpha_2}{3} \end{bmatrix} \begin{bmatrix} C_1 \\ C_2 \end{bmatrix} \quad (\text{A.14})$$

where α_1 is the pre-factor to the reaction term (see Eqn. 3.17 above), evaluated using values at the first node, e.g. $\alpha_1 = 4f\Delta_1(D_c)_1/h_1L_1$ and similarly for α_2 .

Putting it all together, one obtains the elemental matrix equations:

$$[M]_{2 \times 2} \begin{bmatrix} \dot{C}_1(t) \\ \dot{C}_2(t) \end{bmatrix} = \begin{bmatrix} J_0 \\ J_1 \end{bmatrix} - [D]_{2 \times 2} \begin{bmatrix} C_1(t) \\ C_2(t) \end{bmatrix} + [\alpha]_{2 \times 2} \begin{bmatrix} C_1^*(t) \\ C_2^*(t) \end{bmatrix} - [\alpha]_{2 \times 2} \begin{bmatrix} C_1(t) \\ C_2(t) \end{bmatrix} \quad (\text{A.15})$$

Note that this approach can be take even if C^* depends non-linearly on another variable; the central concept is that if the elements are small enough, a linear variation is always a good approximation to any distribution. The non-linearity doesn't really change anything, because the C^* term is simply evaluated at the nodal positions (*i.e.* it may be the water concentration raised to some power, but it is treated as a constant flux term in solution of the transport equation).

The preceding elemental matrix equations describe a single element within the structure, which in our case is the matrix crack. The combination of the individual elemental matrix equations yields a global matrix that describes the connectivity of our chosen element and node configuration. Consider two elements that are connected; call the left element Element #1 and the right Element #2; number the nodes from left to right (three of them). We seek to form a 'global' system equations that allow us to solve for the nodal concentrations. Physics dictates that the net molecular flux at an interior node

has to sum to zero: the number of molecules flowing from element #1 has to equal the number of molecules flowing into element #2. This means that $-J_1^{(1)}$ (the flux out of element #1) is equal to $J_0^{(2)}$; the minus sign takes into account the sign convention that the flux out of the element is negative and the flux into an element is positive. In other words, $J_1^{(1)} + J_0^{(2)} = 0$. If we call J_i the next flux gained or lost at a node, we have the following (ignoring the generation term):

$$\begin{aligned} & \frac{D_1}{\ell_1} \begin{bmatrix} 1 & -1 & 0 \\ -1 & 1 & 0 \\ 0 & 0 & 0 \end{bmatrix} \begin{bmatrix} C_1(t) \\ C_2(t) \\ C_3(t) \end{bmatrix} + \frac{D_2}{\ell_2} \begin{bmatrix} 0 & 0 & 0 \\ 0 & 1 & -1 \\ 0 & -1 & 1 \end{bmatrix} \begin{bmatrix} C_1(t) \\ C_2(t) \\ C_3(t) \end{bmatrix} + \quad (\text{A.16}) \\ & \ell_1 \begin{bmatrix} \frac{1}{3} & \frac{1}{6} & 0 \\ \frac{1}{6} & \frac{1}{3} & 0 \\ 0 & 0 & 0 \end{bmatrix} \begin{bmatrix} \dot{C}_1(t) \\ \dot{C}_2(t) \\ \dot{C}_3(t) \end{bmatrix} + \ell_2 \begin{bmatrix} 0 & 0 & 0 \\ 0 & \frac{1}{3} & \frac{1}{6} \\ 0 & \frac{1}{6} & \frac{1}{3} \end{bmatrix} \begin{bmatrix} \dot{C}_1(t) \\ \dot{C}_2(t) \\ \dot{C}_3(t) \end{bmatrix} = \begin{bmatrix} J_1 \\ 0 \\ J_3 \end{bmatrix} \end{aligned}$$

where J_1 is the species flux into the left end of the first element (a boundary condition) and J_3 is the species flux out of the right end of the second element (the other boundary condition). We can repeat this as often as necessary for interior nodes; the result is a

system of equations of the form:

$$[D]_{NxN} \begin{bmatrix} C_1(t) \\ \vdots \\ C_N(t) \end{bmatrix}_{Nx1} + [M]_{NxN} \begin{bmatrix} \dot{C}_1(t) \\ \vdots \\ \dot{C}_N(t) \end{bmatrix}_{Nx1} = \begin{bmatrix} J_1 \\ 0 \\ \vdots \\ 0 \\ J_N \end{bmatrix}_{Nx1} \quad (\text{A.17})$$

Note that if the diffusivity of the elements (i.e. that of the matrix crack) changes with time or temperature, one simply has to form the global matrices at each time step.

The numerical solution is found by solving the coupled set of equations above, subject to two boundary conditions and a set of initial conditions. (Recall that the original PDE was second order in space (requiring two boundary conditions) and first order in time (requiring initial values for all the nodal variables). Boundary conditions must be applied prior to inversion because the $[D]$ and $[M]$ matrices are singular until after imposition of the boundary conditions.

It is interesting to note that in the diffusion problem a crack that arrests in the matrix is identical to problem of a complete through crack, assuming (i) diffusion through the matrix is slower than along a bridged crack and (ii) the coordinate in the arrested crack corresponds to one-half that of the completely cracked specimen. In the arrested crack problem, the boundary condition at the tip of the crack is zero flux; this is identical to the symmetry condition for a complete through crack where the specimen is twice the bridged crack length.

For flux boundary conditions, one does not need to rearrange the equations: simply

impose the nodal flux J_0 at the left edge and J_1 at the right edge. For mixed boundary conditions, *i.e.* prescription of one concentration and one flux, one reduce the equations accordingly. For example, consider zero flux at the right edge and a prescribed concentration at left edge, *i.e.* $C_1(t)$ is prescribed concentration on the right edge as a function of time. Then we have $J_N = 0$, and the first row of the global system is not needed (since it describes evolution of C_1). The remaining equations of the global system are, for degrees of freedom $j = 2, N$ are:

$$\begin{aligned} \left(D_{j1}\dot{C}_1 + D_{j2}\dot{C}_2 + \dots + D_{2N}\dot{C}_N \right) &= J_2 - (D_{j1}C_1 + D_{j2}C_2 + \dots + D_{2N}C_N) \\ &- (\alpha_{j1}C_1 + \alpha_{j2}C_2 + \dots + \alpha_{2N}C_N) \\ &+ (\alpha_{j1}C_1^* + \alpha_{j2}C_2^* + \dots + \alpha_{jN}C_N^*) \quad (\text{A.18}) \end{aligned}$$

Since $C_1(t)$ is prescribed, it can be combined with J_2 (which is the next flux at node 2 and is therefore zero), yielding:

$$\begin{aligned} \left(D_{j2}\dot{C}_2 + \dots + D_{2N}\dot{C}_N \right) &= \left[-D_{j1}\dot{C}_1 - D_{j1}C_1 - \alpha_{j1}C_1 + \alpha_{j1}C_1^* \right] - (D_{j2}C_2 + \dots + D_{2N}C_N) \\ &- (\alpha_{j2}C_2 + \dots + \alpha_{2N}C_N) + (\alpha_{j2}C_2^* + \dots + \alpha_{jN}C_N^*) \quad (\text{A.19}) \end{aligned}$$

This effectively eliminates the first column of the global matrices by shifting it to the righthand side of the equation (multiplied by the respective concentrations for node #1, where it acts as a flux term. The solution is then found via direct integration.

Appendix B

Recession Model Code

This appendix documents the code used to calculate the results presented in Chapter 4 of this dissertation.

2 | Base Recession Code_formatted.nb

ln[]=* (*Each function gives the concentration (in mol/m³) of an HxByOz species as a function of temperature (T, Kelvin), water vapor partial pressure (pp, atm), and boria activity (a, unitless). The numbers in the function name indicate which species is calculated, e.g.--C336tipa is H₃B₃O₆ and C23tipa is B₂O₃*)

```
C112tipa[T_, pp_, a_] :=
  1 / (8.21*^-5 * T) ((a) * ((pp / (8.21*^-5 * T)) / (1 / (8.21*^-5 * T)))) *
  Exp[ $\frac{1}{8.314 * T} (- (330.5513296703299 - 0.15782395604395608 T) * 1000)$ ] ^ 0.5;
C313tipa[T_, pp_, a_] := 1 / (8.21*^-5 * T)
  ((a) * ((pp / (8.21*^-5 * T)) / (1 / (8.21*^-5 * T)))) ^ 3 *
  Exp[ $\frac{1}{8.314 * T} (- (-40.35034065934053 + 0.10430131868131862 T) * 1000)$ ] ^ 0.5;
C336tipa[T_, pp_, a_] := 1 / (8.21*^-5 * T)
  ((a) ^ 3 * ((pp / (8.21*^-5 * T)) / (1 / (8.21*^-5 * T)))) ^ 3 *
  Exp[ $\frac{1}{8.314 * T} (- (-94.2604505494506 + 0.15240956043956044 T) * 1000)$ ] ^ 0.5;
C23tipa[T_, pp_, a_] := 1 / (8.21*^-5 * T) ((a) * Exp[ $\frac{-(393.49 - 0.1739 T) * 1000}{8.314 * T}$ ]]);
```

(*cTota gives the sum of each individual HxByOz species*)

```
cTota[T_, pp_, a_] :=
  1 / (8.21*^-5 * T) ((a) * ((pp / (8.21*^-5 * T)) / (1 / (8.21*^-5 * T)))) *
  Exp[ $\frac{1}{8.314 * T} (- (330.5513296703299 - 0.15782395604395608 T) * 1000)$ ] ^ 0.5 +
  1 / (8.21*^-5 * T) ((a) * ((pp / (8.21*^-5 * T)) / (1 / (8.21*^-5 * T)))) ^ 3 *
  Exp[ $\frac{1}{8.314 * T} (- (-40.35034065934053 + 0.10430131868131862 T) * 1000)$ ] ^ 0.5 +
  1 / (8.21*^-5 * T) ((a) ^ 3 * ((pp / (8.21*^-5 * T)) / (1 / (8.21*^-5 * T)))) ^ 3 *
  Exp[ $\frac{1}{8.314 * T} (- (-94.2604505494506 + 0.15240956043956044 T) * 1000)$ ] ^ 0.5 +
  1 / (8.21*^-5 * T) ((a) * Exp[ $\frac{-(393.49 - 0.1739 T) * 1000}{8.314 * T}$ ]]);
(*T in K, a is unitless *)
```

Reaction product concentrations vs. temperature and water vapor, any activity
(Figure 2)

Diffusivity

Concentrations of reaction products for fixed boria activity $a = 0.25$ (hard code)

These functions are identical to the above, only they have the activity of boria hard-coded to be 0.25. For general results where the activity is difference, use code in preceding section.

```
ln[101]= C112tip[T_, pp_] :=
  1 / (8.21*^-5 * T)  $\left( (0.25) * ((pp / (8.21*^-5 * T)) / (1 / (8.21*^-5 * T))) * \right.$ 
     $\left. \text{Exp}\left[\frac{- (330.5513296703299 - 0.15782395604395608 T) * 1000}{8.314 * T}\right] \right)^{0.5};$ 
C313tip[T_, pp_] := 1 / (8.21*^-5 * T)
   $\left( (0.25) * ((pp / (8.21*^-5 * T)) / (1 / (8.21*^-5 * T))) \right)^3 * \text{Exp}\left[\frac{1}{8.314 * T} (- (-40.35034065934053 + 0.10430131868131862 T) * 1000)\right]^{0.5};$ 
C336tip[T_, pp_] := 1 / (8.21*^-5 * T)
   $\left( (0.25) \right)^3 * \left( (pp / (8.21*^-5 * T)) / (1 / (8.21*^-5 * T)) \right)^3 * \text{Exp}\left[\frac{- (-94.2604505494506 + 0.15240956043956044 T) * 1000}{8.314 * T}\right]^{0.5};$ 
  (*T in K, Conc in mol/m^3*)
C23tip[T_, pp_] := 1 / (8.21*^-5 * T)  $\left( (0.25) * \text{Exp}\left[\frac{- (393.49 - 0.1739 T) * 1000}{8.314 * T}\right] \right);$ 
  (*T in K, Conc in mol/m^3*)
cTot[T_, pp_] :=
  1 / (8.21*^-5 * T)  $\left( (0.25) * ((pp / (8.21*^-5 * T)) / (1 / (8.21*^-5 * T))) * \text{Exp}\left[\frac{1}{8.314 * T} (- (330.5513296703299 - 0.15782395604395608 T) * 1000)\right] \right)^{0.5} +$ 
  1 / (8.21*^-5 * T)  $\left( (0.25) * ((pp / (8.21*^-5 * T)) / (1 / (8.21*^-5 * T))) \right)^3 * \text{Exp}\left[\frac{1}{8.314 * T} (- (-40.35034065934053 + 0.10430131868131862 T) * 1000)\right]^{0.5} +$ 
  1 / (8.21*^-5 * T)  $\left( (0.25) \right)^3 * \left( (pp / (8.21*^-5 * T)) / (1 / (8.21*^-5 * T)) \right)^3 * \text{Exp}\left[\frac{1}{8.314 * T} (- (-94.2604505494506 + 0.15240956043956044 T) * 1000)\right]^{0.5} +$ 
  1 / (8.21*^-5 * T)  $\left( (0.25) * \text{Exp}\left[\frac{- (393.49 - 0.1739 T) * 1000}{8.314 * T}\right] \right);$ 
  (*T in K, Conc in mol/m^3*)
```

4 | Base Recession Code_formatted.nb

Molecular diffusivity calculation (code)

```

In[107]:= DiffAvg[T_, pp_, mAvg_, vAvg_, ekAvg_] := Module[{sigAvg, coliAvg, ekAir, tAvg},
  mO2 := 32;
  mH2O := 18;

  ekbO2 := 106.7;
  ekbH2O := 809.1;

  TbHB02 := 491 + 273; (*Kelvin*)
  TbH3B03 := 573; (*Kelvin, from Wikipedia*)
  TmH3B306 := 449; (*Kelvin, from Wikipedia on metaboric acid*)
  TmB203 = 723; (*Kelvin, from Wikipedia*)

  sigAvg = Mean[ {.841 * vAvg ^ (1/3), 3.4} ];
  ekAir = ekbH2O * pp + ekbO2 * (1 - pp);
  tAvg = T / (ekAvg * ekAir) ^ 0.5;
  coliAvg = 1.06036 / (tAvg) ^ 0.15610 + 0.193 / Exp[0.47635 * tAvg] +
    1.03587 / Exp[1.52996 * tAvg] + 1.76474 / Exp[3.89411 * tAvg];

  ((0.0018583 * T ^ (3/2)) / (1 * sigAvg ^ 2 * coliAvg))
  ( (1 / mAvg + 1 / (18 * pp + 32 * (1 - pp))) ^ 1/2 / 100 ^ 2 ];
  (*Pressure in atm, Temp in K, mw in g/mol, diffusion coefficient in m^2/s*)

```

Knudsen diffusivity calculation (code)

```

In[106]:= DKnuAvg[T_, pp_, s_, mAvg_] :=  $\frac{2 \text{ s}}{3} \left( \frac{8 * 8.314 * 1000 * T}{\text{Pi} * \text{mAvg}} \right)^{0.5}$ ;
  (*mw in g/mol, m^2/s*)

```

Effective diffusivity as a function of Knudsen and molecular diffusivity (code)

```

In[*]:= DeffAvg[T_, pp_, s_, mAvg_, dcurr_] :=
  DKnuAvg[T, pp, s, mAvg] * dcurr / (DKnuAvg[T, pp, s, mAvg] + dcurr); (*m^2/s*)

```

Effective diffusivity in recession gap as a function of dimensionless time (code)

6 | Base Recession Code_formatted.nb

```

In[*]:= DcTau[T_, pp_, Δ_, tau_] := Module[{Dko, Dm, c112, c313, c336, c23,
  ConcSum, w112, w313, w336, w23, lPre, mAvg, vAvg, ekAvg, nAvg, nu},
  (*calculate the concentration of each HxByOz product as
  a function of temperature, partial pressure (pp)*)
  c112 = C112tip[T, pp];
  c313 = C313tip[T, pp];
  c336 = C336tip[T, pp];
  c23 = C23tip[T, pp];
  ConcSum = c112 + c313 + c336 + c23;
  (*physical constants needed for
  the molecular diffusion coefficient calculation*)
  mHB02 := 43.81 (*g/mol*);
  mH3B03 := 61.81;
  mH3B306 := 131.43;
  mB203 := 69.6182;

  TbHB02 := 491 + 273; (*Kelvin*)
  TbH3B03 := 573; (*Kelvin, from Wikipedia*)
  TmH3B306 := 449; (*Kelvin, from Wikipedia on metaboric acid*)
  TmB203 = 723; (*Kelvin, from Wikipedia*)

  (*calculate the weighting factor for each product*)
  w112 = c112 / ConcSum;
  w313 = c313 / ConcSum;
  w336 = c336 / ConcSum;
  w23 = c23 / ConcSum;
  lPre = w112 + w313 + 3 * w336 + 2 * w23;

  (*calculate average physical properties based on weighting factors*)
  mAvg = Total[{w112 * mHB02, w313 * mH3B03, w336 * mH3B306, w23 * mB203}];
  (*average molecular weight*)
  nAvg = Total[{w112 * 3, w313 * 7, w336 * 12, w23 * 5}];
  vAvg = 20.1 + 0.88 * mAvg + 13.4 * nAvg;
  ekAvg = Total[{w112 * 1.15 * TbHB02,
    w313 * 1.15 * TbH3B03, w336 * 1.92 * TmH3B306, w23 * 1.92 * TmB203}];

  Dm = DiffAvg[T, pp, mAvg, vAvg, ekAvg];
  Dko = DKnuAvg[T, pp, Δ, mAvg];

  Dm * (tau + 2 * (Dm Sqrt[tau] / Dko + (2 * Dm * (Dm + Dko) / Dko ^ 2) * Log[Dm + Dko * (1 - Sqrt[tau])]))
];

```

Oxidation & time to closure

Parabolic rate constant (code)

```
In[108]:= Bcomb[T_, pp_] := Module[{bo2, bh2o},
  bo2 = (1.1*^-8) * Exp[-245*^3 / (8.314 * T)];
  bh2o = 4.8*^-14 * Exp[-75*^3 / (8.314 * T)];
  bo2 * (1 - pp) ^2 + bh2o pp ^2]; (*T in K,
pp is partial pressure of water vapor in atm, B in m^2/s*)
```

Time to closure of recession gap (code)

```
In[186]:= tcSec[T_, pp_, w_] := Module[{bo2, bh2o, btot},
  (*bo2, bh2o values taken from Hay and
  Chater (dry air) and Hay and Corns (steam), respectively*)
  bo2 = 1.1*^-8 * Exp[-245*^3 / (8.314 * T)];
  bh2o = 4.8*^-14 * Exp[-75*^3 / (8.314 * T)];
  btot = bo2 * (1 - pp) ^2 + bh2o pp ^2 ;
   $\left(\frac{w * 1.8}{2 (1.8 - 1)}\right)^2 \left(\frac{1}{btot}\right)];$  (*output is in seconds*)
```

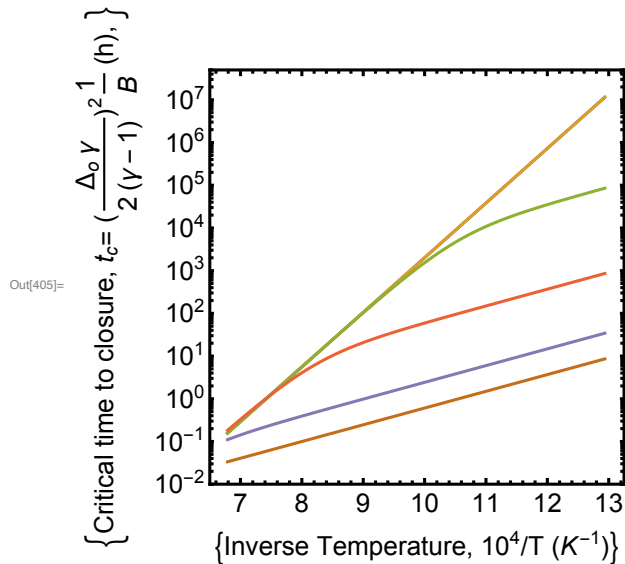
8 | Base Recession Code_formatted.nb

Critical times as a function of temperature (Figure 3A)

```

In[404]:= tcset = Table[Table[{1*^4/T, tcSec[T, pval, 100*^-9]/3600}, {T, 773, 1473}],
  {pval, {0, 10^-4, 10^-2, 10^-1, 0.5, 1}}];
ListLogPlot[tcset, Joined -> True, Frame -> True,
  BaseStyle -> {FontFamily -> "Arial", FontSize -> 17},
  ImageSize -> Medium, PlotRange -> {{6.5, 13.25}, {1*^-2, 5*^7}},
  FrameStyle -> Directive[Black, Thick], AspectRatio -> 1, PlotStyle -> Thick,
  FrameTicks -> {{LogTicks, StripTickLabels[LogTicks]}, Automatic},
  FrameLabel -> {{"Inverse Temperature, 10^4/T (K^-1)",
    {"Critical time to closure, t_c = (frac{Delta_o V}{2 (gamma - 1)})^2 frac{1}{B} (h)", ""}}]

```



Critical times as a function of water partial pressure (Figure 3B)

```

In[189]:= tcpset = Table[Table[{10^pval, tcSec[273 + T, 10^pval, 300*^-9]/3600},
  {pval, -3, 0, 0.1}], {T, 500, 1200, 100}];

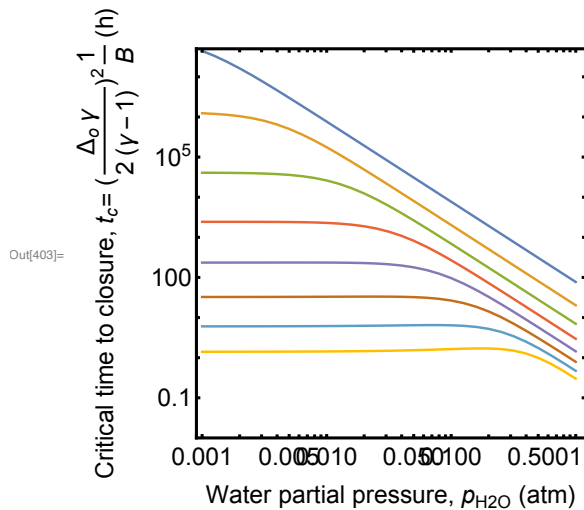
```



```

In[403]:= ListLogLogPlot[tcpsset, Joined → True, Frame → True,
  BaseStyle → {FontFamily → "Arial", FontSize → 16},
  ImageSize → Medium, PlotRange → {{9*^-4, 1.2}, {1*^-2, 5*^7}},
  FrameStyle → Directive[Black, Thick], AspectRatio → 1,
  FrameLabel → {{"Critical time to closure,  $t_c = \left(\frac{\Delta_o \gamma}{2(\gamma - 1)}\right)^2 \frac{1}{B}$  (h)", ""},
    {"Water partial pressure,  $p_{H_2O}$  (atm)", ""}}]

```



```

In[*]:= LRtau[Tc_, pp_, Δum_] := Module[{T, Δ, tau, β, Dko, Dm, c112, c313, c336, c23,
  ConcSum, w112, w313, w336, w23, lPre, mAvg, vAvg, ekAvg, nAvg, nu},
  T = Tc + 273;
  Δ = Δum * 10^-6;
  tau = Table[1 - Cos[(Pi/2.) (i - 1)/200], {i, 1, 200 + 1}];
  (*calculate the concentration of each HxByOz
  product as a function of temperature, partial pressure (pp)*)
  c112 = C112tip[T, pp];
  c313 = C313tip[T, pp];
  c336 = C336tip[T, pp];
  c23 = C23tip[T, pp];
  ConcSum = c112 + c313 + c336 + c23;
  (*physical constants needed for
  the molecular diffusion coefficient calculation*)
  mHB02 := 43.81 (*g/mol*);
  mH3B03 := 61.81;
  mH3B306 := 131.43;
  mB203 := 69.6182;

```

10 | Base Recession Code_formatted.nb

```

TbHB02 := 491 + 273; (*Kelvin*)
TbH3B03 := 573; (*Kelvin, from Wikipedia*)
TmH3B306 := 449; (*Kelvin, from Wikipedia on metaboric acid*)
TmB203 = 723; (*Kelvin, from Wikipedia*)

(*calculate the weighting factor for each product*)
w112 = c112 / ConcSum;
w313 = c313 / ConcSum;
w336 = c336 / ConcSum;
w23 = c23 / ConcSum;
lPre = w112 + w313 + 3 * w336 + 2 * w23;

(*calculate average physical properties based on weighting factors*)
mAvg = Total[{w112 * mHB02, w313 * mH3B03, w336 * mH3B306, w23 * mB203}];
(*average molecular weight*)
nAvg = Total[{w112 * 3, w313 * 7, w336 * 12, w23 * 5}];
vAvg = 20.1 + 0.88 * mAvg + 13.4 * nAvg;
ekAvg = Total[{w112 * 1.15 * TbHB02,
  w313 * 1.15 * TbH3B03, w336 * 1.92 * TmH3B306, w23 * 1.92 * TmB203}];

Dm = DiffAvg[T, pp, mAvg, vAvg, ekAvg];
Dko = DKnuAvg[T, pp, Δ, mAvg];
β = Dko / Dm;
nu = Sqrt[ $\frac{lPre \cdot 1.8^2 \cdot 1.18 \cdot 10^{-5} \cdot cTot[T, pp] \cdot Dm}{2 \cdot Bcomb[T, pp] \cdot (1.8 - 1)^2}$ ];
Table[{tau[[i]], Δum * 10-3
  (nu * (tau[[i]] + 2  $\frac{Sqrt[tau[[i]]}{\beta}$  +  $\frac{2(1+\beta)}{\beta^2} \text{Log}[\frac{1+\beta-\beta Sqrt[tau[[i]]}{1+\beta}]$ ))0.5
  }, {i, 1, Length[tau]}]
];

In[*]= LRtauR[Tc_, pp_, Δum_, tau_] := Module[{T, Δ, β, Dko, Dm, c112, c313, c336, c23,
  ConcSum, w112, w313, w336, w23, lPre, mAvg, vAvg, ekAvg, nAvg, nu},
  T = Tc + 273;
  Δ = Δum * 10-6;

  (*calculate the concentration of each HxByOz
  product as a function of temperature, partial pressure (pp)*)
  c112 = C112tip[T, pp];
  c313 = C313tip[T, pp];
  c336 = C336tip[T, pp];
  c23 = C23tip[T, pp];
  ConcSum = c112 + c313 + c336 + c23;

```

```

(*physical constants needed for
the molecular diffusion coefficient calculation*)
mHB02 := 43.81 (*g/mol*);
mH3B03 := 61.81;
mH3B306 := 131.43;
mB203 := 69.6182;

TbHB02 := 491+273; (*Kelvin*)
TbH3B03 := 573; (*Kelvin, from Wikipedia*)
TmH3B306 := 449; (*Kelvin, from Wikipedia on metabolic acid*)
TmB203 = 723; (*Kelvin, from Wikipedia*)

(*calculate the weighting factor for each product*)
w112 = c112/ConcSum;
w313 = c313/ConcSum;
w336 = c336/ConcSum;
w23 = c23/ConcSum;
lPre = w112 + w313 + 3 * w336 + 2 w23;

(*calculate average physical properties based on weighting factors*)
mAvg = Total[{w112 * mHB02, w313 * mH3B03, w336 * mH3B306, w23 * mB203}];
(*average molecular weight*)
nAvg = Total[{w112 * 3, w313 * 7, w336 * 12, w23 * 5}];
vAvg = 20.1 + 0.88 mAvg + 13.4 nAvg;
ekAvg = Total[{w112 * 1.15 * TbHB02,
w313 * 1.15 * TbH3B03, w336 * 1.92 * TmH3B306, w23 * 1.92 * TmB203}];

Dm = DiffAvg[T, pp, mAvg, vAvg, ekAvg];
Dko = DKnuAvg[T, pp, Δ, mAvg];
β = Dko/Dm;
nu = Sqrt[ $\frac{lPre \cdot 1.8^2 \cdot 1.18 \cdot 10^{-5} \cdot cTot[T, pp] \cdot Dm}{2 \cdot Bcomb[T, pp] \cdot (1.8 - 1)^2}$ ];
Table[ $\left\{ \tau[[i]], \Delta m \cdot 10^{-3} \left( nu \cdot \left( \tau[[i]] + 2 \frac{\text{Sqrt}[\tau[[i]]]}{\beta} + \frac{2(1+\beta)}{\beta^2} \text{Log}\left[ \frac{1+\beta - \beta \text{Sqrt}[\tau[[i]]]}{1+\beta} \right] \right) \right)^{0.5} \right\}, \{i, 1, \text{Length}[\tau]\}$ ];
];

```

Maximum recession length (at closure)

Maximum recession at closure (code)

12 | Base Recession Code_formatted.nb

```

In[391]:= Lmaxdelo[T_, pp_, Δ_] := Module[{Dko, Dm, c112, c313, c336, c23,
  ConcSum, w112, w313, w336, w23, lPre, mAvg, vAvg, ekAvg, nAvg, nu},
  (*calculate the concentration of each HxByOz product as
  a function of temperature, partial pressure (pp)*)
  c112 = C112tip[T, pp];
  c313 = C313tip[T, pp];
  c336 = C336tip[T, pp];
  c23 = C23tip[T, pp];
  ConcSum = c112 + c313 + c336 + c23;
  (*physical constants needed for
  the molecular diffusion coefficient calculation*)
  mHB02 := 43.81 (*g/mol*);
  mH3B03 := 61.81;
  mH3B306 := 131.43;
  mB203 := 69.6182;

  TbHB02 := 491 + 273; (*Kelvin*)
  TbH3B03 := 573; (*Kelvin, from Wikipedia*)
  TmH3B306 := 449; (*Kelvin, from Wikipedia on metaboric acid*)
  TmB203 = 723; (*Kelvin, from Wikipedia*)

  (*calculate the weighting factor for each product*)
  w112 = c112 / ConcSum;
  w313 = c313 / ConcSum;
  w336 = c336 / ConcSum;
  w23 = c23 / ConcSum;
  lPre = w112 + w313 + 3 * w336 + 2 * w23;

  (*calculate average physical properties based on weighting factors*)
  mAvg = Total[{w112 * mHB02, w313 * mH3B03, w336 * mH3B306, w23 * mB203}];
  (*average molecular weight*)
  nAvg = Total[{w112 * 3, w313 * 7, w336 * 12, w23 * 5}];
  vAvg = 20.1 + 0.88 * mAvg + 13.4 * nAvg;
  ekAvg = Total[{w112 * 1.15 * TbHB02,
    w313 * 1.15 * TbH3B03, w336 * 1.92 * TmH3B306, w23 * 1.92 * TmB203}];

  Dm = DiffAvg[T, pp, mAvg, vAvg, ekAvg];
  Dko = DKnuAvg[T, pp, Δ, mAvg];

  nu = Sqrt[
$$\frac{lPre \cdot 1.8^2 \cdot 1.18 \cdot 10^{-5} \cdot cTot[T, pp] \cdot Dm}{2 \cdot Bcomb[T, pp] \cdot (1.8 - 1)^2}$$
];
  nu * 
$$\left(1 + 2 \frac{Dm}{Dko} + \frac{2 Dm (Dm + Dko)}{Dko^2} \log\left[\frac{Dm}{Dm + Dko}\right]\right)^{0.5}$$


```

Printed by Wolfram Mathematica Student Edition

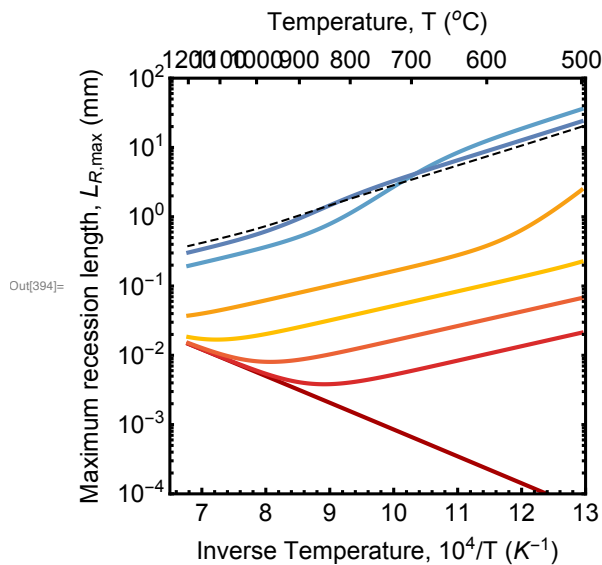
Max. recession vs. temperature (Figure 4A)

```

In[192]:= tset = Table[Table[{10^4/T, 0.3*^-3 Lmaxdelo[T, pval, 300*^-9]}, {T, 773, 1473}],
  {pval, {0, 10^-11, 10^-9, 10^-7, 10^-5, 0.01, 0.05, 0.1}}];

In[392]:= Caxis = Table[{10^4/T, T-273}, {T, 773, 1473, 100}];
SetOptions[LogTicks, LogPlot -> True];
ListLogPlot[tset, Joined -> True, Frame -> True,
  BaseStyle -> {FontFamily -> "Arial", FontSize -> 16},
  ImageSize -> Medium, PlotRange -> {{6.5, 13}, {10^-4, 10^2}},
  FrameStyle -> Directive[Black, Thick], AspectRatio -> 1, PlotStyle ->
  {{Thickness[0.01], ColorData[99][1]}, {Thickness[0.01], ColorData[93][1]},
  {Thickness[0.01], ColorData[97][4]}, {Thickness[0.01], ColorData[97][8]},
  {Thickness[0.01], ColorData[97][13]}, {Thickness[0.01], ColorData[97][7]},
  {Thickness[0.01], ColorData[97][1]}, {Thickness[0.005], Dashed, Black}},
  FrameTicks -> {{LogTicks, StripTickLabels[LogTicks]}, {Automatic, Caxis}},
  FrameLabel -> {"Maximum recession length, LR,max (mm)", ""},
  {"Inverse Temperature, 10^4/T (K^-1)", "Temperature, T (°C)"}]

```



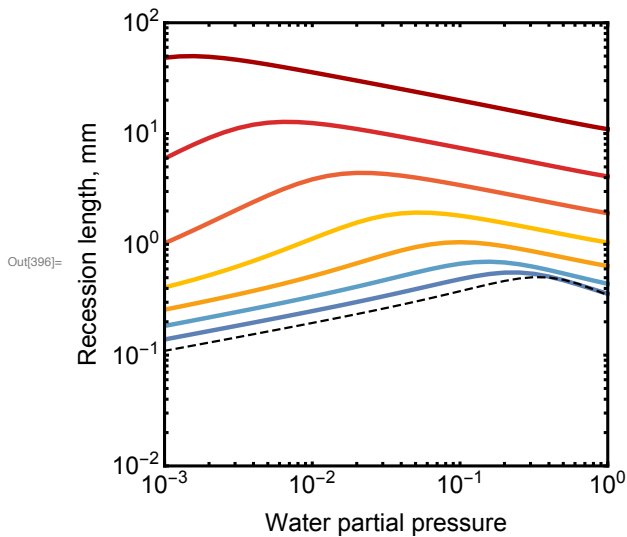
14 | Base Recession Code_formatted.nb

Max. recession vs. water partial pressure (Figure 4B)

```

In[395]= pmset = Table[Table[{10^pp, 300 × 10^-6 Lmaxdelo[273 + T, 10^pp, 300*^-9]},
  {pp, -3, 0, 0.1}], {T, 500, 1200, 100}];
ListLogLogPlot[pmset, Joined → True, BaseStyle →
  {FontFamily → "Arial", FontSize → 16}, ImageSize → Medium,
  FrameStyle → Directive[Black, Thick], AspectRatio → 1,
  FrameTicks → {{LogTicks, StripTickLabels[LogTicks]},
  {LogTicks, StripTickLabels[LogTicks]}}, PlotStyle →
  {{Thickness[0.01], ColorData[99][1]}, {Thickness[0.01], ColorData[93][1]},
  {Thickness[0.01], ColorData[97][4]}, {Thickness[0.01], ColorData[97][8]},
  {Thickness[0.01], ColorData[97][13]}, {Thickness[0.01], ColorData[97][7]},
  {Thickness[0.01], ColorData[97][1]}, {Thickness[0.005], Dashed, Black}},
  PlotRange → {{0.001, 1}, {0.01, 100}}, Frame → True,
  FrameLabel → {"Water partial pressure", "Recession length, mm"}]

```



Max. recession vs. coating thickness (Figure 5)

```

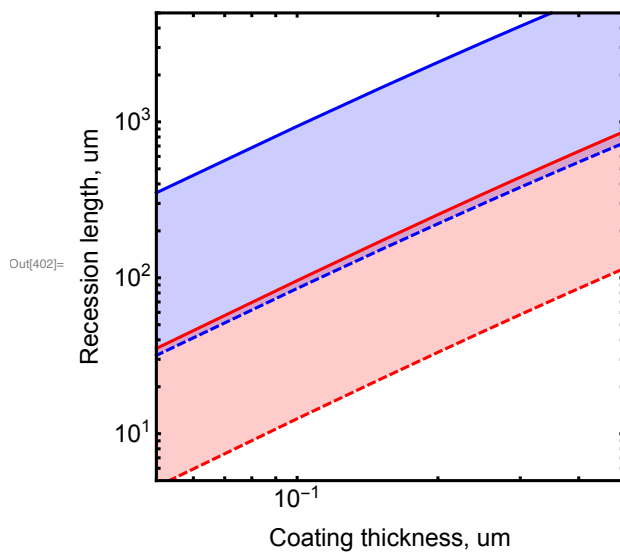
In[397]= coolwet = Table[{d0, d0 Lmaxdelo[600 + 273, 0.99, d0 10^-6]}, {d0, 0.05, 0.5, 0.05}];
cooldry = Table[{d0, d0 Lmaxdelo[600 + 273, 10^-5, d0 10^-6]}, {d0, 0.05, 0.5, 0.05}];
hotwet = Table[{d0, d0 Lmaxdelo[1000 + 273, 0.99, d0 10^-6]}, {d0, 0.05, 0.5, 0.05}];
hotdry = Table[{d0, d0 Lmaxdelo[1000 + 273, 10^-5, d0 10^-6]}, {d0, 0.05, 0.5, 0.05}];

```

```

In[402]:= (*SetOptions[LogTicks, LogPlot→ False];*)
ListLogLogPlot[{coolwet, cooldry, hotwet, hotdry},
  Joined→ True, Frame→ True, AspectRatio→ 1, FrameTicks→
  {{LogTicks, StripTickLabels[LogTicks]}, {LogTicks, StripTickLabels[LogTicks]}},
  PlotRange→ {{0.05, 0.5}, {5, 5000}}, PlotStyle→
  {{Thick, Blue}, {Thick, Blue, Dashed}, {Thick, Red}, {Thick, Red, Dashed}},
  FrameStyle→ Directive[Black, Thick], Filling→ {1→ {2}, 3→ {4}},
  BaseStyle→ {FontFamily→ "Arial", FontSize→ 16}, ImageSize→ Medium,
  FrameLabel→ {"Coating thickness, um", "Recession length, um"}]

```



Concentration and recession distributions

Dimensionless variables for FEA code inputs

```

In[109]:= etaBeta[TC_, pp_, Δoum_, aFullum_, hum_] :=
Module[{a, c112, c313, c336, c23, ConcSum, w112, w313,
  w336, w23, lPre, mAvg, vAvg, ekAvg, nAvg, nu, sigAvg, coliAvg,
  ekAir, tAvg, val, Dm, Dk, B, mO2, mH2O, ekbO2, ekbH2O},

  T = TC + 273.; Δo = Δoum 10^-6; aFull = aFullum 10^-6; h = hum 10^-6;
  val = {f → 0.5, R → 5*^-6, VBN → 1.18*^-5, γ → 1.8};
  a = aFull/2;

```

16 | Base Recession Code_formatted.nb

```

c112 = 1 / (8.21*^-5 * T) ((0.25) * ((pp / (8.21*^-5 * T)) / (1 / (8.21*^-5 * T))) *
  Exp[ $\frac{1}{8.314 * T} (- (330.5513296703299 - 0.15782395604395608 T) * 1000)$ ]) ^ 0.5;
c313 = 1 / (8.21*^-5 * T) ((0.25) * ((pp / (8.21*^-5 * T)) / (1 / (8.21*^-5 * T))) ^ 3 *
  Exp[ $\frac{1}{8.314 * T} (- (-40.35034065934053 + 0.10430131868131862 T) * 1000)$ ]) ^ 0.5;
c336 = 1 / (8.21*^-5 * T) ((0.25) ^ 3 * ((pp / (8.21*^-5 * T)) / (1 / (8.21*^-5 * T))) ^ 3 *
  Exp[ $\frac{1}{8.314 * T} (- (-94.2604505494506 + 0.15240956043956044 T) * 1000)$ ]) ^ 0.5;
(*T in K, Conc in mol/m^3*)
c23 = 1 / (8.21*^-5 * T) ((0.25) * Exp[ $\frac{-(393.49 - 0.1739 T) * 1000}{8.314 * T}$ ]);
(*T in K, Conc in mol/m^3*)
ConcSum = c112 + c313 + c336 + c23;
(*T in K, Conc in mol/m^3*)
w112 = c112 / ConcSum;
w313 = c313 / ConcSum;
w336 = c336 / ConcSum;
w23 = c23 / ConcSum;
lPre = w112 + w313 + 3 * w336 + 2 w23;

mO2 = 32;
mH2O = 18;

ekbO2 = 106.7;
ekbH2O = 809.1;

TbHB02 = 491 + 273; (*Kelvin*)
TbH3B03 = 573; (*Kelvin, from Wikipedia*)
TmH3B306 = 449; (*Kelvin, from Wikipedia on metaboric acid*)
TmB203 = 723; (*Kelvin, from Wikipedia*)

mHB02 := 43.81 (*g/mol*);
mH3B03 := 61.81;
mH3B306 := 131.43;
mB203 := 69.6182;

(*calculate average physical properties based on weighting factors*)
mAvg = Total[{w112 * mHB02, w313 * mH3B03, w336 * mH3B306, w23 * mB203}];
(*average molecular weight*)
nAvg = Total[{w112 * 3, w313 * 7, w336 * 12, w23 * 5}];
vAvg = 20.1 + 0.88 mAvg + 13.4 nAvg;

```



```

ekAvg = Total[{w112 * 1.15 * TbHB02,
  w313 * 1.15 * TbH3B03, w336 * 1.92 * TmH3B306, w23 * 1.92 * TmB203}];

sigAvg = Mean[{0.841 * vAvg^(1/3), 3.4}];
ekAir = ekbH20 * pp + ekb02 * (1 - pp);
tAvg = T / (ekAvg + ekAir)^0.5;
coliAvg = 1.06036 / (tAvg)^0.15610 + 0.193 / Exp[0.47635 * tAvg] +
  1.03587 / Exp[1.52996 * tAvg] + 1.76474 / Exp[3.89411 * tAvg];

Dm = ((0.0018583 * T^(3/2)) / (1 * sigAvg^2 * coliAvg))
  (1/mAvg + 1/(18 * pp + 32 * (1 - pp)))^(1/2) / 100^2;
(*Pressure in atm, Temp in K, mw in g/mol, diffusion coefficient in m^2/s*)

Dk = 2/3 * Δo * (8 * 8.314 * 1000 * T / (Pi * mAvg))^0.5; (*mw in g/mol, m^2/s*)

bo2 = 1.1 * 10^-8 * Exp[-245 * 10^3 / (8.314 * T)];
bh2o = 4.8 * 10^-14 * Exp[-75 * 10^3 / (8.314 * T)];
B = bo2 * (1 - pp)^2 + bh2o * pp^2;
(*T in K, pp is partial pressure of water vapor in atm, B in m^2/s*)

η0 = VBN ConcSum lPre Dm γ^2 / (2 (γ - 1)^2 B) /. val;
η1 = Dm γ^2 Δo^2 / (4 (γ - 1)^2 B a^2) /. val;
η2 = f Dm lPre γ^2 Δo^2 / ((γ - 1)^2 B R h) /. val;
β = Dk / Dm;
Lmax = Sqrt[η0 (1 + 2/β + (2 (1 + β) / β^2) Log[1 / (1 + β)])];
{β, η0, η1, η2, Lmax}
]

```

Base FEA code

18 | *Base Recession Code_formatted.nb*

```

In[1327]:= GetD[x_] := Module[{i, j, nodes, De, Dglob, le, ne},
  (* Initialize the global conductivity matrix to zero *)
  Dglob = Table[0, {i, 1, Length[x]}, {j, 1, Length[x]}];
  (* Global assembly: assembled over all elements,
  which are one less than # of nodes*)
  Table[
    i = ne; j = ne + 1; le = x[[j]] - x[[i]];
    (* diffusivity matrix for one element, element #=ne*)
    De = (1.0/le) {{1, -1}, {-1, 1}};
    Dglob[[i, i]] = Dglob[[i, i]] + De[[1, 1]];
    Dglob[[i, j]] = Dglob[[i, j]] + De[[1, 2]];
    Dglob[[j, i]] = Dglob[[j, i]] + De[[2, 1]];
    Dglob[[j, j]] = Dglob[[j, j]] + De[[2, 2]];
    , {ne, 1, Length[x] - 1}];
  (* Output the global diffusivity matrix *)
  Dglob
]

In[1328]:= GetA[x_,  $\alpha$ _] := Module[{i, j, nodes, Ae, Aglob, ne, le,  $\alpha$ 1,  $\alpha$ 2},
  (* Initialize the global conductivity matrix to zero *)
  Aglob = Table[0, {i, 1, Length[x]}, {j, 1, Length[x]}];
  (* Global assembly: assembled over all elements,
  which are one less than # of nodes*)
  Table[
    i = ne; j = ne + 1; le = x[[j]] - x[[i]];
    (* reaction matrix for one element, element #=ne*)
     $\alpha$ 1 =  $\alpha$ [[i]];  $\alpha$ 2 =  $\alpha$ [[j]];
    Ae = le {{ $\alpha$ 1/3,  $\alpha$ 2/6}, { $\alpha$ 1/6,  $\alpha$ 2/3}};
    Aglob[[i, i]] = Aglob[[i, i]] + Ae[[1, 1]];
    Aglob[[i, j]] = Aglob[[i, j]] + Ae[[1, 2]];
    Aglob[[j, i]] = Aglob[[j, i]] + Ae[[2, 1]];
    Aglob[[j, j]] = Aglob[[j, j]] + Ae[[2, 2]];
    , {ne, 1, Length[x] - 1}];
  (* Output the global reaction matrix *)
  Aglob
]

```

```

In[1329]:= GetRed[x_, Lr_, Co_, τ_, η0_, η1_, η2_, β_] :=
Module[{ndof, α, Dc, Amat, Dmat, Dred, Ared, RHSred, C1},
  ndof = Length[Co];
  Dc = β (1 - Sqrt[τ]) / (1 + β - β Sqrt[τ]);
  (* HERE I KEEP α as η2 Dc/Lr AS PRE-FACTOR OF A-MATRIX *)
  α = Table[η2 Dc / Lr[[i]], {i, 1, Length[Lr]}];

  Amat = GetA[x, α]; Ared = Amat[[2 ;; All, 2 ;; All]];
  Dmat = η1 GetD[x]; Dred = Dmat[[2 ;; All, 2 ;; All]];

  (* Reduced RHS to impose concentration at first node *)
  RHSred = Table[0., {i, 2, ndof}];
  C1 = Co[[1]];
  RHSred[[1]] = -Dmat[[2, 1]] C1 - Amat[[2, 1]] C1 + Amat[[2, 1]];
  {Dred, Ared, RHSred}]

In[1330]:= GetStep[x_, Lr_, Co_, τ_, η0_, η1_, η2_, β_, dt_] :=
Module[{Diff, A, RHS, ndof, Csv, Dc, Cnew, Ctot, Lnew},
  ndof = Length[Co];
  {Diff, A, RHS} = GetRed[x, Lr, Co, τ, η0, η1, η2, β];
  Csv = Table[1., {i, 2, ndof}];
  Cnew = LinearSolve[Diff + A, RHS + A.Csv];
  Ctot = Join[{Co[[1]]}, Cnew];

  Dc = β (1 - Sqrt[τ]) / (1 + β - β Sqrt[τ]);
  Lnew =
  Table[Lr[[i]] + dt (1/2) η0 Dc (1 - Ctot[[i]]) / (Lr[[i]]), {i, 1, Length[Lr]}];
  {Ctot, Lnew}]

```

20 | Base Recession Code_formatted.nb

Get concentration and recession distribution at specified times (Figure 6A and 6B)

```

In[216]:= GetDist[Tc_, pp_, Δc_, af_, hmat_, Nel_, timesoutput_] :=
Module[{ex, C0, L0, Cold, Lold, output, new, cold, L0fin, η0, η1, η2, β, Lmax, Ldist,
  Pdist, Cdist, times, Cdata, Ldata, timefunc, steps, Cdistout, Ldistout},
  Nt = 300;
  times = Table[(1 - Cos[(Pi/2.) (i - 1) / Nt]) ^ 2, {i, 1, Nt + 1}];

  {β, η0, η1, η2, Lmax} = etaBeta[Tc, pp, Δc, af, hmat];
  Lmax = Sqrt[η0 (1 + 2/β + (2 (1 + β) / β ^ 2) Log[1 / (1 + β)])];
  ex = Table[1 - Cos[(Pi/2.) (i - 1) / Nel], {i, 1, Nel + 1}];

  (*Print["Constants: ", {β, η0, η1, η2, Lmax}];*)
  C0 = Table[1., {i, 1, Nel + 1}]; (* initial concentration*)
  L0 = Table[1., {i, 1, Nel + 1}]; (* initial recession length *)
  C0[[1]] = 0.; (* entry concentration: bc*)
  Cold = C0;
  Lold = L0;
  output = Table[
    ti = times[[i]];
    dt = times[[i + 1]] - times[[i]];
    new = GetStep[ex, Lold, Cold, ti, η0, η1, η2, β, dt];
    Cold = new[[1]];
    Lold = new[[2]];
    {Cold, Lold}, {i, 1, Length[times] - 1}];
  Cdata = output[[All, 1]];
  Ldata = output[[All, 2]];
  Cdist = Table[
    Table[{0.5 ex[[i]], Cdata[[j, i]]}, {i, 1, Nel + 1}, {j, 1, Length[output]}];
  Ldist = Table[Table[{0.5 ex[[i]], 0.3 * 10^-3 * Ldata[[j, i]]}, {i, 1, Nel + 1},
    {j, 1, Length[output]}];

  (*Here I find the entries associated with specified times,
  and create lists of those distributions*)
  timefunc = Interpolation[times];
  steps = Table[Floor[t /. FindRoot[timefunc[t] = timesoutput[[i]], {t, 10, 1, Nt}],
    {i, 1, Length[timesoutput]}];
  Cdistout = Table[Cdist[[j]], {j, steps}];
  Ldistout = Table[Ldist[[j]], {j, steps}];
  {Cdistout, Ldistout}
]

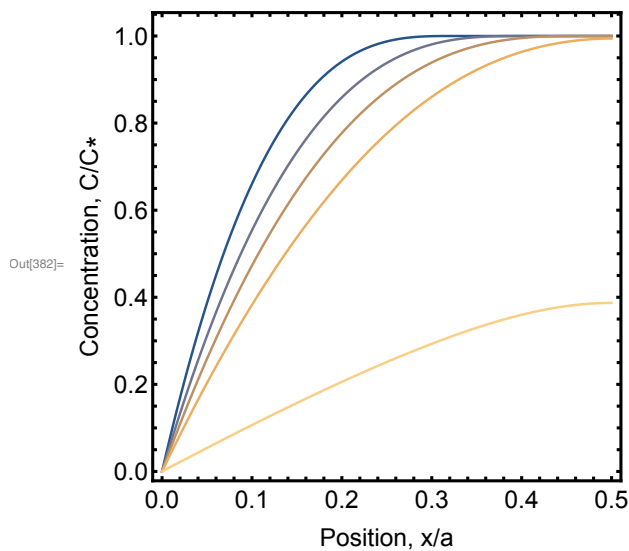
```

(*Original code, no mods Nt = 300, Nel = 200*)

```
In[217]:= case = GetDist[750, 0.1, 0.3, 1000, 1.0, 200, {0.2, 0.4, 0.6, 0.8, 0.99}];
```

FindRoot: The point {300.} is at the edge of the search region {1., 300.} in coordinate 1 and the computed search direction points outside the region.

```
In[382]:= ListPlot[case[[1]], Frame → True, AspectRatio → 1,
  Joined → True, FrameStyle → Directive[Black, Thick], FrameTicks →
  {{LinTicks, StripTickLabels[LinTicks]}, {LinTicks, StripTickLabels[LinTicks]}},
  PlotStyle → {ColorData["M10DefaultDensityGradient"][0],
  ColorData["M10DefaultDensityGradient"][0.2],
  ColorData["M10DefaultDensityGradient"][0.4],
  ColorData["M10DefaultDensityGradient"][0.6],
  ColorData["M10DefaultDensityGradient"][0.8]},
  BaseStyle → {FontFamily → "Arial", FontSize → 16}, ImageSize → Medium,
  FrameLabel → {"Position, x/a", "Concentration, C/C*"}]
```

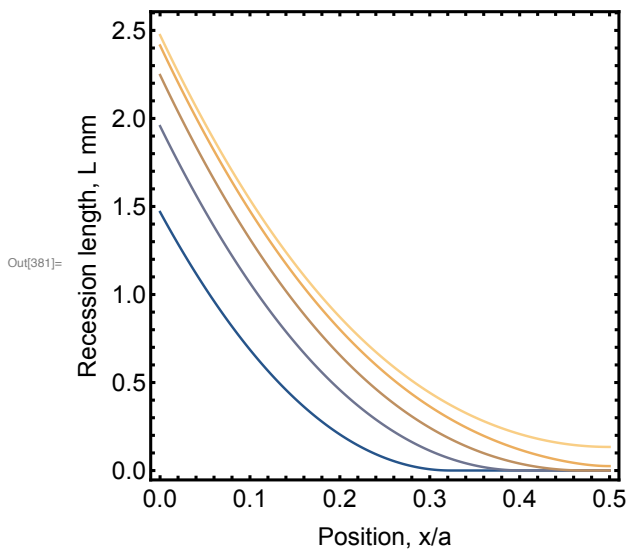


22 | Base Recession Code_formatted.nb

```

In[381]:= ListPlot[case[[2]], Frame → True, AspectRatio → 1,
  Joined → True, FrameStyle → Directive[Black, Thick], FrameTicks →
  {{LinTicks, StripTickLabels[LinTicks]}, {LinTicks, StripTickLabels[LinTicks]}},
  PlotStyle → {ColorData["M10DefaultDensityGradient"][0],
  ColorData["M10DefaultDensityGradient"][0.2],
  ColorData["M10DefaultDensityGradient"][0.4],
  ColorData["M10DefaultDensityGradient"][0.6],
  ColorData["M10DefaultDensityGradient"][0.8]},
  BaseStyle → {FontFamily → "Arial", FontSize → 16}, ImageSize → Medium,
  FrameLabel → {"Position, x/a", "Recession length, L mm"}]

```



Get final L^* distribution for various temperatures ([Figure 7A](#))

Code for L^* distribution

T_c = temperature in Celcius
 pp = partial pressure of water (atm)
 Δc = coating thickness (microns)
 af = specimen half - width (microns)
 h_{mat} = matrix crack opening (microns)
 N_{el} = number of elements

```

In[222]:= RunItFast[Tc_, pp_, Δc_, af_, hmat_, Nel_] :=
Module[{ex, C0, L0, Cold, Lold, output, new, cold,
  L0fin, η0, η1, η2, β, Lmax, Ldist, Pdist, times, ti, dt},

  times = Table[(1 - Cos[(Pi/2.) (i - 1) / 300]) ^ 2, {i, 1, 301}];
  {β, η0, η1, η2, Lmax} = etaBeta[Tc, pp, Δc, af, hmat];
  Lmax = Sqrt[η0 (1 + 2/β + (2 (1 + β) / β^2) Log[1 / (1 + β)])];
  ex = Table[1 - Cos[(Pi/2.) (i - 1) / Nel], {i, 1, Nel + 1}];

  (*Print["Constants: ", {β, η0, η1, η2, Lmax}];*)
  C0 = Table[1., {i, 1, Nel + 1}]; (* initial concentration*)
  L0 = Table[1., {i, 1, Nel + 1}]; (* initial recession length *)
  C0[[1]] = 0.; (* entry concentration: bc*)
  Cold = C0;
  Lold = L0;
  output = Table[
    ti = times[[i]];
    dt = times[[i + 1]] - times[[i]];
    new = GetStep[ex, Lold, Cold, ti, η0, η1, η2, β, dt];
    Cold = new[[1]];
    Lold = new[[2]];
    {cold, Lold}, {i, 1, Length[times] - 1}];
  L0fin = Last[output][[All, 2]];
  Ldist = Table[{ex[[i]], L0fin[[i]]}, {i, 1, Length[L0fin]}];
  Pdist = af Last[Select[Ldist, #[[2]] > Exp[-1.] Lmax &]][[1]];
  {Lmax, First[L0fin], Ldist, Pdist}
]

```

Data for L* distribution at different temperatures & plot

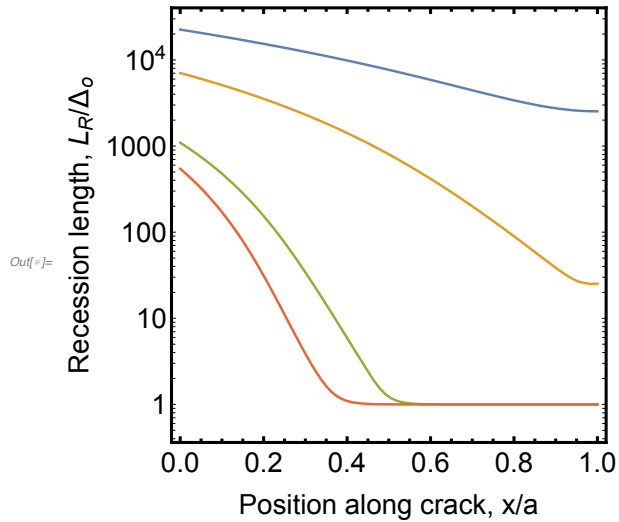
```

In[223]:= case1 = RunItFast[600, 0.1, 0.3, 1000, 1.0, 100];
case2 = RunItFast[750, 0.1, 0.3, 1000, 1.0, 100];
case3 = RunItFast[1000, 0.1, 0.3, 1000, 1.0, 100];
case4 = RunItFast[1200, 0.1, 0.3, 1000, 1.0, 100];

```

24 | Base Recession Code_formatted.nb

```
In[229]:= ListLogPlot[{case1[[3]], case2[[3]], case3[[3]], case4[[3]]},
  PlotRange → All, Frame → True, FrameStyle → Thick,
  BaseStyle → {FontFamily → "Arial", FontSize → 18}, AspectRatio → 1,
  FrameLabel → {"Position along crack, x/a", "Recession length,  $L_R/\Delta_o$ "},
  Joined → True, LabelStyle → Black]
```



Get x^*/h vs. L_{max}/h (Figure 7B)

Code for x^*/h vs. L_{max}/h

Tc = temperature in Celcius
 pp = partial pressure of water (atm)
 Δc = coating thickness (microns)
 af = specimen half-width (microns)
 hmat = matrix crack opening (microns)
 Nel = number of elements
 Ntimes = number of time steps


```

In[*]:= Pin[Tc_, pp_, Δc_, af_, hmat_, Nel_, Ntimes_] :=
Module[{ex, C0, L0, Cold, Lold, output, new, cold, L0fin, η0,
  η1, η2, β, Lmax, Pdist, Ldist, Lfunc, Lpen, times, xstar, ti, dt},

  times = Table[(1 - Cos[(Pi/2.) (i - 1)/Ntimes])^2, {i, 1, Ntimes + 1}];

  {β, η0, η1, η2, Lmax} = etaBeta[Tc, pp, Δc, af, hmat];
  Lmax = Sqrt[η0 (1 + 2/β + (2 (1 + β) / β^2) Log[1 / (1 + β)])];
  ex = Table[1 - Cos[(Pi/2.) (i - 1)/Nel], {i, 1, Nel + 1}];

  (*Print["Constants: ", {β, η0, η1, η2, Lmax}];*)
  C0 = Table[1., {i, 1, Nel + 1}]; (* initial concentration*)
  L0 = Table[1., {i, 1, Nel + 1}]; (* initial recession length *)
  C0[[1]] = 0.; (* entry concentration: bc*)
  Cold = C0;
  Lold = L0;
  output = Table[
    ti = times[[i]];
    dt = times[[i + 1]] - times[[i]];
    new = GetStep[ex, Lold, Cold, ti, η0, η1, η2, β, dt];
    Cold = new[[1]];
    Lold = new[[2]];
    {cold, Lold}, {i, 1, Length[times] - 1}];
  L0fin = Last[output][[All, 2]];
  Ldist = Table[{ex[[i]], L0fin[[i]]}, {i, 1, Length[L0fin]}];
  Lfunc = Interpolation[Ldist, InterpolationOrder → 1];
  xstar = af x /. FindRoot[Lfunc[x] == Exp[-1] Lmax, {x, 0.001, 0., 1.}];
  {Δc Lmax/hmat, xstar/hmat}
]

```

Case studies: BN = 100 nm, hmatrix = 0.1, 1, 5 microns

```

In[*]:= dc0101 = Table[Table[Pin[T, pp, 0.1, 10^4, 0.1, 200, 200], {T, {500, 750, 1000, 1200}}],
  {pp, {0.01, 0.5, 0.999}}]

Out[*]:= {{ {76145.5, 3614.94}, {2059.27, 672.954}, {315.623, 300.748}, {180.513, 245.723}},
  {{28450.4, 2091.9}, {3503.07, 838.929}, {1097.1, 523.712}, {762.778, 477.836}},
  {{23935.3, 1919.25}, {2952.99, 773.743}, {923.402, 485.575}, {723.58, 467.167}}

In[*]:= dc0110 = Table[Table[Pin[T, pp, 0.1, 10^4, 5.0, 200, 200], {T, {500, 750, 1000, 1200}}],
  {pp, {0.01, 0.5, 0.999}}]

Out[*]:= {{ {1522.91, 563.363}, {41.1854, 95.1348}, {6.31246, 42.5457}, {3.61026, 34.7914}},
  {{569.009, 295.862}, {70.0614, 118.528}, {21.9421, 74.1229}, {15.2556, 67.4715}},
  {{478.706, 271.498}, {59.0598, 109.417}, {18.468, 68.5788}, {14.4716, 65.9894}}

```

26 | *Base Recession Code_formatted.nb*

```
In[*]:= dc0150 = Table[Table[Pin[T, pp, 0.1, 10^4, 5.0, 200, 200], {T, {500, 750, 1000, 1200}}],
  {pp, {0.01, 0.5, 0.999}}]
Out[*]:= {{1522.91, 563.363}, {41.1854, 95.1348}, {6.31246, 42.5457}, {3.61026, 34.7914}},
  {{569.009, 295.862}, {70.0614, 118.528}, {21.9421, 74.1229}, {15.2556, 67.4715}},
  {{478.706, 271.498}, {59.0598, 109.417}, {18.468, 68.5788}, {14.4716, 65.9894}}
```

Case studies: BN = 300 nm, hmatrix = 0.1, 1, 5 microns

```
In[*]:= dc0301 = Table[Table[Pin[T, pp, 0.3, 10^4, 0.1, 200, 200], {T, {500, 750, 1000, 1200}}],
  {pp, {0.01, 0.5, 0.999}}]
Out[*]:= {{317880., 87.7898}, {8940.16, 576.608}, {1417.48, 251.573}, {824.631, 203.585}},
  {{116678., 1852.09}, {15006.8, 724.181}, {4848.18, 443.465}, {3444.27, 399.373}},
  {{98176.7, 1699.42}, {12670.2, 667.709}, {4089.19, 410.868}, {3270.33, 390.112}}
```

```
In[*]:= dc0310 = Table[Table[Pin[T, pp, 0.3, 10^4, 5.0, 200, 200], {T, {500, 750, 1000, 1200}}],
  {pp, {0.01, 0.5, 0.999}}]
Out[*]:= {{6357.6, 471.403}, {178.803, 81.4803}, {28.3495, 35.6295}, {16.4926, 28.8045}},
  {{2333.56, 265.703}, {300.136, 102.329}, {96.9637, 62.7786}, {68.8854, 56.396}},
  {{1963.53, 240.231}, {253.404, 94.3709}, {81.7839, 58.0133}, {65.4066, 55.1034}}
```

```
In[*]:= dc0350 = Table[Table[Pin[T, pp, 0.3, 10^4, 5.0, 200, 200], {T, {500, 750, 1000, 1200}}],
  {pp, {0.01, 0.5, 0.999}}]
Out[*]:= {{6357.6, 471.403}, {178.803, 81.4803}, {28.3495, 35.6295}, {16.4926, 28.8045}},
  {{2333.56, 265.703}, {300.136, 102.329}, {96.9637, 62.7786}, {68.8854, 56.396}},
  {{1963.53, 240.231}, {253.404, 94.3709}, {81.7839, 58.0133}, {65.4066, 55.1034}}
```

Case studies: BN = 500 nm, hmatrix = 0.1, 1, 5 microns

```
In[*]:= dc0501 = Table[Table[Pin[T, pp, 0.5, 10^4, 0.1, 220, 200], {T, {500, 750, 1000, 1200}}],
  {pp, {0.01, 0.5, 0.999}}]
Out[*]:= {{592492., 3035.42}, {16979.4, 549.047}, {2740.76, 238.03}, {1610.02, 191.292}},
  {{215753., 1787.03}, {28313.6, 692.04}, {9292.51, 420.83}, {6679.86, 375.47}},
  {{181554., 1639.65}, {23923.5, 637.519}, {7846.52, 388.974}, {6345.87, 366.392}}
```

```
In[*]:= dc0510 = Table[Table[Pin[T, pp, 0.5, 10^4, 1.0, 220, 200], {T, {500, 750, 1000, 1200}}],
  {pp, {0.01, 0.5, 0.999}}]
Out[*]:= {{59249.2, 984.77}, {1697.94, 173.488}, {274.076, 75.1469}, {161.002, 60.4058}},
  {{21575.3, 567.824}, {2831.36, 218.708}, {929.251, 133.059}, {667.986, 118.767}},
  {{18155.4, 518.379}, {2392.35, 201.567}, {784.652, 122.813}, {634.587, 116.044}}
```

```

In[ ]:= dc0505 = Table[Table[Pin[T, pp, 0.5, 10^4, 5.0, 220, 200], {T, {500, 750, 1000, 1200}}],
  {pp, {0.01, 0.5, 0.999}}]
Out[ ]:= {{ {11849.8, 458.321}, {339.588, 77.5859}, {54.8152, 33.6065}, {32.2004, 26.9828}},
  {{4315.06, 256.468}, {566.272, 97.781}, {185.85, 59.5113}, {133.597, 53.0994}},
  {{3631.08, 231.806}, {478.47, 90.1415}, {156.93, 54.936}, {126.917, 51.8672}}

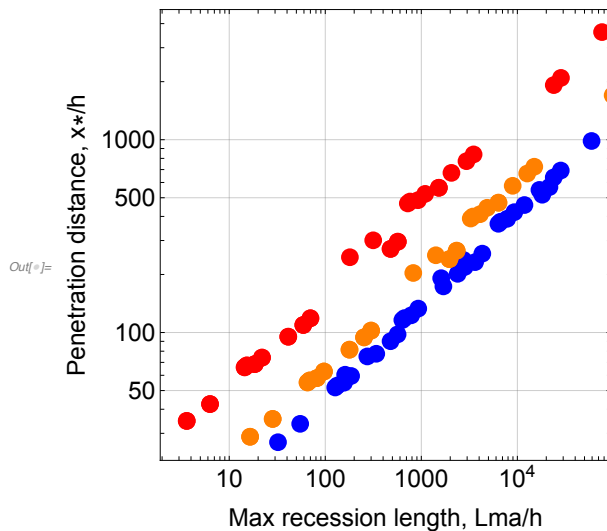
```

Make plot with all data

```

In[ ]:= bn100nm = Join[dc0101, dc0110, dc0150];
bn300nm = Join[dc0301, dc0310, dc0350];
bn500nm = Join[dc0501, dc0510, dc0505];
In[ ]:= Show[ListLogLogPlot[bn100nm, PlotStyle -> {{Thick, Red}}, AspectRatio -> 1,
  GridLines -> Automatic, PlotMarkers -> Graphics[{Red, Disk[]}, ImageSize -> 12],
  Frame -> True, BaseStyle -> {FontFamily -> "Arial", FontSize -> 16},
  FrameLabel -> {"Max recession length, Lma/h", "Penetration distance, x*/h"}],
ListLogLogPlot[bn500nm, PlotMarkers -> Graphics[{Blue, Disk[]}, ImageSize -> 12],
  AspectRatio -> 1, GridLines -> Automatic],
ListLogLogPlot[bn300nm, PlotMarkers -> Graphics[{Orange, Disk[]}, ImageSize -> 12],
  AspectRatio -> 1, GridLines -> Automatic]]

```



Appendix C

Single fiber composite strength

Fragmentation of each phase is governed by a characteristic transfer length δ^* and a characteristic strength σ^* for the respective phase. The transfer length represents the distance over which the axial stress is reduced from its far-field value because of a single break and hence the distance over which another break cannot occur; the next break must occur at a distance $> \delta^*/2$ from the first, at a stress proportional to σ^* . From shear lag theory and weakest link fracture statistics (assuming Weibull strength distributions), the transfer lengths in the two phases are[19, 39, 90, 91]

$$\sigma_f^* = \sigma_f^o \left(\frac{\tau_s L_o}{\sigma_f^o R} \right)^{\frac{1}{m_f+1}} \quad (\text{C.1})$$

The mechanics of fiber fragmentation in a SFC has been analyzed extensively[39, 90, 91]. An accurate approximation of the fiber bundle contribution to the composite stress-strain response following matrix crack saturation and up to the load maximum is obtained from a statistical analysis of fiber fragmentation and frictional sliding, *neglecting*

interactions between neighboring fiber breaks. The result is[39]

$$\frac{\sigma_c}{f\sigma_f^*} = \frac{\epsilon_c E_f}{2\sigma_f^*} \left(1 + \exp \left[- \left(\frac{\epsilon_c E_f}{\sigma_f^*} \right)^{m_f+1} \right] \right) \quad (\text{C.2a})$$

Maximizing Equation C.2a yields the fiber bundle failure strain:

$$\frac{\epsilon_c^{ult} E_f}{\sigma_f^*} = (\alpha - \text{ProductLog}[-\alpha \exp\{\alpha\}])^\alpha \quad (\text{C.2b})$$

where $\alpha \equiv 1/(m_f + 1)$ and $\text{ProductLog}[z]$ is the principal solution for w in $z = w \exp w$. The composite strength is then obtained by substituting Equation C.2b into C.2a, yielding:

$$\sigma_c = f\sigma_f^o \left(\frac{\tau_s L_o}{\sigma_f^o R} \right)^{\frac{1}{m_f+1}} g(m) \quad (\text{C.3})$$

where

$$g(m) = \frac{(\alpha - \text{ProductLog}[-\alpha \exp\{\alpha\}])^\alpha}{2} \left(1 + \exp \left[- ((\alpha - \text{ProductLog}[-\alpha \exp\{\alpha\}])^\alpha)^{m_f+1} \right] \right) \quad (\text{C.4})$$

Appendix D

Strength reduction due to coating recession code

This appendix documents the code used to calculate the results presented in Chapter 6 of this dissertation.

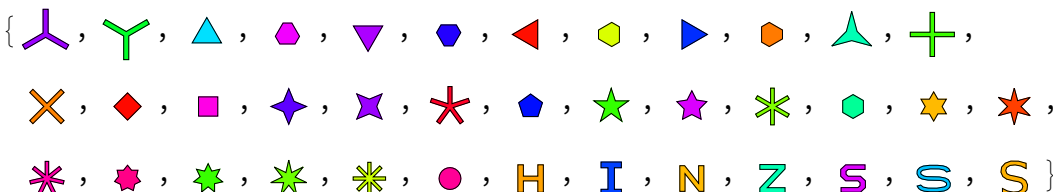
Figure Formatting

This section contains the functions needed for the PlotMarker and CustomTicks packages. These packages are used for figure formatting.

```
In[295]:= Needs["PolygonPlotMarkers`"]
```

```
allShapes = PolygonMarker[All]  
Tooltip[Graphics[{FaceForm[Hue@Random[]],  
EdgeForm[{Black, Thickness[0.003], JoinForm["Miter"]}]}], PolygonMarker[#, 1]],  
ImageSize → 30, PlotRange → 1.5, PlotRangePadding → 0,  
ImagePadding → 0], #] & /@ allShapes
```

```
Out[296]= {TripleCross, Y, UpTriangle, UpTriangleTruncated, DownTriangle,  
DownTriangleTruncated, LeftTriangle, LeftTriangleTruncated, RightTriangle,  
RightTriangleTruncated, ThreePointedStar, Cross, DiagonalCross, Diamond,  
Square, FourPointedStar, DiagonalFourPointedStar, FivefoldCross, Pentagon,  
FivePointedStar, FivePointedStarThick, SixfoldCross, Hexagon, SixPointedStar,  
SixPointedStarSlim, SevenfoldCross, SevenPointedStar, SevenPointedStarNeat,  
SevenPointedStarSlim, EightfoldCross, Disk, H, I, N, Z, S, Sw, Sl}
```

```
Out[297]= {
```

```
In[ ]:= Get[
```

```
"https://raw.githubusercontent.com/mark-caprio/CustomTicks/master/CustomTicks.m"]
```

Thermochemistry and Recession Length

This section contains the thermochemistry and analytical recession

length functions.

```

C112tip[T_, pp_] :=
  1 / (8.21*^-5 * T)  $\left( (0.25) * \left( \frac{pp}{(8.21*^-5 * T)} \right) / \left( 1 / (8.21*^-5 * T) \right) \right) *
  \text{Exp} \left[ \frac{- (330.5513296703299 - 0.15782395604395608 T) * 1000}{8.314 * T} \right] ^{0.5};

C313tip[T_, pp_] := 1 / (8.21*^-5 * T)
   $\left( (0.25) * \left( \frac{pp}{(8.21*^-5 * T)} \right) / \left( 1 / (8.21*^-5 * T) \right) \right) ^3 *
  \text{Exp} \left[ \frac{1}{8.314 * T} (- (-40.35034065934053 + 0.10430131868131862 T) * 1000) \right] ^{0.5};

C336tip[T_, pp_] := 1 / (8.21*^-5 * T)
   $\left( (0.25) ^3 * \left( \frac{pp}{(8.21*^-5 * T)} \right) / \left( 1 / (8.21*^-5 * T) \right) \right) ^3 *
  \text{Exp} \left[ \frac{- (-94.2604505494506 + 0.15240956043956044 T) * 1000}{8.314 * T} \right] ^{0.5};
(*T in K, Conc in mol/m^3*)

C23tip[T_, pp_] := 1 / (8.21*^-5 * T)  $\left( (0.25) * \text{Exp} \left[ \frac{- (393.49 - 0.1739 T) * 1000}{8.314 * T} \right] \right)$ ;
(*T in K, Conc in mol/m^3*)

cTot[T_, pp_] :=
  1 / (8.21*^-5 * T)  $\left( (0.25) * \left( \frac{pp}{(8.21*^-5 * T)} \right) / \left( 1 / (8.21*^-5 * T) \right) \right) * \text{Exp} \left[ \frac{1}{8.314 * T} (- (330.5513296703299 - 0.15782395604395608 T) * 1000) \right] ^{0.5} +
  1 / (8.21*^-5 * T)  $\left( (0.25) * \left( \frac{pp}{(8.21*^-5 * T)} \right) / \left( 1 / (8.21*^-5 * T) \right) \right) ^3 *
  \text{Exp} \left[ \frac{1}{8.314 * T} (- (-40.35034065934053 + 0.10430131868131862 T) * 1000) \right] ^{0.5} +
  1 / (8.21*^-5 * T)  $\left( (0.25) ^3 * \left( \frac{pp}{(8.21*^-5 * T)} \right) / \left( 1 / (8.21*^-5 * T) \right) \right) ^3 *
  \text{Exp} \left[ \frac{1}{8.314 * T} (- (-94.2604505494506 + 0.15240956043956044 T) * 1000) \right] ^{0.5} +
  1 / (8.21*^-5 * T)  $\left( (0.25) * \text{Exp} \left[ \frac{- (393.49 - 0.1739 T) * 1000}{8.314 * T} \right] \right)$ ;
(*T in K, Conc in mol/m^3*)$$$$$$ 
```



```

(*Knudsen diffusion (in m^2/s) as a function of temperature in Kelvin (T),
water content in atm (pp), and the average molecular weight in g/mol (mAvg) *)
DKnuAvg[T_, pp_, s_, mAvg_] :=  $\frac{2 \text{ s}}{3} \left( \frac{8 * 8.314 * 1000 * T}{\text{Pi} * \text{mAvg}} \right)^{0.5}$ ;

(*mw in g/mol, m^2/s*)
(*Molecular diffusion (in m^2/s) as a function of temperature in
Kelvin (T) and water content in atm (pp) for 1 atm total pressure *)
DiffAvg[T_, pp_, mAvg_, vAvg_, ekAvg_] := Module[{sigAvg, coliAvg, ekAir, tAvg},
  mO2 := 32;
  mH2O := 18;

  ekbO2 := 106.7;
  ekbH2O := 809.1;

  TbHB02 := 491 + 273; (*Kelvin*)
  TbH3B03 := 573; (*Kelvin, from Wikipedia*)
  TmH3B306 := 449; (*Kelvin, from Wikipedia on metaboric acid*)
  TmB203 = 723; (*Kelvin, from Wikipedia*)

  sigAvg = Mean[ {.841 * vAvg^(1/3), 3.4} ];
  ekAir = ekbH2O * pp + ekbO2 * (1 - pp);
  tAvg = T / (ekAvg * ekAir)^0.5;
  coliAvg = 1.06036 / (tAvg)^0.15610 + 0.193 / Exp[0.47635 * tAvg] +
    1.03587 / Exp[1.52996 * tAvg] + 1.76474 / Exp[3.89411 * tAvg];

  ((0.0018583 * T^(3/2)) / (1 * sigAvg^2 * coliAvg))
   $\left( \frac{1}{\text{mAvg}} + \frac{1}{18 * \text{pp} + 32 * (1 - \text{pp})} \right)^{1/2} / 100^2$ ];

(*Parabolic rate constant (B, in m^2/s) as a function
of temperature (T, in Kelvin) and water content (pp, in atm)
for interacting oxidants (specifically oxygen and water) *)
Bcomb[T_, pp_] := Module[{bo2, bh2o},
  bo2 = 1.1*^-8 * Exp[-245*^3 / (8.314 * T)];
  bh2o = 4.8*^-14 * Exp[-75*^3 / (8.314 * T)];
  bo2 * (1 - pp)^2 + bh2o pp^2];

ln[283]:= (*The analytical result for recession length at the composite
free surface as a function of temperature (Tc, in Celsius),
water content (pp, in atm), initial coating thickness (Δm, in m),
and normalized time (tau, unitless) *)
LmaxTime[Tc_, pp_, Δm_, tau_] := Module[{T, Dko, Dm, c112, c313, c336, c23,
  ConcSum, w112, w313, w336, w23, lPre, mAvg, vAvg, ekAvg, nAvg, nu},

```

```

(*calculate the concentration of each HxByOz product as
 a function of temperature, partial pressure (pp)*)
T = Tc + 273;
c112 = C112tip[T, pp];
c313 = C313tip[T, pp];
c336 = C336tip[T, pp];
c23 = C23tip[T, pp];
ConcSum = c112 + c313 + c336 + c23;
(*physical constants needed for
 the molecular diffusion coefficient calculation*)
mHB02 := 43.81 (*g/mol*);
mH3B03 := 61.81;
mH3B306 := 131.43;
mB203 := 69.6182;

TbHB02 := 491 + 273; (*Kelvin*)
TbH3B03 := 573; (*Kelvin, from Wikipedia*)
TmH3B306 := 449; (*Kelvin, from Wikipedia on metabolic acid*)
TmB203 = 723; (*Kelvin, from Wikipedia*)

(*calculate the weighting factor for each product*)
w112 = c112 / ConcSum;
w313 = c313 / ConcSum;
w336 = c336 / ConcSum;
w23 = c23 / ConcSum;
lPre = w112 + w313 + 3 * w336 + 2 w23;

m02 = 32;
mH20 = 18;

ekb02 = 106.7;
ekbH20 = 809.1;

(*calculate average physical properties based on weighting factors*)
mAvg = Total[{w112 * mHB02, w313 * mH3B03, w336 * mH3B306, w23 * mB203}];
(*average molecular weight*)
nAvg = Total[{w112 * 3, w313 * 7, w336 * 12, w23 * 5}];
vAvg = 20.1 + 0.88 mAvg + 13.4 nAvg;
ekAvg = Total[{w112 * 1.15 * TbHB02,
  w313 * 1.15 * TbH3B03, w336 * 1.92 * TmH3B306, w23 * 1.92 * TmB203}];
sigAvg = Mean[{0.841 * vAvg^(1/3), 3.4}];
ekAir = ekbH20 * pp + ekb02 * (1 - pp);
tAvg = T / (ekAvg * ekAir)^0.5;

```

$$\text{coliAvg} = 1.06036 / (\text{tAvg})^{0.15610} + 0.193 / \text{Exp}[0.47635 * \text{tAvg}] + 1.03587 / \text{Exp}[1.52996 * \text{tAvg}] + 1.76474 / \text{Exp}[3.89411 * \text{tAvg}];$$

$$\text{Dm} = \left(\frac{0.0018583 * T^{(3/2)}}{1 * \text{sigAvg}^2 * \text{coliAvg}} \right)$$

$$\left(\frac{1}{\text{mAvg}} + \frac{1}{18 * \text{pp} + 32 * (1 - \text{pp})} \right)^{1/2} / 100^2;$$

(*Pressure in atm, Temp in K, mw in g/mol, diffusion coefficient in m²/s*)

$$\text{Dko} = \frac{2}{3} \Delta m \left(\frac{8 * 8.314 * 1000 * T}{\text{Pi} * \text{mAvg}} \right)^{0.5}; \quad (*mw \text{ in g/mol, m}^2/\text{s}*)$$

$$\text{nu} = \text{Sqrt} \left[\frac{\text{lPre} * 1.8^2 * 1.18 * 10^{-5} * \text{cTot}[T, \text{pp}] * \text{Dm}}{2 * \text{Bcomb}[T, \text{pp}] * (1.8 - 1)^2} \right];$$

$$\text{nu} * \left(\text{tau} + 2 * \text{Sqrt}[\text{tau}] \frac{\text{Dm}}{\text{Dko}} + \frac{2 * \text{Dm} * (\text{Dm} + \text{Dko})}{\text{Dko}^2} \text{Log} \left[\frac{\text{Dm} + \text{Dko} - \text{Dko} * \text{Sqrt}[\text{tau}]}{\text{Dm} + \text{Dko}} \right] \right)^{0.5};$$

```
LrSec[Tc_, pp_, Δum_] := (*Calculates the recession length at the
  composite surface in mm for tau values specified by the expression
  (1-cos[(Pi/2)((i-1)/200)]) as a function of temperature (Tc, in Celsius),
  water content (pp, in atm), initial coating thickness (Δum, in um). The
  function output is (time (in seconds), recession length (in mm))*
Module[{T, Δ, tau, tc, β, Dko, Dm, c112, c313, c336, c23, ConcSum,
  w112, w313, w336, w23, lPre, mAvg, vAvg, ekAvg, nAvg, nu},
  T = Tc + 273;
  Δ = Δum * 10-6;
  tau = Table[1 - Cos[(Pi/2.) (i - 1) / 200], {i, 1, 200 + 1}];
  (*calculate the concentration of each HxByOz
  product as a function of temperature, partial pressure (pp)*)
  c112 = C112tip[T, pp];
  c313 = C313tip[T, pp];
  c336 = C336tip[T, pp];
  c23 = C23tip[T, pp];
  ConcSum = c112 + c313 + c336 + c23;
  (*physical constants needed for
  the molecular diffusion coefficient calculation*)
  mHB02 := 43.81 (*g/mol*);
  mH3B03 := 61.81;
  mH3B306 := 131.43;
  mB203 := 69.6182;

  TbHB02 := 491 + 273; (*Kelvin*)
  TbH3B03 := 573; (*Kelvin, from Wikipedia*)
  TmH3B306 := 449; (*Kelvin, from Wikipedia on metaboric acid*)
```

```

TmB203 = 723; (*Kelvin, from Wikipedia*)

(*calculate the weighting factor for each product*)
w112 = c112 / ConcSum;
w313 = c313 / ConcSum;
w336 = c336 / ConcSum;
w23 = c23 / ConcSum;
lPre = w112 + w313 + 3 * w336 + 2 w23;

(*calculate average physical properties based on weighting factors*)
mAvg = Total[{w112 * mHB02, w313 * mH3B03, w336 * mH3B306, w23 * mB203}];
(*average molecular weight*)
nAvg = Total[{w112 * 3, w313 * 7, w336 * 12, w23 * 5}];
vAvg = 20.1 + 0.88 mAvg + 13.4 nAvg;
ekAvg = Total[{w112 * 1.15 * TbHB02,
  w313 * 1.15 * TbH3B03, w336 * 1.92 * TmH3B306, w23 * 1.92 * TmB203}];

Dm = DiffAvg[T, pp, mAvg, vAvg, ekAvg];
Dko = DKnuAvg[T, pp, Δ, mAvg];
β = Dko / Dm;
nu = Sqrt[
$$\frac{lPre \cdot 1.8^2 \cdot 1.18 \cdot 10^{-5} \cdot cTot[T, pp] \cdot Dm}{2 \cdot Bcomb[T, pp] \cdot (1.8 - 1)^2}$$
];

tc = 1.8^2 * Δ^2 / (4 (1.8 - 1)^2 * Bcomb[T, pp]) / 3600;
Table[{tau[[i]] * tc, Δ * 10^3
  (nu * (tau[[i]] + 2 
$$\frac{Sqrt[tau[[i]]}{\beta} + \frac{2(1+\beta)}{\beta^2} \text{Log}\left[\frac{1+\beta - \beta Sqrt[tau[[i]]}{1+\beta}\right]$$

  0.5)}), {i, 1, Length[tau]}]
];

LrNorm[Tc_, pp_, Δum_, Lcmm_] :=
(*Calculates the recession length at the composite surface in mm for
tau values specified by the expression (1-cos[(Pi/2)((i-1)/200])). The
output is (normalized time, recession length (in mm))*
Module[{T, Δ, tau, tc, Lc, Lr, β, Dko, Dm, c112, c313, c336, c23,
  ConcSum, w112, w313, w336, w23, lPre, mAvg, vAvg, ekAvg, nAvg, nu},
  T = Tc + 273;
  Δ = Δum * 10^-6;
  tau = Table[1 - Cos[(Pi/2.) (i - 1) / 200], {i, 1, 200 + 1}];
  Lc = Lcmm * 10^-3;
  (*calculate the concentration of each HxBYOz

```

```

product as a function of temperature, partial pressure (pp)*)
c112 = C112tip[T, pp];
c313 = C313tip[T, pp];
c336 = C336tip[T, pp];
c23 = C23tip[T, pp];
ConcSum = c112 + c313 + c336 + c23;
(*physical constants needed for
the molecular diffusion coefficient calculation*)
mHB02 := 43.81 (*g/mol*);
mH3B03 := 61.81;
mH3B306 := 131.43;
mB203 := 69.6182;

TbHB02 := 491 + 273; (*Kelvin*)
TbH3B03 := 573; (*Kelvin, from Wikipedia*)
TmH3B306 := 449; (*Kelvin, from Wikipedia on metaboric acid*)
TmB203 = 723; (*Kelvin, from Wikipedia*)

(*calculate the weighting factor for each product*)
w112 = c112 / ConcSum;
w313 = c313 / ConcSum;
w336 = c336 / ConcSum;
w23 = c23 / ConcSum;
lPre = w112 + w313 + 3 * w336 + 2 w23;

(*calculate average physical properties based on weighting factors*)
mAvg = Total[{w112 * mHB02, w313 * mH3B03, w336 * mH3B306, w23 * mB203}];
(*average molecular weight*)
nAvg = Total[{w112 * 3, w313 * 7, w336 * 12, w23 * 5}];
vAvg = 20.1 + 0.88 mAvg + 13.4 nAvg;
ekAvg = Total[{w112 * 1.15 * TbHB02,
w313 * 1.15 * TbH3B03, w336 * 1.92 * TmH3B306, w23 * 1.92 * TmB203}];

Dm = DiffAvg[T, pp, mAvg, vAvg, ekAvg];
Dko = DKnuAvg[T, pp, Δ, mAvg];
β = Dko / Dm;
nu = Sqrt[ $\frac{lPre \cdot 1.8^2 \cdot 1.18 \cdot 10^{-5} \cdot cTot[T, pp] \cdot Dm}{2 \cdot Bcomb[T, pp] \cdot (1.8 - 1)^2}$ ];
tc = 1.8^2 * Δ^2 / (4 (1.8 - 1)^2 * Bcomb[T, pp]) / 3600;

Table[Lr = Δum * 10^-3 (nu *
( $\tau[[i]] + 2 \frac{\text{Sqrt}[\tau[[i]]]}{\beta} + \frac{2(1+\beta)}{\beta^2} \text{Log}[\frac{1+\beta-\beta \text{Sqrt}[\tau[[i]]]}{1+\beta}]$ )^0.5)];

```

```

      {tau[[i]], Lr }, {i, 1, Length[tau]}]
];

```

Figures used in Chapter 6

Figure 6.2: Retained strength as a function of recession length, time

Code

```

In[286]:= compStrengthNorm[f_, LgIn_, LcIn_, TcIn_, ppIn_, ΔIn_] :=
  (*Outputs the residual strength as a function of time*)
  Module[{ T, Ef, Em, Ec, σmo, Lo, mm, R, σfo, mf, Lg, Lc, τs, Lr, LrR, λc,
    λr, δfs, δms, α, σfs, σms, sTh, tc, maxStrain, σfrs, compSII, compSI,
    compVal, compSp, toutput, compoutput, tTrans, TStep, ppStep, wStep, ΔR,
    ppR, TcR, LrM, envOutput, tauM1, tauM, tauR, LrV, term, sTrans, trans1},

    TStep = 3;
    ppStep = 3;
    wStep = 1;

    (*Create the temperature, water vapor, and coating thickness arrays*)
    TcR = Array[# &, TStep, {TcIn}];
    ppR = Array[# &, ppStep, {ppIn}];
    ΔR = Array[# &, wStep, {ΔIn}] * 10-6;

    τs = 20 ; (*MPa*)
    Em = 400.*^3; (*MPa*)
    σmo = 100.; (*MPa*)
    Lo = 1. ; (*m*)
    mm = 5.;
    R = 5.0*^-6; (*m*)
    Ef = 400.0*^3; (*MPa*)
    σfo = 1500.; (*MPa*)
    mf = 5.;
    Lg = LgIn * 1*^-3; (*m*)
    Lc = LcIn * 1*^-3; (*m*)

```

$$\alpha = 1 / (mf + 1);$$

$$E_c = f * E_f + (1 - f) * E_m;$$

$$\delta fs = R \left(\frac{\sigma fo}{\tau s} \right)^{\alpha} (mf / (mf + 1)) \left(\frac{Lo}{R} \right)^{\alpha} (1 / (mf + 1));$$

$$\delta ms = R \left(\frac{\sigma mo (1 - f)}{f * \tau s} \right)^{\alpha} (mm / (mm + 1)) \left(\frac{Lo}{R} \right)^{\alpha} (1 / (mm + 1));$$

$$\sigma fs = \sigma fo * \left(\frac{\tau s * Lo}{\sigma fo * R} \right)^{\alpha} (1 / (mf + 1));$$

$$\sigma ms = \sigma mo \left(\frac{f * \tau s * Lo}{(1 - f) \sigma mo * R} \right)^{\alpha} (1 / (mm + 1));$$

$$\text{maxStrain} = (\alpha - \text{ProductLog}[-\alpha * \text{Exp}[\alpha]])^{\alpha};$$

$$\text{compSp} = \frac{f * \sigma fs * \text{maxStrain}}{2} (1 + \text{Exp}[-(\text{maxStrain})^{\alpha} (mf + 1)]);$$

$$\text{compSII} = f * \sigma fs * \left(\frac{\delta fs / Lg}{mf * E} \right)^{\alpha} (1 / mf);$$

$$\lambda c = Lc / \delta ms;$$

(*The maximum recession length is set by the crack spacing, Lc*)

$$LrM = Lc / 2;$$

envOutput =

```
Table[tc = 1.8^2 * ΔR[[k]]^2 / (4 (1.8 - 1)^2 * Bcomb[TcR[[i]] + 273, ppR[[j]]];
```

```
(*Set precision to 5 because sometimes when tau = 0 the recession length yields zero but with a very small (10^-10) imaginary component*)
```

```
Lr = SetPrecision[ΔR[[k]] * LmaxTime[TcR[[i]], ppR[[j]], ΔR[[k]], tau], 5];
```

```
(*Solve for the time to
```

```
remove all of the coating for the set of conditions *)
```

```
tauM1 = NSolve[Lr == LrM && tau < 1.1, tau, Reals, 3];
```

```
If[tauM1 == {}, tauM = 1, tauM = tauM1[[1, 1, 2]]];
```

```
(*Create a non-linear distribution for tau*)
```

```
tauR =
```

```
Join[{0}, Table[(Cos[(3 Pi / 2.) + (Pi / 2.) (i - 1) / 200])^2, {i, 2, 201}]] * tauM;
```

```
(*Run through time to find the decrease in composite strength*)
```

```
toutput = Table[(*LrV = Lr/.tau -> tauR[[q]];
```

```
λr = LrV / δms;*)
```

```

σfrs = σfs * (1 - 2 LrLc) ^ (1 / (mf + 1));

compSI =  $\frac{f * \sigma_{frs} * \maxStrain}{2} (1 + \text{Exp}[-(\maxStrain)^{(mf + 1)})]$ ;
(*Check that DI gives a real number. If not, set to zero. Then take the
larger of the two values as the composite strength for the timestep*)
If[Element[compSI, Reals], , compSI = 0];
If[compSI > compSII, compVal = compSI, compVal = compSII];
(*composite strength is in MPa*)
{2 LrLc, compVal / compSp}, {LrLc, 0, 0.5, 0.001}];

(*Calculate the transition point for Domain I → Domain II*)
trans1 = Position[toutput, compSII / compSp, 2, 1];

(*If the coating remains after closure,
Find the terminal time (and strength)*)
If[trans1 == {}, sTrans = Null; term = Last[toutput],
sTrans = Extract[toutput, trans1[[1, 1]][[1]]];
term = Null];
tTrans = Join[{sTrans}, {compSII / compSp}];
{TcR[[i]], ppR[[j]], ΔR[[k]], toutput, {tTrans}, {term}}
, {i, 1, Length[TcR]}, {j, 1, Length[ppR]}, {k, 1, Length[ΔR]}]

(*For indexing, the output is: *)
(*envOutput[[T,p,w,data, transition, termination]]*)

]

ln[287]:= compStrengthT[f_, LgIn_, LcIn_, TcIn_, ppIn_, ΔIn_] :=
(*Outputs the residual strength as a function of time*)
Module[{T, Ef, Em, Ec, σmo, Lo, mm, R, σfo, mf, Lg, Lc, τs, Lr, LrR, λc,
λr, δfs, δms, α, σfs, σms, sTh, tc, maxStrain, σfrs, compSII, compSI,
compVal, compSp, toutput, compoutput, tTrans, TStep, ppStep, wStep, ΔR,
ppR, TcR, LrM, envOutput, tauM1, tauM, tauR, LrV, term, sTrans, trans1},

TStep = 3;
ppStep = 3;
wStep = 1;

(*Create the temperature, water vapor, and coating thickness arrays*)
TcR = Array[# &, TStep, {TcIn}];
ppR = Array[# &, ppStep, {ppIn}];
ΔR = Array[# &, wStep, {ΔIn}] * 10^-6;

```



```

τs = 20 ; (*MPa*)
Em = 400.*^3; (*MPa*)
σmo = 100.; (*MPa*)
Lo = 1. ; (*m*)
mm = 5.;
R = 5.0*^-6; (*m*)
Ef = 400.0*^3; (*MPa*)
σfo = 1500.; (*MPa*)
mf = 5.;
Lg = LgIn * 1*^-3; (*m*)
Lc = LcIn * 1*^-3; (*m*)

α = 1 / (mf + 1);
Ec = f * Ef + (1 - f) * Em;

δfs = R (σfo / τs) ^ (mf / (mf + 1)) (Lo / R) ^ (1 / (mf + 1));
δms = R (σmo (1 - f) / (f * τs)) ^ (mm / (mm + 1)) (Lo / R) ^ (1 / (mm + 1));
σfs = σfo * (τs * Lo / (σfo * R)) ^ (1 / (mf + 1));
σms = σmo (f * τs * Lo / ((1 - f) σmo * R)) ^ (1 / (mm + 1));

maxStrain = (α - ProductLog[-α * Exp[α]]) ^ α;

compSp = (f * σfs * maxStrain) / 2 (1 + Exp[-(maxStrain) ^ (mf + 1)]);

compSII = f * σfs * (δfs / Lg) ^ (1 / mf);

λc = Lc / δms;

(*The maximum recession length is set by the crack spacing, Lc*)
LrM = Lc / 2;

envOutput =
Table[tc = 1.8^2 * ΔR[[k]] ^ 2 / (4 (1.8 - 1) ^ 2 * Bcomb[TcR[[i]] + 273, ppR[[j]]]);
(*Set precision to 5 because sometimes when tau = 0 the recession length
yields zero but with a very small (10^-10) imaginary component*)
Lr = SetPrecision[ΔR[[k]] * LmaxTime[TcR[[i]], ppR[[j]], ΔR[[k]], tau], 5];

```

```

(*Solve for the time to
remove all of the coating for the set of conditions *)
tauM1 = NSolve[Lr == LrM && tau < 1.1, tau, Reals, 3];
If[tauM1 == {}, tauM = 1, tauM = tauM1[[1, 1, 2]]];
(*Create a non-linear distribution for tau*)
tauR =
Join[{0}, Table[(Cos[(3 Pi/2.) + (Pi/2.) (i - 1)/200])^2, {i, 2, 201}]] * tauM;
(*Run through time to find the decrease in composite strength*)

toutput = Table[LrV = Lr /. tau -> tauR[[q]];
  lambda_r = LrV / delta_ms;

sigma_fr = sigma_fs * (1 - 2 lambda_r / lambda_c)^(1 / (mf + 1));

compSI = 
$$\frac{f * \sigma_{frs} * \text{maxStrain}}{2} (1 + \text{Exp}[-(\text{maxStrain})^{(mf + 1)}]);$$

(*Check that DI gives a real number. If not, set to zero. Then take the
larger of the two values as the composite strength for the timestep*)
If[Element[compSI, Reals], , compSI = 0];
If[compSI > compSII, compVal = compSI, compVal = compSII];
(*Convert tau to real time in hours, composite strength is in MPa*)
{tauR[[q]] * tc / 3600, compVal / compSp}, {q, 1, Length[tauR]};

(*Calculate the transition point for Domain I -> Domain II*)
trans1 = Position[toutput, compSII / compSp, 2, 1];

(*If the coating remains after closure,
Find the terminal time (and strength)*)
If[trans1 == {}, sTrans = Null; term = Last[toutput],
  sTrans = Extract[toutput, trans1[[1, 1]]][[1]];
  term = Null];
tTrans = Join[{sTrans}, {compSII / compSp}];
{TcR[[i]], ppR[[j]], delta_R[[k]], toutput, {tTrans}, {term}}
, {i, 1, Length[TcR]}, {j, 1, Length[ppR]}, {k, 1, Length[delta_R]}]

(*For indexing, the output is: *)
(*envOutput[[T,p,w,data, transition, termination]]*)

]

compStrengthR[f_, LgIn_] :=
(*Outputs the residual strength as a function of normalized recession*)

```

```
Module[{ T, Ef, Em, Ec,  $\sigma_{mo}$ , Lo, mm, R,  $\sigma_{fo}$ , mf, Lg, Lc,  $\tau_S$ , Lr, LrR,  $\lambda_C$ ,  $\lambda_r$ ,  $\delta_{fs}$ ,
 $\delta_{ms}$ ,  $\alpha$ ,  $\sigma_{fs}$ ,  $\sigma_{ms}$ , sTh, tc, maxStrain,  $\sigma_{frs}$ , compSII, compSI, compVal,
compSp, toutput, compoutput, tTrans, TStep, ppStep, wStep,  $\Delta R$ , ppR,
TcR, LrM, envOutput, tauM1, tauM, tauR, LrV, term, sTrans, trans1},
```

```
 $\tau_S = 20$ ; (*MPa*)
Em = 400.*^3; (*MPa*)
 $\sigma_{mo} = 100.$ ; (*MPa*)
Lo = 1.; (*m*)
mm = 5.;
R = 5.0*^-6; (*m*)
Ef = 400.0*^3; (*MPa*)
 $\sigma_{fo} = 1500.$ ; (*MPa*)
mf = 5.;
Lg = LgIn * 1*^-3; (*m*)
```

```
 $\alpha = 1 / (mf + 1)$ ;
Ec = f * Ef + (1 - f) * Em;
```

$$\delta_{fs} = R \left(\frac{\sigma_{fo}}{\tau_S} \right)^{\alpha} \left(\frac{mf}{mf + 1} \right)^{\alpha} \left(\frac{Lo}{R} \right)^{\alpha} \left(\frac{1}{mf + 1} \right)^{\alpha};$$

$$\delta_{ms} = R \left(\frac{\sigma_{mo} (1 - f)}{f * \tau_S} \right)^{\alpha} \left(\frac{mm}{mm + 1} \right)^{\alpha} \left(\frac{Lo}{R} \right)^{\alpha} \left(\frac{1}{mm + 1} \right)^{\alpha};$$

$$\sigma_{fs} = \sigma_{fo} * \left(\frac{\tau_S * Lo}{\sigma_{fo} * R} \right)^{\alpha} \left(\frac{1}{mf + 1} \right)^{\alpha};$$

$$\sigma_{ms} = \sigma_{mo} \left(\frac{f * \tau_S * Lo}{(1 - f) * \sigma_{mo} * R} \right)^{\alpha} \left(\frac{1}{mm + 1} \right)^{\alpha};$$

```
maxStrain = ( $\alpha$  - ProductLog[- $\alpha$  * Exp[ $\alpha$ ]]) ^  $\alpha$ ;
```

$$\text{compSp} = \frac{f * \sigma_{fs} * \text{maxStrain}}{2} (1 + \text{Exp}[-(\text{maxStrain})^{\alpha} (mf + 1)]);$$

$$\text{compSII} = f * \sigma_{fs} * \left(\frac{\delta_{fs} / Lg}{mf * E} \right)^{\alpha} \left(\frac{1}{mf} \right)^{\alpha};$$

```
toutput = Table[
```

$$\sigma_{frs} = \sigma_{fs} * (1 - 2 LrLc)^{\alpha} \left(\frac{1}{mf + 1} \right)^{\alpha};$$

$$\text{compSI} = \frac{f * \sigma_{frs} * \text{maxStrain}}{2} (1 + \text{Exp}[-(\text{maxStrain})^{\alpha} (mf + 1)]);$$

```

(*Check that DI gives a real number. If not, set to zero. Then take the
larger of the two values as the composite strength for the timestep*)
If[Element[compSI, Reals], , compSI = 0];
If[compSI > compSII, compVal = compSI, compVal = compSII];
(*Convert tau to real time in hours, composite strength is in MPa*)
{LrLc * 2, compVal / compSp}, {LrLc, 0, 0.5, 0.001}];

```

```

(*Calculate the transition point for Domain I → Domain II*)
trans1 = Position[toutput, compSII / compSp, 2, 1];

```

```

(*If the coating remains after closure,
Find the terminal time (and strength)*)
If[trans1 == {}, sTrans = Null; term = Last[toutput],
sTrans = Extract[toutput, trans1[[1, 1]][[1]]];
term = Null];
tTrans = Join[{sTrans}, {compSII / compSp}];
{toutput, {tTrans}, {term}}
]

```

```

In[289]:= slg1lR = compStrengthR[0.3, 4.];
slg1R = compStrengthR[0.3, 8.];
slg2R = compStrengthR[0.3, 40.];
slg3R = compStrengthR[0.3, 100.];

```

```

LrvalLg = LrNorm[700., 0.15, 0.35, 4.];

```

```

In[294]:= slg4R = compStrengthR[0.3, 50.];

```

Figure 6.2: Retained strength as a function of recession length relative to crack spacing

```

In[380]:= ListPlot[{slg3R[[1]], slg3R[[2]], slg2R[[1]], slg2R[[2]],
  slg1R[[1]], slg1R[[2]], slg1LR[[1]], slg1LR[[2]]}, Joined -> {True},
  PlotStyle -> {{Thick, ColorData[97, "ColorList"][[4]]},
  White, {Thick, ColorData[97, "ColorList"][[3]]},
  White, {Thick, ColorData[97, "ColorList"][[2]]}, White,
  {Thick, ColorData[97, "ColorList"][[1]]}, White},
  PlotMarkers -> {None, Graphics[{EdgeForm[ColorData[97, "ColorList"][[4]]],
  PolygonMarker["Disk", Offset[25]]}, AlignmentPoint -> {0, 0}},
  None, Graphics[{EdgeForm[ColorData[97, "ColorList"][[3]]],
  PolygonMarker["Disk", Offset[25]]}, AlignmentPoint -> {0, 0}},
  None, Graphics[{EdgeForm[ColorData[97, "ColorList"][[2]]],
  PolygonMarker["Disk", Offset[25]]}, AlignmentPoint -> {0, 0}},
  None, Graphics[{EdgeForm[ColorData[97, "ColorList"][[1]]],
  PolygonMarker["Disk", Offset[25]]}, AlignmentPoint -> {0, 0}}},
  Frame -> {True, True, True, False}, FrameStyle -> Directive[Thick, Black],
  FrameTicks -> {{LinTicks, None}, {LinTicks, StripTickLabels[LinTicks]}},
  FrameLabel -> {{ "Residual strength,  $\sigma_c^{ult}/\sigma_{pristine}$ ", ""},
  {"Normalized recession,  $2L_R/L_C$ ", " $L_g = 8/40/100$  mm"}},
  BaseStyle -> {FontFamily -> "Arial", FontSize -> 16},
  PlotRange -> {{-0.02, 1.02}, {-0.02, 1.02}}, AspectRatio -> 1, ImageSize -> Medium]

```

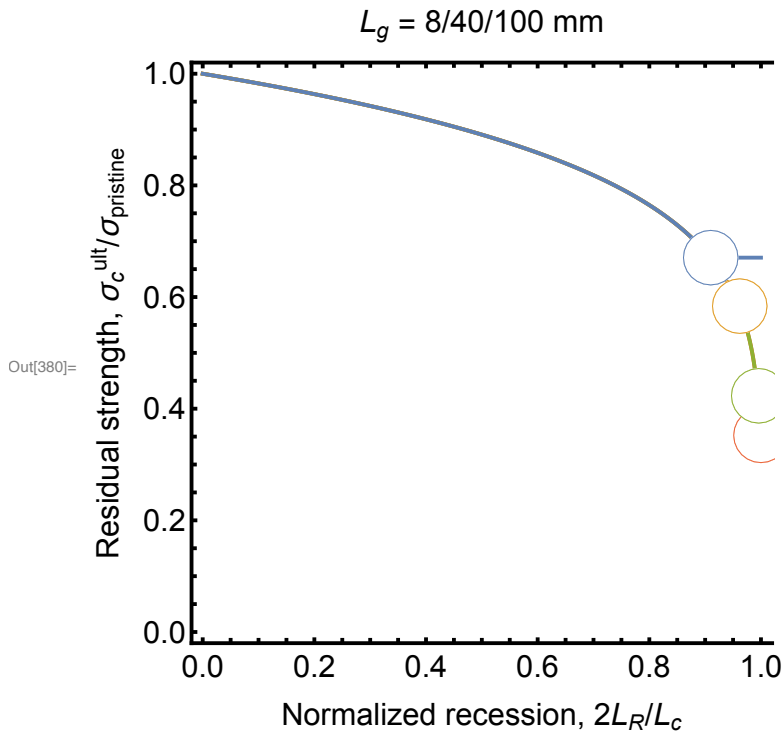


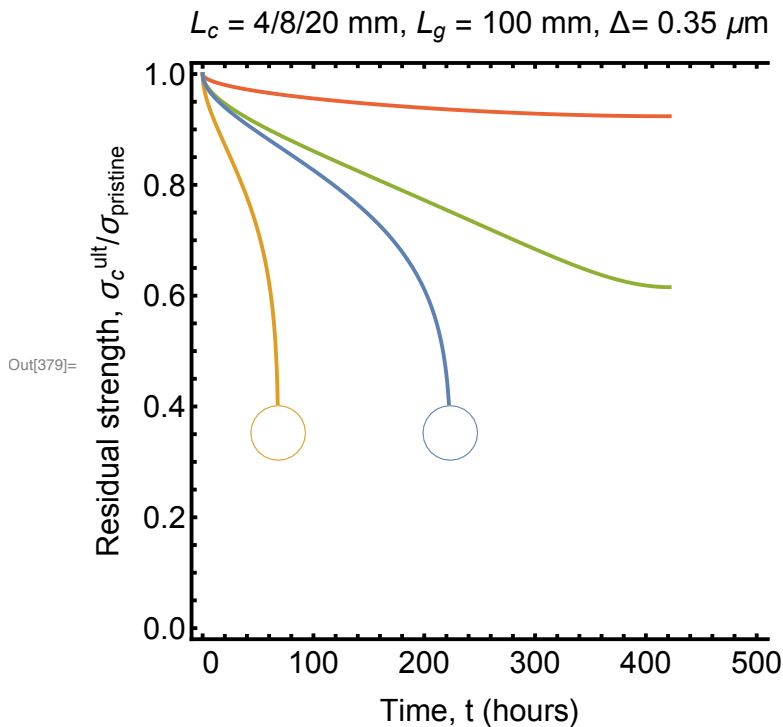
Figure 6.3: Retained strength, maximum recession length as a function of time

```
In[330]:= slc1 = compStrengthT[0.3, 100., 4., {700., 1000.}, {0., 0.3}, {0.35, 0.35}];  
          slc2 = compStrengthT[0.3, 100., 8., {700., 1000.}, {0., 0.3}, {0.35, 0.35}];  
          slc3 = compStrengthT[0.3, 100., 20., {700., 1000.}, {0., 0.3}, {0.35, 0.35}];  
  
In[299]:= slc2v2 = compStrengthT[0.3, 100., 8., {700., 1000.}, {0., 0.3}, {0.6, 0.6}];
```

```

In[379]= ListPlot[{slc3[[1, 2, 1, 4]], slc3[[1, 2, 1, 5]], slc2[[1, 2, 1, 4]],
  slc2[[1, 2, 1, 5]], slc1[[1, 2, 1, 4]], slc1[[1, 2, 1, 5]],
  slc2v2[[1, 2, 1, 4]], slc2v2[[1, 2, 1, 5]]}, Joined -> {True},
  PlotStyle -> {{Thick, ColorData[97, "ColorList"][[4]]},
  White, {Thick, ColorData[97, "ColorList"][[3]]},
  White, {Thick, ColorData[97, "ColorList"][[2]]}, White,
  {Thick, ColorData[97, "ColorList"][[1]]}, White},
  PlotMarkers -> {None, Graphics[{EdgeForm[ColorData[97, "ColorList"][[4]]],
  PolygonMarker["Disk", Offset[10]]}, AlignmentPoint -> {0, 0}},
  None, Graphics[{EdgeForm[ColorData[97, "ColorList"][[3]]],
  PolygonMarker["Disk", Offset[10]]}, AlignmentPoint -> {0, 0}},
  None, Graphics[{EdgeForm[ColorData[97, "ColorList"][[2]]],
  PolygonMarker["Disk", Offset[25]]}, AlignmentPoint -> {0, 0}},
  None, Graphics[{EdgeForm[ColorData[97, "ColorList"][[1]]],
  PolygonMarker["Disk", Offset[25]]}, AlignmentPoint -> {0, 0}}],
  Frame -> {True, True, True, False}, FrameStyle -> Directive[Thick, Black],
  FrameTicks ->
  {{LinTicks, StripTickLabels[LinTicks]}, {LinTicks, StripTickLabels[LinTicks]}},
  FrameLabel -> {{ "Residual strength,  $\sigma_c^{ult}/\sigma_{pristine}$ ", ""},
  {"Time, t (hours)", " $L_c = 4/8/20$  mm,  $L_g = 100$  mm,  $\Delta = 0.35$   $\mu\text{m}$ "}}},
  BaseStyle -> {FontFamily -> "Arial", FontSize -> 16},
  PlotRange -> {{-10, 510}, {-0.02, 1.02}}, AspectRatio -> 1, ImageSize -> Medium]

```



```

In[334]= LrLcval = LrSec[700., 0.15, 0.35];
  Lrval2 = LrSec[700., 0.15, 0.6];

```

```

In[378]:= ListPlot[{Lrval2, LrLcval}, Joined → {True},
  PlotStyle → {{Thick, ColorData[97, "ColorList"][[4]]},
    {Thick, ColorData[97, "ColorList"][[3]]}, White,
    {Thick, ColorData[97, "ColorList"][[2]]}, White,
    {Thick, ColorData[97, "ColorList"][[1]]}, White},
  PlotMarkers → {None, None, Graphics[{EdgeForm[ColorData[97, "ColorList"][[3]]],
    PolygonMarker["Disk", Offset[5]]}, AlignmentPoint → {0, 0}],
    None, Graphics[{EdgeForm[ColorData[97, "ColorList"][[2]]],
    PolygonMarker["Disk", Offset[5]]}, AlignmentPoint → {0, 0}],
    None, Graphics[{EdgeForm[ColorData[97, "ColorList"][[1]]],
    PolygonMarker["Disk", Offset[5]]}, AlignmentPoint → {0, 0}]},
  Frame → {True, True, True, False}, FrameStyle → Directive[Thick, Black],
  FrameTicks → {{LinTicks, LinTicks}, {LinTicks, None}},
  FrameLabel → {"Recession length, Lr (mm)", ""},
    {"Time, t (hours)", "700C, 0.15 atm, Δ= 0.35 μm"}},
  BaseStyle → {FontFamily → "Arial", FontSize → 16},
  PlotRange → {{-10, 510}, {-0.1, 5.1}}, AspectRatio → 1, ImageSize → Medium]

```

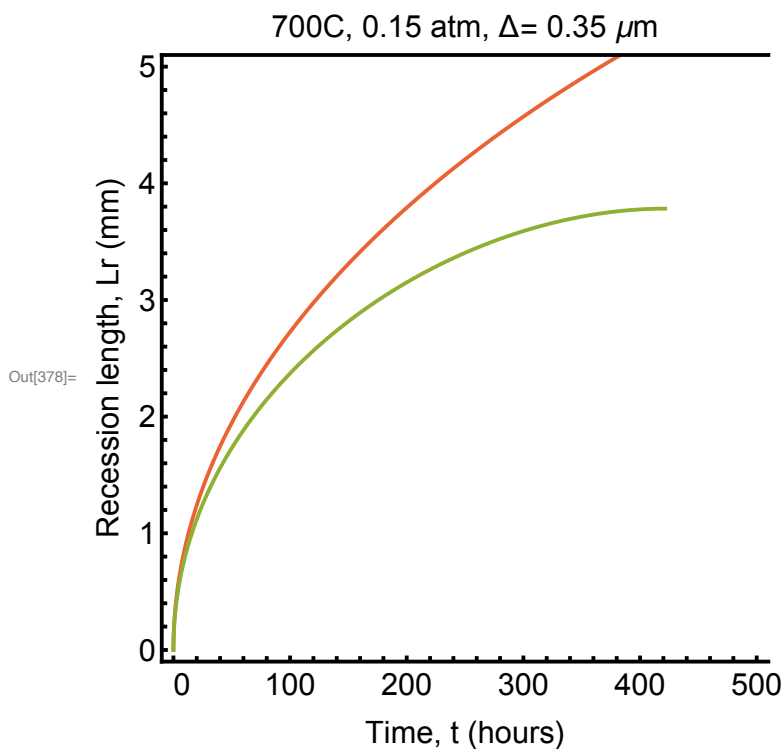


Figure 6.4: Impact of environment on terminal time

Code


```

In[300]:= termTimes[f_, LgIn_, LcIn_, TcIn_, ppIn_, ΔIn_] :=
  (*Inputs (in order): f, gauge length in um, crack spacing in um,
  {lower temperature bound, upper temperature bound} (in Celsius),
  {lower water vapor bound, upper water vapor bound}(in atm),
  {lower BN thickness bound, upper BN thickness bound}(in um)*)

  (*Outputs (in order): Temperature, water vapor, BN thickness,
  time to seal the gap (in hours), time to remove all coating (in hours)*)

Module[{T, Ef, Em, Ec, σmo, Lo, mm, R, σfo, mf, Lg, Lc, τs, Lr, LrR, λc, λr, δfs,
  δms, α, σfs, σms, sTh, tc, maxStrain, σfrs, compSII, compSI, compVal,
  toutput, compoutput, trans, TStep, ppStep, wStep, Δv, ΔR, ppR, TcR,
  LrM, envOutput, tauM1, tauM, tauR, LrV, term, tSeal, tRem, tauDII},

  Lg = LgIn * 1*^-3; (*m*)
  Lc = LcIn * 1*^-3; (*m*)
  Δv = ΔIn * 1*^-6; (*m*)

  (*Create the temperature, water vapor, and coating thickness arrays*)
  TcR = Table[i, {i, First[TcIn], Last[TcIn], 5}];
  TStep = Length[TcR];
  ppR = Array[(1 - Cos[# (Pi/2.)])^2 &, 51, {ppIn}];

  ppStep = Length[ppR];
  (*ppR = Array[#&, ppStep, {ppIn}];*)
  ΔR = Array[# &, 1, {Δv}];
  wStep = Length[ΔR];

  τs = 20; (*MPa*)
  Em = 400.*^3; (*MPa*)
  σmo = 100.; (*MPa*)
  Lo = 1.; (*m*)
  mm = 5.;
  R = 5.0*^-6; (*m*)
  Ef = 400.0*^3; (*MPa*)
  σfo = 1500.; (*MPa*)
  mf = 5.;

  α = 1 / (mf + 1);
  Ec = f * Ef + (1 - f) * Em;

```

$$\delta fs = R \left(\frac{\sigma fo}{\tau S} \right)^{\left(mf / (mf + 1) \right)} \left(\frac{Lo}{R} \right)^{\left(1 / (mf + 1) \right)};$$

$$\delta ms = R \left(\frac{\sigma mo (1 - f)}{f * \tau S} \right)^{\left(mm / (mm + 1) \right)} \left(\frac{Lo}{R} \right)^{\left(1 / (mm + 1) \right)};$$

$$\sigma fs = \sigma fo * \left(\frac{\tau S * Lo}{\sigma fo * R} \right)^{\left(1 / (mf + 1) \right)};$$

$$\sigma ms = \sigma mo \left(\frac{f * \tau S * Lo}{(1 - f) \sigma mo * R} \right)^{\left(1 / (mm + 1) \right)};$$

$$\text{maxStrain} = (\alpha - \text{ProductLog}[-\alpha * \text{Exp}[\alpha]])^{\alpha};$$

$$\text{compSII} = f * \sigma fs * \left(\frac{\delta fs / Lg}{mf * E} \right)^{\left(1 / mf \right)};$$

$$Lc = LcIn * 1 *^{-3}; (*m*)$$

(*Find the Lr/Lc value that gives DII behavior
(where strength in domain I = strength in domain II). Lr/Lc must
be less than or equal to 0.5. NSolve doesn't work if you try to
use mm. This value is independent of environmental conditions*)

$$\text{LrV} = \text{NSolve}\left[\left(\frac{\delta fs}{Lg * mf * E}\right)^{\left(1 / mf\right)} == \frac{(1 - 2 \text{LrLc})^{\left(1 / (mf + 1)\right)} * \text{maxStrain}}{2}\right. \\ \left. (1 + \text{Exp}[-(\text{maxStrain})^{\left(mf + 1\right)}]) \&\& \text{LrLc} < 0.51, \text{LrLc}, \text{Reals}\right][[1, 1, 2]] * Lc;$$

envOutput = Table[

Tc = TcR[[i]];

pp = ppR[[j]];

Δ = ΔR[[k]];

tc = 1.8^2 * Δ^2 / (4 (1.8 - 1)^2 * Bcomb[Tc + 273, pp]) / 3600;

LrM = Δ * LmaxTime[Tc, pp, Δ, 1];

(*If the maximum recession length is larger than the value required
to reach DII, then compute the time required to reach the DII
recession value. Otherwise, the recession channel closes first.*)

If[LrM > LrV, tII = NSolve[LrV == Δ * LmaxTime[Tc, pp, Δ, tau] && tau < 1.1,
tau, Reals, 3][[1, 1, 2]] * tc, tII = Null];

{Tc, pp, Δ, tc, tII}

```

, {i, 1, Length[TcR]}, {j, 1, Length[ppR]}, {k, 1, Length[ΔR]};

(*For indexing, the output is: *)
(*envOutput[[T,p,w, time to seal the gap, time to remove all coating]]*)

TdatSeal = Flatten[Table[{envOutput[[i, j, k, 1]], envOutput[[i, j, k, 4]]},
  {j, 1, ppStep}, {k, 1, wStep}, {i, 1, TStep}], 1];
TdatRem = Flatten[Table[{envOutput[[i, j, k, 1]], envOutput[[i, j, k, 5]]},
  {j, 1, ppStep}, {k, 1, wStep}, {i, 1, TStep}], 1];

ppdatSeal = Flatten[Table[{envOutput[[i, j, k, 2]], envOutput[[i, j, k, 4]]},
  {i, 1, TStep}, {k, 1, wStep}, {j, 1, ppStep}], 1];
ppdatRem = Flatten[Table[{envOutput[[i, j, k, 2]], envOutput[[i, j, k, 5]]},
  {i, 1, TStep}, {k, 1, wStep}, {j, 1, ppStep}], 1];

{TdatRem, TdatSeal, ppdatRem, ppdatSeal, envOutput}

]

```

Figure Output

```

In[301]:= (*Inputs (in order): f, Lg, Lc,
{lower temperature bound, upper temperature bound},
{lower water vapor bound, upper water vapor bound},
{lower BN thickness bound, upper BN thickness bound}*)
(*Outputs (in order): Temperature data, remaining coating;
temperature data, sealed; water vapor data,
remaining coating; water vapor, sealed; all data unsorted*)
lcbase = termTimes[0.3, 100., 4., {700., 1000.}, {0., 1.}, {0.35, 0.35}];
lcbasel = termTimes[0.3, 100., 0.5, {700., 1000.}, {0., 1.}, {0.35, 0.35}];
lcbaseM1 = termTimes[0.3, 100., 1., {700., 1000.}, {0., 1.}, {0.35, 0.35}];
lcbaseM12 = termTimes[0.3, 100., 2, {700., 1000.}, {0., 1.}, {0.35, 0.35}];

lcbaselg2 = termTimes[0.3, 8., 4., {700., 1000.}, {0., 1.}, {0.35, 0.35}];
lcbasel1g2 = termTimes[0.3, 8., 0.5, {700., 1000.}, {0., 1.}, {0.35, 0.35}];
lcbaseM11g2 = termTimes[0.3, 8., 1., {700., 1000.}, {0., 1.}, {0.35, 0.35}];
lcbaseM121g2 = termTimes[0.3, 8., 2, {700., 1000.}, {0., 1.}, {0.35, 0.35}];

```

```

In[376]:= SetOptions[LogTicks, LogPlot → True, LogPlot → E];
Show[ListLogPlot[lcbasel[[3, 21]], Joined → True,
  PlotStyle → ColorData["DeepSeaColors"][0.3]], (*Lc = 0.5 mm*)

ListLogPlot[lcbaseMl[[3, 21]], Joined → True,
  PlotStyle → ColorData["DeepSeaColors"][0.5]], (*Lc = 1 mm*)

ListLogPlot[lcbaseMl2[[3, 21]], Joined → True,
  PlotStyle → ColorData["DeepSeaColors"][0.75]], (*Lc = 2 mm*)

ListLogPlot[lcbasel[[3, 21]], Joined → True,
  PlotStyle → ColorData["DeepSeaColors"][0.9]], (*Lc = 4 mm*)

ListLogPlot[lcbasel[[4, 21]], Joined → True,
  PlotStyle → ColorData[97, "ColorList"][[2]]],

ListLogPlot[lcbaselg2[[3, 21]], Joined → True,
  PlotStyle → {Dotted, ColorData["DeepSeaColors"][0.3]}], (*Lc = 0.5 mm*)

ListLogPlot[lcbaseMlg2[[3, 21]], Joined → True,
  PlotStyle → {Dotted, ColorData["DeepSeaColors"][0.5]}], (*Lc = 1 mm*)

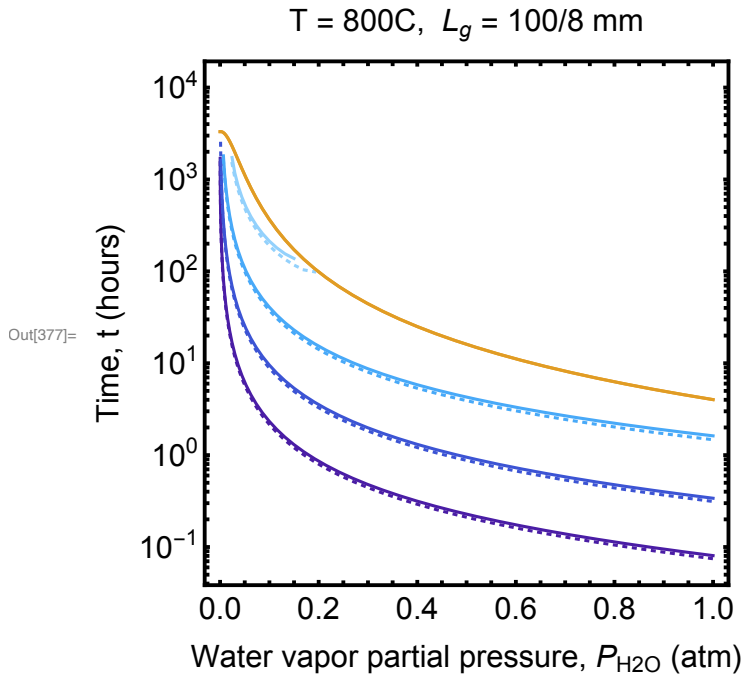
ListLogPlot[lcbaseMl2g2[[3, 21]], Joined → True,
  PlotStyle → {Dotted, ColorData["DeepSeaColors"][0.75]}], (*Lc = 2 mm*)

ListLogPlot[lcbaselg2[[3, 21]], Joined → True,
  PlotStyle → {Dotted, ColorData["DeepSeaColors"][0.9]}], (*Lc = 4 mm*)

ListLogPlot[lcbaselg2[[4, 21]], Joined → True,
  PlotStyle → ColorData[97, "ColorList"][[2]]],

Frame → True, FrameStyle → Directive[Thick, Black], FrameTicks →
  {{LogTicks, StripTickLabels[LogTicks]}, {LinTicks, StripTickLabels[LinTicks]}},
FrameLabel → {{ "Time, t (hours)", ""}, {"Water vapor partial pressure, PH2O (atm)",
  "T = 800C, Lg = 100/8 mm"(*Lc = 0.5/1/2/4 mm, Δ = 0.35 μm*)}},
BaseStyle → {FontFamily → "Arial", FontSize → 16},
PlotRange → {{-0.01, 1.01}, {Log[0.05], Log[10 000]}},
AspectRatio → 1, ImageSize → Medium]

```



```

In[311]:= lcbasev2 = termTimes[0.3, 100., 4., {700., 1000.}, {0., 1.}, {0.5, 0.5}];
lcbaselv2 = termTimes[0.3, 100., 0.5, {700., 1000.}, {0., 1.}, {0.5, 0.5}];
lcbaseMlv2 = termTimes[0.3, 100., 1., {700., 1000.}, {0., 1.}, {0.5, 0.5}];
lcbaseMl2v2 = termTimes[0.3, 100., 2., {700., 1000.}, {0., 1.}, {0.5, 0.5}];

```

```

In[374]:= SetOptions[LogTicks, LogPlot → True, LogPlot → E];
Show[ListLogPlot[lcbaseLv2[[3, 21]], Joined → True,
  PlotStyle → ColorData["DeepSeaColors"][0.3]], (*Lc = 0.5 mm*)

ListLogPlot[lcbaseMlv2[[3, 21]], Joined → True,
  PlotStyle → ColorData["DeepSeaColors"][0.5]], (*Lc = 1 mm*)

ListLogPlot[lcbaseMl2v2[[3, 21]], Joined → True,
  PlotStyle → ColorData["DeepSeaColors"][0.75]], (*Lc = 2 mm*)

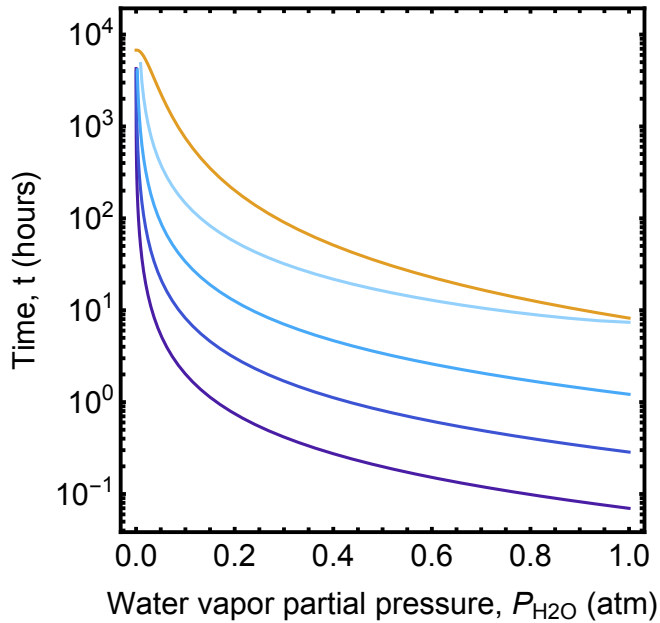
ListLogPlot[lcbasev2[[3, 21]], Joined → True,
  PlotStyle → ColorData["DeepSeaColors"][0.9]], (*Lc = 4 mm*)

ListLogPlot[lcbasev2[[4, 21]], Joined → True,
  PlotStyle → ColorData[97, "ColorList"][[2]]],

Frame → True, FrameStyle → Directive[Thick, Black], FrameTicks →
  {{LogTicks, StripTickLabels[LogTicks]}, {LinTicks, StripTickLabels[LinTicks]}},
FrameLabel → {{ "Time, t (hours)", ""}, {"Water vapor partial pressure, PH2O (atm)",
  "T = 800C, Lg = 100/8 mm"(*Lc = 0.5/1/2/4 mm, Δ = 0.35 μm*)}},
BaseStyle → {FontFamily → "Arial", FontSize → 16},
PlotRange → {{-0.01, 1.01}, {Log[0.05], Log[10 000]}},
AspectRatio → 1, ImageSize → Medium]

```

T = 800C, L_g = 100/8 mm



Out[375]=

```

In[372]:= SetOptions[LogTicks, LogPlot → True, LogPlot → E];

Show[ListLogPlot[lcbasel[[1, 32]], Joined → True,
  PlotStyle → ColorData["DeepSeaColors"][0.3] (*Lc = 0.5 mm*),
ListLogPlot[lcbaseMl[[1, 32]], Joined → True,
  PlotStyle → ColorData["DeepSeaColors"][0.5] (*Lc = 1mm*),
ListLogPlot[lcbaseMl2[[1, 32]], Joined → True,
  PlotStyle → ColorData["DeepSeaColors"][0.75] (*Lc = 2mm*),
ListLogPlot[lcbasel[[1, 32]], Joined → True,
  PlotStyle → ColorData["DeepSeaColors"][0.9] (*Lc = 4mm*),
ListLogPlot[lcbasel[[2, 32]], Joined → True,
  PlotStyle → ColorData[97, "ColorList"][[2]]],

ListLogPlot[lcbaselLg2[[1, 32]], Joined → True,
  PlotStyle → {Dotted, ColorData["DeepSeaColors"][0.3]} (*Lc = 0.5 mm*),
ListLogPlot[lcbaseMlLg2[[1, 32]], Joined → True,
  PlotStyle → {Dotted, ColorData["DeepSeaColors"][0.5]} (*Lc = 1mm*),
ListLogPlot[lcbaseMl2Lg2[[1, 32]], Joined → True,
  PlotStyle → {Dotted, ColorData["DeepSeaColors"][0.75]} (*Lc = 2mm*),
ListLogPlot[lcbaselLg2[[1, 32]], Joined → True,
  PlotStyle → {Dotted, ColorData["DeepSeaColors"][0.9]} (*Lc = 4mm*),
ListLogPlot[lcbaselLg2[[2, 32]], Joined → True,
  PlotStyle → ColorData[97, "ColorList"][[2]]],
PlotRange → {{675, 1025}, {Log[0.5], Log[500]}},
Frame → True, FrameStyle → Directive[Thick, Black], FrameTicks →
  {{LogTicks, StripTickLabels[LogTicks]}, {LinTicks, StripTickLabels[LinTicks]}},
FrameLabel → {{ "Time, t (hours)", ""}, {"Temperature, T (°C)",
  "0.2 atm H2O, Lg = 100/8 mm" (*, Δ = 0.35 μm, Lc = 0.5/1/2/4 mm*)}},
BaseStyle → {FontFamily → "Arial", FontSize → 16}, AspectRatio → 1,
ImageSize → Medium]

```

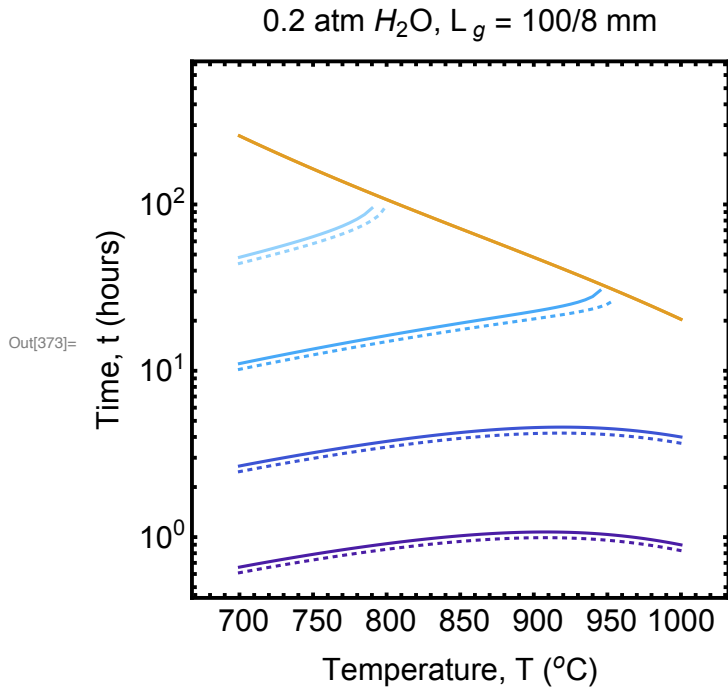


Figure 6.5: Domain map of mechanism controlling terminal strength

Code

```

In[319]:= LcCritG[f_, LgIn_, TcIn_, ppIn_, ΔIn_] :=
Module[{τs, Δ, TcR, Tc, ppR, pp, Ef, Em, Ec, σmo, Lo, mm, R, σfo, mf,
  Lg, Lc, Lr, LrM, LcV, LrLcV, λc, λr, δfs, δms, α, σfs, σms, sTh, tc,
  maxStrain, σfrs, compSII, compSI, compVal, output, tSort, lSort, LcVout},

  TcR = Array[# &, 25, {TcIn}];
  ppR = Flatten[Table[j * 10.^(-i), {i, 4, 1, -1}, {j, 1.25, 10, 0.25}], 1];

  τs = 20.; (*MPa*)
  Δ = ΔIn * 10^-6; (*m*)
  Em = 400.*^3; (*MPa*)
  σmo = 100.; (*MPa*)
  Lo = 1.; (*m*)
  mm = 5.;
  R = 5.0*^-6; (*m*)
  Ef = 400.0*^3; (*MPa*)
  σfo = 1500.; (*MPa*)
  mf = 5.;
  Lg = LgIn * 1*^-3; (*m*)

```



```

δfs = R  $\left(\frac{\sigma_{fo}}{\tau_s}\right)^{\alpha} \left(\frac{mf}{mf+1}\right) \left(\frac{Lo}{R}\right)^{\alpha} \left(\frac{1}{mf+1}\right)$ ;
α = 1/(mf+1);
maxStrain = (α - ProductLog[-α * Exp[α]])^α;
(*Find the Lr/Lc value that gives DII behavior
 (where strength in domain I = strength in domain II). Lr/Lc must
 be less than or equal to 0.5. NSolve doesn't work if you try to
 use mm. This value is independent of environmental conditions*)

LrLcV = NSolve[ $\left(\frac{\delta fs}{Lg * mf * E}\right)^{\alpha} \left(\frac{1}{mf}\right) == \frac{(1 - 2 LrLc)^{\alpha} \left(\frac{1}{mf+1}\right) * maxStrain}{2}$ 
 (1 + Exp[-(maxStrain)^(mf+1)]) && LrLc < 0.51, LrLc, Reals][[1, 1, 2]];
(*If the required recession length (for a given crack spacing)
 is greater than the maximum recession length at closure
 then you'll always get closure for larger crack spacings*)

output = Table[Tc = TcR[[i]];
 pp = ppR[[j]];

 (*Find the maximum recession length for the given conditions.*)
 LrM = Δ * LmaxTime[Tc, pp, Δ, 1];
 (*Solve for the crack spacing
 required to achieve the maximum recession length*)
 LcV = LrM/LrLcV;
 (*Need to check that LrM never exceeds Lg*)
 If[LcV > Lg, LcVout = Lg, LcVout = LcV];

 {Tc, pp, LcVout * 1*^3}, {j, 1, Length[ppR]}, {i, 1, Length[TcR]}
 ];
 Flatten[output, 1]
 ]

```

Code

```

In[320]:= DelCritG[f_, LgIn_, TcIn_, ppIn_, LcIn_] :=
Module[{τs, TcR, Tc, ppR, pp, Ef, Em, Ec, σmo, Lo, mm, R, σfo, mf, Lg, Lc,
 Lr, LrM, LcV, LrLcV, λc, λr, δfs, δms, α, σfs, σms, sTh, tc, maxStrain,
 σfrs, compSII, compSI, compVal, output, tSort, lSort, LcVout},

TcR = Array[# &, 25, {TcIn}];
ppR = Flatten[Table[j * 10.^(-i), {i, 4, 1, -1}, {j, 1.25, 10, 0.25}], 1];

τs = 20.; (*MPa*)

```

```

Em = 400.*^3; (*MPa*)
σmo = 100.; (*MPa*)
Lo = 1.; (*m*)
mm = 5.;
R = 5.0*^-6; (*m*)
Ef = 400.0*^3; (*MPa*)
σfo = 1500.; (*MPa*)
mf = 5.;
Lg = LgIn * 1*^-3; (*m*)
Lc = LcIn * 1*^-3; (*m*)

δfs = R  $\left(\frac{\sigma_{fo}}{\tau_S}\right)^{mf/(mf+1)} \left(\frac{L_o}{R}\right)^{1/(mf+1)}$ ;
α = 1/(mf+1);
maxStrain = (α - ProductLog[-α * Exp[α]])^α;
(*Find the Lr/Lc value that gives DII behavior
 (where strength in domain I = strength in domain II). Lr/Lc must
 be less than or equal to 0.5. NSolve doesn't work if you try to
 use mm. This value is independent of environmental conditions*)

LrLcV = NSolve[ $\left(\frac{\delta fs}{L_g * mf * E}\right)^{1/mf} == \frac{(1 - 2 LrLc)^{1/(mf+1)} * maxStrain}{2}$ 
 (1 + Exp[-(maxStrain)^(mf+1)]) && LrLc < 0.51, LrLc, Reals][[1, 1, 2]];
(*If the required recession length (for a given crack spacing)
 is greater than the maximum recession length at closure
 then you'll always get closure for larger crack spacings*)

output = Table[Tc = TcR[[i]];
 pp = ppR[[j]];
 (*Find the maximum recession length for the given conditions.*)
 del = NSolve[LcV * LrLcV == Δv * LmaxTime[Tc, pp, Δv, 1], Δv, Reals][[1, 1, 2]] ;

 {Tc, pp, del * 1*^6}, {j, 1, Length[ppR]}, {i, 1, Length[TcR]}
];
Flatten[output, 1]
]
DomainMapSfull[f_, LgIn_, LcIn_, TcIn_] :=
Module[{τs, Δ, TcR, Tc, ppR, pp, Ef, Em, Ec, σmo, Lo, mm,
 R, σfo, mf, Lg, Lc, Lr, λc, λr, δfs, δms, α, σfs, σms, sTh, tc,
 maxStrain, σfrs, compSII, compSI, compVal, output, tSort, lSort},
 (*Full pp range*)
 (*TcR = Array[#,144,{TcIn}];
 ppR = Flatten[Table[j*10.^(-i),{i,4,1,-1},{j,1.25,10,0.25}],1];*)

```

```
TcR = Array[# &, 144, {TcIn}];
ppR = Flatten[Table[j * 10.^(-i), {i, 4, 1, -1}, {j, 1.25, 10, 0.25}], 1];
```

```
 $\tau_s = 20.;$  (*MPa*)
 $\Delta = 0.35 \times 10^{-6};$  (*m*)
 $E_m = 400. \times 10^3;$  (*MPa*)
 $\sigma_{m0} = 100.;$  (*MPa*)
 $L_0 = 1.;$  (*m*)
 $mm = 5.;$ 
 $R = 5.0 \times 10^{-6};$  (*m*)
 $E_f = 400.0 \times 10^3;$  (*MPa*)
 $\sigma_{f0} = 1500.;$  (*MPa*)
 $mf = 5.;$ 
 $L_g = L_{gIn} \times 1 \times 10^{-3};$  (*m*)
 $L_c = L_{cIn} \times 1 \times 10^{-3};$  (*m*)
```

```
 $\alpha = 1 / (mf + 1);$ 
 $E_c = f * E_f + (1 - f) * E_m;$ 
```

$$\delta f_s = R \left(\frac{\sigma_{f0}}{\tau_s} \right)^{mf / (mf + 1)} \left(\frac{L_0}{R} \right)^{1 / (mf + 1)};$$

$$\delta m_s = R \left(\frac{\sigma_{m0} (1 - f)}{f * \tau_s} \right)^{mm / (mm + 1)} \left(\frac{L_0}{R} \right)^{1 / (mm + 1)};$$

$$\sigma_{fs} = \sigma_{f0} * \left(\frac{\tau_s * L_0}{\sigma_{f0} * R} \right)^{1 / (mf + 1)};$$

$$\sigma_{ms} = \sigma_{m0} \left(\frac{f * \tau_s * L_0}{(1 - f) \sigma_{m0} * R} \right)^{1 / (mm + 1)};$$

```
maxStrain = ( $\alpha - \text{ProductLog}[-\alpha * \text{Exp}[\alpha]]$ ) $\alpha$ ;
```

$$\text{compSII} = f * \sigma_{fs} * \left(\frac{\delta f_s}{L_g * mf * E} \right)^{1 / mf};$$

(*Find the L_r/L_c value that gives DII behavior
(where strength in domain I = strength in domain II). L_r/L_c must
be less than or equal to 0.5. NSolve doesn't work if you try to
use mm. This value is independent of environmental conditions*)

$$L_r V = \text{NSolve} \left[\left(\frac{\delta f_s}{L_g * mf * E} \right)^{1 / mf} == \frac{(1 - 2 L_r L_c)^{1 / (mf + 1)} * \text{maxStrain}}{2} \right]$$

```

(1 + Exp[-(maxStrain)^(mf + 1)]) && LrLc < 0.51, LrLc, Reals][[1, 1, 2]] * Lc;

output = Table[Tc = TcR[[i]];
  pp = ppR[[j]];
  (* Calculate the closure time in hours for the given conditions *)
  tc = 1.8^2 * Δ^2 / (4 (1.8 - 1)^2 * Bcomb[Tc + 273, pp]) / 3600;

  (*Find the maximum recession length for the given conditions.*)
  LrM = Δ * LmaxTime[Tc, pp, Δ, 1];
  (*If the recession length at closure is longer than the recession
  length to hit DII then the composite will hit Domain II first
  (disk, blue, -1). If the recession length at closure is smaller than
  needed to hit DII then the composite will seal (diamond, orange, 1).*)
  If[LrM > LrV, sOut = compSII,
    σfrs = σfs * (1 - 2 LrM / Lc)^(1 / (mf + 1));
    sOut =  $\frac{f * \sigma_{frs} * \maxStrain}{2} (1 + \text{Exp}[-(\maxStrain)^{(mf + 1)})]$  (*compSI*]);
  {Tc, pp, sOut}, {j, 1, Length[ppR]}, {i, 1, Length[TcR]}
];
Flatten[output, 1]
]

```

Figure Output

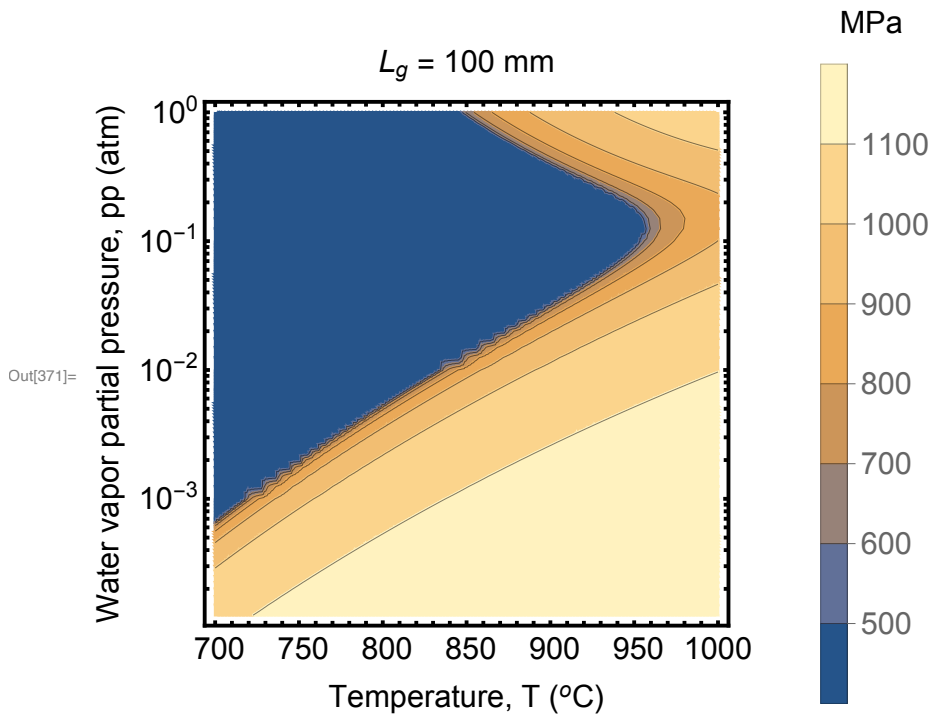
```

In[322]:= crL32 = LcCritG[0.3, 100., {700., 1000.}, {0., 1.}, 0.35];
In[323]:= sLc = DomainMapSfull[0.3, 100., 2., {700., 1000.}];
(*Crack spacing, Lc = 2 mm*)

```

```
In[370]:= SetOptions[LogTicks, LogPlot → True];
```

```
ListContourPlot[sLc, Frame → True,
  FrameStyle → Directive[Thick, Black], FrameTicks →
  {{LogTicks, StripTickLabels[LogTicks]}, {LinTicks, StripTickLabels[LinTicks]}},
  PlotLegends → BarLegend[Automatic, LegendLabel → "MPa"], (*ContourLabels→ All,*),
  (*Contours → 10,*) ScalingFunctions → {None, "Log10"},
  LabelStyle → {FontFamily → "Arial", FontSize → 16},
  FrameLabel → {"Water vapor partial pressure, pp (atm)", ""},
  {"Temperature, T (°C)", "Lg = 100 mm"}},
  BaseStyle → {FontFamily → "Arial", FontSize → 16}, ImageSize → Medium ]
```



```
In[368]:= SetOptions[LogTicks, LogPlot → True];
```

```
ListContourPlot[crL32, Frame → True,
  FrameStyle → Directive[Thick, Black], FrameTicks →
  {{LogTicks, StripTickLabels[LogTicks]}, {LinTicks, StripTickLabels[LinTicks]}},
  PlotLegends → BarLegend[Automatic, LegendLabel → "Lc,crit (mm)",
  ContourLabels → All, (*Contours → 10,*) ScalingFunctions → {None, "Log10"},
  LabelStyle → {FontFamily → "Arial", FontSize → 16},
  FrameLabel → {"Water vapor partial pressure, pp (atm)", ""},
  {"Temperature, T (°C)", "Lg = 100 mm"}},
  BaseStyle → {FontFamily → "Arial", FontSize → 16}, ImageSize → Medium ]
```

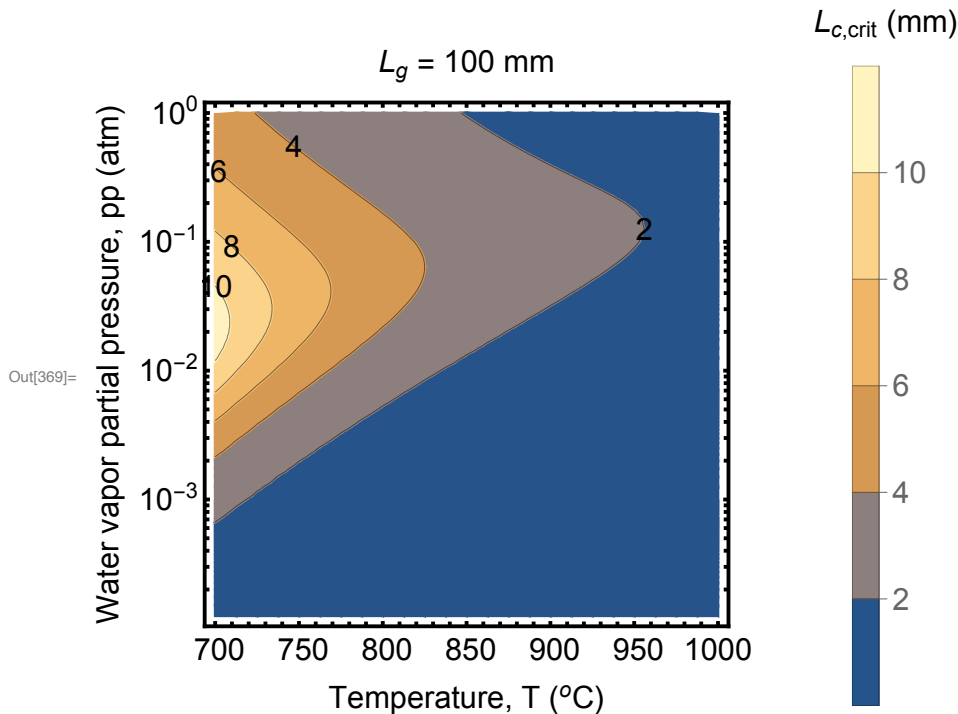


Figure 6.7: Retained strength as a function of environment

Code

```
In[277]:= DomainMapSR2D[f_, LgIn_, LcIn_, TcIn_, ppIn_, ΔIn_] :=
  Module[{τs, Δ, TcR, Tc, ppR, pp, Ef, Em, Ec, σmo, Lo, mm,
    R, σfo, mf, Lg, Lc, Lr, λc, λr, δfs, δms, α, σfs, σms, sTh, tc,
    maxStrain, σfrs, compSII, compSI, compVal, output, ppdata, Tcdata},

  TcR = Table[i, {i, First[TcIn], Last[TcIn], 5}];
  ppR = Array[(1 - Cos[# Pi / 2.]) ^ 2 &, 51, {ppIn}];
```

```

τs = 20.; (*MPa*)
Δ = ΔIn * 10^-6; (*m*)
Em = 400.*^3; (*MPa*)
σmo = 100.; (*MPa*)
Lo = 1.; (*m*)
mm = 5.;
R = 5.0*^-6; (*m*)
Ef = 400.0*^3; (*MPa*)
σfo = 1500.; (*MPa*)
mf = 5.;
Lg = LgIn * 1*^-3; (*m*)
Lc = LcIn * 1*^-3; (*m*)

α = 1 / (mf + 1);
Ec = f * Ef + (1 - f) * Em;

δfs = R (σfo / τs) ^ (mf / (mf + 1)) (Lo / R) ^ (1 / (mf + 1));
δms = R (σmo (1 - f) / (f * τs)) ^ (mm / (mm + 1)) (Lo / R) ^ (1 / (mm + 1));
σfs = σfo * (τs * Lo / (σfo * R)) ^ (1 / (mf + 1));
σms = σmo (f * τs * Lo / ((1 - f) σmo * R)) ^ (1 / (mm + 1));

maxStrain = (α - ProductLog[-α * Exp[α]]) ^ α;

compSII = f * σfs * (δfs / (Lg * mf * E)) ^ (1 / mf);
compSI = (f * σfs * maxStrain / 2) (1 + Exp[-(maxStrain) ^ (mf + 1)]);

(*Find the Lr/Lc value that gives DII behavior
 (where strength in domain I = strength in domain II). Lr/Lc must
 be less than or equal to 0.5. NSolve doesn't work if you try to
 use mm. This value is independent of environmental conditions*)

LrV = NSolve[(δfs / (Lg * mf * E)) ^ (1 / mf) == (1 - 2 LrLc) ^ (1 / (mf + 1)) * maxStrain / 2
 (1 + Exp[-(maxStrain) ^ (mf + 1)]) && LrLc < 0.51, LrLc, Reals][[1, 1, 2]] * Lc;

output = Table[Tc = TcR[[i]];

```

```

pp = ppR[[j]];
(* Calculate the closure time in hours for the given conditions *)
tc = 1.8^2 * Δ^2 / (4 (1.8 - 1)^2 * Bcomb[Tc + 273, pp]) / 3600;

(*Find the maximum recession length for the given conditions.*)
LrM = Δ * LmaxTime[Tc, pp, Δ, 1];
(*If the recession length at closure is longer than the recession
length to hit DII then the composite will hit Domain II first and
the strength is compSII/compSI. If the recession length at closure
is smaller than needed to hit DII then the composite will seal
and the strength will be in DI but reduced from the pristine.*)
If[LrM > LrV, sOut = compSII / compSI,
σfrs = σfs * (1 - 2 LrM / Lc) ^ (1 / (mf + 1));
compSIr =  $\frac{f * \sigma_{frs} * \text{maxStrain}}{2} (1 + \text{Exp}[-(\text{maxStrain})^{(mf + 1)}])$ ;
sOut = compSIr / (compSI)];
{Tc, pp, sOut}, {j, 1, Length[ppR]}, {i, 1, Length[TcR]}
];
Tcdata = Table[{output[[i, j, 1]], output[[i, j, 3]]},
{i, 1, Length[ppR]}, {j, 1, Length[TcR]};

ppdata = Table[{output[[i, j, 2]], output[[i, j, 3]]},
{j, 1, Length[TcR]}, {i, 1, Length[ppR]};
{Tcdata, ppdata}
]

```

Figure

```

In[278]:= st2D = DomainMapSR2D[0.3, 100., 4., {700., 1000.}, {0., 1.}, 0.35];
In[279]:= st2D1 = DomainMapSR2D[0.3, 100., 4., {700., 1000.}, {0., 1.}, 0.1];
st2D3 = DomainMapSR2D[0.3, 100., 4., {700., 1000.}, {0., 1.}, 1.0];

```

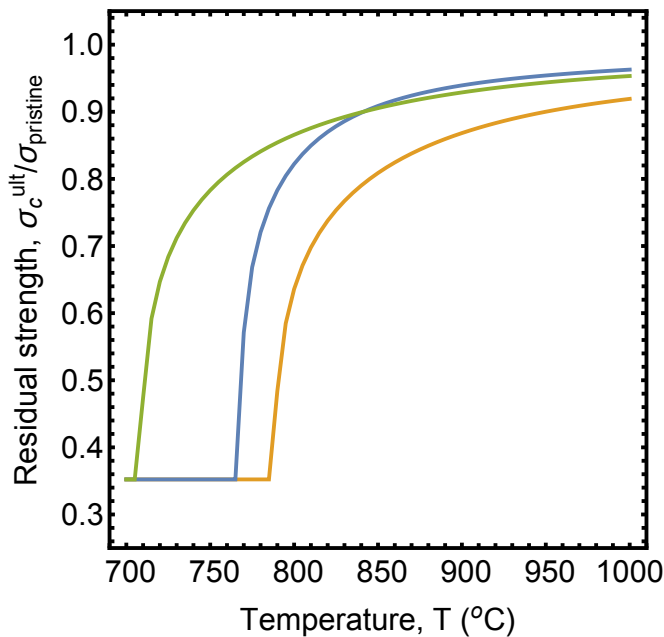


```

In[367]:= (*0.15 atm, 0.01 atm, 1 atm*)
ListPlot[{st2D[[1, 30]], st2D[[1, 16]], st2D[[1, 51]] (*,
  st2D2[[1,30]],st2D2[[1,51]],st2D2[[1,16]]*)}, Joined → True,
PlotStyle → {{Thick, ColorData[97, "ColorList"][[2]]},
  {Thick, ColorData[97, "ColorList"][[1]]},
  {Thick, ColorData[97, "ColorList"][[3]]}, {Dotted,
  ColorData[97, "ColorList"][[2]]}, {Dotted, ColorData[97, "ColorList"][[3]]},
  {Dotted, ColorData[97, "ColorList"][[1]]}, {Dashed,
  ColorData[97, "ColorList"][[2]]}, {Dashed, ColorData[97, "ColorList"][[3]]},
  {Dashed, ColorData[97, "ColorList"][[1]]}},
(*PlotMarkers→{None, Graphics[{EdgeForm[ColorData[97,"ColorList"][[3]]],
  PolygonMarker["Disk",Offset[5]]},AlignmentPoint→{0,0}],
None, Graphics[{EdgeForm[ColorData[97,"ColorList"][[2]]],
  PolygonMarker["Disk",Offset[5]]},AlignmentPoint→{0,0}],
None, Graphics[{EdgeForm[ColorData[97,"ColorList"][[1]]],
  PolygonMarker["Disk",Offset[5]]},AlignmentPoint→{0,0}]}},*)
Frame → True, FrameStyle → Directive[Thick, Black], FrameTicks →
  {{LinTicks, StripTickLabels[LinTicks]}, {LinTicks, StripTickLabels[LinTicks]}},
FrameLabel → {{ "Residual strength,  $\sigma_c^{ult}/\sigma_{pristine}$ ", ""},
  {"Temperature, T (°C)", "Lg = 100 mm, Lc = 4 mm, Δo= 0.35 μm"}},
BaseStyle → {FontFamily → "Arial", FontSize → 16},
PlotRange → {{690, 1010}, {0.25, 1.05}}, AspectRatio → 1, ImageSize → Medium]

```

$L_g = 100 \text{ mm}, L_c = 4 \text{ mm}, \Delta_o = 0.35 \mu\text{m}$



Out[367]=

```

In[365]:= SetOptions[LogTicks, LogPlot → True, LogPlot → E];
Show[ListLogPlot[lcbase[[1, 51]], Joined → True,
  PlotStyle → {{Thick, ColorData[97, "ColorList"][[3]]}}, (*Lc = 4 mm*)
ListLogPlot[lcbase[[2, 51]], Joined → True,
  PlotStyle → ColorData[97, "ColorList"][[3]]],

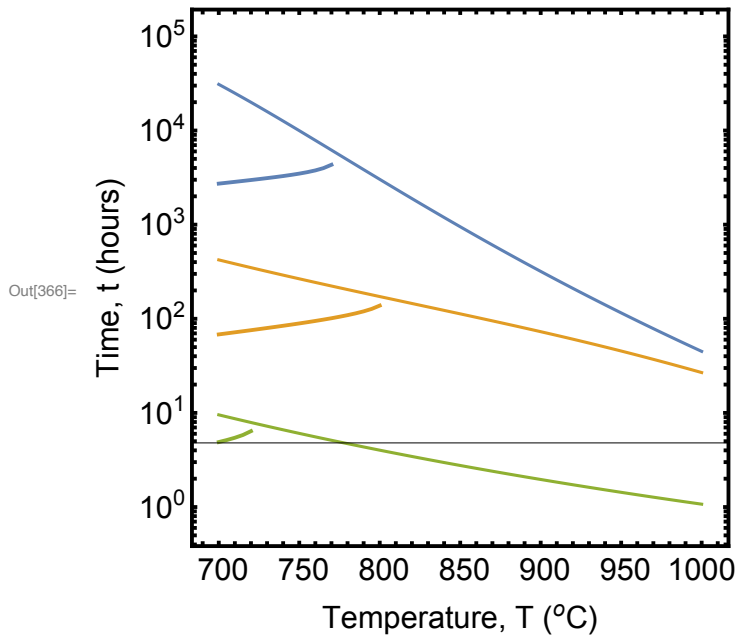
ListLogPlot[lcbase[[1, 30]], Joined → True,
  PlotStyle → {{Thick, ColorData[97, "ColorList"][[2]]}}, (*Lc = 4 mm*)
ListLogPlot[lcbase[[2, 30]], Joined → True,
  PlotStyle → ColorData[97, "ColorList"][[2]]],

ListLogPlot[lcbase[[1, 16]], Joined → True,
  PlotStyle → {{Thick, ColorData[97, "ColorList"][[1]]}}, (*Lc = 4 mm*)
ListLogPlot[lcbase[[2, 16]], Joined → True,
  PlotStyle → ColorData[97, "ColorList"][[1]]],

PlotRange → {{690, 1010}, {Log[0.5], Log[1*^5]}},
Frame → True, FrameStyle → Directive[Thick, Black], FrameTicks →
  {{LogTicks, StripTickLabels[LogTicks]}, {LinTicks, StripTickLabels[LinTicks]}},
FrameLabel → {{ "Time, t (hours)", ""}, {"Temperature, T (°C)",
  "0.2 atm H2O, Lg = 100/8 mm"(*, Δ = 0.35 μm, Lc = 0.5/1/2/4 mm*)}},
BaseStyle → {FontFamily → "Arial", FontSize → 16}, AspectRatio → 1,
ImageSize → Medium]

```

0.2 atm H_2O , $L_g = 100/8$ mm

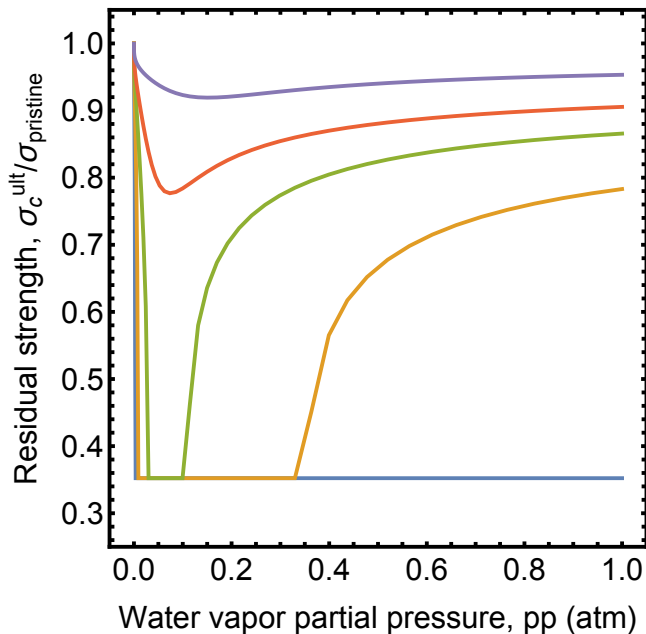


```

In[364]:= (*700, 750, 800, 850, 1000C*)
ListPlot[{st2D[[2, 1]], st2D[[2, 11]],
  st2D[[2, 21]], st2D[[2, 31]], st2D[[2, 61]]}, Joined → True,
PlotStyle → {{Thick, ColorData[97, "ColorList"][[1]]},
  {Thick, ColorData[97, "ColorList"][[2]]},
  {Thick, ColorData[97, "ColorList"][[3]]}, {Thick,
  ColorData[97, "ColorList"][[4]]}, {Thick, ColorData[97, "ColorList"][[5]]}},
(*PlotMarkers→{None, Graphics[{EdgeForm[ColorData[97,"ColorList"][[3]]],
  PolygonMarker["Disk",Offset[5]]},AlignmentPoint→{0,0}],
  None, Graphics[{EdgeForm[ColorData[97,"ColorList"][[2]]],
  PolygonMarker["Disk",Offset[5]]},AlignmentPoint→{0,0}],
  None, Graphics[{EdgeForm[ColorData[97,"ColorList"][[1]]],
  PolygonMarker["Disk",Offset[5]]},AlignmentPoint→{0,0}}],*)
Frame → True, FrameStyle → Directive[Thick, Black], FrameTicks →
  {{LinTicks, StripTickLabels[LinTicks]}, {LinTicks, StripTickLabels[LinTicks]}},
FrameLabel → {{ "Residual strength,  $\sigma_c^{ult}/\sigma_{pristine}$ ", ""},
  {"Water vapor partial pressure, pp (atm)",
  "Lg = 100 mm, Lc = 4 mm, Δ = 0.35 μm"}},
BaseStyle → {FontFamily → "Arial", FontSize → 16},
PlotRange → {{-.05, 1.05}, {0.25, 1.05}},
AspectRatio → 1, ImageSize → Medium]

```

$L_g = 100 \text{ mm}, L_c = 4 \text{ mm}, \Delta = 0.35 \text{ } \mu\text{m}$



Out[364]=

```

In[362]:= SetOptions[LogTicks, LogPlot → True, LogPlot → E];
Show[ListLogPlot[lcbase[[3, 1]], Joined → True,
  PlotStyle → {{Thick, ColorData[97, "ColorList"][[1]]}}, (*Lc = 4 mm*)
ListLogPlot[lcbase[[4, 1]], Joined → True,
  PlotStyle → ColorData[97, "ColorList"][[1]]],

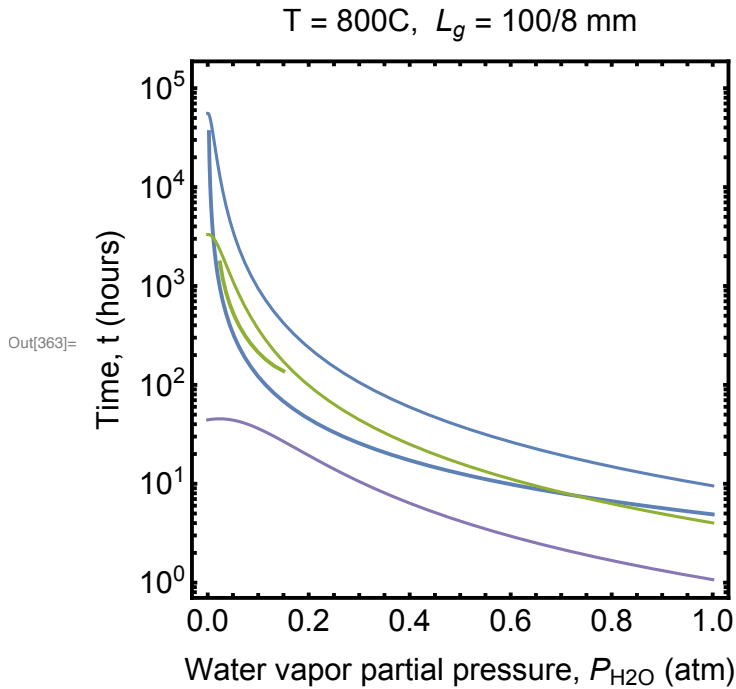
(*ListLogPlot[lcbase[[3,11]],Joined→True,
  PlotStyle→{{Thick,ColorData[97,"ColorList"][[2]]}},(*Lc = 4 mm*)
ListLogPlot[lcbase[[4,11]],Joined→True,
  PlotStyle→ColorData[97,"ColorList"][[2]]],
*)
ListLogPlot[lcbase[[3, 21]], Joined → True,
  PlotStyle → {{Thick, ColorData[97, "ColorList"][[3]]}}, (*Lc = 4 mm*)
ListLogPlot[lcbase[[4, 21]], Joined → True,
  PlotStyle → ColorData[97, "ColorList"][[3]]],

(*ListLogPlot[lcbase[[3,31]],Joined→True,
  PlotStyle→{{Thick,ColorData[97,"ColorList"][[4]]}},(*Lc = 4 mm*)
ListLogPlot[lcbase[[4,31]],Joined→True,
  PlotStyle→ColorData[97,"ColorList"][[4]]],*)

ListLogPlot[lcbase[[3, 61]], Joined → True,
  PlotStyle → {{Thick, ColorData[97, "ColorList"][[5]]}}, (*Lc = 4 mm*)
ListLogPlot[lcbase[[4, 61]], Joined → True,
  PlotStyle → ColorData[97, "ColorList"][[5]]],

Frame → True, FrameStyle → Directive[Thick, Black], FrameTicks →
  {{LogTicks, StripTickLabels[LogTicks]}, {LinTicks, StripTickLabels[LinTicks]}},
FrameLabel → {{ "Time, t (hours)", ""}, {"Water vapor partial pressure, PH2O (atm)",
  "T = 800C, Lg = 100/8 mm"(*Lc = 0.5/1/2/4 mm, Δ= 0.35 μm*)}},
BaseStyle → {FontFamily → "Arial", FontSize → 16},
PlotRange → {{-0.01, 1.01}, {Log[0.9], Log[1*^5]}},
AspectRatio → 1, ImageSize → Medium]

```



Code

```

In[233]:= impLc[f_, LgIn_, LcIn_, TcIn_, ppIn_, ΔIn_] :=
Module[{τs, Δ, TcR, Tc, ppR, pp, Ef, Em, Ec, σmo, Lo, mm,
  R, σfo, mf, Lg, Lc, Lr, λc, λr, δfs, δms, α, σfs, σms, sTh, tc,
  maxStrain, σfrs, compSII, compSI, compVal, output, ppdata, Tcdata},

  Tc = TcIn;
  pp = ppIn;

  τs = 20.; (*MPa*)
  Δ = ΔIn * 10^-6; (*m*)
  Em = 400.*^3; (*MPa*)
  σmo = 100.; (*MPa*)
  Lo = 1.; (*m*)
  mm = 5.;
  R = 5.0*^-6; (*m*)
  Ef = 400.0*^3; (*MPa*)
  σfo = 1500.; (*MPa*)
  mf = 5.;
  Lg = LgIn * 1*^-3; (*m*)

  LcR = Array[# &, 200, {LcIn}] * 1*^-3; (*m*)

  α = 1 / (mf + 1);

```

$$E_c = f * E_f + (1 - f) * E_m;$$

$$\delta f_s = R \left(\frac{\sigma_{fo}}{\tau_s} \right)^{mf / (mf + 1)} \left(\frac{L_o}{R} \right)^{1 / (mf + 1)};$$

$$\delta m_s = R \left(\frac{\sigma_{mo} (1 - f)}{f * \tau_s} \right)^{mm / (mm + 1)} \left(\frac{L_o}{R} \right)^{1 / (mm + 1)};$$

$$\sigma_{fs} = \sigma_{fo} * \left(\frac{\tau_s * L_o}{\sigma_{fo} * R} \right)^{1 / (mf + 1)};$$

$$\sigma_{ms} = \sigma_{mo} \left(\frac{f * \tau_s * L_o}{(1 - f) \sigma_{mo} * R} \right)^{1 / (mm + 1)};$$

$$\text{maxStrain} = (\alpha - \text{ProductLog}[-\alpha * \text{Exp}[\alpha]])^\alpha;$$

$$\text{compSII} = f * \sigma_{fs} * \left(\frac{\delta f_s}{L_g * mf * E} \right)^{1 / mf};$$

$$\text{compSI} = \frac{f * \sigma_{fs} * \text{maxStrain}}{2} (1 + \text{Exp}[-(\text{maxStrain})^{mf + 1}]);$$

(* Calculate the closure time in hours for the given conditions *)

$$t_c = 1.8^{\Delta^2} * \Delta^2 / (4 (1.8 - 1)^{\Delta^2} * \text{Bcomb}[T_c + 273, pp]) / 3600;$$

(*Find the Lr/Lc value that gives DII behavior

(where strength in domain I = strength in domain II). Lr/Lc must be less than or equal to 0.5. NSolve doesn't work if you try to use mm. This value is independent of environmental conditions*)

$$\text{LrVnorm} = \text{NSolve}\left[\left(\frac{\delta f_s}{L_g * mf * E}\right)^{1 / mf} == \frac{(1 - 2 \text{LrLc})^{1 / (mf + 1)} * \text{maxStrain}}{2}\right.$$

$$\left. (1 + \text{Exp}[-(\text{maxStrain})^{mf + 1}]) \&\& \text{LrLc} < 0.51, \text{LrLc}, \text{Reals}\right][[1, 1, 2]];$$

(*Find the maximum recession length for the given conditions.*)

$$\text{LrM} = \Delta * \text{LmaxTime}[T_c, pp, \Delta, 1];$$

Table[Lc = LcR[[i]]];

$$\text{LrV} = \text{LrVnorm} * \text{Lc};$$

If[LrM > LrV, sOut = compSII / (compSI),

$$\sigma_{frs} = \sigma_{fs} * (1 - 2 \text{LrM} / \text{Lc})^{1 / (mf + 1)};$$

$$\text{compSIr} = \frac{f * \sigma_{frs} * \text{maxStrain}}{2} (1 + \text{Exp}[-(\text{maxStrain})^{mf + 1}]);$$

$$\text{sOut} = \text{compSIr} / (\text{compSI});$$

{Lc * 1*^3, sOut}, {i, 1, Length[LcR]}

]

In[232]:= termTlc[f_, LgIn_, LcIn_, TcR_, ppR_, ΔIn_] :=

(*Inputs (in order): f, gauge length in um, crack spacing in um,

```

{lower temperature bound, upper temperature bound} (in Celsius),
{lower water vapor bound, upper water vapor bound} (in atm),
{lower BN thickness bound, upper BN thickness bound} (in um)*

(*Outputs (in order): Temperature, water vapor, BN thickness,
time to seal the gap (in hours), time to remove all coating (in hours)*)

Module[{ T, Tc, Δ, pp, Ef, Em, Ec, σmo, Lo, mm, R, σfo, mf, Lg, LcR, τs, Lr,
  LrR, λc, λr, δfs, δms, α, σfs, σms, sTh, tc, maxStrain, σfrs, compSII,
  compSI, compVal, toutput, compoutput, trans, TStep, ppStep, wStep, Δv,
  ΔR, LrM, envOutput, tauM1, tauM, tauR, LrV, term, tSeal, tRem, tauDII},

  Lg = LgIn * 1*^-3; (*m*)
  LcR = LcR = Array[# &, 200, {LcIn}] * 1*^-3; (*m*)
  Δv = ΔIn * 1*^-6; (*m*)

  (*Create the temperature, water vapor, and coating thickness arrays*)
  TStep = Length[TcR];
  ppStep = Length[ppR];

  ΔR = Array[# &, 1, {Δv}];
  wStep = Length[ΔR];

  τs = 20 ; (*MPa*)
  Em = 400.*^3; (*MPa*)
  σmo = 100.; (*MPa*)
  Lo = 1. ; (*m*)
  mm = 5.;
  R = 5.0*^-6; (*m*)
  Ef = 400.0*^3; (*MPa*)
  σfo = 1500.; (*MPa*)
  mf = 5.;

  α = 1 / (mf + 1);
  Ec = f * Ef + (1 - f) * Em;

  δfs = R  $\left(\frac{\sigma_{fo}}{\tau_s}\right)^{\wedge} (mf / (mf + 1)) \left(\frac{Lo}{R}\right)^{\wedge} (1 / (mf + 1));$ 
  δms = R  $\left(\frac{\sigma_{mo} (1 - f)}{f * \tau_s}\right)^{\wedge} (mm / (mm + 1)) \left(\frac{Lo}{R}\right)^{\wedge} (1 / (mm + 1));$ 

```

$$\sigma_{fs} = \sigma_{fo} * \left(\frac{\tau_s * L_o}{\sigma_{fo} * R} \right)^{1 / (mf + 1)};$$

$$\sigma_{ms} = \sigma_{mo} \left(\frac{f * \tau_s * L_o}{(1 - f) \sigma_{mo} * R} \right)^{1 / (mm + 1)};$$

$$\text{maxStrain} = (\alpha - \text{ProductLog}[-\alpha * \text{Exp}[\alpha]])^{\alpha};$$

$$\text{compSII} = f * \sigma_{fs} * \left(\frac{\delta_{fs} / L_g}{mf * E} \right)^{1 / mf};$$

(*Find the Lr/Lc value that gives DII behavior
(where strength in domain I = strength in domain II). Lr/Lc must
be less than or equal to 0.5. NSolve doesn't work if you try to
use mm. This value is independent of environmental conditions*)

```
envOutput = Table[
  Tc = TcR[[i]];
  pp = ppR[[j]];
  Δ = ΔR[[k]];

  tc = 1.8^2 * Δ^2 / (4 (1.8 - 1)^2 * Bcomb[Tc + 273, pp]) / 3600;
  LrM = Δ * LmaxTime[Tc, pp, Δ, 1];

  Table[LrV = NSolve[ $\left( \frac{\delta_{fs}}{L_g * mf * E} \right)^{1 / mf} ==$ 
     $\frac{(1 - 2 LrLc)^{1 / (mf + 1)} * \text{maxStrain}}{2}$  (1 + Exp[-(maxStrain)^(mf + 1)]) &&
    LrLc < 0.51, LrLc, Reals][[1, 1, 2]] * LcR[[q]];
  (*If the maximum recession length is larger than the value required
  to reach DII, then compute the time required to reach the DII
  recession value. Otherwise, the recession channel closes first.*)
  If[LrM > LrV, tII = NSolve[LrV == Δ * LmaxTime[Tc, pp, Δ, tau] && tau < 1.1,
    tau, Reals, 3][[1, 1, 2]] * tc, tII = Null];
  {Tc, pp, Δ, LcR[[q]] * 1^3, tc, tII}
  , {q, 1, Length[LcR]}]
  , {i, 1, Length[TcR]}, {j, 1, Length[ppR]}, {k, 1, Length[ΔR]}];

(*For indexing, the output is: *)
(*envOutput[[T,p,w, Lc, time to seal the gap, time to remove all coating]]*)
```



```

TdatSeal = Flatten[Table[{envOutput[[i, j, k, q, 4]], envOutput[[i, j, k, q, 5]]},
  {j, 1, ppStep}, {k, 1, wStep}, {i, 1, TStep}, {q, 1, Length[LcR]}], 1];
TdatRem = Flatten[Table[{envOutput[[i, j, k, q, 4]], envOutput[[i, j, k, q, 6]]},
  {j, 1, ppStep}, {k, 1, wStep}, {i, 1, TStep}, {q, 1, Length[LcR]}], 1];

ppdatSeal = Flatten[Table[{envOutput[[i, j, k, q, 4]], envOutput[[i, j, k, q, 5]]},
  {i, 1, TStep}, {k, 1, wStep}, {j, 1, ppStep}, {q, 1, Length[LcR]}], 1];
ppdatRem = Flatten[Table[{envOutput[[i, j, k, q, 4]], envOutput[[i, j, k, q, 6]]},
  {i, 1, TStep}, {k, 1, wStep}, {j, 1, ppStep}, {q, 1, Length[LcR]}], 1];

{TdatRem, TdatSeal, ppdatRem, ppdatSeal, envOutput}

]

```

```

In[231]:= impDel[f_, LgIn_, LcIn_, TcIn_, ppIn_, ΔIn_] :=
Module[{τs, Δ, ΔR, TcR, Tc, ppR, pp, Ef, Em, Ec, σmo, Lo, mm,
  R, σfo, mf, Lg, Lc, Lr, λc, λr, δfs, δms, α, σfs, σms, sTh, tc,
  maxStrain, σfrs, compSII, compSI, compVal, output, ppdata, Tcdata},

```

```
Tc = TcIn;
```

```
pp = ppIn;
```

```
τs = 20.; (*MPa*)
```

```
ΔR = Array[# &, 100, {ΔIn}] * 10^-6; (**)
```

```
Em = 400.*^3; (*MPa*)
```

```
σmo = 100.; (*MPa*)
```

```
Lo = 1.; (**)
```

```
mm = 5.;
```

```
R = 5.0*^-6; (**)
```

```
Ef = 400.0*^3; (*MPa*)
```

```
σfo = 1500.; (*MPa*)
```

```
mf = 5.;
```

```
Lg = LgIn * 1*^-3; (**)
```

```
Lc = LcIn * 1*^-3; (**)
```

```
α = 1 / (mf + 1);
```

```
Ec = f * Ef + (1 - f) * Em;
```

$$\delta fs = R \left(\frac{\sigma fo}{\tau s} \right)^{\alpha} (mf / (mf + 1)) \left(\frac{Lo}{R} \right)^{\alpha} (1 / (mf + 1));$$

$$\delta ms = R \left(\frac{\sigma mo (1 - f)}{f * \tau s} \right)^{\alpha} (mm / (mm + 1)) \left(\frac{Lo}{R} \right)^{\alpha} (1 / (mm + 1));$$

```

σfs = σfo * ( (τs * Lo) / (σfo * R) ) ^ (1 / (mf + 1));
σms = σmo * ( (f * τs * Lo) / ((1 - f) σmo * R) ) ^ (1 / (mm + 1));

maxStrain = (α - ProductLog[-α * Exp[α]]) ^ α;

compSII = f * σfs * ( (δfs) / (Lg * mf * E) ) ^ (1 / mf);
compSI = (f * σfs * maxStrain) / 2 * (1 + Exp[-(maxStrain) ^ (mf + 1)]);

(*Find the Lr/Lc value that gives DII behavior
 (where strength in domain I = strength in domain II). Lr/Lc must
 be less than or equal to 0.5. NSolve doesn't work if you try to
 use mm. This value is independent of environmental conditions*)
LrVnorm = NSolve[ ( (δfs) / (Lg * mf * E) ) ^ (1 / mf) == (1 - 2 LrLc) ^ (1 / (mf + 1)) * maxStrain / 2
 (1 + Exp[-(maxStrain) ^ (mf + 1)]) && LrLc < 0.51, LrLc, Reals][[1, 1, 2]];

LrV = LrVnorm * Lc; (*m*)

Table[Δ = ΔR[[i]];

 (*Find the maximum recession length for the given conditions.*)
LrM = Δ * LmaxTime[Tc, pp, Δ, 1];
If[LrM > LrV, sOut = compSII / (compSI),
 σfrs = σfs * (1 - 2 LrM / Lc) ^ (1 / (mf + 1));
 compSIr = (f * σfrs * maxStrain) / 2 * (1 + Exp[-(maxStrain) ^ (mf + 1)]);
 sOut = compSIr / (compSI)];

 {Δ * 1*^6, sOut}, {i, 1, Length[ΔR]}
]
]

In[230]:= termTdel[f_, LgIn_, LcIn_, TcR_, ppR_, ΔIn_] :=
 (*Inputs (in order): f, gauge length in um, crack spacing in um,
 {lower temperature bound, upper temperature bound} (in Celsius),
 {lower water vapor bound, upper water vapor bound}(in atm),
 {lower BN thickness bound, upper BN thickness bound}(in um)*)

```

(*Outputs (in order): Temperature, water vapor, BN thickness,
time to seal the gap (in hours), time to remove all coating (in hours)*)

```
Module[{ T, Tc, Δ, pp, Ef, Em, Ec, σmo, Lo, mm, R, σfo, mf, Lg, Lc, τs, Lr,
  LrR, λc, λr, δfs, δms, α, σfs, σms, sTh, tc, maxStrain, σfrs, compSII,
  compSI, compVal, toutput, compoutput, trans, TStep, ppStep, wStep, Δv,
  ΔR, LrM, envOutput, tauM1, tauM, tauR, LrV, term, tSeal, tRem, tauDII},
```

```
Lg = LgIn * 1*^-3; (*m*)
```

```
Lc = LcIn * 1*^-3; (*m*)
```

(*Create the temperature, water vapor, and coating thickness arrays*)

```
TStep = Length[TcR];
```

```
ppStep = Length[ppR];
```

```
ΔR = Array[# &, 100, {ΔIn}] * 10^-6; (*m*)
```

```
wStep = Length[ΔR];
```

```
τs = 20; (*MPa*)
```

```
Em = 400.*^3; (*MPa*)
```

```
σmo = 100.; (*MPa*)
```

```
Lo = 1.; (*m*)
```

```
mm = 5.;
```

```
R = 5.0*^-6; (*m*)
```

```
Ef = 400.0*^3; (*MPa*)
```

```
σfo = 1500.; (*MPa*)
```

```
mf = 5.;
```

```
α = 1 / (mf + 1);
```

```
Ec = f * Ef + (1 - f) * Em;
```

$$\delta fs = R \left(\frac{\sigma fo}{\tau s} \right)^{\alpha} \left(\frac{mf}{mf + 1} \right) \left(\frac{Lo}{R} \right)^{\alpha} \left(\frac{1}{mf + 1} \right);$$

$$\delta ms = R \left(\frac{\sigma mo (1 - f)}{f * \tau s} \right)^{\alpha} \left(\frac{mm}{mm + 1} \right) \left(\frac{Lo}{R} \right)^{\alpha} \left(\frac{1}{mm + 1} \right);$$

$$\sigma fs = \sigma fo * \left(\frac{\tau s * Lo}{\sigma fo * R} \right)^{\alpha} \left(\frac{1}{mf + 1} \right);$$

$$\sigma ms = \sigma mo \left(\frac{f * \tau s * Lo}{(1 - f) \sigma mo * R} \right)^{\alpha} \left(\frac{1}{mm + 1} \right);$$

```
maxStrain = ( $\alpha$  - ProductLog[- $\alpha$  * Exp[ $\alpha$ ]]) ^  $\alpha$ ;
```

```
compSII = f *  $\sigma$ fs *  $\left(\frac{\delta fs / Lg}{mf * E}\right)^{1/mf}$ ;
```

```
(*Find the Lr/Lc value that gives DII behavior
 (where strength in domain I = strength in domain II). Lr/Lc must
 be less than or equal to 0.5. NSolve doesn't work if you try to
 use mm. This value is independent of environmental conditions*)
```

```
envOutput = Table[
  Tc = TcR[[i]];
  pp = ppR[[j]];
   $\Delta$  =  $\Delta$ R[[k]];

  tc = 1.8^2 *  $\Delta$ ^2 / (4 (1.8 - 1)^2 * Bcomb[Tc + 273, pp]) / 3600;
  LrM =  $\Delta$  * LmaxTime[Tc, pp,  $\Delta$ , 1];

  LrV = NSolve[ $\left(\frac{\delta fs}{Lg * mf * E}\right)^{1/mf} == \frac{(1 - 2 LrLc)^{1/(mf + 1)} * maxStrain}{2} (1 +$ 
    Exp[-(maxStrain)^(mf + 1)]) && LrLc < 0.51, LrLc, Reals][[1, 1, 2]] * Lc;
  (*If the maximum recession length is larger than the value required
   to reach DII, then compute the time required to reach the DII
   recession value. Otherwise, the recession channel closes first.*)
  If[LrM > LrV, tII = NSolve[LrV ==  $\Delta$  * LmaxTime[Tc, pp,  $\Delta$ , tau] && tau < 1.1,
    tau, Reals, 3][[1, 1, 2]] * tc, tII = Null];
  {Tc, pp,  $\Delta$ , tc, tII}

, {i, 1, Length[TcR]}, {j, 1, Length[ppR]}, {k, 1, Length[ $\Delta$ R]}];
```

```
(*For indexing, the output is: *)
(*envOutput[[T,p,w, time to seal the gap, time to remove all coating]]*)
```

```
tcSort = Table[{envOutput[[i, j, k, 3]], envOutput[[i, j, k, 4]]},
  {i, 1, TStep}, {j, 1, ppStep}, {k, 1, wStep}];
t2Sort = Table[{envOutput[[i, j, k, 3]], envOutput[[i, j, k, 5]]},
  {i, 1, TStep}, {j, 1, ppStep}, {k, 1, wStep}];
```

```
(*TdatRem = Table[{envOutput[[i,j,k,3]],envOutput[[i,j,k,5]]},
```

```

    {j,1,ppStep},{i, 1,TStep},{k,1,wStep}}];

ppdatSeal =Table[{envOutput[[i,j,k,3]],envOutput[[i,j,k,4]]},
  {i, 1,TStep},{j,1,ppStep},{k,1,wStep}];
ppdatRem = Table[{envOutput[[i,j,k,3]],envOutput[[i,j,k,5]]},
  {i, 1,TStep},{j,1,ppStep},{k,1,wStep}];*)

{tcSort, t2Sort, envOutput}

]

```

Figure

```

In[234]:= Lc701 = impLc[0.3, 100., {1., 100}, 700., 0.1, 0.35];
Lc701b = impLc[0.3, 200., {1., 100}, 700., 0.1, 0.35];
Lc710 = impLc[0.3, 100., {1., 100}, 700., 1.0, 0.35];
Lc77501 = impLc[0.3, 100., {1., 100}, 775., 0.1, 0.35];
Lc77510 = impLc[0.3, 100., {1., 100}, 775., 1.0, 0.35];
Lc8501 = impLc[0.3, 100., {1., 100}, 850., 0.1, 0.35];
Lc8510 = impLc[0.3, 100., {1., 100}, 850., 1.0, 0.35];
Lc1001 = impLc[0.3, 100., {1., 100}, 1000., 0.1, 0.35];
Lc1010 = impLc[0.3, 100., {1., 100}, 1000., 1.0, 0.35];

In[243]:= Lc801 = impLc[0.3, 100., {1., 100}, 800., 0.1, 0.35];
Lc801b = impLc[0.3, 200., {1., 100}, 800., 0.1, 0.35];
Lc802 = impLc[0.3, 100., {1., 100}, 800., 0.2, 0.35];
Lc805 = impLc[0.3, 100., {1., 100}, 800., 0.5, 0.35];
Lc810 = impLc[0.3, 100., {1., 100}, 800., 1.0, 0.35];

In[248]:= Lc8011 = impDel[0.3, 100., 4., 800., 0.1, {0.1, 1.0}];
Lc801b1 = impDel[0.3, 200., 4., 800., 0.1, {0.1, 1.0}];
Lc8021 = impDel[0.3, 100., 4., 800., 0.2, {0.1, 1.0}];
Lc8051 = impDel[0.3, 100., 4., 800., 0.5, {0.1, 1.0}];
Lc8101 = impDel[0.3, 100., 4., 800., 1.0, {0.1, 1.0}];

In[253]:= Lc7011 = impDel[0.3, 100., 4., 700., 0.1, {0.1, 1.0}];
Lc701b1 = impDel[0.3, 200., 4., 700., 0.1, {0.1, 1.0}];
Lc775011 = impDel[0.3, 100., 4., 775., 0.1, {0.1, 1.0}];
Lc85011 = impDel[0.3, 100., 4., 850., 0.1, {0.1, 1.0}];
Lc10011 = impDel[0.3, 100., 4., 1000., 0.1, {0.1, 1.0}];

In[258]:= Clear[tau]
timeValLc = termTlc[0.3, 100., {1., 100.},
  {700., 775., 800., 850., 1000.}, {0.1, 0.2, 0.5, 1.0}, {0.35, 0.35}];

```

```
In[260]:= timeValDel = termTdel[0.3, 100., 4.,  
    {700., 775., 800., 850., 1000.}, {0.1, 0.2, 0.5, 1.0}, {0.1, 1.0}];
```

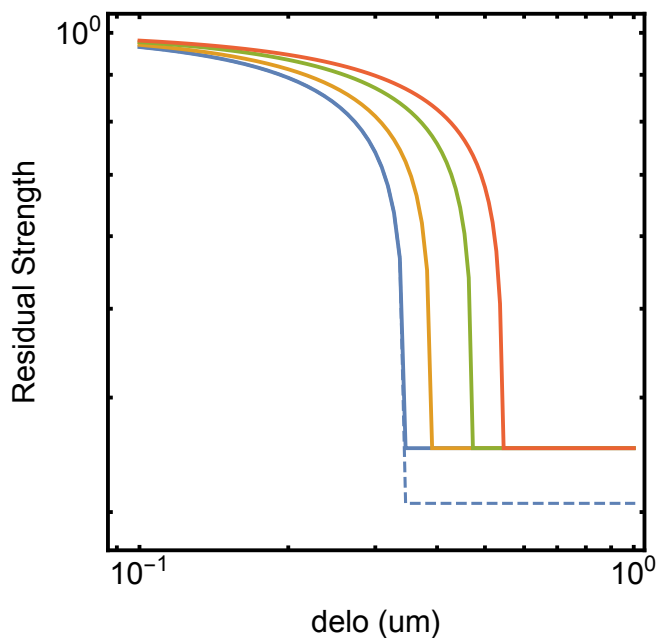
Figure 6.8, 6.9: Retained strength, terminal time as a function of crack spacing (6.8) and initial BN coating thickness (6.9)

```

In[360]:= SetOptions[LogTicks, LogPlot -> True];
ListLogLogPlot[{Lc8011, Lc801b1, Lc8021, Lc8051, Lc8101}, Joined -> True,
  PlotStyle -> {{Thick, ColorData[97, "ColorList"][[1]]},
    {Dashed, ColorData[97, "ColorList"][[1]]},
    {Thick, ColorData[97, "ColorList"][[2]]}, {Thick,
      ColorData[97, "ColorList"][[3]]}, {Thick, ColorData[97, "ColorList"][[4]]},
    {Thick, ColorData[97, "ColorList"][[5]]}},
  (*PlotMarkers->{ Graphics[{EdgeForm[ColorData[97,"ColorList"][[1]]],
    PolygonMarker["Disk",Offset[5]]},AlignmentPoint->{0,0}],
    Graphics[{EdgeForm[ColorData[97,"ColorList"][[2]]],
      PolygonMarker["Disk",Offset[5]]},AlignmentPoint->{0,0}], Graphics[
      {EdgeForm[ColorData[97,"ColorList"][[3]]},PolygonMarker["Disk",Offset[5]]},
      AlignmentPoint->{0,0}],Graphics[{EdgeForm[ColorData[97,"ColorList"][[4]]],
        PolygonMarker["Disk",Offset[5]]},AlignmentPoint->{0,0}}},*)
  Frame -> True, FrameStyle -> Directive[Thick, Black],
  FrameTicks -> {{LogTicks, StripTickLabels[LogTicks]},
    {LogTicks, StripTickLabels[LogTicks]}}, FrameLabel ->
    {"Residual Strength", ""}, {"delo (um)", "Lg = 100 mm, 800C, Lc = 4 mm"}},
  BaseStyle -> {FontFamily -> "Arial", FontSize -> 16}, PlotRange -> All,
  (*PlotRange->{{-2,202},{-0.05,1.05}},*)AspectRatio -> 1, ImageSize -> Medium]

```

Lg = 100 mm, 800C, Lc = 4 mm



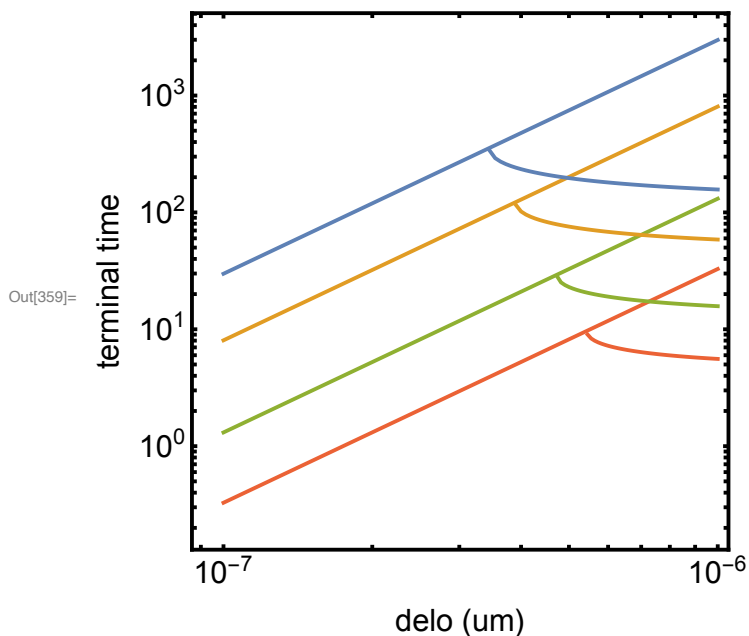
Out[361]=

```

In[358]:= SetOptions[LogTicks, LogPlot → True];
ListLogLogPlot[{timeValDel[[1, 3, 1]], timeValDel[[1, 3, 2]], timeValDel[[1, 3, 3]],
  timeValDel[[1, 3, 4]], timeValDel[[2, 3, 1]], timeValDel[[2, 3, 2]],
  timeValDel[[2, 3, 3]], timeValDel[[2, 3, 4]]}, Joined → True,
PlotStyle → {{Thick, ColorData[97, "ColorList"][[1]]},
  (*{Dashed, ColorData[97, "ColorList"][[1]]}, *)
  {Thick, ColorData[97, "ColorList"][[2]]}, {Thick,
  ColorData[97, "ColorList"][[3]]}, {Thick, ColorData[97, "ColorList"][[4]]}
  (*, {Thick, ColorData[97, "ColorList"][[5]]} *)},
(*PlotMarkers → { Graphics[{EdgeForm[ColorData[97, "ColorList"][[1]]]},
  PolygonMarker["Disk", Offset[5]]}, AlignmentPoint → {0, 0}],
  Graphics[{EdgeForm[ColorData[97, "ColorList"][[2]]]},
  PolygonMarker["Disk", Offset[5]]}, AlignmentPoint → {0, 0}], Graphics[
  {EdgeForm[ColorData[97, "ColorList"][[3]]}, PolygonMarker["Disk", Offset[5]]},
  AlignmentPoint → {0, 0}], Graphics[{EdgeForm[ColorData[97, "ColorList"][[4]]]},
  PolygonMarker["Disk", Offset[5]]}, AlignmentPoint → {0, 0}}], *)
Frame → True, FrameStyle → Directive[Thick, Black],
FrameTicks → {{LogTicks, StripTickLabels[LogTicks]},
  {LogTicks, StripTickLabels[LogTicks]}}, FrameLabel →
  {"terminal time", ""}, {"delo (um)", "Lg = 100 mm, 800C, Lc = 4 mm"}},
BaseStyle → {FontFamily → "Arial", FontSize → 16}, PlotRange → All,
(*PlotRange → {{-2, 202}, {-0.05, 1.05}}, *) AspectRatio → 1, ImageSize → Medium]

```

Lg = 100 mm, 800C, Lc = 4 mm

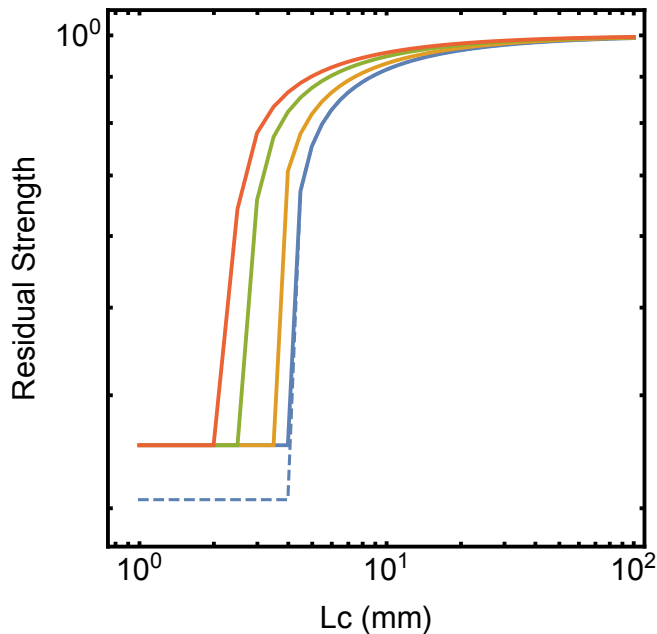



```

In[356]:= (*0.1 atm; 0.1 atm, Lg = 200; 0.2 atm, 0.5 atm, 1 atm *)
SetOptions[LogTicks, LogPlot -> True];
ListLogLogPlot[{Lc801, Lc801b, Lc802, Lc805, Lc810}, Joined -> True,
  PlotStyle -> {{Thick, ColorData[97, "ColorList"][[1]]},
    {Dashed, ColorData[97, "ColorList"][[1]]},
    {Thick, ColorData[97, "ColorList"][[2]]}, {Thick,
      ColorData[97, "ColorList"][[3]]}, {Thick, ColorData[97, "ColorList"][[4]]},
    {Thick, ColorData[97, "ColorList"][[5]]}},
  (*PlotMarkers->{ Graphics[{EdgeForm[ColorData[97,"ColorList"][[1]]],
    PolygonMarker["Disk",Offset[5]]},AlignmentPoint->{0,0}],
  Graphics[{EdgeForm[ColorData[97,"ColorList"][[2]]],
    PolygonMarker["Disk",Offset[5]]},AlignmentPoint->{0,0}], Graphics[
    {EdgeForm[ColorData[97,"ColorList"][[3]]},PolygonMarker["Disk",Offset[5]]},
    AlignmentPoint->{0,0}],Graphics[{EdgeForm[ColorData[97,"ColorList"][[4]]],
    PolygonMarker["Disk",Offset[5]]},AlignmentPoint->{0,0}}},*)
Frame -> True, FrameStyle -> Directive[Thick, Black],
FrameTicks -> {{LogTicks, StripTickLabels[LogTicks]},
  {LogTicks, StripTickLabels[LogTicks]}}, FrameLabel ->
  {"Residual Strength", ""}, {"Lc (mm)", "Lg = 100 mm, 800C, Δo = 0.35 μm"}},
BaseStyle -> {FontFamily -> "Arial", FontSize -> 16}, PlotRange -> All,
(*PlotRange->{{-2,202},{-0.05,1.05}},*)AspectRatio -> 1, ImageSize -> Medium]

```

$L_g = 100 \text{ mm}, 800\text{C}, \Delta_o = 0.35 \mu\text{m}$



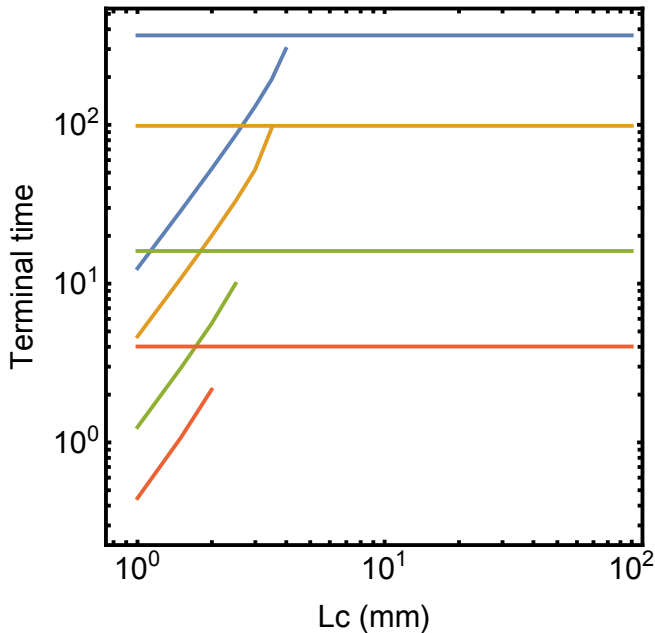
Out[357]=

```

In[354]:= (*0.1 atm; 0.1 atm, Lg = 200; 0.2 atm, 0.5 atm, 1 atm *)
SetOptions[LogTicks, LogPlot -> True];
ListLogLogPlot[{timeValLc[[3, 3, 1]], timeValLc[[3, 3, 2]],
  timeValLc[[3, 3, 3]], timeValLc[[3, 3, 4]], timeValLc[[4, 3, 1]],
  timeValLc[[4, 3, 2]], timeValLc[[4, 3, 3]], timeValLc[[4, 3, 4]]}, Joined -> True,
PlotStyle -> {{Thick, ColorData[97, "ColorList"][[1]]},
  (*{Dashed, ColorData[97, "ColorList"][[1]]}, *)
  {Thick, ColorData[97, "ColorList"][[2]]}, {Thick,
  ColorData[97, "ColorList"][[3]]}, {Thick, ColorData[97, "ColorList"][[4]]}
  (*, {Thick, ColorData[97, "ColorList"][[5]]} *)},
(*PlotMarkers -> { Graphics[{EdgeForm[ColorData[97, "ColorList"][[1]]],
  PolygonMarker["Disk", Offset[5]]}, AlignmentPoint -> {0, 0}],
  Graphics[{EdgeForm[ColorData[97, "ColorList"][[2]]],
  PolygonMarker["Disk", Offset[5]]}, AlignmentPoint -> {0, 0}], Graphics[
  {EdgeForm[ColorData[97, "ColorList"][[3]]}, PolygonMarker["Disk", Offset[5]]}],
  AlignmentPoint -> {0, 0}], Graphics[{EdgeForm[ColorData[97, "ColorList"][[4]]],
  PolygonMarker["Disk", Offset[5]]}, AlignmentPoint -> {0, 0}}], *)
Frame -> True, FrameStyle -> Directive[Thick, Black],
FrameTicks -> {{LogTicks, StripTickLabels[LogTicks]},
  {LogTicks, StripTickLabels[LogTicks]}}, FrameLabel ->
  {"Terminal time", ""}, {"Lc (mm)", "Lg = 100 mm, 800C, Δo = 0.35 μm"}},
BaseStyle -> {FontFamily -> "Arial", FontSize -> 16}, PlotRange -> All,
(*PlotRange -> {{-2, 202}, {-0.05, 1.05}}, *) AspectRatio -> 1, ImageSize -> Medium]

```

$L_g = 100 \text{ mm}, 800\text{C}, \Delta_o = 0.35 \mu\text{m}$



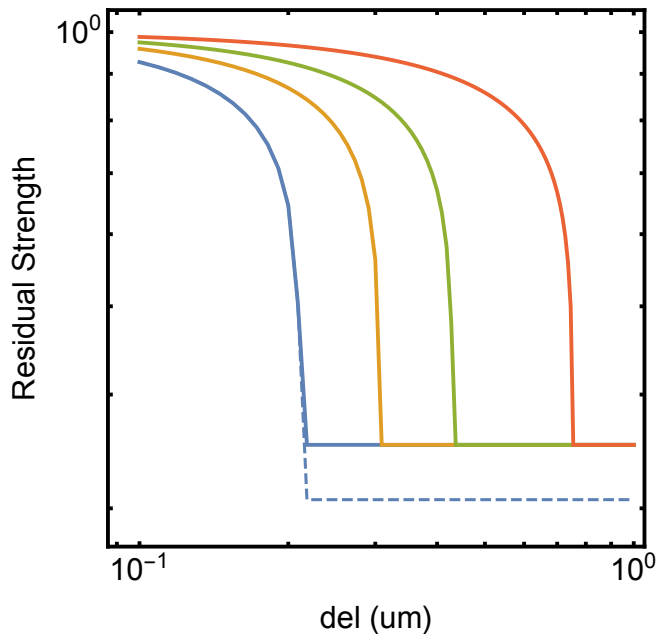
Out[355]=

```

In[352]:= (*700 C; 700C, Lg = 200 mm; 775C; 850C; 1000C*)
SetOptions[LogTicks, LogPlot → True];
ListLogLogPlot[{Lc7011, Lc701b1, Lc775011, Lc85011, Lc10011}, Joined → True,
  PlotStyle → {{Thick, ColorData[97, "ColorList"][[1]]},
    {Dashed, ColorData[97, "ColorList"][[1]]},
    {Thick, ColorData[97, "ColorList"][[2]]}, {Thick,
      ColorData[97, "ColorList"][[3]]}, {Thick, ColorData[97, "ColorList"][[4]]},
    {Thick, ColorData[97, "ColorList"][[5]]}},
  (*PlotMarkers→{ Graphics[{EdgeForm[ColorData[97,"ColorList"][[1]]],
    PolygonMarker["Disk",Offset[5]]},AlignmentPoint→{0,0}],
  Graphics[{EdgeForm[ColorData[97,"ColorList"][[2]]],
    PolygonMarker["Disk",Offset[5]]},AlignmentPoint→{0,0}], Graphics[
    {EdgeForm[ColorData[97,"ColorList"][[3]]},PolygonMarker["Disk",Offset[5]]},
    AlignmentPoint→{0,0}],Graphics[{EdgeForm[ColorData[97,"ColorList"][[4]]],
    PolygonMarker["Disk",Offset[5]]},AlignmentPoint→{0,0}}],*)
Frame → True, FrameStyle → Directive[Thick, Black],
FrameTicks → {{LogTicks, StripTickLabels[LogTicks]},
  {LogTicks, StripTickLabels[LogTicks]}}, FrameLabel →
  {{ "Residual Strength", ""}, {"del (um)", "Lg = 100 mm, 0.1 atm, Lc = 4 mm"}},
BaseStyle → {FontFamily → "Arial", FontSize → 16}, PlotRange → All,
(*PlotRange→{{-2,202},{-0.05,1.05}},*)AspectRatio → 1, ImageSize → Medium]

```

$L_g = 100 \text{ mm}, 0.1 \text{ atm}, L_c = 4 \text{ mm}$

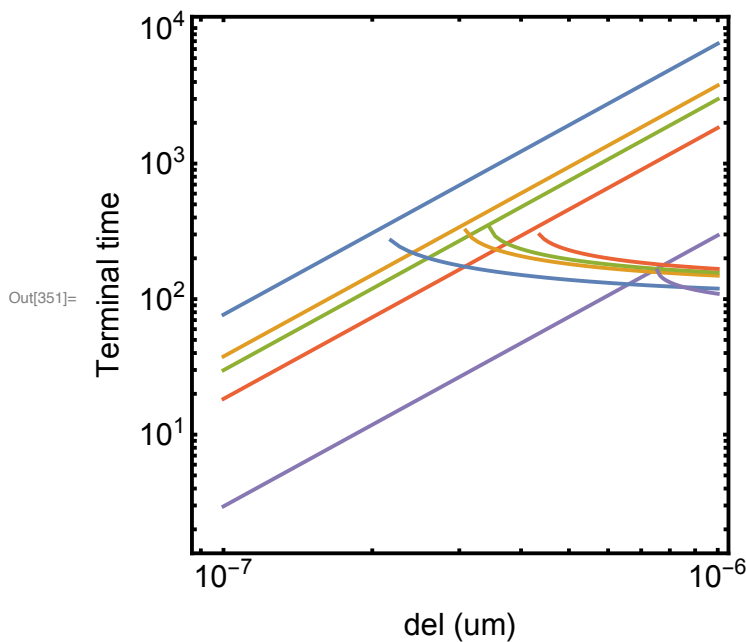


```

In[350]:= (*700 C; 700C, Lg = 200 mm; 775C; 850C; 1000C*)
SetOptions[LogTicks, LogPlot → True];
ListLogLogPlot[{timeValDel[[1, 1, 1]], timeValDel[[1, 2, 1]],
  timeValDel[[1, 3, 1]], timeValDel[[1, 4, 1]], timeValDel[[1, 5, 1]],
  timeValDel[[2, 1, 1]], timeValDel[[2, 2, 1]], timeValDel[[2, 3, 1]],
  timeValDel[[2, 4, 1]], timeValDel[[2, 5, 1]]}, Joined → True,
PlotStyle → {{Thick, ColorData[97, "ColorList" ][[1]]},
  (*{Dashed,ColorData[97,"ColorList" ][[1]]},*)
  {Thick, ColorData[97, "ColorList" ][[2]]}, {Thick,
  ColorData[97, "ColorList" ][[3]]}, {Thick, ColorData[97, "ColorList" ][[4]]},
  {Thick, ColorData[97, "ColorList" ][[5]]}},
(*PlotMarkers→{ Graphics[{EdgeForm[ColorData[97,"ColorList" ][[1]]],
  PolygonMarker["Disk",Offset[5]]},AlignmentPoint→{0,0}],
  Graphics[{EdgeForm[ColorData[97,"ColorList" ][[2]]],
  PolygonMarker["Disk",Offset[5]]},AlignmentPoint→{0,0}], Graphics[
  {EdgeForm[ColorData[97,"ColorList" ][[3]]},PolygonMarker["Disk",Offset[5]]},
  AlignmentPoint→{0,0}],Graphics[{EdgeForm[ColorData[97,"ColorList" ][[4]]],
  PolygonMarker["Disk",Offset[5]]},AlignmentPoint→{0,0}}},*)
Frame → True, FrameStyle → Directive[Thick, Black],
FrameTicks → {{LogTicks, StripTickLabels[LogTicks]},
  {LogTicks, StripTickLabels[LogTicks]}}, FrameLabel →
  {"Terminal time", ""}, {"del (um)", "Lg = 100 mm, 0.1 atm, Lc = 4 mm"}},
BaseStyle → {FontFamily → "Arial", FontSize → 16}, PlotRange → All,
(*PlotRange→{{-2,202},{-0.05,1.05}},*)AspectRatio → 1, ImageSize → Medium]

```

$L_g = 100 \text{ mm}, 0.1 \text{ atm}, L_c = 4 \text{ mm}$

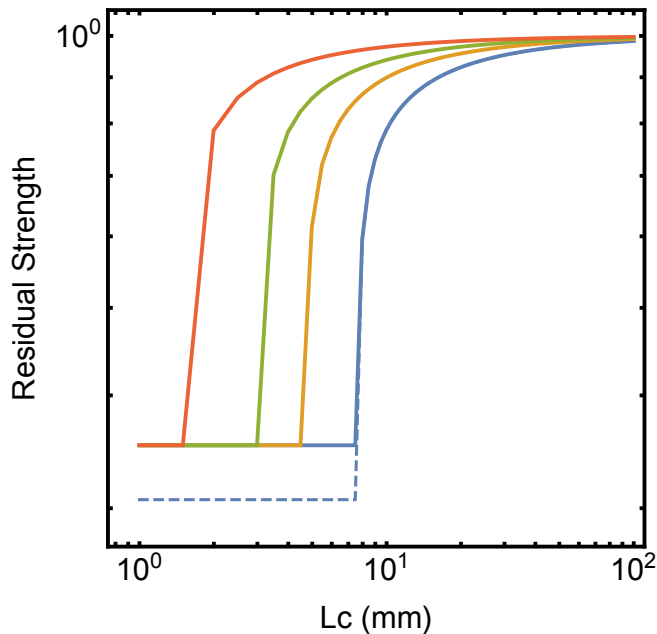


```

In[348]:= (*700 C; 700C, Lg = 200 mm; 775C; 850C; 1000C*)
SetOptions[LogTicks, LogPlot -> True];
ListLogLogPlot[{Lc701, Lc701b, Lc77501, Lc8501, Lc1001}, Joined -> True,
  PlotStyle -> {{Thick, ColorData[97, "ColorList"][[1]]},
    {Dashed, ColorData[97, "ColorList"][[1]]},
    {Thick, ColorData[97, "ColorList"][[2]]}, {Thick,
      ColorData[97, "ColorList"][[3]]}, {Thick, ColorData[97, "ColorList"][[4]]},
    {Thick, ColorData[97, "ColorList"][[5]]}},
  (*PlotMarkers->{ Graphics[{EdgeForm[ColorData[97,"ColorList"][[1]]],
    PolygonMarker["Disk",Offset[5]]},AlignmentPoint->{0,0}],
  Graphics[{EdgeForm[ColorData[97,"ColorList"][[2]]],
    PolygonMarker["Disk",Offset[5]]},AlignmentPoint->{0,0}], Graphics[
    {EdgeForm[ColorData[97,"ColorList"][[3]]},PolygonMarker["Disk",Offset[5]]},
    AlignmentPoint->{0,0}],Graphics[{EdgeForm[ColorData[97,"ColorList"][[4]]],
    PolygonMarker["Disk",Offset[5]]},AlignmentPoint->{0,0}}],*)
  Frame -> True, FrameStyle -> Directive[Thick, Black], FrameTicks ->
    {{LogTicks, StripTickLabels[LogTicks]}, {LogTicks, StripTickLabels[LogTicks]}},
  FrameLabel -> {{ "Residual Strength", ""},
    {"Lc (mm)", "Lg = 100 mm, 0.1 atm, Δo = 0.35 μm"}},
  BaseStyle -> {FontFamily -> "Arial", FontSize -> 16}, PlotRange -> All,
  (*PlotRange->{{-2,202},{-0.05,1.05}},*)AspectRatio -> 1, ImageSize -> Medium]

```

$L_g = 100 \text{ mm}, 0.1 \text{ atm}, \Delta_o = 0.35 \mu\text{m}$

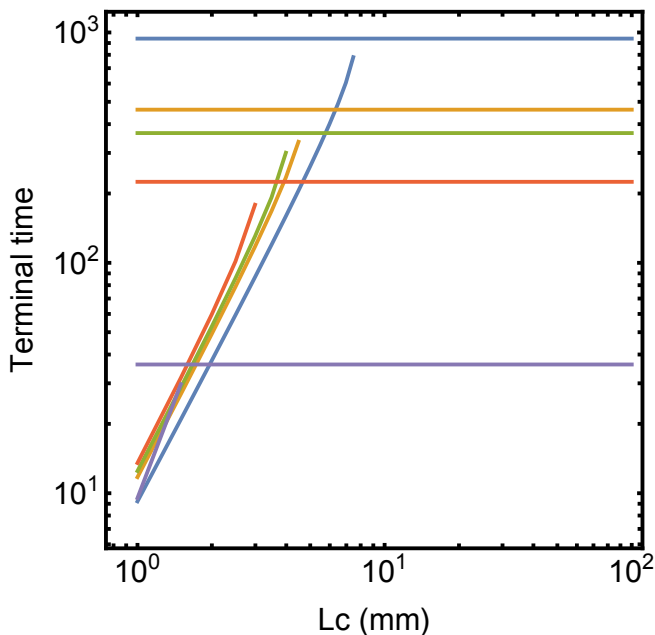


```

In[346]:= (*700 C; 700C, Lg = 200 mm; 775C; 850C; 1000C*)
SetOptions[LogTicks, LogPlot -> True];
ListLogLogPlot[{timeValLc[[3, 1, 1]], timeValLc[[3, 2, 1]],
  timeValLc[[3, 3, 1]], timeValLc[[3, 4, 1]], timeValLc[[3, 5, 1]],
  timeValLc[[4, 1, 1]], timeValLc[[4, 2, 1]], timeValLc[[4, 3, 1]],
  timeValLc[[4, 4, 1]], timeValLc[[4, 5, 1]]}, Joined -> True,
PlotStyle -> {{Thick, ColorData[97, "ColorList"][[1]]},
  (*{Dashed,ColorData[97,"ColorList"][[1]]},*)
  {Thick, ColorData[97, "ColorList"][[2]]}, {Thick,
  ColorData[97, "ColorList"][[3]]}, {Thick, ColorData[97, "ColorList"][[4]]},
  {Thick, ColorData[97, "ColorList"][[5]]}},
(*PlotMarkers->{ Graphics[{EdgeForm[ColorData[97,"ColorList"][[1]]],
  PolygonMarker["Disk",Offset[5]]},AlignmentPoint->{0,0}],
Graphics[{EdgeForm[ColorData[97,"ColorList"][[2]]],
  PolygonMarker["Disk",Offset[5]]},AlignmentPoint->{0,0}], Graphics[
  {EdgeForm[ColorData[97,"ColorList"][[3]]},PolygonMarker["Disk",Offset[5]]},
  AlignmentPoint->{0,0}],Graphics[{EdgeForm[ColorData[97,"ColorList"][[4]]],
  PolygonMarker["Disk",Offset[5]]},AlignmentPoint->{0,0}}},*)
Frame -> True, FrameStyle -> Directive[Thick, Black],
FrameTicks -> {{LogTicks, StripTickLabels[LogTicks]},
  {LogTicks, StripTickLabels[LogTicks]}}, FrameLabel ->
  {"Terminal time", ""}, {"Lc (mm)", "Lg = 100 mm, 0.1 atm, Δo = 0.35 μm"}},
BaseStyle -> {FontFamily -> "Arial", FontSize -> 16}, PlotRange -> All,
(*PlotRange->{{-2,202},{-0.05,1.05}},*)AspectRatio -> 1, ImageSize -> Medium]

```

$L_g = 100 \text{ mm}, 0.1 \text{ atm}, \Delta_o = 0.35 \mu\text{m}$



Out[347]=

Figure 6.6: Domain map of strength contours, time contours

Code

```

In[223]:= DomainMapS[f_, LgIn_, LcIn_, TcIn_, ppIn_] :=
Module[{τs, Δ, TcR, Tc, ppR, pp, Ef, Em, Ec, σmo, Lo, mm,
  R, σfo, mf, Lg, Lc, Lr, λc, λr, δfs, δms, α, σfs, σms, sTh, tc,
  maxStrain, σfrs, compSII, compSI, compVal, output, tSort, lSort},
(*Full pp range*)
(*TcR = Array[#&,144,{TcIn}];
ppR = Flatten[Table[j*10.^(-i),{i,4,1,-1},{j,1.25,10,0.25}],1];*)

(*Smaller pp range*)
TcR = Array[# &, 72, {TcIn}];
ppR = Flatten[Table[j * 10.^(-i), {i, 1, 1, -1}, {j, 1., 10, 0.25}], 1];

τs = 20.; (*MPa*)
Δ = 0.35*^-6; (*m*)
Em = 400.*^3; (*MPa*)
σmo = 100.; (*MPa*)
Lo = 1.; (*m*)
mm = 5.;
R = 5.0*^-6; (*m*)
Ef = 400.0*^3; (*MPa*)
σfo = 1500.; (*MPa*)
mf = 5.;
Lg = LgIn * 1*^-3; (*m*)
Lc = LcIn * 1*^-3; (*m*)

α = 1 / (mf + 1);
Ec = f * Ef + (1 - f) * Em;

δfs = R  $\left(\frac{\sigma_{fo}}{\tau_s}\right)^{\frac{mf}{mf+1}} \left(\frac{Lo}{R}\right)^{\frac{1}{mf+1}}$ ;
δms = R  $\left(\frac{\sigma_{mo}(1-f)}{f * \tau_s}\right)^{\frac{mm}{mm+1}} \left(\frac{Lo}{R}\right)^{\frac{1}{mm+1}}$ ;
σfs = σfo *  $\left(\frac{\tau_s * Lo}{\sigma_{fo} * R}\right)^{\frac{1}{mf+1}}$ ;
σms = σmo  $\left(\frac{f * \tau_s * Lo}{(1-f) * \sigma_{mo} * R}\right)^{\frac{1}{mm+1}}$ ;

maxStrain = (α - ProductLog[-α * Exp[α]]) ^ α;

```

$$\text{compSII} = f * \sigma_{fs} * \left(\frac{\delta_{fs}}{L_g * m_f * E} \right)^{(1/m_f)};$$

(*Find the Lr/Lc value that gives DII behavior
(where strength in domain I == strength in domain II). Lr/Lc must be less than or equal to 0.5. NSolve doesn't work if you try to use mm. This value is independent of environmental conditions*)

$$\text{LrV} = \text{NSolve}\left[\left(\frac{\delta_{fs}}{L_g * m_f * E}\right)^{(1/m_f)} == \frac{(1 - 2 \text{LrLc})^{(1/(m_f + 1))} * \text{maxStrain}}{2} (1 + \text{Exp}[-(\text{maxStrain})^{(m_f + 1)}]) \&\& \text{LrLc} < 0.51, \text{LrLc}, \text{Reals}\right][[1, 1, 2]] * \text{Lc};$$

```
output = Table[Tc = TcR[[i]];
  pp = ppR[[j]];
  (* Calculate the closure time in hours for the given conditions *)
  tc = 1.8^2 * Δ^2 / (4 (1.8 - 1)^2 * Bcomb[Tc + 273, pp]) / 3600;

  (*Find the maximum recession length for the given conditions.*)
  LrM = Δ * LmaxTime[Tc, pp, Δ, 1];
  (*If the recession length at closure is longer than the recession
  length to hit DII then the composite will hit Domain II first
  (disk, blue, -1). If the recession length at closure is smaller than
  needed to hit DII then the composite will seal (diamond, orange, 1).*)
  If[LrM > LrV, sOut = compSII,
    σfrs = σfs * (1 - 2 LrM / Lc)^(1 / (mf + 1));
    sOut = (f * σfrs * maxStrain) / 2 (1 + Exp[-(maxStrain)^(mf + 1)]) (*compSI*);
  {Tc, pp, sOut}, {j, 1, Length[ppR]}, {i, 1, Length[TcR]}
];
Flatten[output, 1]
]
```

```
finBehvT[f_, LgIn_, LcIn_, TcIn_, ppIn_] :=
Module[{τs, Δ, TcR, Tc, ppR, pp, Ef, Em, Ec, σmo, Lo, mm,
  R, σfo, mf, Lg, Lc, Lr, λc, λr, δfs, δms, α, σfs, σms, sTh, tc,
  maxStrain, σfrs, compSII, compSI, compVal, output, tSort, lSort},

  TcR = Array[# &, 72, {TcIn}];
  ppR = Flatten[Table[j * 10.^(-i), {i, 1, 1, -1}, {j, 1., 10, 0.25}], 1];

  τs = 20.; (*MPa*)
  Δ = 0.35*^-6; (*m*)
```



```

Em = 400.*^3; (*MPa*)
σmo = 100.; (*MPa*)
Lo = 1.; (*m*)
mm = 5.;
R = 5.0*^-6; (*m*)
Ef = 400.0*^3; (*MPa*)
σfo = 1500.; (*MPa*)
mf = 5.;
Lg = LgIn * 1*^-3; (*m*)
Lc = LcIn * 1*^-3; (*m*)

α = 1 / (mf + 1);
δfs = R  $\left(\frac{\sigma_{fo}}{\tau_s}\right)^{mf / (mf + 1)} \left(\frac{L_o}{R}\right)^{1 / (mf + 1)}$ ;
maxStrain = (α - ProductLog[-α * Exp[α]]) ^ α;

(*Find the Lr/Lc value that gives DII behavior
 (where strength in domain I = strength in domain II). Lr/Lc must
 be less than or equal to 0.5. NSolve doesn't work if you try to
 use mm. This value is independent of environmental conditions*)

LrV = NSolve[ $\left(\frac{\delta fs}{L_g * mf * E}\right)^{1 / mf} == \frac{(1 - 2 L_r L_c)^{1 / (mf + 1)} * maxStrain}{2}$ 
 (1 + Exp[- (maxStrain) ^ (mf + 1)]) && LrLc < 0.51, LrLc, Reals][[1, 1, 2]] * Lc;

(*If the required recession length (for a given crack spacing)
 is greater than the maximum recession length at closure
 then you'll always get closure for larger crack spacings*)

output = Table[Tc = TcR[[i]];
 pp = ppR[[j]];

 (*Find the maximum recession length for the given conditions.*)
 LrM = Δ * LmaxTime[Tc, pp, Δ, 1];
 (* Calculate the closure time in hours for the given conditions *)
 tc = 1.8^2 * Δ^2 / (4 (1.8 - 1)^2 * Bcomb[Tc + 273, pp]) / 3600;

 If[LrM > LrV, tOut = NSolve[LrV == Δ * LmaxTime[Tc, pp, Δ, tau] && tau < 1.1,
 tau, Reals, 3][[1, 1, 2]] * tc,
 tOut = tc];
 {Tc, pp, tOut}, {j, 1, Length[ppR]}, {i, 1, Length[TcR]}
 ]

```

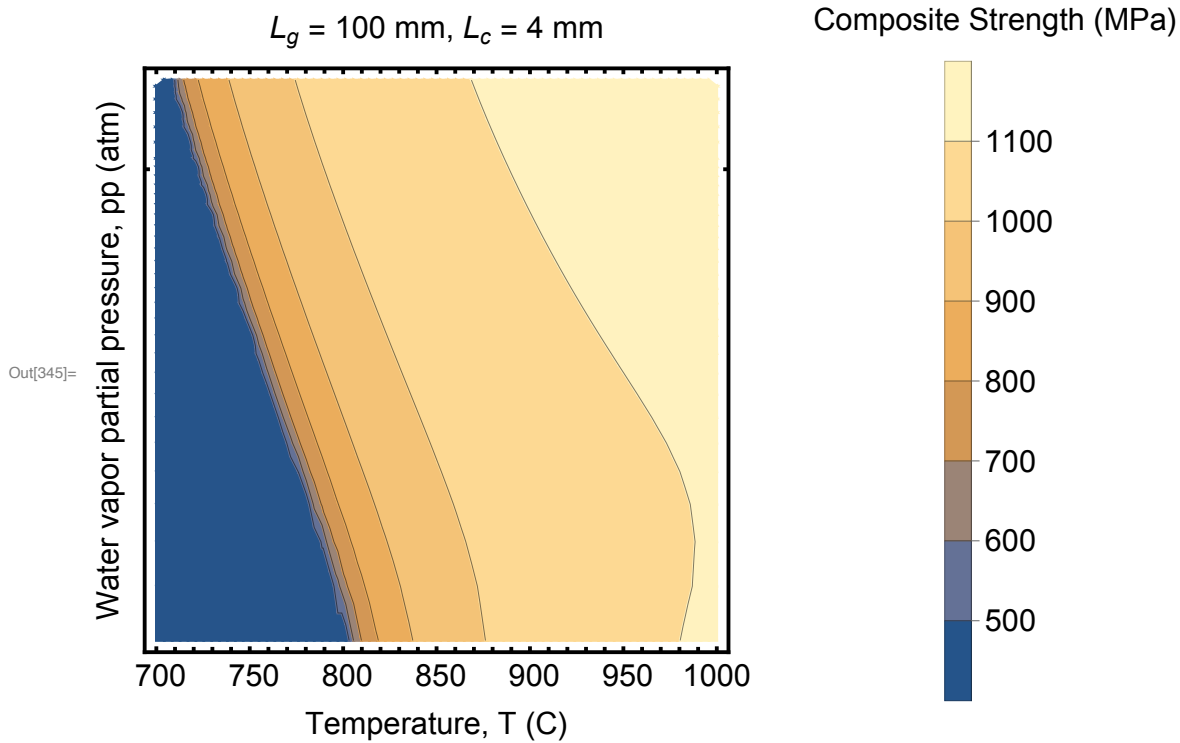
1

Figure

```

In[227]:= dmS2 = DomainMapS[0.3, 100., 4., {700., 1000.}, {0, 1}];
In[345]:= ListContourPlot[dmS2, Frame → True,
  FrameStyle → Directive[Thick, Black], FrameTicks →
    {{LogTicks, StripTickLabels[LogTicks]}, {LinTicks, StripTickLabels[LinTicks]}},
  ScalingFunctions → {None, "Log10"},
  FrameLabel → {"Water vapor partial pressure, pp (atm)", ""},
    {"Temperature, T (C)", "Lg = 100 mm, Lc = 4 mm"}},
  (*Table[ColorData["M10DefaultDensityGradient"][i], {i, 0, 1, 1./8}], *)
  Contours → {500, 600, 700, 800, 900, 1000, 1100},
  PlotLegends → BarLegend[Automatic, LegendLabel → "Composite Strength (MPa)",
  LabelStyle → {Black, FontFamily → "Arial", FontSize → 16},
  BaseStyle → {FontFamily → "Arial", FontSize → 16}, ImageSize → Medium ]

```



```

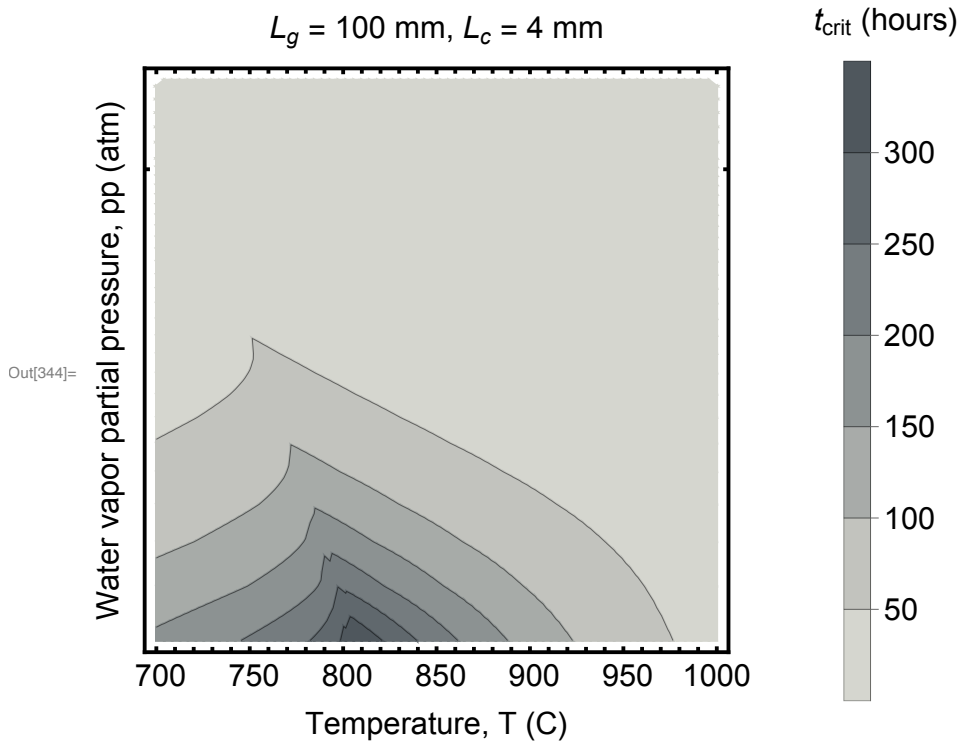
In[225]:= crT32 = Flatten[finBehvT[0.3, 100., 4., {700., 1000.}, {0., 1.}], 1];

```

```

In[344]:= ListContourPlot[crT32, PlotRange → All, Frame → True,
  FrameStyle → Directive[Thick, Black], FrameTicks →
    {{LogTicks, StripTickLabels[LogTicks]}, {LinTicks, StripTickLabels[LinTicks]}},
  ScalingFunctions → {None, "Log10"},
  ContourShading → Table[ColorData["GrayTones"][i], {i, 0.9, 0, -1./11}],
  PlotLegends → BarLegend[Automatic, LegendLabel → "tcrit (hours)",
  LabelStyle → {Black, FontFamily → "Arial", FontSize → 16},
  FrameLabel → {"Water vapor partial pressure, pp (atm)", ""},
    {"Temperature, T (C)", "Lg = 100 mm, Lc = 4 mm"}},
  BaseStyle → {FontFamily → "Arial", FontSize → 42, ImageSize → Medium}

```



Bibliography

- [1] R. Hay and R. Chater, *Oxidation kinetics strength of Hi-Nicalon-S SiC fiber after oxidation in dry and wet air*, *J. Am. Ceram. Soc.* **100** (2017), no. 9 4110–4130.
- [2] C. Ramberg, G. Cruciani, K. Spear, and R. Tressler, *Passive-oxidation kinetics of high-purity silicon carbide from 800°C to 1100°C*, *J. Am. Ceram. Soc.* **79** (1996), no. 11 2897–2911.
- [3] L. Ogbuji and E. Opila, *A comparison of the oxidation kinetics of SiC and Si₃N₄*, *J. Electrochem. Soc.* **142** (1995), no. 3 925–930.
- [4] G. Chollon, *Oxidation behaviour of ceramic fibers from the Si-C-M-O system and related sub-systems*, *J. Euro. Ceram. Soc.* **20** (2000) 1959–1974.
- [5] E. Boakye, P. Mogilevsky, T. Parthasarathy, R. Hay, J. Welter, and R. Kerans, *Monazite coatings on SiC fibers II: Oxidation protection*, *J. Am. Ceram. Soc.* **89** (2006), no. 11 3481–3490.
- [6] B. Deal and A. Grove, *General relationship for the thermal oxidation of silicon*, *Journal of Applied Physics* **36** (1965), no. 12 3770–3778.
- [7] E. Opila, *Variation on the oxidation rate of silicon carbide with vapour pressure*, *J. Am. Ceram. Soc.* **82** (1999), no. 3 625–636.
- [8] R. Hay and R. Corns, *Passive oxidation kinetics for glass and cristobalite formation on Hi-Nicalon-S SiC fibers in steam*, *J. Am. Ceram. Soc.* **101** (2018), no. 11 5241–5456.
- [9] N. Jacobson, G. Morscher, D. Bryant, and R. Tressler, *High temperature oxidation of boron nitride: II, boron nitride layers in composites*, *J. Am. Ceram. Soc.* **82** (1999), no. 6 1473–82.
- [10] A. Bunsell and A. Piant, *A review of the development of three generations of small diameter silicon carbide fibres*, *J. Mater. Sci.* **41** (2006) 823–839.
- [11] F. Zok, *Ceramic-matrix composites enable revolutionary gains in turbine engine efficiency*, *Am. Ceram. Soc. Bull.* **95** (2016), no. 5 22–28.
- [12] P. Wang, F. Liu, H. Wang, L. Hao, and Y. Gou, *A review of third generation SiC fibers and SiC_f/SiC composites*, *J. Mater. Sci. Technol.* **35** (2019) 2743–2750.
- [13] D. B. Marshall and B. N. Cox, *Integral textile ceramic structures*, *Annu. Rev. Mater. Res.* **38** (2008) 425–443.
- [14] M.-Y. He and J. W. Hutchinson, *Crack deflection at an interface between dissimilar elastic materials*, *Int. J. Solids Structures* **25** (1989), no. 9 1053–1067.

- [15] D. Marshall and A. Evans, *Failure mechanisms in ceramic-fiber/ceramic-matrix composites*, *J. Amer. Ceram. Soc.* **68** (1985), no. 5 225–231.
- [16] W. Curtin, *Exact theory of fibre fragmentation in a single-filament composite*, *J. Mat. Sci.* **26** (1991) 5239–5253.
- [17] M. Thouless and A. Evans, *Effects of pull-out on the mechanical properties of ceramic-matrix composites*, *Acta metall.* **36** (1988), no. 3 517–522.
- [18] E. Callaway, P. Christodoulou, and F. Zok, *Deformation, rupture and sliding of fiber coatings in ceramic composites*, *J. Mech. Phys. Solids.* **132** (2019) 103673.
- [19] W. Curtin, *Multiple matrix cracking in brittle matrix composites*, *Acta. Metall. Mater.* **41** (1993), no. 5 1369–77.
- [20] M. Sutcu, *Weibull statistics applied to fiber failure in ceramic composites and work of fracture*, *Acta. Metall.* **37** (1989), no. 2 651–61.
- [21] W. Weibull, *A statistical theory of the strength of materials*, *R Swedish Inst Eng Res* **151** (1939) 1–45.
- [22] W. Weibull, *A statistical distribution function of wide applicability*, *J. Appl. Mech.* **18** (1951) 293–297.
- [23] D. Marshall, B. Cox, and A. Evans, *The mechanics of matrix cracking in brittle-matrix fiber composites*, *Acta. Metall.* **33** (1985), no. 11 2013–21.
- [24] B. Budiansky, J. Hutchinson, and A. Evans, *Matrix fracture in fiber-reinforced ceramics*, *J. Mech. Phys. Solids* **34** (1986), no. 2 167–89.
- [25] W. Gauthier, F. Pailler, J. Lamon, and R. Pailler, *Oxidation of silicon carbide fibers during static fatigue in air at intermediate temperatures*, *J. Am. Ceram. Soc.* **92** (2009), no. 9 2067–2073.
- [26] T. Mah, N. Hecht, D. McCullum, J. Hoenigman, H. Kim, A. Katz, and H. Lipsitt, *Thermal stability of sic fibres (nicalon)*, *J. Mater. Sci.* **19** (1984) 1191–1201.
- [27] A. Elkin and M. Barsoum, *Grain growth and strength degradation of SiC monofilaments at high temperatures*, *J. Mater. Sci.* **31** (1996) 6119–6123.
- [28] R. Naslain, *Design, preparation and properties of non-oxide CMCs for application in engines and nuclear reactors: an overview*, *Compos. Sci. Technol.* **64** (2004) 155–170.
- [29] R. Naslain, R. J.-F. Pailler, and J. L. Lamon, *Single- and multilayered interphases in SiC/SiC composites exposed to severe environmental conditions: An overview*, *Int. J. Appl. Ceram. Technol.* **7** (2010), no. 3 263–275.

- [30] K. Prewo and J. Brennan, *High-strength silicon carbide fibre-reinforced glass-matrix composites*, *J. Mater. Sci.* **15** (1980), no. 2 463–468.
- [31] F. Heredia, J. McNulty, F. Zok, and A. Evans, *Oxidation embrittlement probe for ceramic-matrix composites*, *J. Am. Ceram. Soc.* **78** (1995), no. 8 2097–100.
- [32] D. Poerschke, M. Rossol, and F. Zok, *Intermediate temperature internal oxidation of a SiC / SiCN composite with a polymer-derived matrix*, *J. Am. Ceram. Soc.* **99** (2016), no. 9 3120–3128.
- [33] L. Ogbuji, *A pervasive mode of oxidative degradation in a SiC-SiC composite*, *J. Am. Ceram. Soc.* **81** (1998), no. 11 2777–2784.
- [34] A. Evans, F. Zok, R. McMeeking, and Z. Du, *Models of high-temperature, environmentally assisted embrittlement in ceramic-matrix composites*, *J. Amer. Ceram. Soc.* **79** (1996), no. 9 2345–2352.
- [35] G. Morscher, J. Hurst, and D. Brewer, *Intermediate-temperature stress rupture of a woven Hi-Nicalon, BN-interphase, SiC-matrix composite in air*, *J. Am. Ceram. Soc.* **83** (2000), no. 6 1441–49.
- [36] E. Lara-Curzio, *Stress-rupture of nicalon/SiC continuous fiber ceramic composites in air at 950°C*, *J. Am. Ceram. Soc.* **80** (1997), no. 12 3268–3272.
- [37] R. Hay, *Growth stress in SiO_2 during oxidation of sic fibers*, *J. Appl. Phys.* **111** (2012) 063527.
- [38] W. Xu, F. Zok, and R. McMeeking, *Model of oxidation-induced fiber fracture in SiC/SiC composites*, *J. Am. Ceram. Soc.* **97** (2014), no. 11 3676–3683.
- [39] E. Callaway and F. Zok, *Tensile response of unidirectional ceramic minicomposites*, *J. Mech. Phys. Solids.* **138** (2020) 103903.
- [40] C. Chateau, L. Gélébart, M. Bornert, J. Crépin, E. Boller, C. Sauder, and W. Ludwig, *In situ x-ray microtomography characterization of damage in sicf/sic minicomposites*, *Composites Science and Technology* **71** (2011), no. 6 916–924.
- [41] E. Opila and M. Boyd, *Oxidation of SiC fiber-reinforced SiC matrix composites with a BN interphase*, *Mater. Sci. Forum* **696** (2011) 342–347.
- [42] K. Detwiler and E. Opila, *Oxidation of SiC/BN/SiC ceramic matrix composites in dry and wet oxygen at intermediate temperatures*, *J. Eur. Ceram. Soc.* **42** (2022) 4110–4120.
- [43] P. Carminati, S. Jacques, and F. Rebillat, *Oxidation/corrosion of BN-based coatings as prospective interphases for SiC/SiC composites*, *J. Eur. Ceram. Soc.* **41** (2021), no. 5 3120–31.

- [44] T. Parthasarathy, C. Przybyla, R. Hay, and M. Cinibulk, *Modeling environmental degradation of SiC-based fibers*, *J. Am. Ceram. Soc.* **99** (2016), no. 5 1725–1734.
- [45] R. Filipuzzi and R. Naslain, *Oxidation mechanisms and kinetics of 1D-SiC/C/SiC composite materials:II, modeling*, *J. Am. Ceram. Soc.* **77** (1993), no. 2 467–80.
- [46] T. Parthasarathy, B. Cox, O. Sudre, C. Przybyla, and M. Cinibulk, *Modeling environmentally induced property degradation of SiC/BN/SiC ceramic matrix composites*, *J. Am. Ceram. Soc.* **101** (2018), no. 3 973–997.
- [47] F. Zok, P. Maxwell, K. Kawanishi, and E. Callaway, *Degradation of a SiC-SiC composite in water vapor environments*, *J. Am. Ceram. Soc.* **103** (2020), no. 3 1927–41.
- [48] K. More, P. Tortorelli, L. Walker, N. Miriyala, J. Price, and M. van Roode, *High-temperature stability of SiC-based composites in high-water-vapor-pressure environments*, *J. Am. Ceram. Soc.* **86** (2003), no. 8 1272–1281.
- [49] F. Zok, V. Collier, and M. Begley, *Coating recession effects in ceramic composite strength*, *J. Mech. Phys. Solids* **156** (2021) 104608.
- [50] N. Jacobson, S. Farmer, A. Moore, and H. Sayir, *High temperature oxidation of boron nitride: I, monolithic boron nitride*, *J. Am. Ceram. Soc.* **82** (1999), no. 2 393–398.
- [51] X. Hou, Y. Z., Z. Chen, K.-C. Chou, and B. Zhau, *The reaction mechanism and kinetics of α -BN powder in wet air at 1273 k*, *J. Am. Ceram. Soc.* **96** (2013), no. 6 1877–1882.
- [52] C. Cofer and J. Economy, *Oxidative and hydrolytic stability of boron nitride - a new approach to improving the oxidation resistance of carbonaceous structures*, *Carbon* **33** (1995), no. 4 389–395.
- [53] R. Naslain, A. Guette, F. Rebillat, S. Le Gallet, F. Lamouroux, L. Filipuzzi, and C. Louchet, *Oxidation mechanisms and kinetics of sic-matrix composites and their constituents*, *J. Mater. Sci.* **39** (2004) 7303–7316.
- [54] E. Opila, *Oxidation and volatilization of silica formers in water vapor*, *J. Am. Ceram. Soc.* **86** (2003), no. 8 1238–48.
- [55] E. Opila and R. Hann, *Paralinear oxidation of cvd sic in water vapor*, *J. Am. Ceram. Soc.* **80** (1997), no. 1 197–205.
- [56] E. Opila, *Oxidation-kinetics of chemically vapor-deposited silicon-carbide in wet oxygen*, *J. Am. Ceram. Soc.* **77** (1994), no. 3 730–736.

- [57] O. Flores, R. Bordia, D. Nestler, W. Krenkel, and G. Motz, *Ceramic fibers based on SiC and SiCN systems: Current research, development, and commercial status*, *Adv. Eng. Mater.* **16** (2014), no. 6 621–636.
- [58] J. Schlichting, *Oxygen transport through glass layers formed by a gel process*, *Journal of Non-Crystalline Solids* **63** (1984) 173–181.
- [59] E. Opila, M. Verrilli, and R. Robinson, *Borosilicate glass-induced fiber degradation of SiC/BN/SiC composites exposed in combustion environments*, *Int. J. Appl. Ceram. Technol.* **13** (2016), no. 3 434–442.
- [60] B. McFarland and E. Opila, *Silicon carbide fiber oxidation behavior in the presence of boron nitride*, *J. Am. Ceram. Soc.* **101** (2018), no. 12 5534–5551.
- [61] B. McFarland, V. Avincola, M. Morales, and E. Opila, *Identification of a new oxidation/ dissolution mechanism for boron-accelerated SiC oxidation*, *J. Am. Ceram. Soc.* **103** (2020), no. 9 5214–5231.
- [62] Y. Song, S. Shar, L. Feldman, G. Chung, and J. Williams, *Modified deal grove model for the thermal oxidation of silicon carbide*, *J. Appl. Phys.* **95** (2004), no. 9 4953–4957.
- [63] I. Vickridge, J. Ganem, Y. Hoshino, and I. Trimaille, *Growth of SiO_2 on SiC by dry thermal oxidation: Mechanisms*, *J. Phys. D: Appl. Phys.* **40** (2007) 6254–6263.
- [64] T. Narushima, T. Goto, and T. Hirai, *High-temperature passive oxidation of chemically vapor deposited silicon carbide*, *J. Am. Ceram. Soc.* **72** (1989), no. 8 1386–1390.
- [65] E. Opila, *Influence of alumina reaction tube impurities on the oxidation of chemically-vapor-deposited silicon carbide*, *J. Am. Ceram. Soc.* **78** (1995), no. 4 1107–1110.
- [66] D. S. Fox, *Oxidation behavior of chemically-vapor-deposited silicon carbide and silicon nitride from 1200 to 1600 c*, *Journal of the American Ceramic Society* **81** (1998), no. 4 945–950.
- [67] P. J. Jorgensen, M. E. Wadsworth, and I. B. Cutler, *Effects of water vapor on oxidation of silicon carbide*, *Journal of the American Ceramic Society* **44** (1961), no. 6 258–261.
- [68] J. A. Costello and R. E. Tressler, *Oxidation kinetics of silicon carbide crystals and ceramics: I, in dry oxygen*, *Journal of the American Ceramic Society* **69** (1986), no. 9 674–681.
- [69] H. Ichikawa, *Polymer-derived ceramic fibers*, *Annu. Rev. Mater. Res.* **46** (2016) 335–356.

- [70] R. Hay, *Crystallization kinetics for SiO_2 formed during SiC fiber oxidation in steam*, *J. Am. Ceram. Soc.* **102** (2019) 5587–5602.
- [71] D. Poirier and G. Geiger, *Transport Phenomena in Materials Processing*. The Minerals, Metals & Materials Society, 2016.
- [72] E. Turkdogan, P. Grieveson, and L. Darken, *Enhancement of diffusion-limited rates of vaporization of metals*, *J. Phys. Chem* **67** (1963), no. 8 1647–1654.
- [73] J. Hastie, *High Temperature Vapors: Science and Technology*. Academic Press, 1 ed., 1975.
- [74] K. Klinecicz and R. Reid, *Estimation of critical properties with group contribution methods*, *AIChE Journal* **30** (1984), no. 1 137–142.
- [75] R. Reid, J. M. Prausnitz, and T. Sherwood, *The Properties of Gases and Liquids*. McGraw-Hill, 3 ed., 1977.
- [76] “Chemspider.” <http://chemspider.com>, 2021. Online.
- [77] D. Poerschke, M. Rossol, and F. Zok, *Intermediate temperature oxidative strength degradation of a SiC/SiNC composite with a polymer-derived matrix*, *J. Am. Ceram. Soc.* **100** (2017), no. 4 1606–17.
- [78] G. Morscher and J. Cawley, *Intermediate temperature strength degradation in SiC/SiC composites*, *J. Eur. Ceram. Soc.* **22** (2002), no. 14-15 2777–87.
- [79] O. Gavaldà Diaz, K. Marquardt, S. Harris, L. Gale, L. Vandeperrr, E. Saiz, and F. Guiliani, *Degradation mechanisms of SiC/BN/SiC after low temperature humidity exposure*, *J. Eur. Ceram. Soc.* **40** (2020) 3863–3874.
- [80] F. Lamouroux, R. Naslain, and J. Jouin, *Kinetics and mechanisms of oxidation of 2d woven C/SiC composites: II, theoretical approach*, *J. Am. Ceram. Soc.* **77** (1994), no. 8 2058–68.
- [81] N. Jacobson, D. Fox, and E. Opila, *High temperature oxidation of ceramic matrix composites*, *Pure and Appl. Chem.* **70** (1998), no. 2 493–500.
- [82] G. Morscher, *Tensile stress rupture of SiCf/SiCm minicomposites with carbon and boron nitride interphases at elevated temperatures in air*, *J. Am. Ceram. Soc.* **42** (1997), no. 8 2029–2042.
- [83] H. Hatta, T. Sohtome, Y. Sawada, and A. Shida, *High temperature crack sealant based on $\text{SiO}_2\text{-B}_2\text{O}_3$ for SiC coating on carbon-carbon composites*, *Adv. Compos. Mater.* **12** (2003), no. 2-3 93–106.

- [84] P. Meschter, E. Opila, and N. Jacobson, *Water vapor-mediated volatilization of high-temperature materials*, *Annu. Rev. Mater. Res.* **43** (2013), no. 1 559–88.
- [85] M. Chase, *NIST-JANAF thermochemical tables*. American Institute of Physics for the National Institute of Standards and Technology, Washington, D.C., 4th ed., 1998.
- [86] T. Rockett and W. Foster, *Phase relations in the system boron oxide-silica*, *J. Am. Ceram. Soc.* **48** (1965), no. 2 75–80.
- [87] V. Collier, W. Xu, R. McMeeking, F. Zok, and M. Begley, *Recession of BN coatings in SiC/SiC composites through reaction with water vapor*, *J. Am. Ceram. Soc.* **105** (2021), no. 1 498–511.
- [88] K. Sevener, J. M. Tracy, Z. Chen, J. Kiser, and S. Daly, *Crack opening behavior in ceramic matrix composites*, *J. Am. Ceram. Soc.* **100** (2017) 4734–47.
- [89] C. Chateau, L. Gélébart, M. Bornert, J. Crépin, D. Caldemaison, and C. Sauder, *Modeling of damage in unidirectional ceramic matrix composites and multi-scale experimental validation on third generation SiC/SiC minicomposites*, *J. Mech. Phys. Solids* **63** (2014) 298–319.
- [90] C. Hui, S. Phoenix, M. Ibnabdeljalil, and R. Smith, *An exact closed form solution for fragmentation of weibull fibers in a single filament composite with applications to fiber-reinforced ceramics*, *J. Mech. Phys. Solids.* **43** (1995), no. 10 1551–85.
- [91] W. Curtin, *Theory of mechanical properties of ceramic-matrix composites*, *J. Am. Ceram. Soc.* **74** (1991), no. 11 1837–85.
- [92] R. Cook, D. Malkus, M. Plesha, and R. Witt, *Concepts and Applications of Finite Element Analysis*. Wiley, 4 ed., 2002.